Expanding Weldability of Similar and Dissimilar Thin Sheets by Arc Welding Processes

Swagat Dwibedi

Department of Mechanical Engineering

Indian Institute of Technology Guwahati

January 2026


भारतीय प्रौद्योगिकी संस्थान गुवाहाटी
Indian Institute of Technology Guwahati

Expanding Weldability of Similar and Dissimilar Thin Sheets by Arc Welding Processes

submitted in partial fulfilment of the requirements
for the degree of

Doctor of Philosophy

by

Swagat Dwibedi

(166103014)

Supervisor

Prof. Swarup Bag

Department of Mechanical Engineering

Indian Institute of Technology Guwahati

January 2026

TH-3924_166103014

Department of Mechanical Engineering
Indian Institute of Technology Guwahati
Guwahati-781039
INDIA

CERTIFICATE

It is certified that the work contained in the thesis entitled **"Expanding Weldability of Similar and Dissimilar Thin Sheets by Arc Welding Processes"** submitted by **Mr. Swagat Dwibedi** to the Indian Institute of Technology Guwahati for the award of the degree of Doctor of Philosophy has been carried out under my supervision in the Department of Mechanical Engineering, Indian Institute of Technology Guwahati. This work has not been submitted elsewhere for the award of any other degree or diploma.

The thesis, in my opinion, has reached the standard fulfilling the requirements for the award of degree of Doctor of Philosophy in accordance with the regulations of the Institute.

Date: 30-01-2026

Swarup Bag

Department of Mechanical Engineering,
Indian Institute of Technology Guwahati,
Guwahati, Assam 781039, India

Thesis Approval Sheet

The thesis entitled

Expanding Weldability of Similar and Dissimilar Thin Sheets by Arc Welding Processes

by

Swagat Dwibedi

is approved for the degree of **Doctor of Philosophy**

Examiners

Supervisor

Chairman

Date: 30-01-2026

Place: IIT Guwahati


भारतीय प्रौद्योगिकी संस्थान गुवाहाटी
Indian Institute of Technology Guwahati

Declaration

I declare that the present written submission is my thoughts in my own words. I have adequately been cited and referenced the original sources, where others' ideas have been involved. I also declare that I have followed to all principles of academic morality and honesty and have not neither fabricated nor falsified any idea/data in the present thesis. I realize that any defilement of the above will be cause for disciplinary action by the Institute and can also induce disciplinary action from the sources which have thus not been properly cited.

Date: 30-01-2026 **Swagat Dwibedi**

Roll No: 166103014

Indian Institute of Technology Guwahati

भारतीय प्रौद्योगिकी संस्थान गुवाहाटी • Indian Institute of Technology Guwahati •

Acknowledgement

This thesis results from research carried out at the Indian Institute of Technology Guwahati. I want to express my heartfelt gratitude to all those who supported and assisted me throughout my research. Their encouragement and generosity played a vital role in the successful completion of this thesis, and I am genuinely thankful for the time and help they so kindly offered.

I sincerely appreciate *Prof. Shyamanta M. Hazarika*, Head of the Department, for extending all necessary facilities in department. I want to thank my doctoral committee chairman, *Prof. R. Ganesh Narayanan*, for his valuable suggestions and encouragement during the PhD work. Also, I would like to thank my doctoral committee member *Prof. S. K. Majumder*, for his constructive criticisms and helpful suggestions, which improved the research work. I would also like to express my sincere gratitude to *Prof. Santosha K. Dwivedy* (former Head of the Department) for his invaluable support during my Ph.D.

I would like to acknowledge the experimental facility provided by the Mechanical Engineering Department, Material Science Lab, Advanced Manufacturing Lab, Central Workshop, and Central Instruments Facility (CIF) of IIT Guwahati. The FESEM instrumentation facility provided by the Northeast Centre for Biological Sciences and Healthcare Engineering (NECBH) and the Department of Biotechnology (DBT) of IIT Guwahati is also gratefully acknowledged. Additionally, I would like to acknowledge the National Facility for Texture and OIM Laboratory, IIT Bombay, for EBSD characterization and residual stress measurement. Further, the facility provided by Central Research Facility (CRF), VSSUT, Burla, for the use of SEM and Central Research Facility (CRF), IIT Kharagpur, for the use of XCT is gratefully acknowledged.

I would like to gratefully acknowledge Dr. Sidananda Sarma (CIF) for generously allocating FESEM/EDX slots whenever needed. I also want to take this opportunity to sincerely thank all the technical supervisors, especially Mr. Dilip Chetri, Mr. Gwmchar Baro, Mr. Saiffudin Ahmed, and Mr. Jiten Basumatary for their invaluable assistance in providing the essential equipment required for my work. I would also like to thank my seniors, batchmates, and juniors, especially Uttam Kumar Tarai, Mayuri Baruah, Ajit Kumar Sahu, Soumya Ranjan Nanda, Saibal Kanchan Barik, Ankan Mishra, Akshay Namdeo, Sunil Kumar Biswal, Vivekananda Haldar, Dipankar Saha, Debtanay Das, Avadh Kishore Prasad, Umesh Melkani, Hritaban Acharya, Gaurav Prakash, Akshay Kumar Soni, Vikas Bhushan, and Vipin Kumar Mishra for their help and support throughout different phases of my doctoral work. I would also like to thank one of my students, Suraj Prasad, for assisting in the NPTEL courses. I would also like to take this opportunity to extend my heartfelt thanks to Amrit Das for his invaluable support in providing meals during the final phases of my Ph.D.

Help extended during experimentation by Ayushman Singh Bhadouriya, Deepak Kumar Lodhi, Arindam Kalita, Vishal Jha, and Trishna Bhattacharya are gratefully acknowledged. I would also like to acknowledge the assistance provided by Jahwat Naz and Vikrant Pratap Singh to prepare few samples for microstructural analysis. Special thanks to Ayushman Singh Bhadouriya for his assistance in preparing samples for microstructural analysis.

I would also like to acknowledge Subhadra Sahoo and Nilakantha Sahu for conducting the corrosion testing. I am also grateful to Dr. Momita Das for her time in capturing numerous FESEM images. Help extended by Mr. Subhodeep Jana in carrying out the XCT testing is also gratefully acknowledged. Special thanks to Saibal Kanchan Barik and Vivekananda Haldar for conducting the tensile testing and Gaurav Prakash for his valuable time in conducting the elemental testing. Thanks to Vikrant Pratap Singh for assisting with FESEM imaging for few of my samples. I would also like to specially acknowledge instrument operator Kishore Talukdar, Manoj Kumar Dhal and Koushik Jena.

I would also like to acknowledge the valuable and insightful technical discussions with my Sunil Pathak, Mayuri Baruah, Suyog Jhavar, Uttam Kumar Tarai, Ajit Kumar Sahu, Subhasis Pradhan, Nilakantha Sahu, Vivekananda Haldar, and Dipankar Saha. A big thanks to Vikas Bhushan for consistently being my human alarm clock! Lastly, help extended by Late Minaketan Behera for the use of the SEM facility at VSSUT, Burla, is deeply acknowledged. I would also like to specially thank Himalaya Meher and Shasanka Sekhar Dalai for their support and assistance in various ways.

Most importantly, I am deeply grateful to my parents, my parents-in-law, my wife, and my elder sister for their constant support and encouragement. I am also thankful to my daughter, my son, and my niece for their love. Last but not least, I would like to thank the Supreme Lord for providing me with opportunities throughout my life.

Dedicated to

My Parents (Shri Girija Shankar and Smt. Sudharani),

My Wife (Ipsita), My Daughter (Sharanya), My Son (Shritik),

My Elder Sister (Swati), and My Niece (Shivanya)

भारतीय प्रौद्योगिकी संस्थान गुवाहाटी
Indian Institute of Technology Guwahati

Abstract

Imperfections present in a weld joint critically influence the reliability of the welded structure, which correspond to the failure of the component. Therefore, identification of the defects becomes essential to prevent catastrophic failures. The present investigation aims to explore the joining capability for similar ($Cu_{90}Ni_{10}$) and dissimilar (Cu-SS and SS316L-SS310) combinations of materials using arc-based joining techniques. Firstly, micro-plasma arc welding (M-PAW) of $Cu_{90}Ni_{10}$ thin sheets is established using continuous and pulse current modes. The work focuses on controlling defect formation by applying the least heat supplied. Further enhancement in joint features is attained by better control over the average heat supplied using pulse mode. Using pulse current provides better results in terms of the least depletion of metal, fine equiaxed morphology with reduced secondary dendritic arm spacing, and the lowest number of internal pores. Secondly, the current investigation highlights the importance of arc offset in fabricating bimetallic joints of ferrous (SS304) and non-ferrous (Cu-T2) metals using the gas tungsten arc welding (GTAW) process. The outcome of the current experimental evaluation aids in understanding the significance of arc offset and heat input in achieving a bimetallic joint with sound microstructural and mechanical properties. As the arc offset value increases, the amount of Cu percentage also increases, and the joining mode modifies from welding to weld-brazing mode. Also, excessive heat input causes the formation of solidification cracks, significantly reducing the joint efficiency.

The present investigation also explores the M-PAW process to join a different combination of austenitic stainless steels (ASSs) (SS316L and SS310). It aims to establish a correlation linking the influence of heat input on the formation of different microstructural morphology, variation in joint strength, mode of failure, pore formation and to ensure weld joint remains free from internal defects, hot-cracking, and sensitization. The present work also establishes the role of solidification behaviour on solid-state phase transformation (SSPT) and its effect on the generation of compressive residual. The outcome of the current experiment suggests that a lower level of heat input allows the formation of a high amount of delta ferrite, which generates comparatively more compressive stress as a disparity in thermal expansion coefficient ($\alpha_{Ni} \sim 1.6\ \alpha_{Cr}$) and aids in the reduction of residual stress. Overall, the present work attempts to understand the solidification behaviour as well as its correlation with microstructural features and residual stress distribution for similar and dissimilar fusion welding processes.

Keywords: Solidification cracking, porosity, failure mode, chemical stability, thermo-metallurgical-mechanical model.

TH-3924_166103014

भारतीय प्रौद्योगिकी संस्थान गुवाहाटी • Indian Institute of Technology Guwahati •

Graphical Abstract

Micro-plasma arc welding of 0.7 mm thick $\text{Cu}_{90}\text{Ni}_{90}$ alloy.

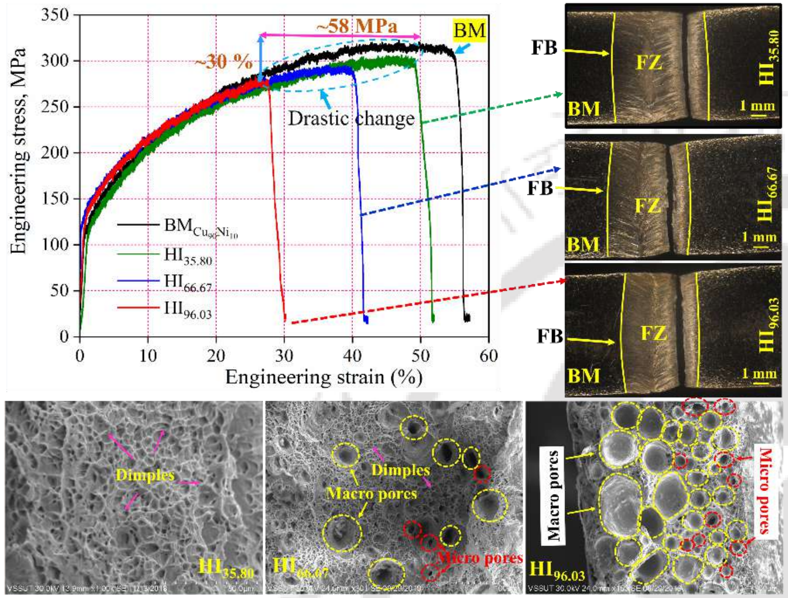

- **Heat input** plays a significant role in the joining of $\mathbf{Cu_{90}Ni_{10}}$ alloy.
- With the increase in heat input, the joint properties declines due to higher pore formation, depletion of material, and increased dendritic arm spacing.

Gas tungsten arc welding of 1 mm thick Cu(T2) and SS304 sheets.

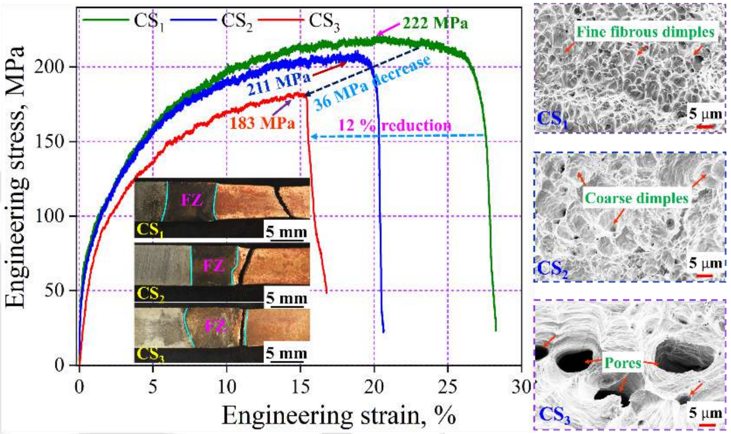

- **Arc offset** is the most dominant factor governing the joining mode and joint properties of **Cu-SS bimetallic joints**.
- With the increase in arc offset (towards Cu-side), the Cu-content increases and the joining mode changes from welding to weld-brazing, which negatively impacts the joints.

Stress generation associated with microstructural evolution

$\gamma_{\text{austenite}}$ matrix	δ_{ferrite} rich dendritic core
$\alpha_{\text{Ni}} \sim (15\text{-}17.5) \times 10^{-6}\ K^{-1}$	$\alpha_{\text{Cr}} \sim (9\text{-}11) \times 10^{-6}\ K^{-1}$
More Ni, Less Cr	More Cr, Less Ni
Tensile stress + + + +	Compressive stress − − − −

- **SSPT** helps to understand the solidification behavior of dissimilar austenitic stainless steel **(SS316L-S310)** joints, which enhances the prediction accuracy of residual stress.
- The difference in the magnitude of the thermal expansion coefficient ($\alpha_{\text{Ni}} \sim 1.6\ \alpha_{\text{Cr}}$) corresponds to tensile residual stress in the γ-region (where Ni % is high) and compressive stress in the dendritic core (where Cr % is high).

Micro-plasma arc welding of dissimilar austenitic stainless steel thin sheets (0.8 mm SS316L and 0.6 mm SS310).

भारतीय प्रौद्योगिकी संस्थान गुवाहाटी • Indian Institute of Technology Guwahati •

CONTENTS

Indian Institute of Technology Guwahati

Indian Institute of Technology Guwahati

Indian Institute of Technology Guwahati

List of Figures

Indian Institute of Technology Guwahati

List of Tables

List of Abbreviations

Abbreviation	Description
RSW	Resistance spot welding
GMAW	Gas metal arc welding
GTAW	Gas tungsten arc welding
M-PAW	Micro-plasma arc welding
LBW	Laser beam welding
EBW	Electron beam welding
HAZ	Heat-affected zone
DOP	Depth of penetration
FB	Fusion boundary
FZ	Fusion zone
ASSs	Austenitic stainless steels
TMM	Thermal-metallurgical-mechanical
CC	Continuous current
FEM	Finite element method
SSPT	Solid-state phase transformation
NDT	Non-destructive testing
OM	Optical microscope
FESEM	Field emission scanning electron microscope
EDX	Energy dispersive X-ray analysis
EBSD	Electron backscattered diffraction
XRD	X-ray diffraction
X-ray CT	X-ray computed tomography
ASME	American Society of Mechanical Engineers
PAW	Plasma arc welding
PC-M-PAW	Pulsed current micro-plasma arc welding
PC	Pulsed current
CC-M-PAW	Continuous current micro-plasma arc welding
CR	Cooling rate
FCC	Face centered cubic
SAW	Submerged arc welding
FCAW	Flux cored arc welding

TH-3924_166103014

Abbreviation	Description
USW	Ultrasonic welding
SDAS	Secondary dendritic arm spacing
UTS	Ultimate tensile strength
EL	Elongation
LCS	Low carbon steel
DMWs	Dissimilar metal welds
GB	Grain boundary
FDM	Finite difference method
CMM	Coordinate-measuring machine
UTM	Universal testing machine
BOP	Bead on plate
DAS	Data acquisition system
DC	Direct current
DCEN	Direct current electrode negative
DT	Destructive testing
SOD	Stand-off distance
IPF	Inverse pole figure
BM	Base metal
VHN	Vickers hardness number
JMAK	John-Mehl-Avrami-Kolmogorov
TTT	Temperature-Time-Transformation
AGS	Average grain size
LAGB	Low angle grain boundary
HAGB	High angle grain boundary
MTD	Maximum texture density
PMZ	Partially melted zone
MUZ	Melted-unmixed zone
RIR	Reference Intensity ratio
PDAS	Primary secondary arm spacing
AF	Austenitic-ferritic
FA	Ferritic-austenitic
BCC	Body centered cubic

Nomenclature

Symbol	Description	Unit
I_p	Peak current	A
I_b	Base current	A
t_{on}	Arc-on time	s
t_{off}	Arc-off time	s
G	Temperature gradient	K/mm
R	Solidification rate	mm/s
$\mathrm{T}_{\mathrm{Liquidus}}$	Liquidus temperature	K
D_{e}	Electrode diameter	mm
D_{n}	Nozzle diameter	mm
W_{c}	Welding current	A
W_{s}	Welding speed	mm/s
F_{p}	Plasma gas flow rate	lpm
F_{s}	Shielding gas flow rate	lpm
V	Voltage	V
$\mathrm{I}_{\mathrm{avg.}}$	Average current	A
Y	Elastic modulus	Pa
υ	Poisson's ratio	-
ψ	Angle between the bisector of incident and diffracted rays	°
d^{o}	Unstrained lattice spacing	Å
d^{ψ}	Strained lattice spacing	Å
k	Thermal conductivity	W/mK
$\dot{\mathrm{h}}_{\mathrm{generation}}$	Volumetric heat generation	$\mathrm{W/m^3}$
v_{w}	welding velocity vector	mm/s
ρ	Density	$\mathrm{kg/m^3}$
C_{p}	Specific heat	J/kgK
T	Temperature	K
$\partial T/\partial t$	Rate of change of temperature	K/s
$\partial T/\partial x$	Temperature gradient	K/mm
h	Heat transfer coefficient	$\mathrm{W/m^2K}$

भारतीय प्रौद्योगिकी संस्थान गुवाहाटी
Indian Institute of Technology Guwahati

Symbol	Description	Unit
σ	Stefan-Boltzmann constant	W/m^2K^4
ε	Emissivity	-
$\dot{q}_f, \dot{q}_r$	Volumetric generation of heat at the front and rear ellipsoids	W/m^2
f_f, f_r	Portion of the heat flux delivered corresponding to front and rear ellipsoids	-
a_f, a_r	Heat source from center to the front and rear ellipsoids	mm
b	Half weld width	mm
c	Penetration depth	mm
p	Power intensity factor	-
r_{eff}	Effective radius of the plasma arc	mm
d_p	Penetration depth	mm
t	Thickness	mm
$U_{(x)}, U_{(y)}, U_{(z)}$	Deflection along x, y, and z axis	mm
ε_{ij}^{total}	Total strain increment	-
b_i^f	Body force vector	N
ε_{ij}^{e}	Elastic strain	-
ε_{ij}^{thm}	Thermal strain	-
ε_{ij}^{p}	Plastic strain	-
$\Delta\varepsilon_{ij}^{pt}$	Phase transformation-induced strain	-
$T_{solidus}$	Solidus temperature	K
$f'_{\gamma}(T_{(t)})$	Phase proportion of the austenitic phase at a temperature (T) and time (t)	-
$k_{\delta\rightarrow\gamma}$	Nucleation and growth rate	-
$n_{\delta\rightarrow\gamma}$	Avrami coefficient to account for the nucleation, followed by growth	-
$f_{\gamma}^{eq.}$	Maximum value of the phase proportion of the γ-phase at the equilibrium stage	-
$T_{\gamma s}, T_{\gamma f}$	$\delta_{ferrite}$ dissolution starts (1673 K) and finish temperature (1273 K)	K
τ_f^*	Fictitious time	s

Indian Institute of Technology Guwahati

Symbol	Description	Unit
$\varepsilon^{\Delta vt}$	Volumetric strain brought on by SSPT during the cooling stage	-
$\Delta f'_{\gamma}$	Instantaneous change in the phase fraction of the austenite phase	-
α_{pt}	Expansion coefficient corresponding to SSPT	K^{-1}
$A_{\delta'}, A_{\gamma'}$	Lattice constant of δ- and γ-phases	-
α	Coefficient of thermal expansion	K^{-1}
$T_{melting}$	Melting temperature	K
$HI_{35.80}$, $HI_{66.67}$, $HI_{96.03}$	Selected process parameters for the similar joining of cupronickel at 35.80, 66.67, and 96.03 J/mm heat input value.	J/mm
P_{min}, P_{max}	Minimum and maximum pore size	µm
N_{pores}	Total number of pores	-
E_{corr}	Potential	V
I_{corr}	Current density	$A.cm^{-2}$
E_p	Passivation voltage	V
R_a	Surface roughness	µm
S11, S22	Components of residual stress	Pa
CS_1, CS_2, CS_3	Selected process parameters for the dissimilar joining of Cu and SS304 at 1.3, 2.0, and 2.7 mm arc offset values.	-
L_{52}, M_{63}, H_{77}	Selected process parameters for the dissimilar joining of ASSs at 52, 63, and 77 J/mm heat input values.	J/mm
W_{top}	Weld dimensions at the top	mm
W_{root}	Weld dimensions at the bottom	mm
$Cr_{eq.}$	Chromium equivalent	-
$Ni_{eq.}$	Nickel equivalent	-

भारतीय प्रौद्योगिकी संस्थान गुवाहाटी • Indian Institute of Technology Guwahati •

Chapter 1

Introduction

1.1 General background

In the present-day scenario, increased miniaturization and micro-joining go hand in hand. The successful joining of micro-components is the primary requirement for success at the micro-scale. Micro-joining finds application in bio-medical implants, sensors, transducers, optoelectronics, and batteries (Zhou, 2008). Although the micro-joint design remains the same as traditional joining methods, researchers employ various micro-joining techniques to outperform the task. Multiple processes have been explored in manufacturing to accomplish sound weld joints at the micro-level with minimal distortion. Recent techniques are being employed to advance further in the field of welding science and technology (Hu et al., 2019; Zhou et al., 2009). Under liquid-state joining processes, resistance-based (resistance spot welding: RSW (Kumar et al., 2022b; Prasad et al., 2024)), arc-based (gas metal arc welding: GMAW (Das et al., 2023), gas tungsten arc welding: GTAW (Nevcanoğlu et al., 2021), micro-plasma arc welding: M-PAW (Aumpiem and Prateepasen, 2021; Prasad et al., 2011) and high-energy beam density (laser beam welding: LBW (Kumar et al., 2022a), electron beam welding: EBW (Nayak and Roy, 2021)) based techniques are employed to join thin sheets (Baruah, 2017).

In the past two decades, the M-PAW and GTAW processes have evolved as an emerging technique for joining thin sheets, providing benefits comparable to high-energy beam density processes (LBW and EBW) at a relatively low cost. Several purposes are achieved with thin sheets, thus tempting researchers to find new techniques for joining thin sheets with minimum defect and high strength (Sahu, 2021). To analyse the current research status on M-PAW and GTAW processes and form a bridge between the current and previous work, the entire research work is divided into two phases: the research work carried out between 2001-2015 is represented as 'previous work' and the research conducted in between 2016-2025 is termed as 'current work.' The significant differences between current and previous research work feature the (a) volume of study carried out on the M-PAW and GTAW processes, (b) extent of research analysis on similar/dissimilar joints, and (c) type of materials explored.

It may be noted that a substantial escalation is observed in the volume of studies carried out on the M-PAW process. An increase of more than three times achieved for the current work (2016-2024: 43 publications) compared to previous work (2001-2015: 14 publications), suggesting a significant increase in implementing the M-PAW process to join thin sheets. Materials explored to join similar and dissimilar thin sheets using the M-PAW process include a wide range of different materials/grades (Steel, Inconel, Aluminum, and Titanium). Similar combination of materials includes Aluminum alloys, (AMg2, AMg4, AMg5, AMg6), Maraging steel, GA-IF steel, SS300 series (SS304, SS304L, SS316L), and SDSS (super duplex stainless steel), Ti-6Al-4V (Grade 5) alloy and IN625, and IN718 alloys. Dissimilar combinations of materials include Inconel (IN625, IN718) to Steel (SS316L) and SS316L to SS310 have been reported. Similarly, GTAW process has also reported joining of a wide range of similar (Alloy C-2000, IN625, IN718, Inconel 738LC, Hastelloy X, Hastelloy B-2, SS series, P91, P92 steel, 1035 Carbon steel, IRSM 41 steel, HSLA, austenitic SS, ferritic SS, duplex SS, super duplex SS, AA 5456 Al alloys, Ti-6Al-4V, AZ31B Mg alloy, and ETP-Cu) and dissimilar (Cu-SS, P91-Inconel, SS-Inconel, SS-Incoloy 800, Mg-Steel, Monel-SS, AA6082-AA7075, IN625-IN718, P91-P92, P91-Incoloy 800HT, SS205-SS216, SS304-SS316, Monel 400-SS904L, nitronic steel-super duplex SS, and duplex SS-Hastelloy C276) materials.

Due to the micro-miniaturization of permanent joining, the processes of welding thin sheets are in high demand (Kumar and Bag, 2019). The use of thin sheets results in a 30% reduction in the overall weight of the automotive vehicle (Liu et al., 2014). Due to the high surface area to volume ratio, demand for reduced weight, and suppression in the emission of exhaust gas of vehicles, thin sheets are widely utilized in automotive and aerospace industries (Suhuddin et al., 2010; Tong et al., 2001), electronics and medical devices, nuclear power, and petrochemical industries (Fukumoto et al., 2008). Specific areas of applications of thin sheets are fuselage structures for aircraft (Nélias et al., 2010), body panels of automobiles (Zhao et al., 2012), thin tubes, pumps, tanks, actuators of electronics items, and medical/surgical appliances (Farid and Molian, 2000), and bellows in aerospace (Wei et al., 2015). The weld joint is considered the weakest link in a welded component, which causes the failure of the manufactured component to be relatively high in the joint region. Hence, a measured approach to establish a set of optimum process parameters becomes an inevitable choice to ensure the joint reliability of thin components (Kay, 1993; Kumar et al., 2014).

The welding of thin sheets involves numerous problems (due to reduced thickness) for designers and manufacturers, leading to a wide variety of imperfections that correspond to the failure of the component. Therefore, identification of the defects becomes essential to prevent catastrophic failures (Goldak and Akhlaghi, 2006; Zolfaghari et al., 2018). Typical defects evolving during the welding of thin sheets are deflection, porosity, root sagging, under-cut, blowholes, and the presence of large heat-affected zone (HAZ) and burn-through (Agrawal et al., 2017; Arif and Chung, 2014; Huang et al., 2016; Ismail et al., 2011; Kumar et al., 2020, 2009a). Most of the defects mentioned above are a function of heat input. Due to the limited requirement of heat supply in joining thin structures, the consequent dimensions of the weld joint are restricted to a small magnitude. Hence, the precise choice of appropriate welding techniques with acceptable process parameters corresponds to minimum defects when joining thin sheets (Kumar et al., 2009b).

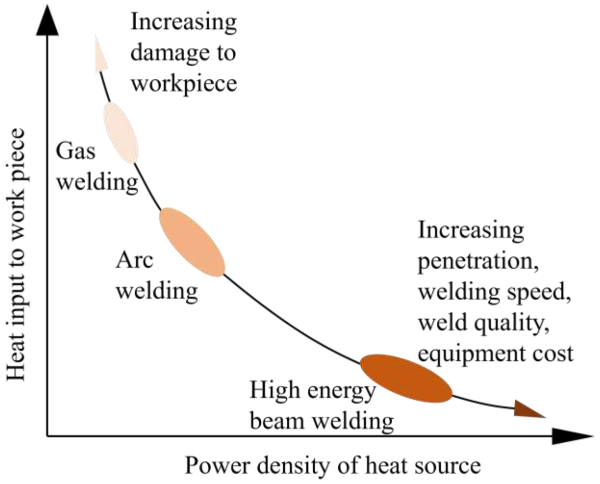

Fig. 1.1 Illustrates variation of heat input with power density of the heat source (Kou, 2003).

A comparison of various liquid state joining techniques (shown in Fig. 1.1) can be accomplished by comparing their 'power density.' With the rise in power density of a process, the heat supplied to the workpiece reduces. Due to the lower heat supply, the workpiece shows enhanced joint quality with reduced heat-affected zone (HAZ), lower distortion, and minimal locked-in stress. Another positive effect that higher power density brings is increased productivity. Because higher power density allows the available heat to focus on a narrow spot, which increases joining speed (productivity). With all the previously stated beneficial impacts, the process cost and power consumption increase (Quigley, 1986; Ireland, 1990; Kou, 2003). The M-PAW and GTAW processes can also join thin sheets but are on the lower side in terms of depth of penetration (DOP), welding speed, and productivity compared to LBW/ EBW processes. However, the process efficiency of M-PAW (0.66) and GTAW (0.70) lies between LBW and EBW. In addition, M-PAW and

GTAW processes offer cost-effectiveness (lower equipment cost and low power consumption) and higher tolerance (gap and positioning) available for joining. Though the power density of the M-PAW and GTAW processes are lower compared to the LBW and EBW processes, it is still comparable enough to produce joints with acceptable quality (minimum HAZ, distortion, metal loss, better metallurgical properties, dimensional stability, repeatability, no loss of alloying elements, and environmental advantages with no requirement of vacuum) (Chaudhary, 2015). Hence, for the present experimentation, the weldability of similar and dissimilar thin sheets is explored by arc-based (M-PAW and GTAW) welding processes.

The present work critically examines the role of input process parameters in producing defect-free welds in the micro-plasma and gas tungsten arc welding of thin structures. With the reduction in thickness, commonly encountered problems like excessive heating (leading to burn-through), grain coarsening (resulting in larger heat-affected zones), diffusion-less phase transformation (high cooling rate), significant distortion, poor surface appearance and reduction of essential chemical elements become more sensitive to the process parameters. It is understood that complete information regarding the process parameters, their ranges, and their effect on the joint quality requires an exhaustive survey to join thin sheets successfully. Therefore, determining optimal process parameters requires careful attention to avoid defects in the resulting structure. Besides selecting the best parameters, the choice of the ideal joining technique plays a vital function in the overall feasibility of the final structure. This work analyses the input process parameters and their extent to control the weld joint characteristics. The current study aims to identify the optimal heat input required to produce a mechanical and material defect-free weld for a thin structure fabrication.

1.2 The problem statement

When copper-nickel (CuNi) alloy solidifies, it forms α-phase (FCC) dendritic morphology, wherein the arms and the interdendritic space are enriched with Ni and Cu, respectively. During solidification, CuNi alloys are prone to either solidification cracking, liquation cracking, or ductility-dip cracking (Collins, 2002; Hondeos and McLean, 1974; JF lancaster Metallurgy of Welding 5th edition, Chapman and Hall, 1993, pp. 158-159), which can be avoided by proper selection of welding parameters. CuNi alloys have numerous applications in naval and marine components, wherein prolonged exposure to water bodies corresponds to corrosion. Nickel is crucial in resisting corrosion, erosion, and cavitation in the marine environment. Iron imparts resistance against impact by moving seawater, and the presence of manganese restricts the formation of oxides and sulfides (Chandra et al., 2019). Increased nickel content increases the alloy's cost (Chuaiphan and Srijaroenpramong, 2019); hence, $Cu_{90}Ni_{10}$ (10 % Ni) is more cost-effective compared to $Cu_{70}Ni_{30}$ (30 % Ni) and is used exhaustively (Powell, 2004). Thus, the current experimentation attempts to understand the weldability of $Cu_{90}Ni_{10}$ alloy by controlling defect formation via optimum heat supplied in continuous mode using the micro-plasma arc welding process. The application of current pulsation attempts further enhancement in joint properties.

The difficulties in dissimilar joining of copper and steel include differences in their melting point, thermal conductivity, coefficient of thermal expansion, specific heat capacity, and limited solubility (Gavrish and Perig, 2020). Materials having a wide variation in the coefficient of thermal expansion value fail during solidification (crack formation (Meng et al., 2019)) or in the course of service usage (thermal fatigue). Differences in the melting point and thermal conductivity value results in the prior melting of one material compared to another (Magnabosco et al., 2006). A higher thermal conductivity value of copper, compared to SS304, hinders reaching the melting point temperature of copper (Kar et al., 2018). Also, poor solid solubility between Cu and Fe (Tosto et al., 2003) always remains an additional concern that promotes liquid separation at the steeper cooling rate (Kar et al., 2016). Due to compositional differences of the materials, macro-segregation (solute segregation) may materialize near the fusion boundary (FB) or away from the FB (in the fusion zone, FZ). Macro-segregation corresponds to degradation of the weld properties, including corrosion resistance, stress-corrosion cracking, reduction in toughness, and hydrogen cracking (Soysal et al., 2016). Contrary to the joining of titanium-aluminium, copper-aluminium, and steel-titanium, copper-steel joining is considered less complicated due to the non-existence of intermetallic compounds (IMCs) (Kuryntsev and Shiganov, 2018). Hence, the current experimental work aims to fabricate a bimetallic joint with minimum metallurgical inhomogeneities that enhance the joint characteristics. Thus, an effort has been made to realize the importance of arc offset and joining mode in the performance of Cu-SS bimetallic joints.

Austenitic stainless steels (ASSs) demonstrate exceptional weldability, but the two most frequent complications arise in weld-decay and hot-cracking. ASSs are moderately ductile and capable of significant shrinkage, but during the cooling cycle, the weldments are susceptible to cracking (Soltani and Tayebi, 2018). Challenges associated with the ASS joints are intensified by the development of carbides along the grain boundary, resulting in weld-decay (Singh and Slathia, 2016). Dissimilar ASS joints are primarily recognized for their superior corrosion-resistant behaviour, better strength at elevated temperatures, and excellent low-temperature fatigue properties. However, with low specific heat and thermal conductivity, high thermal expansion coefficients of ASS often exhibit inferior mechanical properties of welded joints owing to (i) the development of high residual stresses and structural deformation propensity and (ii) ignorance of the role of microstructural attribute in residual stress evolution (Lin and Chou, 1995). Thus, the accurate prediction of residual stress is always of great interest as it paves the road to eliminate or mitigate it. Hence, the current experimentation attempts to comprehend the solidification behaviour and its relationship with the formation of delta ferrite and residual stress distribution.

1.3 Motivation for research

On account of anti-corrosion, anti-bio-fouling characteristics, and resistance to micro-biologically induced corrosion, the utilization of CuNi alloys extends to ship pipes, boiler components, boat hulls, pump impellers/bodies, condenser tubes in hydrogen coolers, evaporator tubes of chilling plants, multi-stage flash distillation units, aqua-culture enclosures, and brake tubing (Abbas et al., 2019; McAuley, 1991; Powell and Webster; Priyadharshini et al., 2017; S.C. et al., 2018). The most widely applied commercial grades of copper-nickel alloys are $Cu_{70}Ni_{30}$ and $Cu_{90}Ni_{10}$, comprising 30% and 10% nickel (Ni), respectively, with a minor portion of iron and manganese. An increase in Ni percentage from 10 to 30 % raises the liquidus temperature, from 1443 to 1513 K, and solidus temperature, from 1373 to 1443 K of the CuNi alloy.

Alloys of copper are widely employed in aerospace components and microelectronics parts due to the high value of thermal and electrical conductivities (401 W/mK, 56 Ms/m) and good ductile properties. Conversely, for practical purposes, the use of copper is restricted due to its high cost and high density (8900 kg/m^3) (Liu et al., 2019). In contrast, austenitic stainless steel (ASS) finds industrial application due to low valuation, high strength, excellent weldability (Haldar and Pal, 2024), and low density (7900 kg/m^3) compared to copper (ElSheikh et al., 2022). However, insufficient thermal dissipation characteristics of ASS lead to the development of unfavorable σ-phase and precipitation of chromium carbide (Roy et al., 2014). Therefore, cost benefits and enhanced performance of both metals can be integrated by opting for a bimetallic joint between copper and steel (Qi et al., 2024). Copper-steel joint finds application exclusively in defense sector

(Bhogendro Meitei et al., 2020), power generation areas (RK et al., 2018), aerospace industries (Zhang et al., 2015), chemical industries (Mai and Spowage, 2004), nuclear sectors (International Thermonuclear Fusion Experiment Reactor-ITER) (Roy et al., 2011), heat exchange components (Cheng et al., 2019), steam turbine power plants (Moharana et al., 2016), plane wave transform linac structure (PTLS), an ultra-high vacuum system (UHVS) (Poo-arporn et al., 2020), large hadron collider (LHC) (Joshi and Badheka, 2019), plasma fusion reactor (Ramachandran and Lakshminarayanan, 2020), cryogenic components (Lusch et al., 2015) (mass flow meter (Ramachandran and Lakshminarayanan, 2020)), power electronics components (Weigl and Schmidt, 2010), electrical parts (Velu and Bhat, 2013), and automobile sectors (Akella et al., 2014). Thus, the broad application areas for copper-steel bimetallic joints necessitate an improved approach to produce a defect-free joint.

The joining of dissimilar ASSs is a popular topic among researchers due to its diverse applications (Shinde and Telsang, 2016). Joining dissimilar grades of austenitic stainless steel (ASS) has found widespread application in the field of automobile, structural engineering, aerospace, medical, offshore industries, chemical plants, and bio-medical areas as implant material and power generation industries and pressurized water reactors (Ma et al., 2018). In particular, the SS300 series offers enhanced corrosion resistance and cryogenic properties due to high chromium and nickel percentages (Durgaprasad et al., 2023). Because of its diverse range of applications, ASS accounts for 70% of the total SS consumption (Vasantharaja et al., 2018).

1.4 Significance of the study and hypothesis statement

In the current experimentation, the key focus is imparted to identify the feasible range of welding parameters for similar and dissimilar joining using micro-plasma and gas tungsten arc welding processes. Micro-plasma arc welding of $Cu_{90}Ni_{10}$ thin sheets (700 μm) is established using continuous and pulse current modes. Using pulse current provides better results in terms of the least depletion of metal, fine equiaxed morphology with reduced secondary dendritic arm spacing, and the lowest internal defects. The current experimental examination on $Cu_{90}Ni_{10}$ alloy reports the importance of process parameters (heat supplied) and current pulsation to enhance weld properties. Understanding process parameters tremendously aid in obtaining joints of acceptable properties, which industries can employ to avoid repetition of work (directly influencing economic aspects) to join $Cu_{90}Ni_{10}$ thin sheets.

The dissimilar welding between Cu(T2) and SS304 is performed using a gas tungsten arc welding process with different arc offsets towards the Cu-side. The critical findings suggest that a drastic decrement in strength and elongation is experienced with increased arc offset value. The current experimental work reports the importance of arc offset and joining mode in the performance of Cu-SS bimetallic joints. Despite the occurrence of porosity within the copper-steel bimetallic joints, the outcome of the present experimental investigation displays the exceptional joining capability of the dissimilar materials. Consequently, the present combination of materials fabricated at the optimized parameters can be deployed for various industrial applications.

In the current work, emphasis is also devoted to develop numerical model to predict residual stress, considering the impact of solid-state phase transformation (SSPT) in micro-plasma arc welded dissimilar austenitic stainless steels. The estimation of residual stress in dissimilar austenitic steels is highly complicated, where the solidification behaviour and morphology are predominant. With this objective, an FE-based TMM model is developed to estimate residual stress accurately by taking into account the phase transformation effect. Thus, an accurate prediction helps to eradicate trial and error-based methods to enhance the performance of the material at reduced cost.

1.5 Layout of the thesis

The thesis is organized into six chapters, covering all aspects of the research objectives. **Chapter 1** introduces the subject, outlines the research objectives, the significance of the current research work, and the overall layout of the thesis. **Chapter 2** includes a detailed literature review of the work of past researchers, which is focused on the weldability of similar ($Cu_{90}Ni_{90}$) and dissimilar (SS316L-SS310, Cu(T2)-SS304) thin sheets by arc-based (micro-plasma and gas tungsten arc welding) welding processes. First, the experimental survey is conducted on process conditions, materials, and the feasibility of liquid-state joining processes is reviewed. The effect of process and solidification parameters on the formation of weld morphology is thoroughly examined for both similar and dissimilar welding. Furthermore, a significant portion is dedicated to the FE-based numerical model and the challenges connected to its deployment. Lastly, based on the literature review, the research gaps and objectives of this thesis are outlined.

Chapter 3 details the experimental investigation of micro-plasma and gas tungsten arc welding processes. The influence of welding speed and current are analyzed to estimate the feasible range of process parameters for the successful joining of similar ($Cu_{90}Ni_{90}$) and

TH-3924_166103014

dissimilar (SS316L-SS310, Cu(T2)-SS304) materials. An experimental study is carried out to understand the weldability of 0.7 mm-thick $Cu_{90}Ni_{10}$ alloy by controlling defect formation via optimum heat supplied in continuous and pulse modes. Also, an attempt is made to successfully join copper (T2 grade) and austenitic stainless steel (304 grade) by offsetting the arc towards the Cu-side using the gas tungsten arc welding process. Finally, a dissimilar combination of austenitic stainless steel (SS316L and SS310) thin sheets are joined using micro-plasma arc welding process. In addition, the weld joints are subjected to destructive and non-destructive testing (NDT) to judge the feasibility of the fabricated joints. The destructive testing includes microstructural analysis (optical microscopy (OM), electron microscopy, and electron backscattered diffraction-EBSD), microhardness evaluation, tensile testing, and fractography analysis. Further, corrosion analysis is accomplished to determine the chemical stability of the joints. X-ray diffraction (XRD) is carried out to confirm the presence of different phases. The NDT used in the present investigation aims to assess residual stress and distortion in the joints. In addition, an advanced NDT (X-ray computed tomography) is accomplished to identify internal defects.

Chapter 4 presents the theoretical formulation to develop thermo-mechanical and thermo-metallurgical-mechanical models. Numerical modeling is implemented by utilizing ABAQUS® software. The dynamic heat flux is incorporated into the numerical model by implementing the DFLUX subroutine within the developed model. The time-temperature data is extracted from the thermal analysis and is used as input into the mechanical analysis for which temperature-dependent properties are applied. Temperature-time data, phase fraction, residual stress, and distortion are extracted using the numerical results. The validation of the numerical model is established with the experimentally achieved data.

Chapter 5 describes the validation of numerical results with the experimental values. An FE-based thermo-mechanical model is employed to reliably predict time-temperature data, weld dimensions, residual stresses, and distortion. The small deformation principle is incorporated to predict the values of deflection, wherein strain and displacement are correlated linearly. Secondly, the influence of heat supplied on the micro-plasma arc welding of 700-µm thick cupronickel alloy in continuous mode is explored, and application of the least heat supplied is recommended. Further enhancement in joint features is attained by better control over the average heat supplied using pulse mode. The next part of the chapter details the joining of copper (T2 grade) and austenitic stainless steel (304 grade) by offsetting the arc towards the Cu-side using the gas tungsten arc welding process. Thus, an effort has been made to realize the importance of arc offset and joining mode in the performance of Cu-SS bimetallic joints. The critical findings suggest that with increased arc offset, the joint demonstrates a variation from welding mode to a weld-brazing mode, where the failure mode deviates from ductile to brittle fracture. Finally, the joining of different grades of austenitic stainless steels is accomplished using the micro-plasma arc welding process. The effect of heat input on the metallurgical, mechanical, and corrosion properties is explored. Further, investigation is carried out to mitigate residual stress by controlling microstructural morphologies that can elude the failures of a welded joint. Therefore, an attempt is made to understand the solidification behaviour of the weld metal and its correlation with delta ferrite formation and residual stress distribution.

Chapter 6 provides a summary of the work along with the conclusions drawn from the previous chapters. It also outlines potential future research directions based on the current efforts. A list of references and a bibliography are included at the end.

Chapter 2

Literature Survey

2.1 Introduction

In the current chapter, an exhaustive literature survey is imparted on the challenges during the joining of similar ($Cu_{90}Ni_{90}$) and dissimilar (SS316L-SS310, Cu(T2)-SS304) thin sheets by arc-based (micro-plasma and gas tungsten arc welding) welding processes. First, the experimental survey is conducted on process conditions, materials, and the feasibility of liquid-state joining processes is reviewed. The effect of process and solidification parameters on the formation of weld morphology is thoroughly examined for both similar and dissimilar welding. The primary governing factor resulting in the degradation of the joint quality is the amount of heat supplied to fabricate a component, which directly affects the microstructural and mechanical properties. Therefore, controlling the heat input influences the metallurgical properties which govern the joint behaviour. Further, understanding the weld enhancement techniques tremendously aids in obtaining joints of acceptable properties. Different techniques employed to improve weld joint properties can be categorized into three folds (prior to/during/post-welding process). Pre- and post-weld heat treatment and shot/laser shock peening before/after the welding period are the factors that improve the mechanical and microstructural properties. The current pulsation, arc oscillation, activated flux, composition of shielding gas, and ultrasonic vibration during welding are add-on factors that influence the weld joint quality. Out of all methods, the current pulsation during welding has been widely used in joining thin sheets to gain better control over the heat input, resulting in enhanced solidification behaviour and joint properties.

The finite element-based computational tool enables the necessary measurement of thermal, metallurgical, and mechanical characteristics that would have been challenging otherwise by experimentation. Emphasis is devoted to develop numerical models to predict residual stress, taking into account the impact of solid-state phase transformation (SSPT). Lastly, based on the literature review, the objectives of this thesis are outlined.

2.2 General background

Welding is a fabrication technique that permanently joins similar or dissimilar materials (Joo et al., 2016). Welding processes can be broadly classified in two different ways, i.e., (i) based on the filler material and (ii) based on the temperature reached during the joining. Joint assembled without the use of filler material is termed autogenous joining, and the joining processes involving the use of filler material of similar composition as that of base material results in homogenous joining, whereas the dissimilar composition of filler material and base material results in heterogeneous joining. Based on the temperature reached during the joining, the welding process is classified into liquid-state, solid-state, and solid-liquid-state. The liquid-state technique encounters temperature exceeding the melting point (MP) temperature of the base material, whereas solid-state joining processes are associated with temperatures of 0.75-0.80 times the MP. Soldering and brazing fall under solid-liquid state joining, in which a filler wire is melted to join two or more materials without melting the parent metals (Granjon, 1991; Khan, 2007; Timings, 2008; Weman, 2011). Welding is an extensively used fabrication method for assembling metals and is necessary for the evolution of almost every item produced by the manufacturing process. Due to resulting tensile stresses in the joints, the weld joint is considered the weakest link in a welded component, which causes the failure of the manufactured component to be relatively high in the joint region. Hence, a measured approach to establish a set of optimum process parameters becomes an inevitable choice to ensure the joint reliability of thin components (Kay, 1993; Kumar et al., 2014).

Welding poses numerous problems for designers and manufacturers, leading to a wide variety of imperfections, which corresponds to the failure of the component. Therefore, identification of the defects becomes essential to prevent catastrophic failures (Goldak and Akhlaghi, 2006; Zolfaghari et al., 2018). ASME (American Society of Mechanical Engineers) states that welding imperfections are divided into 45% poor welding parameters, 32% worker inaccuracy, 12% incorrect method, 10% wrong consumables, and 5% improper weld design (Krolczyk et al., 2016). Hence, determining the ideal parameters becomes necessary to fabricate a joint successfully. Several purposes are achieved with thin sheets, thus tempting researchers to find new techniques for joining thin sheets with minimum defect and high strength. The primary objective of this literature survey is to recognise how different welding methods influence solidification characteristics and mechanical properties in both similar and dissimilar material combinations.

2.3 Micro-plasma and gas tungsten arc welding processes

In the 1940s, the joining technique for magnesium and aluminium (non-ferrous materials) introduced a non-consumable tungsten electrode enveloped by shielding gas to protect the weld region from atmospheric contamination (Russell, 1942), and the process is recognized as gas tungsten arc welding (GTAW) in the modern era. An advanced version of the GTAW process was developed in the 1950s, where a comparatively smaller diameter orifice was utilized to provide separate pathways for the supply of inert gases. It allows the achievement of higher power density from the arc generated, which facilitates the joining of sheets with relatively higher thickness relative to the GTAW process (Gage, 1957). The passage for the inert gases is supplied to form the plasma and shield gases, and this derived version of the GTAW process is presently referred to as the plasma arc welding (PAW) system (Niedermayer, 2022).

The PAW process was developed to provide superior control in the low-amperage joining. PAW falls under the advanced joining (high-energy density) technique, which offers heat energy through a constricted arc (Correa et al., 2008; Das et al., 2018; Hsu and Rubinsky, 1988). PAW is utilized to join weldable materials applicable to the GTAW process (V. Dhinakaran et al., 2017; S. R. Kumar et al., 2018; Zhou et al., 2023). Fig. 2.1(a, b) demonstrates the fundamental differences between GTAW and PAW processes. It is evident that the electrode is placed inside the copper nozzle for the PAW process, and it provides the opportunity to develop a non-transferred arc of the PAW process. The well-stated advantages due to the constriction of plasma arc are narrow HAZ, no risk of tungsten inclusion in the deposited material, highly concentrated arc, narrow and clean weld without any spatter marks, high precision, and enhanced stability (Martikainen and Moisio, 1993; Pasek-Siurek, 2014; Piccini and Svoboda, 2012; Ravichandran et al., 2016; Raymond and Slatter, 1998; Wu et al., 2006; Wu and Huo, 2013; Zhang and Liu, 2007). 100-300 A current range is available for both GTAW and PAW processes, thus supplying higher heat to form a weld for PAW (Martikainen, 1995; Urena et al., 2007; Wang and Chen, 2002). A higher current supply is avoided by designing a micro-variant of PAW where a similar benefit can be achieved in joining thin sheets, and the current can be reduced up to 0.1 A. The M-PAW process can easily be programmed using different joining parameters to produce better-quality welds and is best for joining miniature parts like very thin wires, rods, tubes, and thin sheets (Dwibedi and Jain, 2016). The M-PAW process provides better weld quality than pulsed GTAW and is much more economical than LBW and EBW (V Dhinakaran et al., 2017; Dwibedi and Bag, 2018; Dwibedi and Jain, 2016). Table 2.1 suggests that the M-PAW and GTAW processes are on the lower side in terms of depth of penetration, welding speed, and productivity compared to LBW/EBW. However, the process efficiency of M-PAW and GTAW lies between LBW and EBW and possesses an advantage in terms of allowable tolerance, equipment cost, and portability.

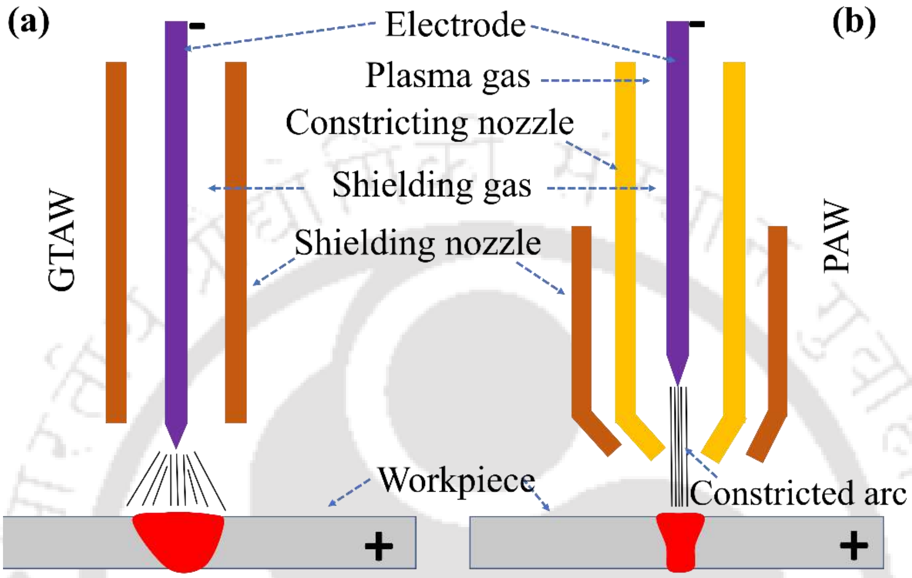

Fig. 2.1 Illustrates the comparison of (a) GTAW and (b) PAW processes (Wu et al., 2014).

Table 2.1 Compares different fusion welding processes on selected parameters (Chaudhary et al., 2019).

Sl. No.	Parameter	GTAW	M-PAW	LBW	EBW
1.	Damage to workpiece	🟧 ****	🟨 ***	**	*
2.	Depth of penetration	🟧 **	🟧 ***	****	*****
3.	Welding speed	🟧 **	🟧 ***	****	*****
4.	Weld quality	🟧 **	🟨 ***	****	*****
5.	Equipment cost	🟩 **	🟩 ***	****	*****
6.	Equipment portability	🟩 ****	🟩 ****	**	*
7.	Allowable tolerance	🟩 *****	🟩 ****	**	*
8.	Mass production scale	🟧 **	🟧 ***	****	*****
		Low: *	Medium: ***		High: *****
Color code	🟧 Lower than LBW and EBW	🟨 Comparable to LBW and EBW		🟩 Better than LBW and EBW	

2.4 Effect of arc pulsation

One of the most widely used variants of the M-PAW process is the PC-M-PAW (Pulsed Current-M-PAW) technique. Permanent joining of materials using fusion welding processes requires melting followed by solidification. Using a pulsed current (PC) allows better control over the magnitude of heat supplied, which directly governs the solidification process. PC supplies the arc for a brief period, followed by 'an interval,' which reduces the overall heat supplied for joining. The 'interval' allows a range of benefits over the continuous current (CC) mode of the M-PAW process. PC mode incorporates current from a maximum to minimum value in a periodic pattern (Prasad et al., 2011). In the case of PC, two levels of current and time exist. The maximum value of current (I_p) is applied for a duration (t_{on}) during which the arc provides adequate heating. I_p provides sufficient heating followed by melting of the base metal. Meanwhile, a minimum value (I_b) of current exists during t_{off}, in which the arc is enough to maintain itself (Kondapalli et al., 2012). Such manoeuvring of current allows tremendous control over the amount of heat input. Pulsed mode finds application for joining thin sheets, requiring strict management to achieve complete DOP without burn-through. Significant benefits of using the PC mode process reported over CC mode are (i) lower heat supplied, (ii) reduced locked-in stress and distortion, (iii) restricted HAZ, (iv) improved solidification behaviour, (v) restriction in the formation of segregation, (vi) enhanced mechanical properties and (vii) reduction of the extra dissipation of heat (Chaudhary, 2015; Prasad, 2019; Sahu, 2021). Fig. 2.2(a, b) compares the average current employed in CC-M-PAW and PC-M-PAW.

Overall, the enhanced properties achieved in PC mode over CC mode are due to the following reasons: (a) the impact on solidification behaviour⟶ PC intensifies fluid motion in the fusion zone, which corresponds to a reduction in temperature variations. It initiates modification in the weld pool dimensions, and such change is assumed to be the driving force that governs the solidification behaviour, i.e., avoids solidification cracking. Solidification cracking prevails when the thermal stresses developed surpass the maximum limit of the solidifying metal; (b) the impact on microstructure and mechanical properties⟶ in the case of the CC process, inter-dendritic spacing remains wider, whereas PC leads to a narrower separation between the dendrites. Such metallurgical changes result in enhanced joint strength. Periodic alteration in the amount of heat input leads to recurrent alternation of the temperature changes, which causes re-melting and disintegration of the developing dendrites. Such fragmented dendrites provide a location for heterogeneous expansion, leading to the formation of equiaxed dendritic morphology. PC also corresponds to the minimized extent of coarse grains in the HAZ, refined microstructural morphology, diminished chances of micro-segregation, and the remote possibility of secondary phase(s) existence; (c) the cooling rate-structure-property relation⟶ PC offers reduced heat input and enhanced heat dissipation between the time interval of I_p. It corresponds to the lowering of the cooling rate (CR) in the fusion zone, which leads to a higher solidification rate. Thus, the applications of PC confines to replace the grain morphology from coarse columnar/cellular grain to fine equiaxed structure results in superior strength of cohesion, and the residual liquid solidifying in the finishing stages helps to refill the cracks that might occur during solidification (Babu et al., 2007; M. Balasubramanian et al., 2008a, 2008b; V. Balasubramanian et al., 2008; Janaki Ram et al., 2004; Kumar et al., 2007; Sundaresan et al., 1999). Table 2.2 explains the influence of current pulsation on microstructure, mechanical, and corrosion behaviour of similar and dissimilar joints fabricated by GTAW and M-PAW processes. Table 2.3 compares the properties of micro-plasma arc welded joints with and without current pulsation.

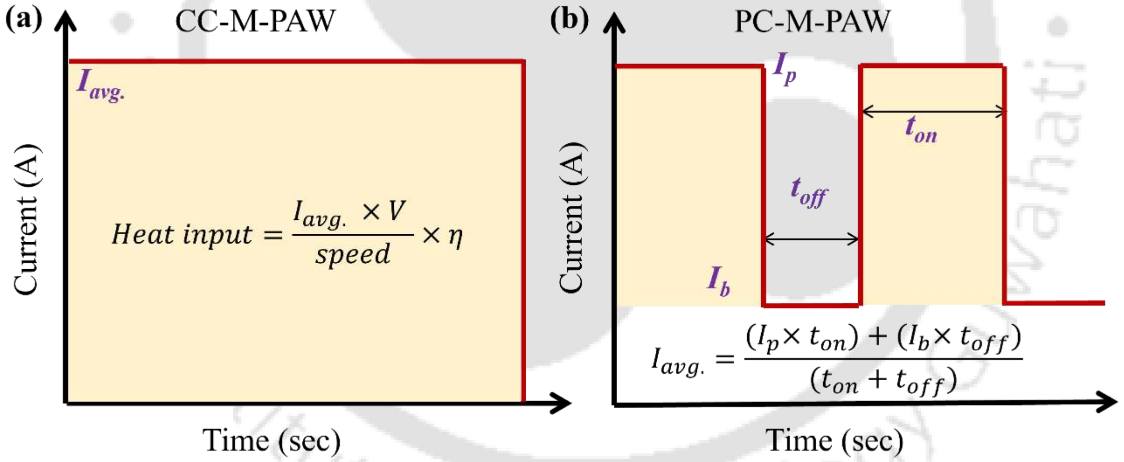

Fig. 2.2. Compares average current employed in (a) CC-M-PAW and (b) PC-M-PAW (Wu et al., 2014).

Table 2.2 Presents the influence of current pulsation on microstructure, mechanical, and corrosion behaviour of weld joints.

Material(s), (Process)	Key benefits of pulse over continuous current on the joint properties (Reference)
Incoloy 825, SAF 2507, (GTAW)	The utilization of pulse current (PC) demonstrated higher impact strength (52 J) than the joints fabricated by continuous current (CC, 41 J). Formation of unwanted phases (Mo, and Nb-rich) led to reduced impact resistance (Kangazian and Shamanian, 2018).
Incoloy 825, SDSS, (GTAW)	Usage of PC led to the formation of a higher level of $\delta_{ferrite}$ (7.1-10.8 %) in the welded joints, which contributed to enhanced impact resistance (~83 J) and corrosion compared to the joints prepared using CC (71 J). The presence of a higher level of $\delta_{ferrite}$ also resulted in better resistance to corrosion (Kangazian and Shamanian, 2019).
UNS S32750, SS321, (GTAW)	Higher toughness (106 J) and pitting resistance (1.03 V) were achieved for PC condition, compared to CC weld joints (102 J, 0.8 V). Also, a higher percentage (50 %) of ferrite was achieved for PC in contrast to CC (40 %) (Abdollahi et al., 2018).
UNS R30155 alloy, (GTAW)	Formation of equiaxed grains resulted in the best joint properties (794 MPa, 40 % EL) using a pulse frequency of 240 Hz, whereas using CC led to the growth of epitaxial grains (~40 µm due to higher heat supplied), resulting in deterioration in the joint properties (731 MPa, 24 % EL) (Rahimi et al., 2020).
N155 superalloy, (GTAW)	Optimum PC frequency (240 Hz) allowed the formation of NiO and Cr_2O_3, which acted as a barrier, and inhibited further reaction (reduced substrate deterioration) during corrosion evaluation at high temperatures (Rahimi et al., 2021).
IN718, SS316L, (M-PAW)	Implementation of PC at 68 J/mm allowed the formation of equiaxed morphology with reduced segregation. PC aided in the formation of desirable microstructural morphology, leading to improved joint efficiency (~108 %) (Sahu and Bag, 2020).
Ti-6Al-4V, (M-PAW)	The application of PC enhanced the joint strength (UTS: 901 MPa) compared to the joints prepared with CC (UTS: 775 MPa). Due to the higher cooling rate, PC allowed the formation of a higher martensite phase with a limited quantity of acicular α_{phase}, which resulted in higher joint properties (Rahimi et al., 2018).
IN718, (M-PAW)	Positive impact of PC led to an increase in the joint strength (764⟶ 898 MPa) and favourable metallurgical changes (inter-dendritic thickness: 1.81 (CC)⟶ 1.12 µm (PC)) compared to CC weld joints (Sahu and Bag, 2021).

Table 2.3 Compares the properties of micro-plasma arc welded joints with and without current pulsation.

Key observations reported by authors (Reference), Figure(s)
Sahu and Bag (Sahu and Bag, 2021) carried out experiments to compare the behaviour of joints (solution treated IN718) fabricated by PC (47 J/mm) and CC (52.8 J/mm), shown in Fig. 2.3(a, b). The strength achieved for the joints was 898 MPa (PC) and 764 MPa (CC), and the efficiency decreased from 96 % (PC) to 81.7 % (CC). The variation in strength resulted due to differences in $G \times R$ and G/R (840 K/s, 87 K/mm for PC and 633 K/s, 49 K/mm for CC). Due to high cooling rate for PC conditions, finer and discontinuous Laves (~1.12 µm) are achieved, whereas, for CC conditions, ~1.81 µm inter-dendritic length is reported. 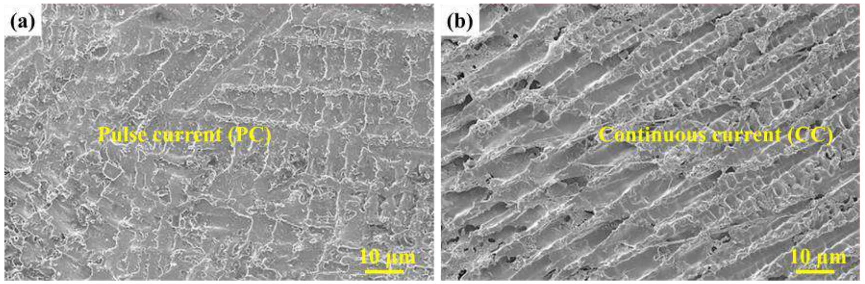   **Fig. 2.3** Microstructure of fusion zone for (a) PC and (b) CC conditions (Sahu and Bag, 2021).
Sahu and Bag (Sahu and Bag, 2020) highlighted the significance of the PC employed for joining IN718-SS316L sheets. Fig. 2.4 (a, b) shows the fusion zone of joints assembled at 48 J/mm (~1214 K/s) and 68 J/mm (~845 K/s). At 48 J/mm, due to higher cooling rate ($G \times R$), the fusion zone shows a finer structure compared to 68 J/mm. The G/R comes out as ~114 for 48 J/mm, and ~92 for 68 J/mm, due to which equiaxed structure is formed at 68 J/mm (due to lower magnitude of G/R ~92), whereas columnar type structure is formed at 48 J/mm (due to higher magnitude of G/R ~114). Columnar shapes enhance intermetallic development, whereas equiaxed shape structures in 68 J/mm contain boundaries enriched with useful elements (Ti, Nb, Mo, and Ni). The joint efficiency at 48 J/mm and 68 J/mm is evaluated as ~100% and ~108%, respectively. The failure portion of the 48 J/mm joint occurred in the fusion zone, whereas the fracture took place away from the FZ (in the HAZ) for the 68 J/mm joint. For the 48 J/mm joint, intermetallic presence in the columnar shape corresponds to the fragile region. For the 68 J/mm joint, an equiaxed shape aids in reducing segregation, due to which vital elements are retained, resulting in enhanced joint quality. The results obtained by the authors suggest that enhancement in joints can be made using PC, leading to equiaxed shape formation in the fusion zone. 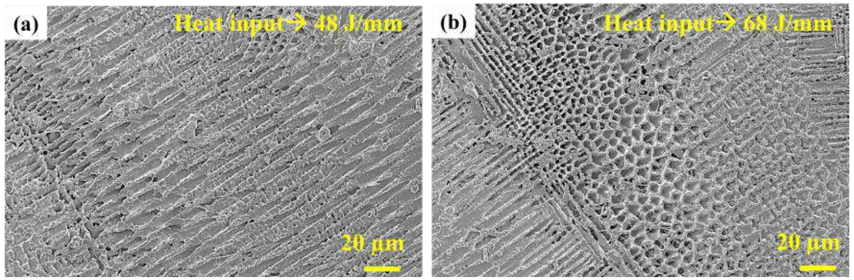   **Fig. 2.4** Fusion zone characteristics of joints formed at (a) 48 J/mm and (b) 68 J/mm (Sahu and Bag, 2020).

Table 2.3 Compares the properties of micro-plasma arc welded joints with and without current pulsation (cont.).

Key observations reported by authors (Reference), Figure(s)	
Sahu et al. (Sahu et al., 2020) employed M-PAW to join SS316L and solution-treated IN718 with PC parameters I_p (19 A), I_b (35 percent of I_p), frequency (4.3 Hz), and welding speed (145-196 mm/min); combined to provide heat input value in the range 48-65 J/mm. Fig. 2.5(a-d) demonstrates the occurrence of micro-fissures towards the interface of the SS316 region and micro-cracks towards the IN718 region for the 48 J/mm joints. For the 65 J/mm weld joints, no such defects (solidification cracks) are reported, and a defect-free weld can be observed in Fig. 2.5(e-h). Another assessment that can be seen in the fusion zone center is the type of structure formed, i.e., columnar for the 48 J/mm and equiaxed for the 65 J/mm joints. Due to contrasting morphologies, variation exists in the weld properties with reduced segregation for the equiaxed type morphology (65 J/mm). The primary reason for the absence of defects in 65 J/mm joints was a reduction in the detrimental phases NbC (11.3 %) and Laves phase (22.7 %), which was acquired by lowering the welding speed. Better microstructural morphology corresponds to enhanced joint strength value with a joint efficiency of ~99.6 % for 48 J/mm and ~104 % for 65 J/mm. The ductility shows a tremendous improvement (close to 90 %) as the weld speed decreases from 196 to 145 mm/min.	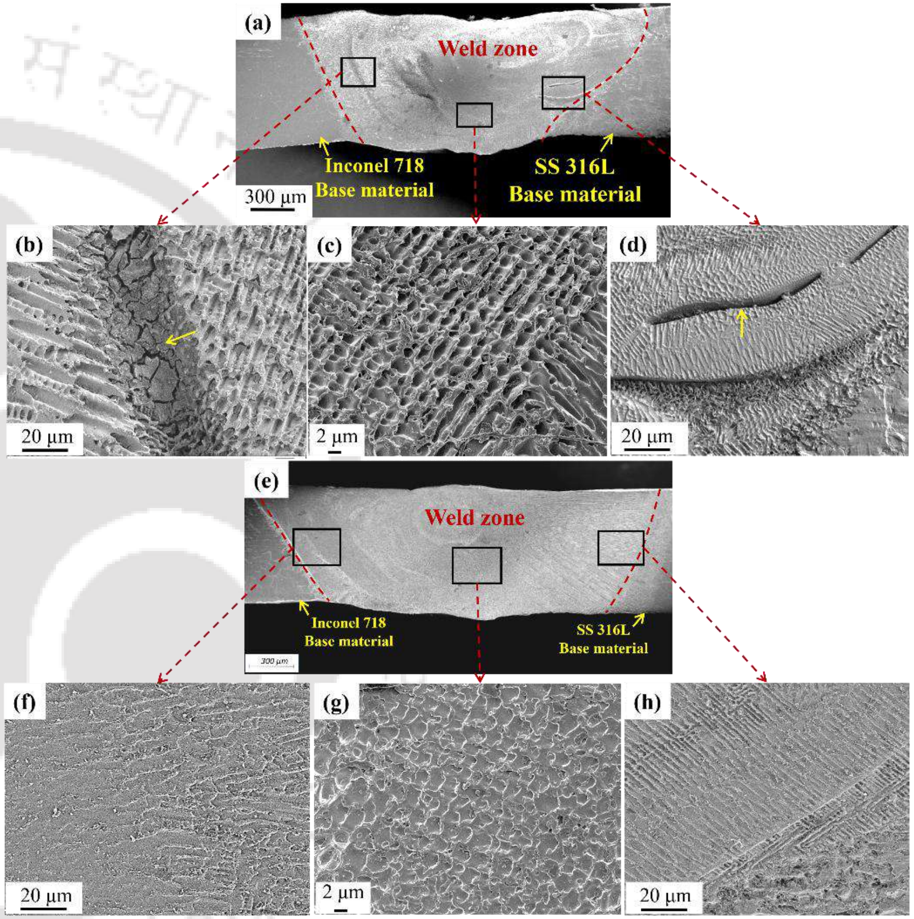 **Fig. 2.5** Fusion zone characteristics of joints formed at (a-d) 48 J/mm and (e-h) 65 J/mm (Sahu et al., 2020).

2.5 Weldability of cupronickel alloy

CuNi alloys have numerous applications in naval and marine components, wherein prolonged exposure to water bodies corresponds to corrosion. Nickel is crucial in providing resistance to corrosion, erosion, and cavitation in the marine environment. Iron imparts resistance against impact by moving seawater, and the presence of manganese restricts the formation of oxides and sulfides (Chandra et al., 2019). On account of anti-corrosion, anti-bio-fouling characteristics, and resistance to micro-biologically induced corrosion, the utilization of CuNi alloys extends to ship pipes, boiler components, boat hulls, pump impellers/bodies, condenser tubes in hydrogen coolers, evaporator tubes of chilling plants, multi-stage flash distillation units, aqua-culture enclosures, and brake tubing (Abbas et al., 2019; McAuley, 1991; Powell and Webster; Priyadharshini et al., 2017; S.C. et al., 2018). The most widely applied commercial grades of copper-nickel alloys are $Cu_{70}Ni_{30}$ and $Cu_{90}Ni_{10}$, comprising 30% and 10% nickel (Ni), respectively, with a minor portion of iron and manganese. An increase in Ni percentage from 10 to 30 % raises the liquidus temperature, from 1443 to 1513 K, and solidus temperature, from 1373 to 1443 K of the CuNi alloy. When CuNi alloy solidifies, it forms α-phase (FCC) dendritic morphology, wherein the arms and the interdendritic space are enriched with Ni and Cu, respectively. During solidification, CuNi alloys are prone to either solidification cracking, liquation cracking, or ductility-dip cracking (Collins, 2002; Hondeos and McLean, 1974; JF lancaster Metallurgy of Welding 5th Edition, Chapman and Hall, 1993), which can be avoided by proper selection of welding parameters.

Table 2.4 describes the significant outcomes of the research work on the joining of the similar joining $Cu_{70}Ni_{30}$ and $Cu_{90}Ni_{10}$ alloys. Apart from the similar joining, dissimilar combinations of CuNi alloys have also been explored by past researchers (Das et al., 2019; Straight et al., 1988). Straight et al. (Straight et al., 1988) reported the influence of defects (cracks) on the dissimilar steel and $Cu_{90}Ni_{10}$ weld joints fabricated by the submerged arc welding (SAW) process. The authors compared the fatigue test results for the specimens with and without defects. The authors also carried out a finite element analysis to analyze the fatigue life of the component. Das et al. (Das et al., 2019) documented the impact of optimum amplitude, weld time and pressure, and on the joint strength of AA1060 and $Cu_{70}Ni_{30}$ alloy permanently joined by ultrasonic welding (USW) technique.

Table 2.4 Presents the major outcome of the recent research work on the weldability of cupronickel alloy.

<table>
<tr><th>Key observations reported by authors (Reference)</th><th>Figure(s)</th></tr>
<tr><td>The authors evaluated bead dimensions and metallurgical evolution of $Cu_{70}Ni_{30}$ and $Cu_{90}Ni_{10}$ laser (CO_2) welded joints by varying input variables (power: 4 and 6 kW, and speed: 1-5 m/min). Based on the input values, the output behaviour of the joints was reported as, i.e., DOP ~1-5.6 mm, width ~1-4.3 mm, aspect ratio ~0.6-2.6, and SDAS ~1-4 µm. Due to the increased applied power, the authors observed a decline in the FZ properties, attributed to thermal softening and a larger secondary dendritic arm spacing (SDAS). Also, within the FZ, variation in the SDAS value (1-4 µm, shown in Fig. 2.6) was reported due to differences in the local cooling rate (Ferro et al., 2005).</td><td>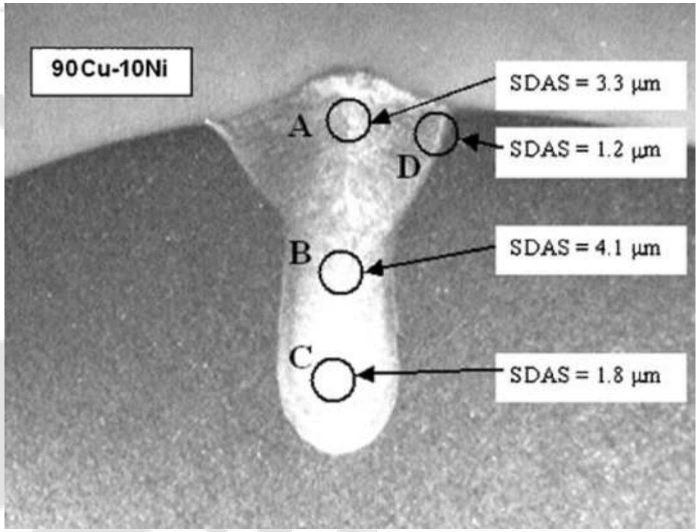
Fig. 2.6 SDAS values for $Cu_{90}Ni_{10}$ weld at 6 kW and 1.6 m/min (Ferro et al., 2005).</td></tr>
<tr><td colspan="2">Joints produced were identified with the existence of porosity and the inclusion of non-metallic content. Another concern in the fabricated joints was the occurrence of spatter, but the absence of IGC (due to < 0.5 % impurity) ensured the manufacturing of good-quality joints. The FZ comprised dendritic morphology, with Ni-rich dendritic cores and Cu-rich inter-dendritic area. Finally, the authors stated inclusions as the primary reason for reduced strength and %EL (Devletian et al., 2006).</td></tr>
<tr><td colspan="2">Joints were analyzed after performing welding multiple times (1, 3, and 5 times). Macrographs revealed porosity and lack of fusion (LOF) in the fusion zone, whereas microscopy images demonstrated the presence of dendritic structure in the fusion zone. The joints produced after welding thrice and five times exhibited 17 % and 27 % lower energy absorbing capacity as compared to the joints welded once. The authors suggested annealing at 650-825 °C to regain the lost impact energy for the joints welded multiple times (Munro, 2013).</td></tr>
</table>

Table 2.4 Presents the major outcome of the recent research work on the weldability of cupronickel alloy (cont.).

Key observations reported by authors (Reference), Figure(s)
$Cu_{70}Ni_{30}$ joints were autogenously assembled using an LBW (fiber, Yb) process to quantify the strength and identify the defects formed. Undercut and porosity defects were common in all the fabricated joints, which caused all the joints to fail in the fusion/heat-affected zone. However, all the fabricated joints were independent of surface cracks. The authors reported a dendritic structure in the fusion zone (shown in Fig. 2.7), with the dendritic arms containing high Ni content and the space between them containing Cu (Cao and Nolting, 2019). 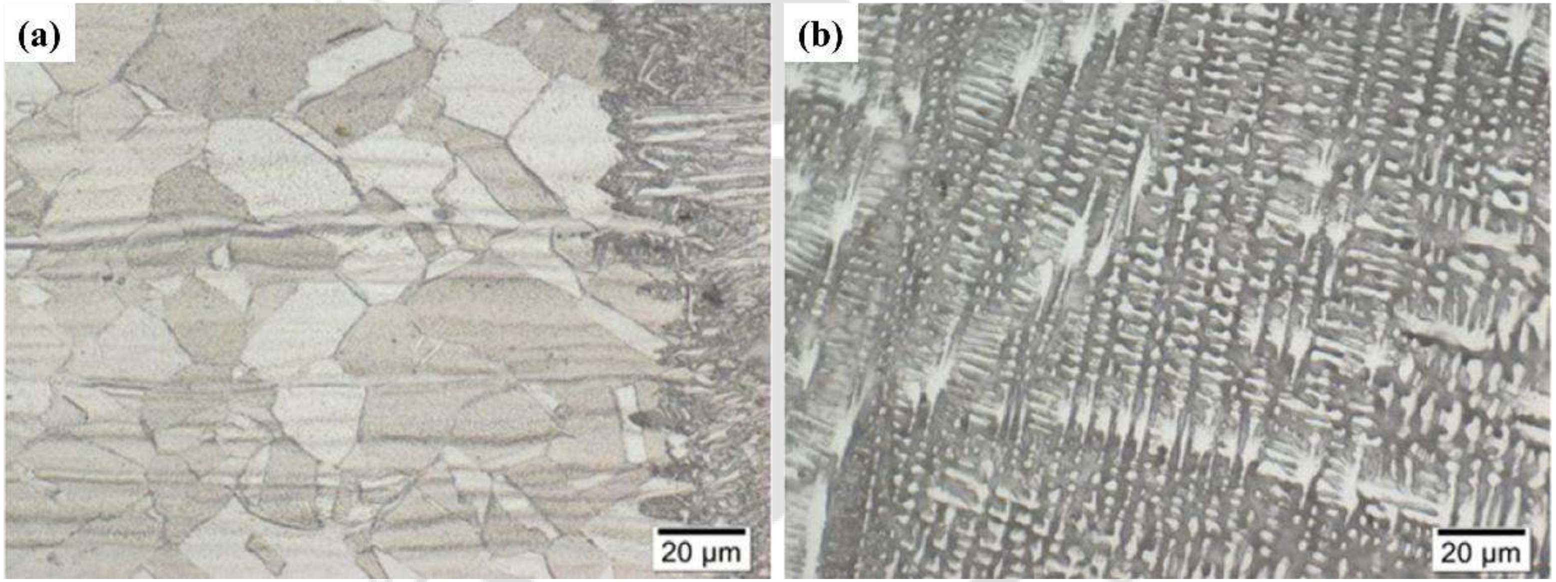 **Fig. 2.7** $Cu_{70}Ni_{30}$ joints illustrating (a) HAZ/FZ and (b) FZ (Cao and Nolting, 2019).

Table 2.4 Presents the major outcome of the recent research work on the weldability of cupronickel alloy (cont.).

Key observations reported by authors (Reference)	Figure(s)
$Cu_{90}Ni_{10}$ and HSCuNi were joined by the GTAW process to examine the corrosion properties in flowing seawater. Between the FZ and HAZ, a higher rate of corrosion was identified for the HAZ (shown in Fig. 2.8) because of galvanic corrosion, and flowing seawater effortlessly removes the corrosion products (due to the modest density of adhesion). Cu_2O accumulates and forms a layer that allows a reaction to happen with Cu_2O, and gradually, additional NiO is produced, further enhancing the corrosion resistance (Xing et al., 2023).	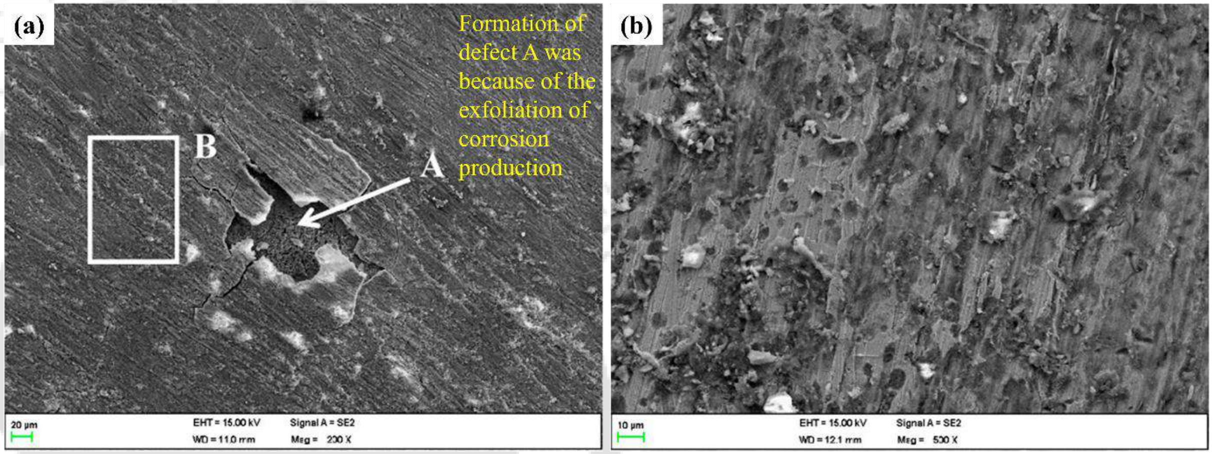 **Fig. 2.8** Corroded SEM images of (a) HAZ and (b) FZ in seawater at a 3 m/s flow rate (Xing et al., 2023).
The joining of $Cu_{70}Ni_{30}$ alloy was established using a CO_2 laser by employing 3.5 kW (power) and 1-2.5 m/min (speed). Joints produced at a 1.5 m/min speed demonstrated fine equiaxed morphology, whereas coarser morphology was reported for 2.5 m/min joints. The UTS and %EL values show a reduction from ~370 MPa, ~16 % for 1.5 m/min joints to ~330 MPa, ~13 % for 2.5 m/min joints. The authors concluded finer equiaxed morphology with uniform distribution enhances the weld properties. The authors also utilized the GTAW process (105 A, 18 V, 2.5 mm/s) and stated the benefits of CO_2 laser over the GTAW process regarding narrower HAZ (Chakravarthy et al., 2014).	

It is evident from the literature survey that cupronickel alloy has been welded by different joining processes (FCAW, GTAW, M-PAW, SAW, USW, LBW + GMAW, and LBW). However, the joining of cupronickel alloy is not yet reported by the M-PAW process. Also, joining of thin cupronickel sheets is not firmly established, and there is an absence of thorough investigation.

2.6 Weldability of dissimilar ferrous and non-ferrous metals

Bimetallic joints are combined to achieve any of the following merits: cost-efficiency, weight reduction, and improved product effectiveness (Chattopadhyay et al., 2022). Different combinations of bimetallic joints commonly fused by liquid-state joining techniques are aluminium-copper (Cha and Choi, 2022), aluminium-steel (Zhao et al., 2022), aluminium-magnesium (Hayat, 2011), aluminium-titanium (Chen et al., 2011), copper-nickel (Chakraborty and Chakraborty, 2007), magnesium-steel (Liu et al., 2024), magnesium-titanium (Thakur and Aravindan, 2024), titanium-invar (Zhou et al., 2024), titanium-steel (Zhang et al., 2020), and Inconel-steel (N. Kumar et al., 2023). One more extensively used bimetallic joint that needs special mention is copper-steel (Bhogendro Meitei et al., 2022).

Alloys of copper are widely employed in aerospace components and microelectronics parts due to the high value of thermal and electrical conductivities (401 W/mK, 56 Ms/m) and good ductile properties. Conversely, for practical purposes, the use of copper is restricted due to its high cost and high density (8900 kg/m^3) (Liu et al., 2019). In contrast, austenitic stainless steel (ASS) finds industrial application due to low valuation, high strength, excellent weldability (Haldar and Pal, 2024), and low density (7900 kg/m^3) compared to copper (ElSheikh et al., 2022). However, insufficient thermal dissipation characteristics of ASS lead to the development of unfavorable σ-phase and precipitation of chromium carbide (Roy et al., 2014). Therefore, cost benefits and enhanced performance of both metals can be integrated by opting for a bimetallic joint between copper and steel (Debin et al., 2020). Copper-steel joint finds application exclusively in defense sector (Bhogendro Meitei et al., 2020), power generation areas (RK et al., 2018), aerospace industries (Zhang et al., 2015), chemical industries (Mai and Spowage, 2004), nuclear sectors (International Thermonuclear Fusion Experiment Reactor-ITER) (Roy et al., 2011), heat exchange components (Cheng et al., 2019), steam turbine power plants (Moharana et al., 2016), plane wave transform linac structure (PTLS), an ultra-high vacuum system (UHVS) (Poo-arporn et al., 2020), large hadron collider (LHC) (Joshi and Badheka, 2019), plasma fusion reactor (Ramachandran and Lakshminarayanan, 2020), cryogenic components (Lusch et al., 2015) (mass flow meter (Ramachandran and Lakshminarayanan, 2020)), power electronics components (Weigl and Schmidt, 2010), electrical parts (Velu and Bhat, 2013), and automobile sectors (Akella et al., 2014). Thus, the broad application areas for copper-steel bimetallic joints necessitate an improved approach to produce a defect-free joint. However, along with the immense benefits, several challenges arise.

Due to the tremendous application areas, dissimilar joining between copper and steel has been attempted multiple times using different fusion joining techniques. That includes shielded metal arc welding (SMAW) (Velu and Bhat, 2013), gas tungsten arc welding (GTAW) (Rafiei and Mostaan, 2019), laser beam welding (LBW) (Ramachandran and Lakshminarayanan, 2020), electron beam welding (EBW) (Siddiquee et al., 2024), and hybrid welding (HW) (Meng et al., 2019) process. The copper-steel fabricated joints are not without defects. The commonly reported defects are spatter (Kar et al., 2018), porosity (Tanmay and Panda, 2023), micro-cracks (Cheng et al., 2019), solidification cracks (Joshi and Badheka, 2019), shrinkage (Magnabosco et al., 2006), lack of fusion (LOF) (Kuryntsev et al., 2017), micro-fissures (Magnabosco et al., 2006) and macro-segregation (Meng et al., 2019).

The literature survey on the dissimilar joining of copper and steel thoroughly discusses the methods to overcome the effect of irregular temperature distribution due to vast differences in thermal conductivities. The different techniques employed by researchers are (i) offsetting/inclining beam/arc towards Cu-side (Guo et al., 2016), (ii) pre-heating the copper base plates (Saranarayanan et al., 2019), and (iii) opting for a suitable joint design (bevel geometry towards Cu (45°) (Joshi and Badheka, 2020), V-shape groove (Saranarayanan et al., 2019), and scarf geometry (Yao et al., 2009)). In addition, the selection of the welding process plays an essential role in either suppressing or mitigating defects during the joining of dissimilar materials (Magnabosco et al., 2006). Table 2.5 provides comprehensive insights into the major challenges, defects reported, key findings, and techniques employed to overcome the difficulties (due to differences in the properties) during Cu-SS joint fabrication by different fusion welding processes.

Table 2.5 Details the major challenges, defects reported, and key findings during fusion welding of Cu-SS bimetallic joints.

<table>
<tr><th>Key observations reported by authors (Reference)</th><th>Figure(s)</th></tr>
<tr><td>Bimetallic joints (C10300, SS304) fabricated with electron beam oscillation (oscillation diameter: 1 mm, oscillation frequency 600 Hz) demonstrated better weld properties (UTS: 252 MPa, %EL: 19 %) with minimum defects (64 pores) contrast to joints assembled without beam oscillation (249 MPa, 17 %, 115 pores). Implementation of beam oscillation allowed enhanced mixing of copper and steel, which also aided in back-filling of microcracks (shown in Fig. 2.9). Enhanced mixing resulted due to overlapping of small melt pools formed during arc oscillation, followed by Marangoni-driven Cu movement through the overlapping melt pools (Kar et al., 2016, 2018).</td><td>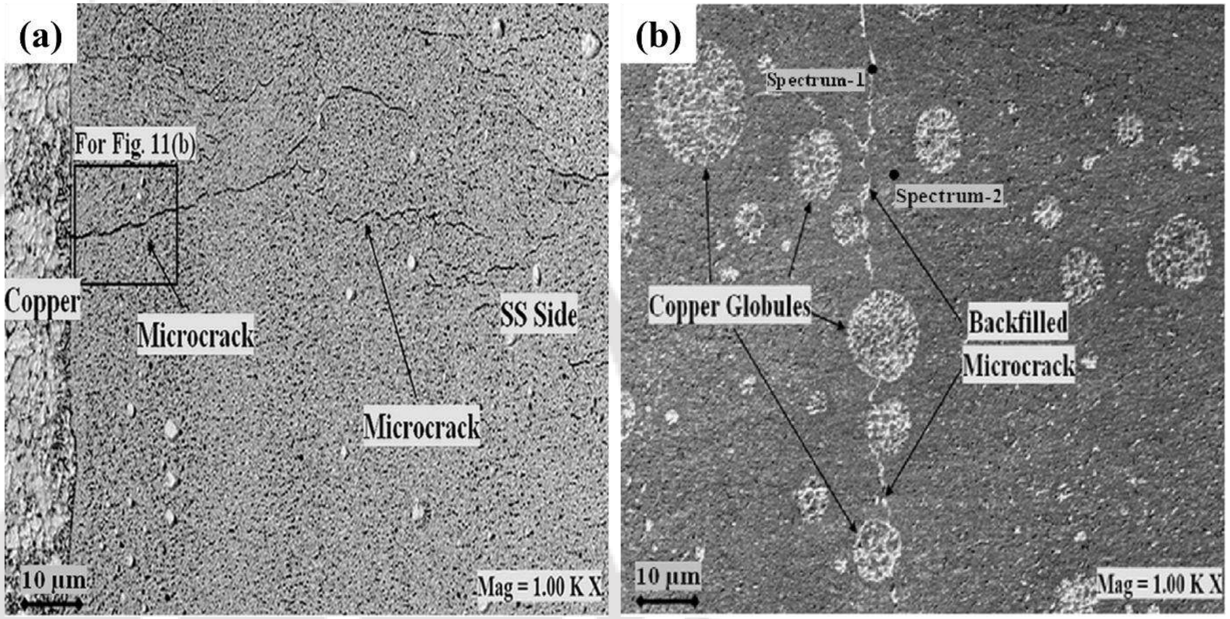

Fig. 2.9 FESEM images of joints demonstrate (a) microcracks (fabricated under no beam oscillation) and (b) back-filling of microcracks (beam oscillation:1 mm) (Kar et al., 2016, 2018).</td></tr>
<tr><td colspan="2">Tosto et al. (Tosto et al., 2003) fabricated Cu-SS joints using the EBW process without beam offset with parameters 15 kW, 398 mA, and 0.6 cm/s. The authors reported the occurrence of non-equilibrium phases and the failure of the binary phase diagram (Cu-Fe) to forecast the microstructural morphology. Due to the higher cooling rate, the existence of non-equilibrium phases (Cu-rich) pointed towards microstructural instability of the joints. Cracks or porosity were non-existent and the failure strength of the bimetallic joint was evaluated as 210 MPa, compared to 215 MPa for pure Cu.</td></tr>
</table>

Table 2.5 Details the major challenges, defects reported, and key findings during fusion welding of Cu-SS bimetallic joints (cont.).

Key observations reported by authors (Reference)	Figure(s)
An arc-based hybrid joining approach was implemented to explore the joint properties of Cu-SS joints. Increase in heat input (281, 354, 486 J/mm) modified the joining mode from weld-brazing (281 J/mm) to non-typical weld-brazing (354 J/mm) to fusion welding (486 J/mm) (shown in Fig. 2.10). Pores and micro-cracks were reported for the 354, 486 J/mm joints with mechanical properties (UTS, %EL) 229 MPa, 84 % and 224 MPa, 81.7 %, respectively. Meanwhile, dual properties of brazing and welding facilitated the formation of joints (281 J/mm) without any defects (226 MPa, 83 %) (Cheng et al., 2019).	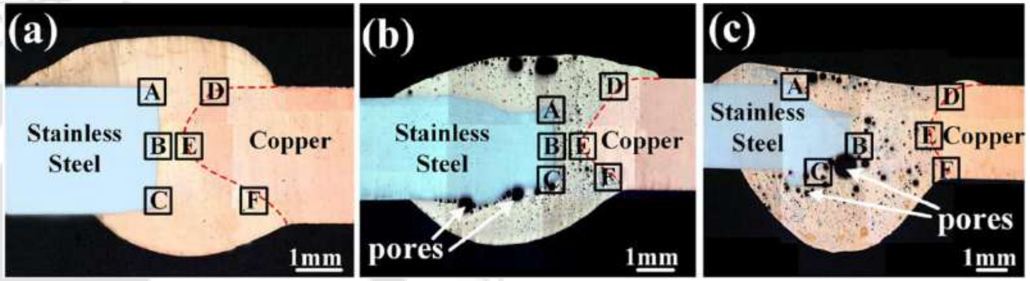 **Fig. 2.10** Macrographs of Cu-SS bimetallic joints fabricated at (a) 281 J/mm (weld-brazing), (b) 354 J/mm (non-typical weld-brazing), and (c) 486 J/mm (fusion welding) (Cheng et al., 2019).
Joints fabricated with the simultaneous application of fiber laser and arc-welding led to the fabrication of defect-free Cu-SS joints at optimum offset value (towards Cu-side). Value of offset lower than 0.5 mm contributed towards a decline in joint properties due to higher melting of steel, which led to macro-segregation (peninsula and islands). On the other hand, offsets higher than 1.0 mm led to depleted joint properties due to coarse (Cu) columnar-type grains (shown in Fig. 2.11). Joints assembled at optimum values (0.5 mm arc offset) led to a maximum strength of 215 MPa, with failure occurring in the Cu-base metal (Meng et al., 2019).	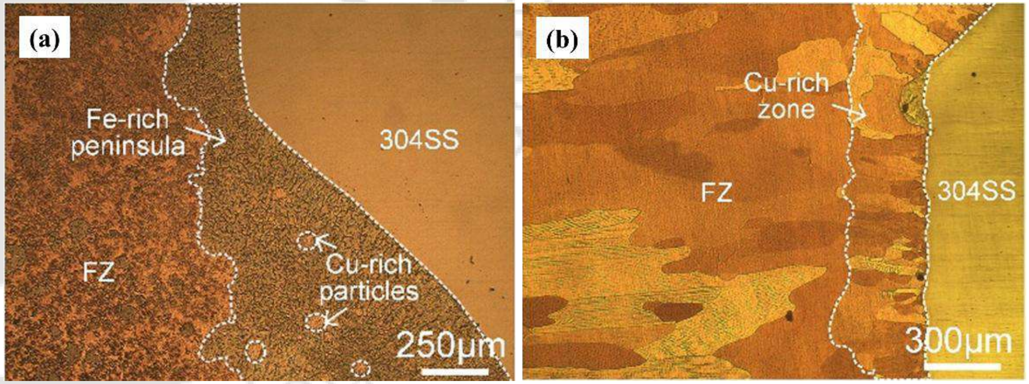 **Fig. 2.11** Fusion zone of Cu-SS dissimilar joints at (a) no arc offset and (b) 1.0 mm arc offset (Meng et al., 2019).

Table 2.5 Details the major challenges, defects reported, and key findings during fusion welding of Cu-SS bimetallic joints (cont.).

Key observations reported by authors (Reference), Figure(s)

Cu plates were subjected to pre-heating (500 ℃), and the joint was suitably designed to compensate for the differences in the thermal properties of Cu and SS. Three different filler materials (Ni-Cu-Fe, SS304, and Cu) were employed to fabricate the Cu-SS joints. Joints formed with Cu-filler wire resulted in excellent joint properties (96 % joint efficiency, 44 % %EL with respect to copper) with no defects reported (shown in Fig. 2.12) (Shiri et al., 2012).

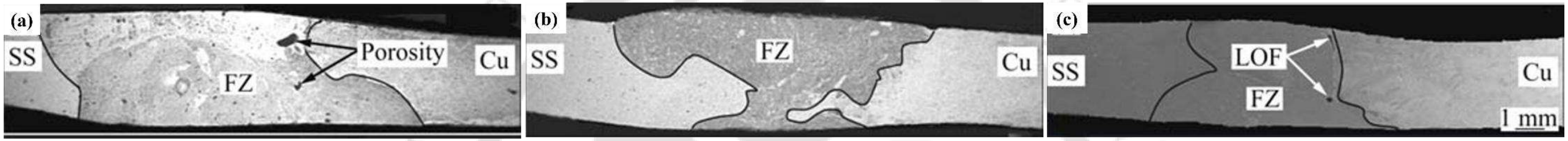

Fig. 2.12 Cu-SS bimetallic joints welded by different filler wires (a) Ni-Cu-Fe, (b) Cu, and (c) SS (Shiri et al., 2012).

Proposed two mechanisms (dependent on the T_{Liquidus} of bulk weld material, $T_{\text{Liquidus (weld)}}$) responsible for the formation of macro-segregation (peninsula, beach) in Cu-SS dissimilar joining. Formation of steel-peninsula occurs when $T_{\text{Liquidus (weld)}} < T_{\text{Liquidus (LCS)}}$, whereas the formation of Cu-beach occurs when $T_{\text{Liquidus (weld)}} > T_{\text{Liquidus (Cu)}}$. Fig. 2.13 represents the Cu-SS bimetallic joint fabricated by the GTAW process with microstructural features demonstrating a Cu-beach and Fe-rich peninsula (Soysal et al., 2016).

Fig. 2.13 Illustrates microstructural features (beach, peninsula, fusion boundary) of Cu-SS dissimilar joint (Soysal et al., 2016).

Beam offset was identified as the most dominant factor (among laser power, speed, and beam offset) that governs the strength of the fabricated bimetallic joints using the LBW process (1.3, 1.9 kW; 20, 30 mm/s). Joint properties illustrated maximum strength (261 MPa at 1.3 kW and 30 mm/s) and minimum strength (66 MPa at 1.9 kW and 30 mm/s) for the welds prepared with beam offset towards Cu-side and SS-side, respectively (Sahul et al., 2020).

Table 2.5 Details the major challenges, defects reported, and key findings during fusion welding of Cu-SS bimetallic joints (cont.).

Key observations reported by authors (Reference)	Figure(s)
Arc offset (0-3 mm, towards Cu-side) was implemented in the GTAW process (90 A, 11 V, 1.414 mm/s) to successfully join Cu and SS in butt configuration. At 1.25 mm arc offset, joint strength of 194 MPa and 83.62 % elongation was achieved. In contrast, the melting of copper was restricted with smaller offset values (0-0.75 mm), and defects (hot cracks, porosity, and LOF) were reported for the arc offset values beyond the optimal range (1.0-2.50 mm). Fig. 2.14(a, b) demonstrates the occurrence of a hot crack for the joint fabricated at 0.75 mm arc offset value, whereas defect-free weld was reported at 1.25 mm arc offset value (Singh et al., 2020, 2021).	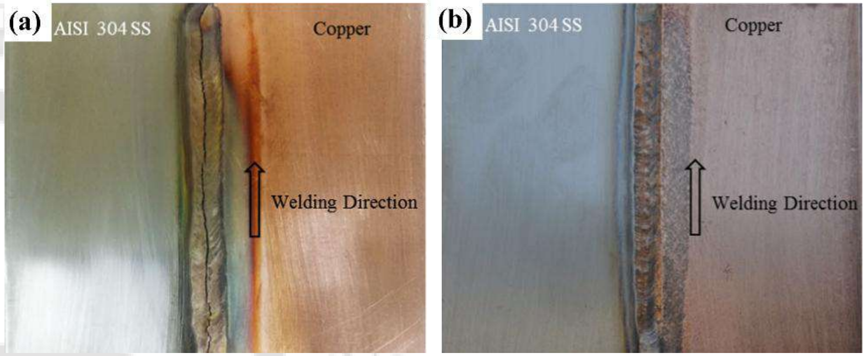 **Fig. 2.14** Depicts Cu-SS dissimilar joints fabricated at (a) 0.75 mm and (b) 1.25 mm arc offset values (Singh et al., 2020, 2021).
Bimetallic joints were produced with and without the addition of filler materials (Ni-based) using the GTAW process (120 A, 150, 200 mm/min). Differences in the joint properties were evident with 85 % efficiency and 35 % elongation for the weldments prepared without filler, whereas 96 % efficiency and 29 % elongation for the joints fabricated with NiCr-3 as filler material (Tanmay and Panda, 2023).	
Dissimilar Cu-SS joints were fabricated using the EBW process with parameters 60 kV, 43-70 mA, and 10 mm/s. Implementation of modest beam offset (0.2 mm SS-side to 1 mm Cu-side) resulted in enhanced joint performance on account of restricted HAZ and limited defects in the FZ. Whereas, an increase in the beam offset led to deterioration in the joint quality, which led to a brittle mode of fracture. Micro-cracks were reported and 250 MPa was achieved as the maximum value of joint strength (Guo et al., 2016).	

It is evident from the literature survey that Cu-SS has been welded using different fusion welding processes (SMAW, GTAW, LBW, EBW, Hybrid). However, the influence of arc offset and heat input is yet to be explored for the joining of Cu and SS without filler wire by the GTAW process.

2.7 Weldability of dissimilar austenitic stainless steels

Dissimilar metal welds (DMWs) involving different stainless-steel grades are extensively utilized to enhance the performance and lower the resulting components' cost. DMW promotes different metals' functionality while conserving their distinctive properties for specific applications (Raghav et al., 2020). In order to reduce the cost and enhance functionality, different grades of austenitic stainless steels (ASSs) are joined in the present study. ASS contains a relatively high weight percentage of nickel and chromium, leading to high resistance to corrosion and crack formation. The austenitic phase is stabilized at room temperature due to nickel's inclusion in the stainless steel matrix (Vashishtha et al., 2017). However, due to the relatively high valuation of nickel, using another grade of steel containing a lower amount of nickel results in cost reduction (Chuaiphan and Srijaroenpramong, 2019).

The joining of dissimilar ASSs is popular among researchers owing to its wide range of applications (Shinde and Telsang, 2016). ASSs are extensively employed in structural engineering usage (Türker et al., 2018), in nuclear reactors, offshore industries, chemical plants, and bio-medical areas as implant material (Shit et al., 2019). In particular, the SS300 series offers enhanced corrosion resistance and cryogenic properties due to the presence of high chromium and nickel percentages (Durgaprasad et al., 2023). Due to such varied application areas, ASSs finds 70 % usage of the total stainless steel consumption (Vasantharaja et al., 2018). ASSs possess excellent weldability, but the two most common complications exist in hot-cracking and sensitization/weld-decay. ASSs are reasonably ductile and can undergo considerable shrinkage, but the joints are sensitive towards cracking during the cooling cycle (Soltani and Tayebi, 2018). Difficulties associated with the ASS weld joint are compounded with the formation of carbides along the grain boundary (GB), leading to sensitization/weld-decay (Singh and Slathia, 2016). Various researchers have outlined the influence of heat input on the joint strength, microstructural morphology, and corrosion resistance characteristics for dissimilar ASS weld fabricated using a fusion welding process. Few researchers reported fine equiaxed structure and reduced inter-dendritic spacing in the fusion zone improve joint strength (Bhattacharya and Kumar, 2016; Huang, 2010; Kumar and Shahi, 2011; Pascu et al., 2016; Saha and Pal, 2019; Tümer and Yılmaz, 2016). Some researchers identified a reduction in corrosion resistance in the weldments with an increased amount of heat input. The authors reported that high heat input corresponds to a reduction in the δ_{ferrite} level and separation of chromium in the weldments, which results in the lowering of chromium percentage (Gil et al., 1988; Jiru et al., 2019; Madhusudhan Reddy et al., 2005; Neissi et al., 2016; Samanta et al., 2008; Yousefi et al., 2015).

Dissimilar ASS joints are primarily recognized for their superior corrosion-resistant behaviour, better strength at elevated temperatures, and excellent low-temperature fatigue properties. However, with low specific heat and thermal conductivity, high thermal expansion coefficients of ASS often exhibit inferior mechanical properties of welded joints owing to (a) the development of high residual stresses and structural deformation propensity and (b) ignorance of the role of microstructural attribute in residual stress evolution (Lin and Chou, 1995). The accurate prediction of residual stress is always of great interest as it paves the road to eliminate or mitigate it.

However, the problem of residual stress arises from the non-uniform heat flux distribution, and it becomes more complex when the welded components have different coefficients of thermal expansion, thermal conductivity, variation in composition change, and different microstructures (Haldar and Pal, 2023; A. Kumar et al., 2023a). Several researchers have made an effort to understand the mechanism for the development and mitigation of residual stresses in dissimilar welded joints (Anawa and Olabi, 2008; A. Kumar et al., 2023b; R. Kumar et al., 2023). Dawes (Dawes, 1992) opined that the grades of ASS expand by 50% more than carbon steels and have poorer heat conductivity; hence, they are more likely to bend and expand unevenly when combined. Usually, high magnitude of residual stress is localized in the heat-affected zone (HAZ) due to phase-change-induced expansion during cooling (Kumar and Nagamani Jaya, 2023). Akbari and Sattari-Far (Akbari and Sattari-Far, 2009) showed that heat input primarily controls the level of residual stress in multi-pass dissimilar welding between stainless steel and carbon steel. The compressive stress in the stainless-steel side reduces with a decrease in heat input. Maurya et al. (Maurya et al., 2023) reported that excessive heat input caused residual stress to rise by 16 and 19%, respectively, in the longitudinal and transverse directions for dissimilar welding of Inconel and stainless steel. In all these cases, the effect of phase transformation was neglected.

The influence of heat input on microstructural evolution and phase transformation effect for similar and dissimilar ASS joints are well studied in the literature. Hsieh et al. (Hsieh, 2008) studied the precipitation and strengthening behaviour of dissimilar ASS joints and identified higher hardness values due to Cr-rich massive δ_{ferrite} at solidified metal. The grain refinement of δ_{ferrite} is enriched upon increasing the number of weld passes for dissimilar

ASS joints (Hsieh and Wu, 2011). Kianersi et al. (Kianersi et al., 2014) observed three different morphologies of $\delta_{ferrite}$ (skeletal, acicular, and lathy) in laser-welded ASS structures. The non-equilibrium phases evolved here due to the rapid cooling of welding processes. Relatively higher heat input or lower cooling rate exhibits coarsening of the ferritic-dendritic core and widening of inter-dendritic spacing, which resulted in dampening of tensile strength of welded joints. Harjo et al. (Harjo et al., 1998) reported that the compressive strain was generated in the ferrite phase, whereas the tensile strain appeared in the $\gamma_{austenite}$ matrix. Further, Thibault et al. (Thibault et al., 2010) observed compressive residual stress in the weld joint due to lowered martensitic transformation temperature of 13%Cr-4%Ni steel alloy. Hsieh et al. (Hsieh et al., 2014) examined the propensity of tensile residual stress enhanced by the enrichment of $\delta_{ferrite}$ content of SS304. A feathery ferrite and compressive stress pattern were observed by Chen et al. (Chen et al., 2019) in the hybrid laser-welding of ASS. However, the mechanism behind the development of stress was not elucidated adequately.

The chemical composition, cooling rate, and primary solidification mode rendered during welding are the main factors influencing the formation of $\delta_{ferrite}$. It is realized that the amount and distribution of $\delta_{ferrite}$ in an ASS weldment is crucial since it determines the thermal stability, mechanical performance, and residual stress generation of the weld joint. The primary reason for the generation of residual stresses is linked with the solidification of the weld. Since the dilution occurs during liquid-to-solid phase transformation, and the solid-state phase transformation (SSPT) occurs after solidification with a differential cooling rate (De and DebRoy, 2011). It is well-known that residual stress tops the list in causing severe damage to a weld specimen (Deng and Murakawa, 2013; Kesavan Nair and Vasudevan, 1995; Olabi and Hashmi, 1993). Therefore, predicting, controlling, and finding ways to reduce stress developed in a welded structure remains the utmost priority.

Researchers have tried to predict residual stresses using experimental measurements aided by numerical models (Feng, 2005; Lindgren, 2006). Deng (Deng, 2009) highlighted the importance of martensitic transformation in the stress generated in medium carbon steel. The variation in the longitudinal stress value was minimized by considering the SSPT effect. Several researchers closely resembled the predicted value with the experimental results by incorporating SSPT (Hamelin et al., 2014; Yaghi et al., 2008; Zubairuddin et al., 2014). Zubairuddin et al. (Zubairuddin et al., 2014) reported drastic variation in predicting the value of transverse stress with (542 MPa) and without (635 MPa) consideration of the phase transformation effect in the 9Cr-1Mo steel joint. The authors suggested that austenite to martensite transformation accounts for a significant difference in the stress value. Hamelin et al. (Hamelin et al., 2014) reported that high welding speed resulted in more martensite because of the high cooling rate. Even the prediction of residual stresses resembled the experimental data when phase transformation plasticity was implemented in the numerical model. Yaghi et al. (Yaghi et al., 2008) reported a stress reversal from tensile to compressive in the fusion zone by including the effect of SSPT and TRIP in the case of P91 steel. Li et al. (Li et al., 2021) observed that consideration of SSPT accurately predicts the residual stress in dissimilar P22-SS304 joints. Kumar and Bag (Kumar and Bag, 2019) predicted a low value (810 MPa) of longitudinal stress considering the phase transformation effect and minimum residual stress under the least heat input (45 J/mm) characterized by high δ_{ferrite} content, finer lath size, and lower inter-dendritic spacing (Kumar et al., 2021). Taraphdar et al. (Taraphdar et al., 2021b) indicated that incorporating the SSPT effect provided significantly better correspondence with the measured value for longitudinal (~205 MPa) and transverse (~230 MPa) stress fields in the case of carbon steel. A similar observation is reported by Kubiak and Piekarska (Kubiak and Piekarska, 2016). Mi et al. (Mi et al., 2016) indicated that physical properties, volume change, and transformation-induced plastic strain are highly influential for reliable estimation of residual stress. Accounting both diffusive and displacive transformations in a TMM improves the welding distortion pattern. In fusion welding of ultra-high strengthened carbon steel, the microstructure consisting of bainite with a lower proportion of martensite also influences the residual stress evolution (Ghafouri et al., 2020). Considering the details of microstructural phenomena and their kinetics during solidification improves the reliability of residual stress calculation.

The measurement of residual stress is one of the most daunting tasks following both destructive and non-destructive techniques. Several researchers have developed contemporary novel techniques to enhance the accuracy of measurement of residual stress components (Elata and Abu-Salih, 2005; Shen et al., 2015; Taraphdar et al., 2020). Shen et al. (Shen et al., 2015) determined surface residual stress based on spherical indentation. The localization of the largest pile-up around an indentation indicates the maximum residual stress. The particular link between pile-up after unloading and biaxial stress allows us to accurately detect the components of residual stress. Taraphdar et al. (Taraphdar et al., 2020) developed a flexible deep hole contour technique that does not need a complete section of the specimen and has the potential to measure through-thickness residual stress patterns with a relatively lower degree of damage of tested samples. Additionally, Elata and

Abu-Salih (Elata and Abu-Salih, 2005) developed a residual stress measurement method following the electromechanical bifurcation response of a clamped-clamped beam. The presence of weld grooves significantly impacts residual stress generation (Taraphdar et al., 2021a). By accommodating the unequal V-groove pattern, the magnitude of residual stress components can be minimized near the root of the weld joint. An alternating weld pass sequence also dampens residual stress generation. However, the application of a single-directional weld pass sequence in an equal double-V groove configuration leads to the agglomeration of higher tensile residual stress (Taraphdar et al., 2021c). Literature indicates that maintaining an optimum level of heat input governs the quality of weld joints, and the presence of tensile residual stress tends to affect the fatigue strength of a weld joint. Thus, the likelihood of compressive stresses in the welded structure is increased when considering the influence of microstructural transformation, which improves the joint quality (Nowacki et al., 2016; Pandey et al., 2018).

It is evident from the literature that thermal stability, mechanical features, and residual stress of dissimilar ASS welding are controlled by the distribution and quantity of δ_{ferrite} at the fusion zone. Further, estimating residual stress in dissimilar austenitic steels is highly complicated, where the solidification behaviour and morphology are predominant. Also, a significant lack of substantial work on dissimilar joints with the incorporation of solid-state phase transformation (SSPT), which has yet to be explored.

2.8 Theoretical model

The physical phenomena involved during a fusion joining process are heat and mass transfer, fluid flow, and phase transformation. It becomes a complex task to analyze these phenomena together hence each phenomenon is de-coupled and then analyzed individually. Due to the complexity involved in a welding process, precise quantification of temperature variation in the weld pool is unrealistic due to the welding process's intricacy and the existence of a high magnitude of temperature. Hence, a finite element (FE) based numerical model helps to overcome the experimental limitations by estimating (i) the temperature in the weld pool temperature and near the HAZ, (ii) the maximum temperature, and (iii) the determination of the cooling rate by evaluating solidification parameters (G: temperature gradient, K/mm and R: solidification velocity, mm/s) (Dixit and Bag, 2017; Jain et al., 2017). In the conduction-based heat transfer model, heat source selection plays the most important role governing the weld bead geometry. Hence, choosing an appropriate heat source in a conduction-based heat transfer model directly influences the bead geometry, heating, and cooling cycles. Evaluating the above-mentioned parameters is extremely difficult to achieve without applying mathematical models.

Application of analytical models for welding processes is restricted due to limiting assumptions (Rosenthal, 1941; Nguyen et al., 1999) that allow the model to be implemented only for basic geometric forms, which often overlook factors like (i) temperature-dependent properties, (ii) latent heat, (iii) fluid flow, and (iv) distribution of heat source. Due to limited application of analytical models, computational models evolved and aided in precisely predicting key features of the weld pool. Various numerical methods, including finite element (Tsirkas et al., 2003; Bag et al., 2009), finite difference (Mazumder and Steen, 1980; Kim et al., 2002; Cherepanov et al., 2006), and finite volume (Taylor et al., 2002; He et al., 2004) are widely implemented for the modeling of welding process. Additionally, the majority of the research work on fusion welding the follows conduction-based heat transfer model (Goldak et al., 1984; Frewin and Scott, 1999; Kim et al., 2002; Chang and Na, 2002; De et al., 2003a). The numerical modeling involving the fusion welding process follows the following steps:

- The welding torch provides the necessary heat to the base metals. Hence, a heat source is required when the arc comes in contact with the base metals, wherein the heat source intensity specifies the bead geometry of the resulting melt pool.
- The arc creates a melt pool, wherein heat transfer occurs, while the remaining part of the domain experiences only heat conduction.
- Once the welding process is completed, it undergoes the process of solidification. The rate at which the cooling occurs governs the resulting microstructure of the joints.
- The resulting welded joint inherently develops permanent deformation and locked-in stresses.

In the next section, heat sources used in the different joining processes are discussed in detail.

2.8.1 Heat source model

The concept behind using a heat source model is to replicate the welding process using a surface or body (volumetric) heat flux to successfully perform the numerical modeling to fetch the temperature distribution during the joining process. To perform numerical simulation of thin structures, the choice of the heat source and its parameters plays a vital role (Sun et al., 2014). To predict the temperature field, Rosenthal (Rosenthal, 1941) tried using analytical methods for static and linear arc-based joining methods. However, it failed to successfully predict the heat source temperature at the center, and temperature-dependent properties were also neglected (Eagar and Tsai, 1983). Pavelic (Pavelic, 1969) proposed a distributed heat source as an alternative to a point/line heat source for the first time. The results demonstrated better accuracy than Rosenthal's outcome. Several researchers superimposed Pavelic's disc-shaped model with the finite element modeling to achieve improved accuracy in predicting temperature distribution. Friedman applied the Gaussian-aided disc model by using the FE method and reported improved temperature history compared to the model developed by Rosenthal (Friedman, 1975). A surface heat flux was first introduced to numerically model the thermal behaviour by implementing finite difference method (FDM) (Mazumder and Steen, 1980). Mazumder and Steen utilized a Gaussian-based heat source and assumed Beer-Lambert's equation for absorption of energy for penetration within the melt pool. Chande and Mazumder (Chande and Mazumder, 1984) enhanced the previous model by incorporating temperature-dependent properties and latent heat of fusion. Surface heat flux might be used for shallow depth of penetration. However, a surface heat flux lacks complete penetration depth during thermal analysis. Goldak et al. (Goldak, 1985) introduced double-ellipsoidal heat source distribution that can be implemented to achieve deeper penetration in processes like gas metal arc welding (GMAW), however, lacks complete penetration in high-energy density processes having high depth-to-width ratio. If the weld pool shape deviates from an ellipsoidal shape, then different heat source models are opted (Du et al., 2004; Yadaiah and Bag, 2012, 2014; Bag and Amin, 2020). Yadaiah and Bag (Yadaiah and Bag, 2012) estimated the heat source parameters of the double-ellipsoidal model and assumed it to be a function of weld velocity. Du et al. (Du et al., 2004) implemented a hybrid heat source comprising a Gaussian plane at the top surface and a cylindrical shape along the weld thickness. The estimated results were in good agreement with the experimental results for titanium alloys. Yadaiah and Bag (Yadaiah and Bag, 2014) established an egg-shaped heat source by altering the double-ellipsoidal heat source to reduce the input parameters of the heat source. Different FE-related numerical models are developed and used for computational analysis by various researchers (B. Kumar et al., 2018), wherein the heat source model selection mainly depends on the joining process and dimensions of the resulting weld bead profile. Baruah and Bag (Baruah and Bag, 2016) recent computational work on the M-PAW process indicates that a Gaussian distribution body heat flux with decreasing intensity in-depth direction appears to be the ideal option for estimation of weld bead profile.

Hence, it's evident that the selection of a heat source plays a significant role in correctly identifying the temperature distribution in the weld pool (Zacharia et al., 1989). Nevertheless, incorporating a precise and appropriate heat source model in thermal analysis is inadequately documented. A body (volumetric) heat source is frequently implemented in the conduction-based heat transfer model to make up for the impact of the convective mode of heat transfer in the melt pool. In the next section, the conduction-based heat transfer model is discussed in detail.

2.8.2 Conduction based heat transfer model

The weld pool geometry is crucial in determining the joint properties of the weld. Precise quantification of the temperature field in the weld pool and HAZ significantly predicts the temperature-time data and weld geometry (Jou, 2003). An FE-based transient thermal analysis aids in determining the temperature fields and bead geometry, wherein all three modes (conduction, convection, and radiation) of heat transfer are considered. The accuracy of the developed model is verified by comparing the numerical results with the experimental values. To establish the temperature distribution during the joining, the energy conservation equation is applied. A classical heat conduction equation is applied to determine the amount of heat transferred during the arc-based welding process. The conduction-based heat transfer model is generally applied because it is computationally economical and simpler to implement (De et al., 2003b; Trivedi et al., 2007). Thus, preference is given to the conduction-based heat transfer model in contrast to transport (convective) phenomena-based models for thin sheets involving rapid heating and cooling. Bag and De (Bag and De, 2010) reported that conduction-based heat transfer models are suited to weld pools of smaller geometry, whereas transport phenomena-based heat transfer models are suitable for the larger weld pool areas. De et al. (De et al., 2003b) proposed a 2D axisymmetric numerical analysis of heat transfer in the laser spot welding process, wherein a double-ellipsoidal heat source was used to represent the laser heat source by assuming a conduction-based heat transfer model. The authors reported good agreement between the numerical results in predicting the weld bead geometry. Wu et al. (Wu et al., 2014b) precisely predicted the weld melt line in the keyhole PAW process by implementing a conduction-based heat source model using a Gaussian-shaped heat source. Baruah and Bag (Baruah and Bag, 2016) applied a conduction-based heat transfer model to predict the temperature field and bead geometry of micro-plasma arc welded Ti-6Al-4V alloy. The authors used a Gaussian-shaped surface heat flux and successfully predicted the weld bead size with an error of 15 %. The authors applied a Gaussian-shaped heat source with intensity decreasing exponentially in the thickness direction. The authors reported complete penetration depth for the 0.5 mm thin sheets. Further, the authors (Baruah and Bag, 2017) predicted the temperature field and bead geometry for micro-plasma arc welded SS304 and low carbon steel (LCS). The authors used the same heat source model previously used for Ti-6Al-4V alloy and estimated the temperature profile and bead dimensions. Sahu and Bag (Sahu and Bag, 2021) performed thermal modeling to evaluate the cooling rate and bead size for micro-plasma arc welded 0.7 mm IN718 alloy. The authors used a conduction-based heat source and applied a double ellipsoidal model to estimate the bead size with an error of 7.3 % (shown in Fig. 2.17, Table 2.6). The authors estimated the temperature gradient ($G, K/mm$) value from the numerical model and utilized the welding velocity as solidification rate ($R, mm/s$) to calculate the cooling rate. The authors (Sahu and Bag, 2020) reported the limitations of the double-ellipsoidal model for application in the case of dissimilar materials having wide differences in their thermal properties. Hence, the authors implemented a quadruple-ellipsoidal heat source to estimate the bead geometry and temperature distribution for micro-plasma arc welded IN718 and SS316L. Numerical modeling of thin sheets has been explored by past researchers; however, numerical modeling of thin sheets related to cupronickel alloys and dissimilar ASSs by micro-plasma arc welding process has yet to be explored.

One of the most common issues related to thin sheet joining remains the generation of residual stress and a distorted structure, which has a detrimental influence on the welded component. Hence, estimating stress and distortion becomes inherently necessary for thin welded structures.

2.8.3 Thermo-mechanical and thermo-metallurgical-mechanical (TMM) model

The development of a numerical model that can accurately predict the value of residual stress and weld-induced distortion remains a crucial part of any welding process. With the recent advancement in FE-based software, estimation of stress and distortion can be achieved at smoothly and effectively. The FE-based computational tool enables the necessary measurement of thermal (temperature and solidification parameters), metallurgical (phase transformation), and mechanical (residual stress and distortion) characteristics that would have been challenging otherwise by experimentation (Trivedi et al., 2006). However, to achieve the aforementioned characteristics, the establishment of the heat transfer model with the proper selection of heat source becomes inherently necessary.

Camilleri et al. (Camilleri et al., 2005) estimated the value of angular deflection by using finite element method (FEM) analysis for thin sheets fabricated by liquid-state joining technique. Depradeux and Jullien (Depradeux and Jullien, 2004) performed sequentially coupled thermo-mechanical analysis for the GTAW process to predict the mechanical characteristics of the welded joints, wherein the output of the thermal analysis was used as an input for the mechanical analysis. Deng and Murakawa (Deng and Murakawa, 2008) performed thermo-mechanical analysis on 1 mm thin sheets of low carbon steel (LCS). The authors highlighted the importance of geometrical non-linearity and large deformation theory in predicting thin sheets' deformation. Saikia et al. (Saikia et al., 2019) applied a thermo-mechanical model to predict the temperature field, bead geometry, stress, and distortion in micro-plasma arc welded maraging steel. Baruah and Bag (Baruah and Bag, 2016, 2017) neglected the influence of phase transformation and implemented a thermo-mechanical model to estimate the thermal and mechanical characteristics. The authors (Baruah and Bag, 2017) evaluated distortion (shown in Fig. 2.18 (Table 2.6) for low carbon steel and SS304 fabricated at 59.4 J/mm by M-PAW process. Further, the authors (Baruah and Bag, 2016) estimated the value of residual stress along the weld (shown in Fig. 2.19, Table 2.7) for Ti-6Al-4V weld fabricated by M-PAW process. However, the accuracy in predicting the mechanical characteristics is enhanced by considering the TMM model for dual-phase materials like the stainless steel and the Ti-6Al-4V. Kumar and Bag (Kumar and Bag, 2019) and Kumar et al. (Kumar et al., 2021) considered the effect of phase transformation in estimating the stress value for Ti-6Al-4V and SS304, respectively. Fig. 2.20 (Table 2.7) represents the transformation of δ_{ferrite} during SSPT at 45 J/mm for the SS304 joint processed by the LBW process (Kumar et al., 2021).

Hence, it can be concluded that thermo-mechanical and thermo-metallurgical-mechanical (TMM) models may be opted for depending on the type of material. For single-phase materials, where no phase transformation occurs, the thermo-mechanical model is sufficient to estimate the necessary values of temperature field, bead geometry, stress, and distortion. However, for dual-phase materials (stainless steel, Ti-6Al-4V), phase transformation occurs, wherein the thermo-metallurgical-mechanical model should be implemented to estimate the phase fraction in addition to the characteristics evaluated in the thermo-mechanical model earlier.

Table 2.6 Presents the validation of weld bead geometry and distortion contour obtained from numerical analysis.

Key observations reported by authors (Reference)	Figure(s)
The authors developed a 3D finite element thermal model and implemented a double ellipsoidal volumetric heat source to predict the weld geometry and temperature distribution for IN718 0.7 mm thin joints. A conduction-based heat transfer model with temperature-dependent thermal and mechanical properties with necessary BC's (Neumann and Dirichlet BC's) and suitable assumptions was deployed. The predicted results (shown in Fig. 2.15) were within the acceptable range with a maximum 7.3 % error (Sahu and Bag, 2021).	 **Fig. 2.15** Validation of a numerical model for IN718 joint fabricated at 52.8 J/mm by M-PAW process (Sahu and Bag, 2021).
The authors developed a 3D thermo-mechanical FE model to predict temperature distribution, bead dimensions, stress, and distortion for 0.5 mm thin sheets by implementing a body heat source with decreasing intensity in the thickness direction. The authors reported that the difference in thermal conductivity resulted in different bead sizes (2.132 mm for SS304 and 1.446 mm for low carbon steel: LCS) at 59.5 J/mm. Also, larger HAZ is achieved for LCS compared to SS304 due to the higher thermal diffusivity (α) value of LCS (α_{LCS} ~11.72, α_{SS304} ~4.2 m^2/s). The difference in the maximum value of deflection (Fig. 2.16(a, b)) is also observed for LCS (~3.56 mm) and SS304 (~4.37 mm) at 59.4 J/mm. The authors concluded by stating k and α as the vital material properties that govern the weld properties (Baruah and Bag, 2017).	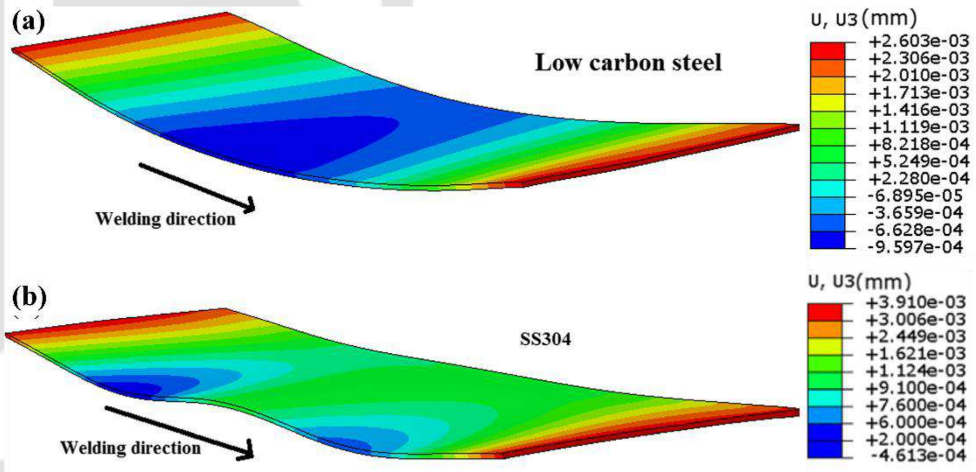 **Fig. 2.16** Illustrates distortion contour for (a) LCS and (b) SS304 fabricated at 59.4 J/mm by M-PAW process (Baruah and Bag, 2017).

Table 2.7 Presents the prediction of residual stress and phase fraction obtained from numerical analysis.

Key observations reported by authors (Reference), Figure(s)	
Baruah and Bag (Baruah and Bag, 2016) developed a 3D FE thermo-mechanical model to predict the temperature and stress distribution for 0.5 mm Ti-6Al-4V sheets fabricated by the M-PAW process. The authors sequentially coupled thermos-mechanical analysis by first performing a transient thermal analysis followed by thermo-mechanical (thermo-elastic-plastic) analysis. Due to the symmetry of the weld domain, the authors considered half of the geometry to save computational time. The authors predicted the stress (shown in Fig. 2.17) value along the weld direction and reported longitudinal stress as the primary contributor to the overall developed residual stress. For the developed model, a maximum error of 15 % was reported. During the mechanical analysis, the authors neglected the strain value due to phase transformation and considered strain due to elastic, plastic, and thermal strain.	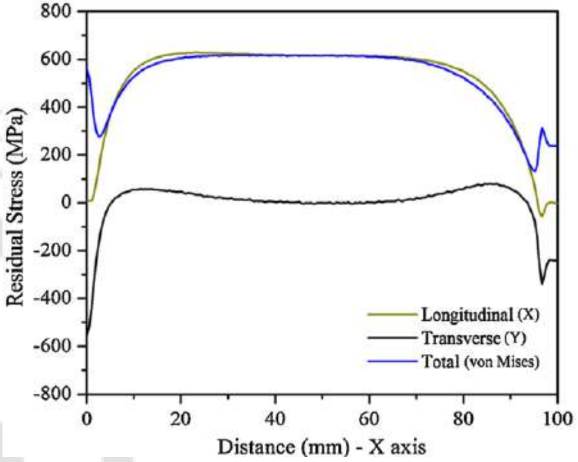 **Fig. 2.17** Stress along the weld (4 mm/s, 11 A) for Ti-6Al-4V weld fabricated by M-PAW process (Baruah and Bag, 2016).
Kumar et al. (Kumar et al., 2021) developed a 3D FE-based TMM model to identify the influence of microstructural characteristics on the developed residual stress value. SS304 thin sheets were welded by LBW process and the resulting δ_{ferrite} value was evaluated experimentally and predicted numerically (shown in Fig. 2.18). The phase fraction and residual stresses were computed employing TMM model including the effect of solid-state phase transformation (SSPT). The authors reported that the occurrence of δ_{ferrite} phase led to reduced stress value due to the generation of compressive residual stress in the dendritic core of the austenitic matrix. The developed model reported a maximum variation of ±50 MPa with the experimental value.	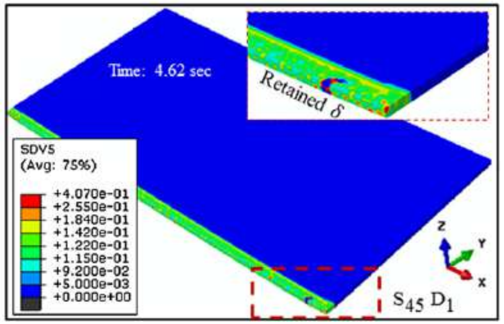 **Fig. 2.18** Transformation of δ_{ferrite} during SSPT at 45 J/mm for SS304 joint processed by LBW process (Kumar et al., 2021).

2.9 Summary

This chapter explores the difficulties associated with joining similar ($Cu_{90}Ni_{10}$) and dissimilar materials (Cu-SS and SS316L-SS310) from a practical perspective. First, the challenges encountered with the joining of cupronickel alloy are analysed. A significant portion of the chapter is dedicated to studying the effect of different fusion welding processes on mechanical, metallurgical, and corrosion behaviour of cupronickel alloys. A part of the chapter is also devoted to investigating the beneficial effect of current pulsation on joint properties. A summary of the key findings from this chapter is presented below:

- The literature highlights the key benefits of using pulse current in joining thin sheets to gain better control over the heat input, resulting in enhanced solidification behaviour and improved metal flow, leading to grain refinement.
- The literature on the joining of cupronickel alloy indicates limited research work has been conducted in thin sheet joining. Further, the similar joining of cupronickel alloy has not been addressed by the micro-plasma arc welding process. Also, the impact of pulsed current on joint properties is yet to be reported.
- Many published literatures are reported related to dissimilar joining of copper and steel employing different fusion welding processes. However, limited study is associated with gas tungsten arc welding of Cu and SS without the use of filler wire.
- The review on theoretical modeling of thin sheets suggests the application of a volumetric heat source and conduction-based heat source model to perform the numerical analysis. The development of a 3D FE-based model becomes essential for similar and dissimilar joining, which aids in minimizing the cost and efforts required for experimentation. It is to be noted that limited study is reported on the numerical analysis being applied to the micro-plasma arc welding process.
- There is a gap in the advancement of the thermo-metallurgical-mechanical model in thin sheets joining of dissimilar austenitic stainless steels that relates the microstructural morphology with the residual stress generation. Further, the influence of phase transformation plays an important role in the accurate prediction of residual stress and distortion.

2.10 Research objectives

The current research aims to identify the weldability of similar and dissimilar combination of materials using arc-based welding processes. To accomplish the research objectives, the following units are completed throughout the research period.

- To produce a stable joint for cupronickel ($Cu_{90}Ni_{10}$) thin sheets using continuous current (CC) micro-plasma arc welding process, and further enhancement in joint properties is attempted by the application of current pulsation.
- To join Cu(T2) and SS304 by using gas tungsten arc welding process to achieve minimum metallurgical non-uniformities and defect formation that enhance the joint characteristics.
- To investigate the mitigation of residual stress on the dissimilar steel (SS316L-SS310) joint by controlling microstructural morphologies and to understand the solidification behaviour of the weld metal and its correlation with delta ferrite formation and residual stress distribution.
- Development of a three-dimensional finite element (FE) based sequentially coupled thermo-mechanical and thermo-metallurgical-mechanical (TMM) model to reliably predict time-temperature data, weld dimensions, residual stresses, and distortion for joining of cupronickel alloy and dissimilar austenitic stainless steels, respectively.

2.11 Scope of the present work

Based on the literature review, the subsequent units are completed throughout the research period to accomplish the following research objectives:

- To understand the weldability of $Cu_{90}Ni_{10}$ alloy by controlling defect formation via optimum heat supplied in continuous mode using the M-PAW process. The application of current pulsation attempts further enhancement in joint properties.
- To join Cu(T2) and SS304 by offsetting the arc towards Cu-side using the GTAW process and achieve minimum metallurgical non-uniformities that enhance the joint characteristics.
- To join a different combination of ASSs (SS316L and SS310) using the M-PAW process and to establish a correlation linking the influence of heat input on the formation of different microstructural morphology, variation in joint strength, mode of failure, pore formation, and determine the optimal level of heat input that ensures weld joint remains free from internal defects, hot-cracking, and sensitization/weld-decay.
- To investigate the mitigation of residual stress by controlling microstructural morphologies that can elude the failures of a welded joint. Therefore, an attempt is made to understand the dependence of cooling rate on solid-state phase transformation and its effect on the generation of compressive residual stress in dissimilar welding of ASSs.

भारतीय प्रौद्योगिकी संस्थान गुवाहाटी • Indian Institute of Technology Guwahati •

Chapter 3

Experimental Methodology

3.1 Introduction

Experimental investigations remain an inherent necessity to envelope the input process parameters in the feasible range which ensures defect-free weld with excellent joint properties. The process starts with experiments at a preliminary level, followed by the identification of feasible parameters. This chapter deals with the experimental methodology used in the present thesis work, starting from sample preparation, welding procedure, microstructural and mechanical characterization. The optical microscope (OM), field emission scanning electron microscope (FESEM), energy dispersive X-ray analysis (EDX), and Electron Backscatter Diffraction (EBSD) evaluation techniques are used. Further, corrosion analysis is accomplished to determine the chemical stability of the joints. The NDT involved in the present investigation is to assess surface topology, measurement of distortion, and locked-in stress in the joints. Distortion in the joints is measured using coordinate-measuring machine (CMM) and surface topology is identified using non-contact surface profilometer. In addition, an advanced NDT (X-ray computed tomography: X-ray CT) is carried out to identify internal defects. The welded joints are also subjected to uniaxial tensile test using universal testing machine (UTM), microhardness testing using Vickers microhardness tester, and facture analysis. X-ray diffraction (XRD) technique is also utilized to confirm the presence of different phases. In addition, the present chapter also presents the specifications and description of the sophisticated instruments used for the characterization.

3.2 Research methodology

Fig. 3.1 illustrates the sequence of operations followed in the current investigation. Process parameters are classified into two broad categories, i.e., (i) fixed/constant parameters and (ii) variable parameters. Trial experimentation is performed to identify feasible process parameters. After several trial experimentations, variable welding parameters are optimized, and a visual inspection of the weldments is carried out to inspect the weldments. Trail runs are identified in such a way that it envelops complete 'stable' joining zone. The absence of irregular beads, root sagging, cracks, spatter, or undercuts is considered to be a 'stable' weld. To quantify the joint quality, the so-termed 'stable' weld joints are subjected to metallurgical analysis to identify grain morphology, NDT to evaluate the presence of internal imperfections, mechanical testing to determine strength and mode of failure, followed by distortion and stress analysis.

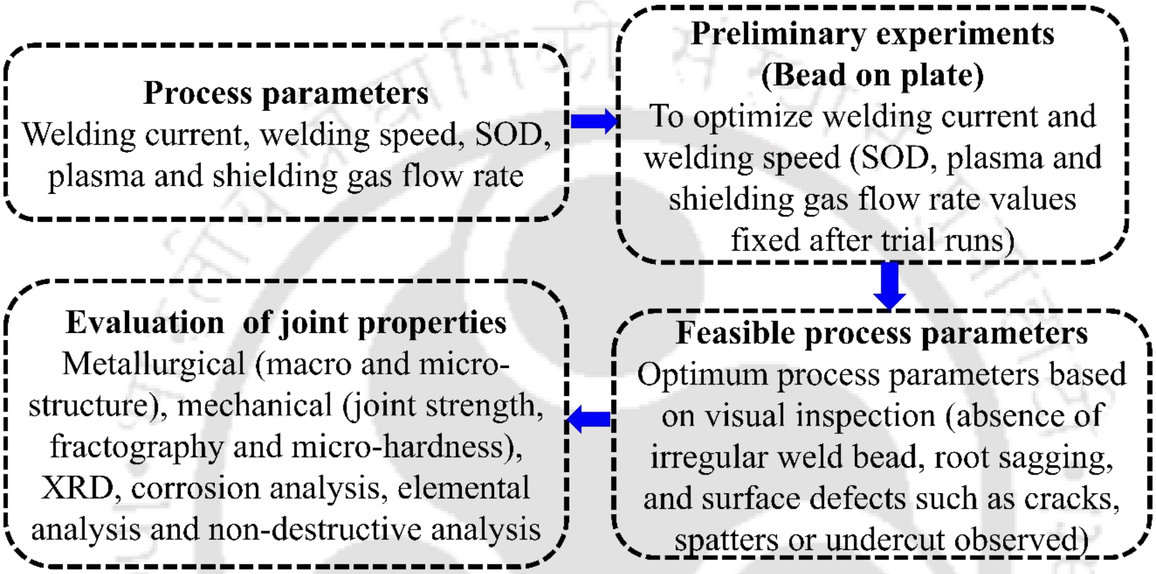

Fig. 3.1 Flow chart illustrating the sequence adopted for the present work.

3.3 Micro-plasma arc welding of cupronickel alloy

The experimental setup consists of the power source, arrangement for linear movement of the workpiece, and fixture to hold the workpiece. A direct current (DC) power supply (*Model no. MP-50, EWM,* supplied from Germany) produces the necessary heat required to fuse the materials. Fig. 3.2 represents the experimental layout employed for the present investigation. The workpiece, along with the fixture, is mounted on an arrangement capable of providing variable speed as desired. Inert gas (Argon) is employed to generate the plasma arc and shield the weld joint from surrounding contamination. The control system allows to manage the amount of inert gas inflow and set the current as required. The cooling system cools the copper nozzle after completion of the welding operation. The plasma welding torch is kept still, whereas the fixture and the workpiece are mounted on a manipulator system, which moves ahead in a route attached to the work table. The manipulator (a motor-driven machine) is controlled using a speed regulator.

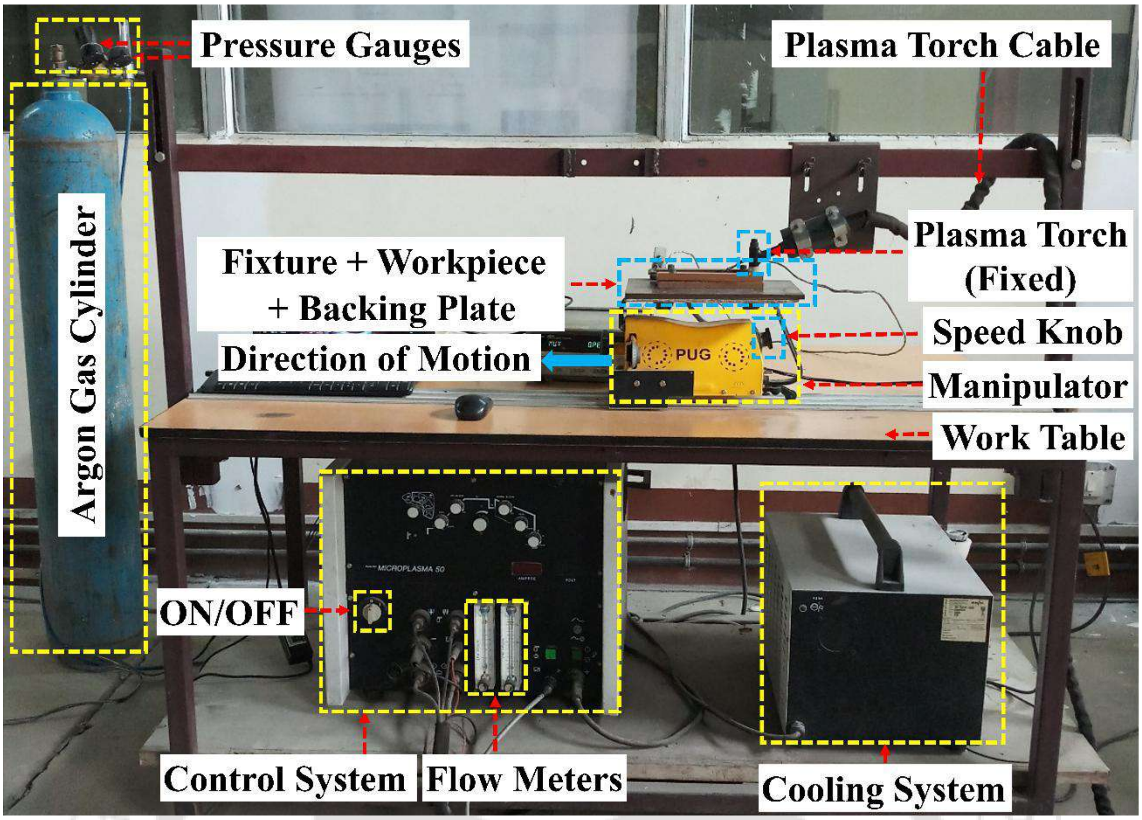

Fig. 3.2 Experimental layout employed for micro-plasma arc welding of thin sheets.

A data acquisition system (DAS) (*Make: Agilent, model no. 34972A*), together with bench link data-logger, software is employed to govern the test, present outputs, and accumulate information for additional evaluation. The combined system (DAS and data logger) is used with a multiplexer to obtain temperature-time (dT/dt) details at the desired thermocouple position with the assistance of a K-type thermocouple. The scan rate is fixed using the configuration unit available in the DAS, and the obtained temperature-time (dT/dt) data is displayed on the computer screen connected to the DAS. To validate the reliability of the thermal model, a K-type thermocouple (shown in Fig.3.3(a)) is used to extract dT/dt data, wherein the operating temperature of the thermocouple is between 73-1533 K for single usage, and the reliability of the thermocouple follows the ASTM E230 standard. Fig. 3.3(b) depicts a schematic (top view) of the thermocouple attached at a 1.5-2.0 mm distance from the weld centerline. A thermocouple is attached to the thin sheets using a spot-welding machine (*Dyna.Weld, Model: TAU 100*). Thin sheets are tightly clamped using bolts to avoid distortion and positioned so that the space between the sheets is kept at a minimal degree.

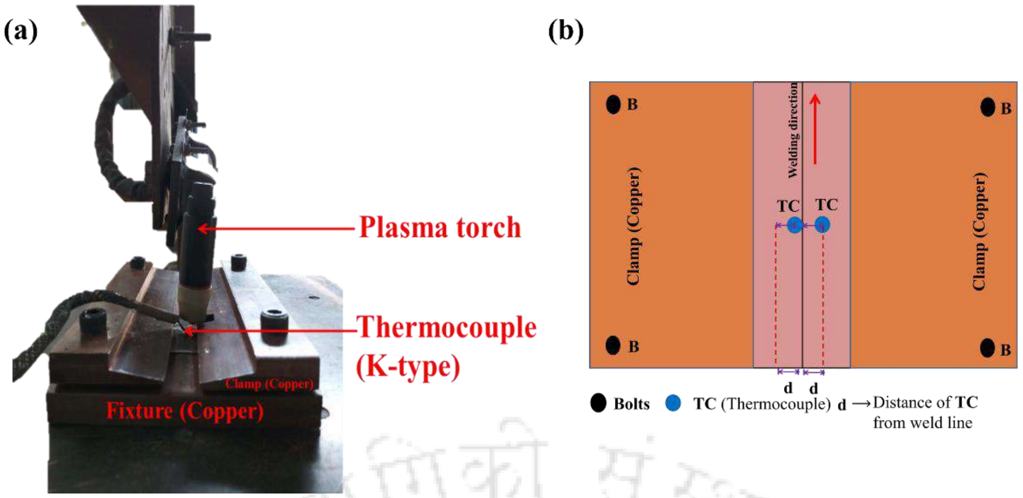

Fig. 3.3 Illustrates (a) Photograph of experimental measurement of temperature using K-type thermocouple (b) schematic (top view) of experimental measurement of temperature.

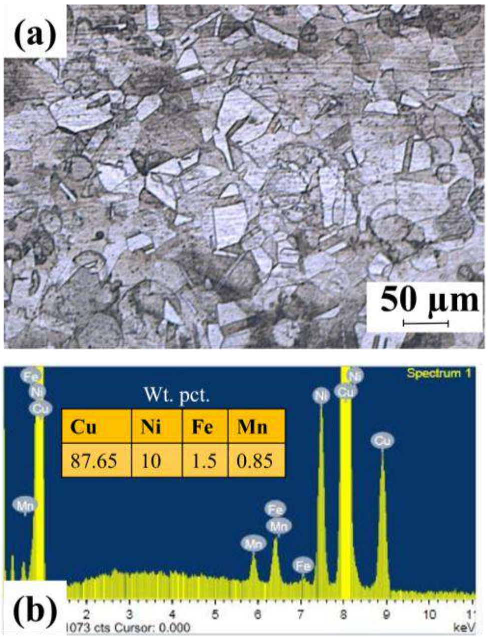

Fig. 3.4 Depicts (a) microstructure and (b) elemental analysis of cupronickel base metal.

$Cu_{90}Ni_{10}$ thin sheet of dimensions 140 mm × 60 mm × 0.7 mm is extracted from a sheet of larger size using a sheet shearing machine. The chemical composition of $Cu_{90}Ni_{10}$ alloy derived utilizing energy dispersive x-ray analysis is identified as Cu (87.65 %), Ni (10 %), Fe (1.5 %), and Mn (0.85) (in wt. %). Fig. 3.4(a) depicts the microstructure of the base material of the $Cu_{90}Ni_{10}$, and Fig. 3.4(b) represents the elemental distribution of parent material due to EDX analysis. EDX analysis confirms the presence of the alloying elements (Fe and Mn). To avoid oil/dirt fragments, edge preparation and polishing followed by cleaning is the sequence of operations accomplished before the sheets are joined permanently. Fig. 3.5 represents process parameters (primary and secondary) and their corresponding effect on the joint characteristics. In the present experimentation, attention is imparted towards the primary parameters of welding current and speed (alternatively portrayed as heat input/length) that must be optimized to produce a 'stable-weld' joint.

Table 3.1 represents the preliminary process parameters (variable and fixed) used in the current examination to join $Cu_{90}Ni_{10}$ thin sheets. After several trial experiments, variable welding parameters are optimized, and a visual inspection of the weldments is carried out to inspect the weldments. Trail runs are identified to envelop a complete 'stable' joining zone. A tungsten electrode (2 wt. % thorium) of diameter (D_e) 1 mm positioned inside a copper nozzle (D_n) of 1.2 mm is employed to generate the required heat flux using a direct current electrode negative (DCEN) polarity. Welding current (W_c, 8-15 A) and welding speed (W_s, 1.89-6.12 mm.s^{-1}) form a suitable combination of parameters to produce a 'stable-weld' joint. The value of argon gas flow rates is optimized to be 0.7 lpm (plasma gas, F_p) and 5.5 lpm (shielding gas, F_s) so that the generated arc remains stable without causing turbulence/spatter defect in the weld joint. The plasma torch is positioned vertically, and an autogenous joining is formed by applying continuous welding mode. The absence of irregular beads, root sagging, cracks, spatter, or undercut is considered a 'stable-joint.' To gauge the joint quality, the so-called 'stable-joint' is subjected to DT and NDT to quantify the weld properties.

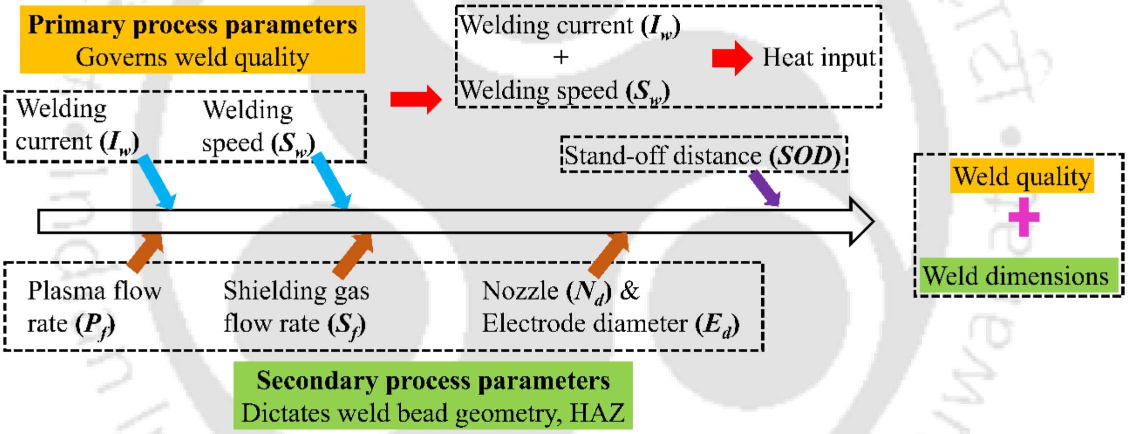

Fig. 3.5 Illustrates the cause-and-effect diagram for the M-PAW process.

Table 3.1 Preliminary process parameters used for fabricating $Cu_{90}Ni_{10}$ weld joint.

Joining parameters	Units	Value(s) used for the present investigation
	Variable parameters	
Welding current, W_c	A	8-15
Welding speed, W_s	mm/s	1.89-6.12
Plasma gas flow rate, F_p	lpm	0.7
Shielding gas flow rate, F_s	lpm	5.5
Stand-off distance, SOD	mm	2

Fixed parameters⟶ D_e: 1.2 mm, D_n: 1.0 mm, Torch orientation- 90^0 with respect to the workpiece, Polarity- DCEN, Filler material- autogenous

Fig. 3.6(a) represents the different welding current and speed combinations, resulting in contrasting weld joint types. The joint type formed falls under three groups, 'insufficient-heating,' 'stable-joint,' and 'over-heating.' Applying heat input lower/higher than the optimum range corresponds to weld joints of inferior/unacceptable quality. The optimum range of heat input results in forming a 'stable-joint' joint, free from defects, as per visual examination. Fig. 3.6(b-e) illustrates the weld joint's appearance formed at varying welding parameters using a low-magnification optical microscope (stereomicroscope). The weld appearance under different welding parameters is categorized as (a) 'insufficient-heating' or no penetration due to inadequate supply of heat flux, (b) 'stable-joint' or regular weld bead due to an appropriate amount of heat flux, and (c-d) 'over-heating' or irregular weld or melt-through due to the application of heat flux beyond the optimum value. Table 3.2 demonstrates all possible combinations of W_c and W_s along with the computed values of heat input evaluated using Eq. (3.1), in which values of voltage (V) and efficiency (η) are substituted as 25 V and 0.66 (Baruah and Bag, 2016), respectively.

$$\text{Heat input (J/mm)} = \frac{\text{welding current} \times \text{voltage}}{\text{welding speed}} \times \eta \tag{3.1}$$

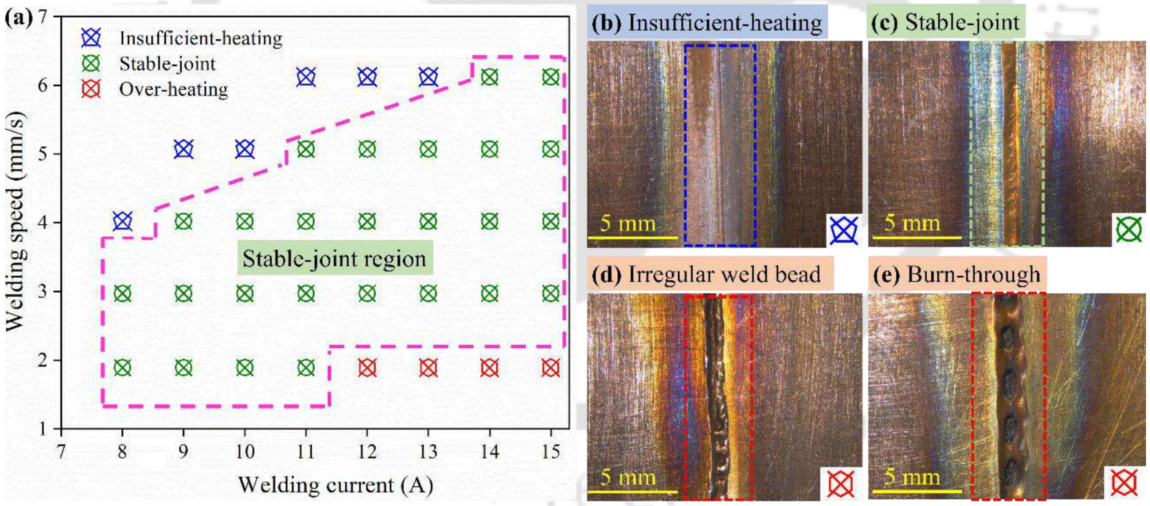

Fig. 3.6 Illustrates (a) welding current and welding speed process window and weld appearance under different welding parameters, (b) insufficient-heating, (c) stable-joint, and (d-e) over-heating.

To understand the influence of heat input on the behaviour of joint characteristics, three combinations of welding parameters covering the full range of heat input are selected, including a minimum, a mid-value, and a maximum value, yielding a 'stable-weld' joint. Table 3.3 represents the three different cases considered for the present study. The different tests conducted on the $Cu_{90}Ni_{10}$ weld joints fabricated at varying heat inputs and the corresponding critical observations noted are mentioned in Table 3.4.

Table 3.2 Heat input for the full-factorial design of experiments for welding current and welding speed for $Cu_{90}Ni_{10}$ alloy.

W_c (A) →	8	9	10	11	12	13	14	15
W_s (mm s^{-1}) ↓	←			Heat input (J/mm)				→
1.89	69.84	78.57	87.30	**96.03**	104.76	113.49	122.22	130.95
2.97	44.44	50.00	55.56	61.11	**66.67**	72.22	77.78	83.33
4.02	32.84	36.94	41.04	45.15	49.25	53.36	57.46	61.57
5.07	26.04	29.29	32.54	**35.80**	39.05	42.31	45.56	48.82
6.12	21.57	24.26	26.96	29.66	32.35	35.05	37.75	40.44
Joint quality →	'Insufficient heating'			'Stable-bead'			'Over heating'	

Table 3.3 Heat input selected for the joining of $Cu_{90}Ni_{10}$ alloy.

Sl. No.	W_c (A)	W_s (mm/s)	Heat input (J/mm)	Nomenclature
1.	11	5.07	35.80	$HI_{35.80}$
2.	12	2.97	66.67	$HI_{66.67}$
3.	11	1.89	96.03	$HI_{96.03}$

Table 3.4 The test conducted on the joints fabricated at $HI_{35.80}$, $HI_{66.67}$, and $HI_{96.03}$.

Sl. No.	Test conducted/ASTM standard	Key observations
1.	Temperature measurement/ASTM E230	Peak temperature
2.	Macrostructural characterization/ASTM E340	Bead dimensions, demarcate the FB and FZ
3.	Optical microscopy/ASTM E407	Microstructural morphology
4.	Electron microscopy/ASTM E407	Dendritic structure
5.	Microstructural characterization (EBSD)	Grain size distribution
6.	Surface topology	Surface quality

Table 3.4 The test conducted on the joints fabricated at $HI_{35.80}$, $HI_{66.67}$, and $HI_{96.03}$ (cont.).

Sl. No.	Test conducted/ASTM standard	Key observations
7.	X-ray CT	Internal imperfections (porosity)
8.	Tensile test/ASTM E8	Joint strength and ductility
9.	Macro-and Micro-Fractography	Fracture location and mode of failure
10.	Microhardness/ASTM E384	Confirms the variation in grain size/type
11.	Corrosion analysis/ASTM G59	Corrosion resistance
12.	Residual stress measurement/ASTM E2860	Determination of locked-in stress
13.	Distortion analysis	Deflection along and across the weld

The benefits of current pulsation highlighted in Section 2.4 of Chapter 2 recommend its application for thin sheets. Hence, implementing pulsed current (PC) can further enhance the joint properties of $Cu_{90}Ni_{10}$ alloy. A PC-M-PAW (shown in Fig. 3.7) with parameters I_p (peak current) ~ 21.5 A, I_b (base current) ~ 29 % of I_p, t_{on} (arc on time) ~ 0.39 s, t_{off} (arc off time) ~ 0.89 s are combined to supply a 35.50 J/mm heat ($HI_{35.50,\ PC}$) to join $Cu_{90}Ni_{10}$ thin sheets. The average pulse current ($I_{avg.}$) is calculated using Eq. (3.2).

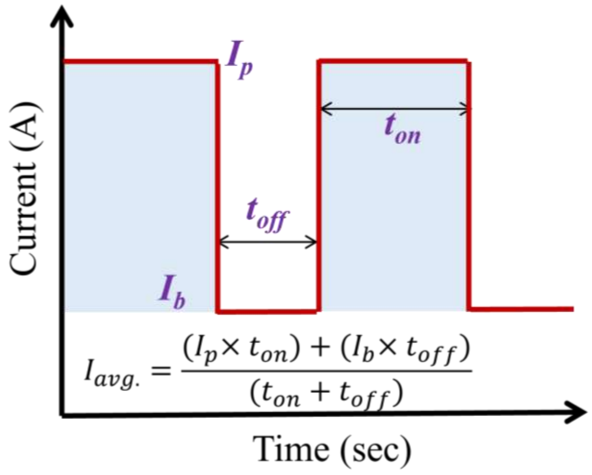

Fig. 3.7 Illustrates pulsed current characteristics.

$$I_{avg.} = \frac{(I_p \times t_{on}) + (I_b \times t_{off})}{(t_{on} + t_{off})} \tag{3.2}$$

The total volume of the weld pool is positively correlated to the welding current. Therefore, if the current applied is more than the required value at a given welding speed, it may tend to melt through the thickness. On the contrary, if the current is too low, inadequate penetration or incomplete fusion may result. Theoretically, the weld width increases in size with increase in heat input (i.e. increase in current or decrease in welding speed; keeping other parameters constant). Stable welding is obtained by combining welding current and speed. Beyond a specific limit of the heat input, burnout of the material occurs. As greater heat input results in a bigger and wider fusion zone, an increase in the value of heat input increases the width of the fusion zone. A positive linear relation between heat input and weld width can be observed from Fig. 3.8(a-c) in which $Cu_{90}Ni_{10}$ joints are formed at different heat input values, showing an increasing trend in weld width with increasing values of heat input (35.70, 66.67, and 96.03 J/mm).

Fig. 3.9(a) depicts the variation of weld width (cap, root) for the different cases, in which with the increase in heat provided ($HI_{35.80}$, $HI_{66.67}$, $HI_{96.03}$), weld width also increases (1.16, 1.54, 1.80 mm), but up to a certain extent, beyond which (~96 J/mm) insignificant effect is noted and further rise (~105 J/mm) in heat provided results in irregular weld/burn-through. A vital aspect noted from Fig. 3.9(b) is the 'concave shape crater defect,' in which metal loss is observed in the weld cap region, and the resulting shape becomes upward concave. With the rise in heat input, metal loss increases (0.14, 0.18, 0.25 mm), directly impacting the joint properties.

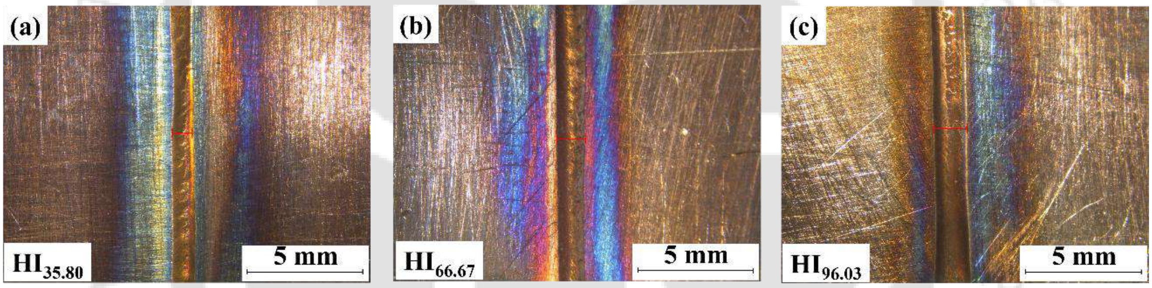

Fig. 3.8 Macrographs (top view) of weld bead with increasing value of heat input (a) $HI_{35.80}$, (b) $HI_{66.67}$, and (c) $HI_{96.03}$.

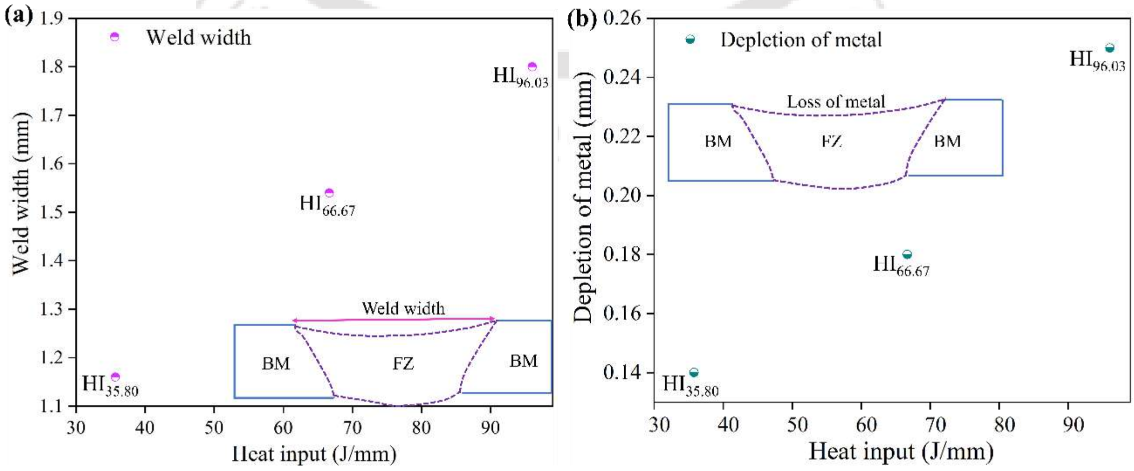

Fig. 3.9 Illustrates the influence of heat input on (a) weld width and (b) metal depletion.

3.4 Gas tungsten arc welding of ferrous and non-ferrous metals

Cu(T2) and SS304 sheets with 1 mm thickness are selected to form a bimetallic joint. The selected pair of materials are subjected to a mechanical and chemical decontamination process, which ensures the removal of impurities. Fig. 3.10(a, b) illustrates the experimental layout employed for Cu and SS gas tungsten arc welding. The workpiece, along with the fixture, is mounted on an arrangement capable of providing variable speed as desired. Inert gas (Argon, 99.99 % pure) is employed to shield the weld joint from surrounding contamination. The control system allows the management of the amount of inflow of inert gas and setting the current as required. The cooling system cools the copper nozzle after completion of the welding operation. The welding torch is kept still, whereas the fixture and the workpiece are mounted on a manipulator system, which moves ahead in a route attached to the work table. The manipulator (a motor-driven machine) is controlled using a speed regulator. The base metals are joined together with a GTAW (*Model: PI Plasma 350*) setup using straight polarity. The sheets are tightly clamped (to avoid distortion) onto the fixture, and the fixture is placed on an electrically powered carriage. Table 3.5 details the chemical composition, and Fig. 3.11(a-f) illustrates the optical microstructure, inverse pole figure (IPF) map, and grain boundary (GB) map of the base metals.

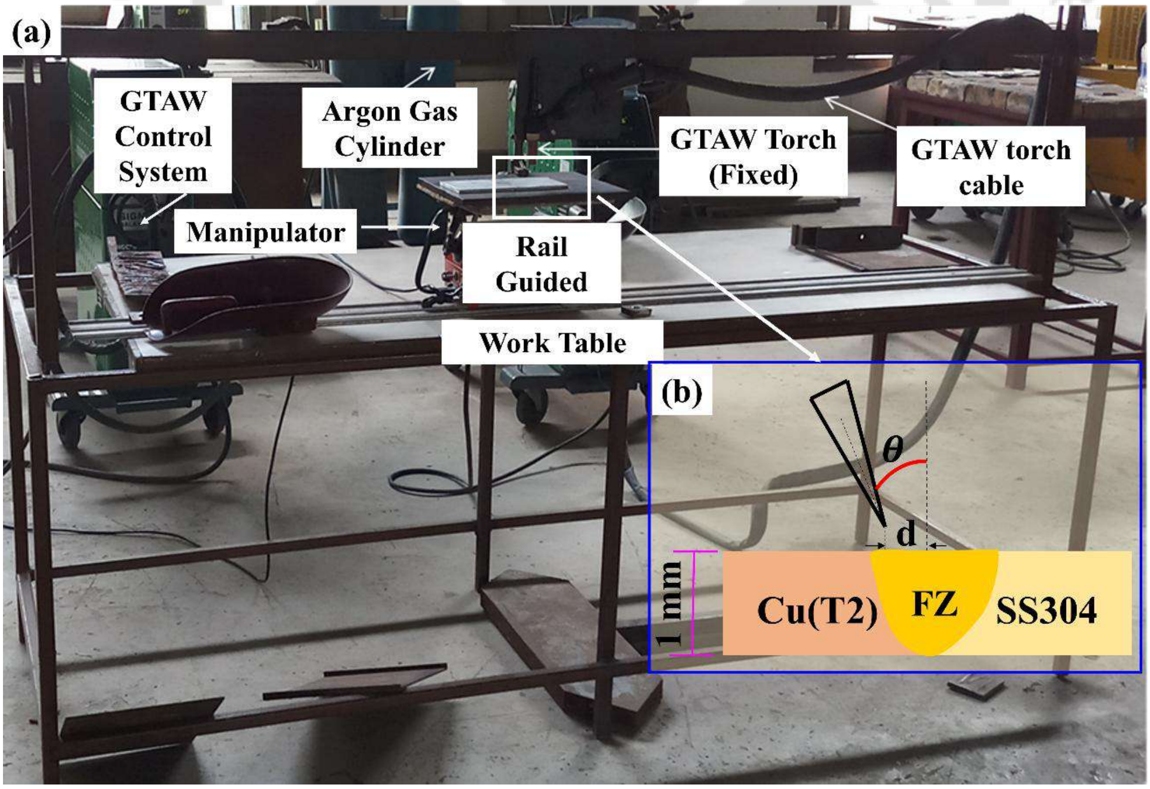

Fig. 3.10 Experimental layout employed for the gas tungsten arc welding of Cu(T2) and SS304.

Table 3.5 Chemical composition of the base metals Cu(T2) and SS304 (wt. %).

Element	Ni	S	Pb	Si	Cu
Cu(T2)	0.002	0.003	0.001	0.004	Balance
Element	Cr	Ni	Mn	Si	Fe
SS304	17.90	7.80	1.5	0.4	Balance

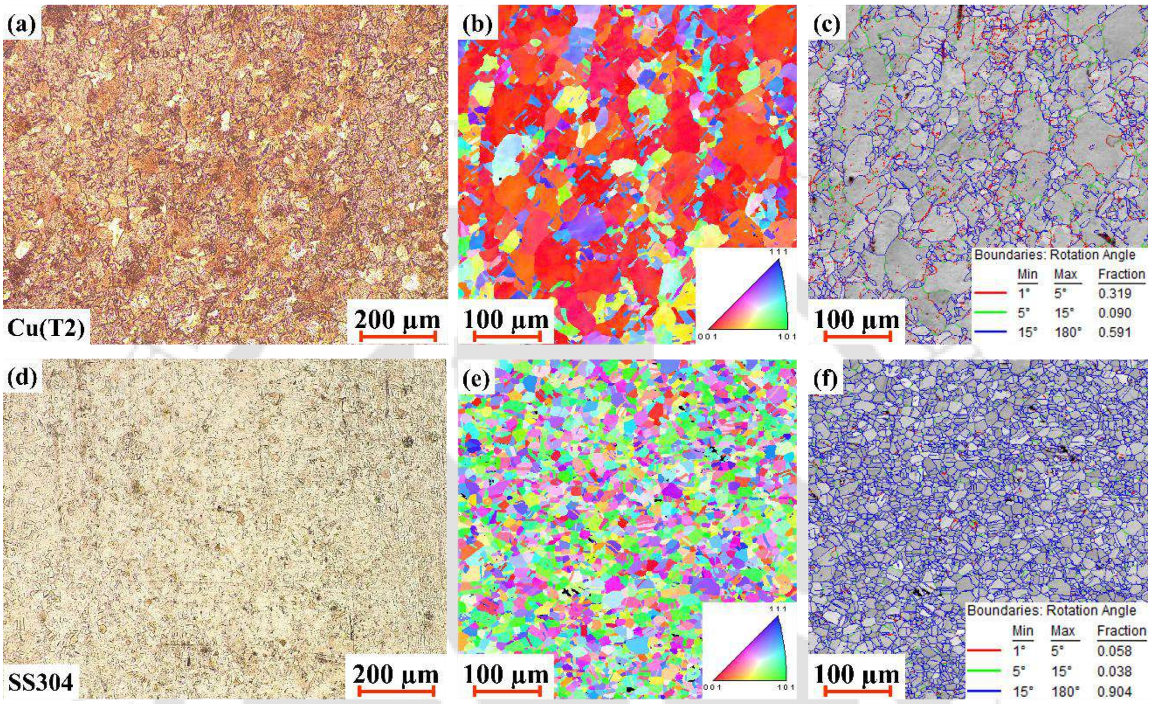

Fig. 3.11 Depicts the microstructure, IPF map, and GB map of base materials (a-c) Cu(T2) and (d-f) SS304.

To avoid heat dissipation, the material of the fixture is designed with mild steel. Table 3.6 highlights the process parameters, heat input, and weld quality inter-relation. The weld quality falls into four categories: (i) no melting of Cu-base material, (ii) incomplete fusion, (iii) fusion without any visible defects, and (iv) fusion with solidification cracks. Joints fabricated at ~308 J/mm fall under the fusion category without any visible defects. The arc offset is maintained between 1.3 and 2.7 mm for the present experimentation. Without arc offset, SS304 melts completely, whereas Cu(T2) remains unmelted. Values of offset less than 1.30 mm led to limited melting of Cu(T2), whereas offset larger than 2.7 mm resulted in a lack of fusion. Based on the optimum process conditions, three cases (CS_1, CS_2, and CS_3, illustrated in Table 3.7 and Fig. 3.12) are selected to understand the influence of arc offset on the joint properties. To understand the significance of heat input, ~339 J/mm (CS_4) is selected, and its joint properties are compared with the best results obtained from CS_1,

CS_2, and CS_3 joints. The values of heat input are evaluated using Eq. (3.3), in which values of voltage (V) and efficiency (η) are substituted as 14 V and 0.7, respectively.

$$\text{Heat input (J/mm)} = \frac{\text{welding current} \times \text{voltage}}{\text{welding speed}} \times \eta \qquad (3.3)$$

Table 3.6 Process parameters, heat input, and weld quality for Cu-SS bimetallic joints.

Sl. No.	Welding Current (A)	Welding speed (mm/s)	Heat input (J/mm)	Weld quality
1.	90	5.31	~166	No melting of Cu(T2) base material
2.	100		~185	
3.	110		~203	
4.	90	3.18	~277	Incomplete fusion
5.	100		**~308**	Fusion without any visible defects (Absence of inconsistent weld bead, spatter, hot cracking, undercut, and lack of fusion)
6.	110		~339	Fusion with solidification cracks

Shielding gas flow rate: 12.5 lpm, Nozzle to workpiece tip distance: 3 mm, Torch inclination: 6°, Tungsten electrode diameter: 1.6 mm, Copper nozzle diameter: 2.4 mm, Polarity: DCEN, Number of passes: single, Filler material: no filler wire used, Arc offset (towards Cu-side): 1.3, 2.0, 2.7 (mm)

Table 3.7 Presents the heat input and arc offset selected for the present investigation in the joining of Cu-SS bimetallic joints.

Sl. No.	Heat input (J/mm)	Arc offset (towards Cu-side), mm	Designation
1.	~308	1.3	CS_1
2.		2.0	CS_2
3.		2.7	CS_3

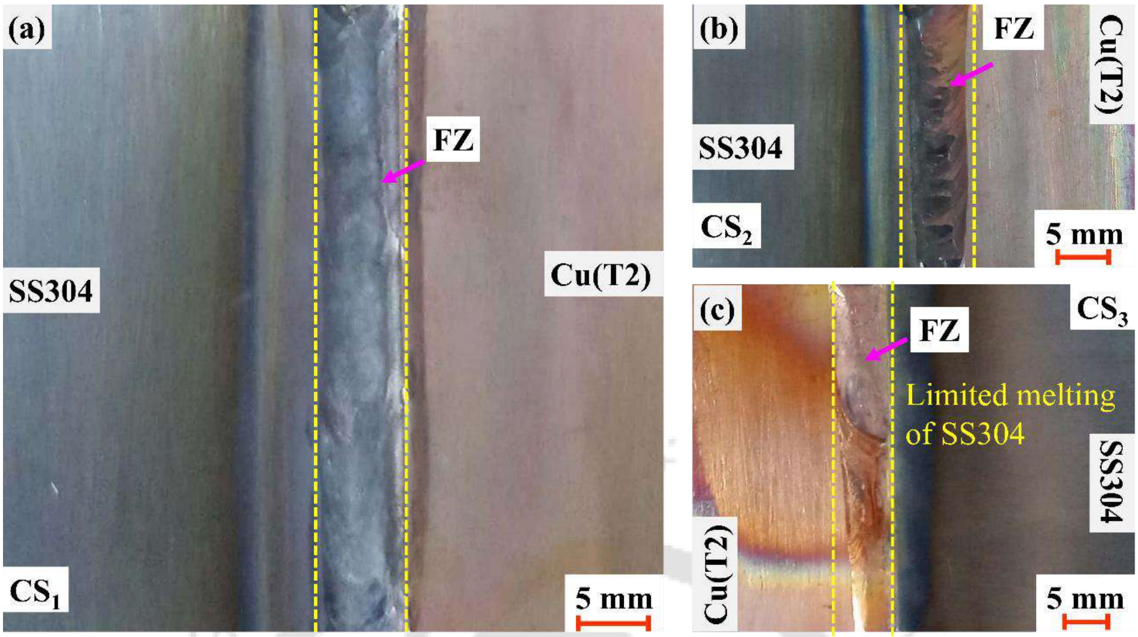

Fig. 3.12 Depicts the top view of the Cu-SS bimetallic joints without any visible defects for (a) CS_1, (b) CS_2, and (c) CS_3 weld conditions.

To ensure the integrity of the fabricated joints, the joints are subjected to a wide range of testing procedures. The testing procedure starts with metallurgical characterization, for which the test coupons are extracted across the joints. The test coupons undergo mandatory metallographic practices (Step I: polishing with SiC 240-2400 emery papers and water; Step II: polishing with velvet cloth and 0.5 µm diamond paste to achieve a mirror-like finish; and Step III: etching with HCl: 50 ml + H_2O: 100 ml + $FeCl_3$: 5 gm to uncover the microstructural morphology). Then it is analysed under optical and electron microscopy, which provides only qualitative information regarding the occurrence of different morphology. To quantify the compositional distribution, elemental (point, line, and area) analysis is carried out on the welded specimens. Further, the X-ray diffractometers (XRD) technique is utilized to quantify the occurrence of different phases.

To identify the internal imperfections, X-ray computed tomography (X-ray CT), a non-destructive testing method is utilized for determining defects by positioning the sample in a rotary stage in the middle of an X-ray origin and a matrix identifier. Determination of the mechanical (tensile and microhardness) properties is achieved by utilizing a 250 kN-UTM (universal testing machine) and a Vickers microhardness machine. Evaluation of tensile properties aids in quantifying the joint strength and the extent of plastic deformation (ductility). In contrast, microhardness assessment guides understanding of the variation (microstructural inhomogeneities) across the different weld regions. Further, broken tensile samples are utilized to spot the failure site and failure mode. Table 3.8 summarizes the methods used to characterize the fabricated bimetallic joints and the corresponding critical features investigated.

Table 3.8 Techniques used for Cu-SS joint characterization.

Sl. No.	Characterization method	Key features investigated
1.	Optical microscope	FZ, FB, macro-segregation
2.	Field emission Scanning electron microscope	Extent of intermixing between Cu(T2) and SS304
3.	Energy dispersive X-ray analysis	Elemental analysis
4.	X-ray Diffractometers	Presence of Cu and Fe peaks
5.	X-ray computed tomography	Occurrence of internal defects
6.	Uniaxial tensile test	Strength and ductility
7.	Macro-and Micro-Fractography	Fracture location and mode of failure
8.	Microhardness	Confirms non-uniformities in the FZ

3.5 Micro-plasma arc welding of dissimilar austenitic stainless steels

Thin austenitic stainless steel (ASS) sheets (SS316L and SS310) are autogenously joined using the M-PAW process with 800 µm and 600 µm thicknesses, respectively. The elemental composition (Table 3.9) of the base metals SS316L and SS310 primarily comprises Cr and Ni, including minor alloying elements (Si, Mn, Mo), and the rest Fe. The complete experimental setup is presented earlier in Fig. 3.2. The experimental setup consists of the power source, arrangement for linear movement of the workpiece, and fixture to hold the workpiece. A DC power supply produces the necessary heat required to fuse the materials. Argon gas is used to create the arc and shield the fusion zone from atmospheric inclusions, while the control system, together with the cooling system, is used to control the heat source. The cooling system cools the copper nozzle after completion of the welding operation. The plasma torch is held stationary, whereas the fixture and the workpiece are mounted on a manipulator system, which moves ahead in a route attached to the work table. Two K-type thermocouples are attached on each sheet (SS316L and SS310) to collect the temperature-time data for validating the reliability of the thermal model.

Table 3.9 Chemical composition (wt. %) of base materials.

Base metals	Cr	C	Ni	Si	Mn	Mo	Fe
SS316L	18.45	0.02	8.95	0.73	1.51	2.16	Bal.
SS310	25.24	0.07	19.21	1.65	0.89	0.22	Bal.

ASS sheets to be joined are first ensured with proper edge preparation, followed by polishing and cleaning with acetone to make sure that the sheets remain free from any dirt/oil particles. In the present experimentation, attention is imparted towards the primary parameters of welding current and welding speed (alternatively portrayed as heat input/length) that must be optimized to produce a 'stable-weld' joint. Difficulty in joining increases with reduction in thickness; hence, precise control over the heat input is essential to produce a joint of acceptable properties. A combination of 8-15 A (welding current, W_c) and 2.15-4.65 mm/s (welding speed, W_s) is used for the preliminary experimentation. The welding speed is bracketed by setting to a minimum value and increasing the welding current until the burn-through occurs. The smooth occurrence of the weld bead and the non-existence of any visual imperfections are considered as the selection criteria for post-characterization. The value of argon gas flow rates (F_p and F_s) is adjusted to achieve a stable plasma arc for providing necessary heat energy and shielding the fusion zone from atmospheric contamination without creating turbulence in the fusion zone. The range of welding parameters used to perform preliminary experimentation is presented in Table 3.10.

Table 3.10 Preliminary process parameters used for the dissimilar joining of austenitic stainless steels (SS316L and SS310).

Variable parameters	Value(s)
Welding current, W_c (A)	8-15
Welding speed, W_s (mm/s)	2.15-4.65
Plasma gas flow rate, F_p (lpm)	0.7
Shielding gas flow rate, F_s (lpm)	7
Stand-off distance, SOD (mm)	2
Fixed parameters: Nozzle diameter 1.2 mm, electrode diameter 1.0 mm, Torch orientation: vertical, No. of passes: single, Plasma and shielding gas: 99.99 % commercially pure Ar, Welding mode: continuous current, polarity: DCEN	

Fig. 3.13(a-d) presents the process window for dissimilar weld joints. The different combinations of current (8-15 A) and speed (2.15-4.65 mm/s) lead to any of the following three weld conditions: (i) insufficient heating leads to no melting/no fusion, (ii) optimum/sufficient heat input corresponds to the formation of uniform weld bead with no visual imperfections, and (iii) overheating leads to burn through of the joints. Table 3.11 displays the heat supplied for the full-factorial combination of welding current and speed. The feasible het input range is identified as 52-77 J/mm, in which dissimilar joints produced are free from any visual imperfections such as undercut, cracking, underfill, and sagging. The plasma and shielding gas flow rates are 0.7 lpm and 7 lpm, respectively. The nozzle and electrode diameters used are 1.2 mm and 1.0 mm, respectively. From the feasible range, three parameters (52 J/mm: L_{52}, 63 J/mm: M_{63}, and 77 J/mm: H_{77}) are selected as the criteria of low, medium, and high heat input (represented in Table 3.12) context to study the effect of heat input on joint characteristics and the influence of phase transformation on residual stresses.

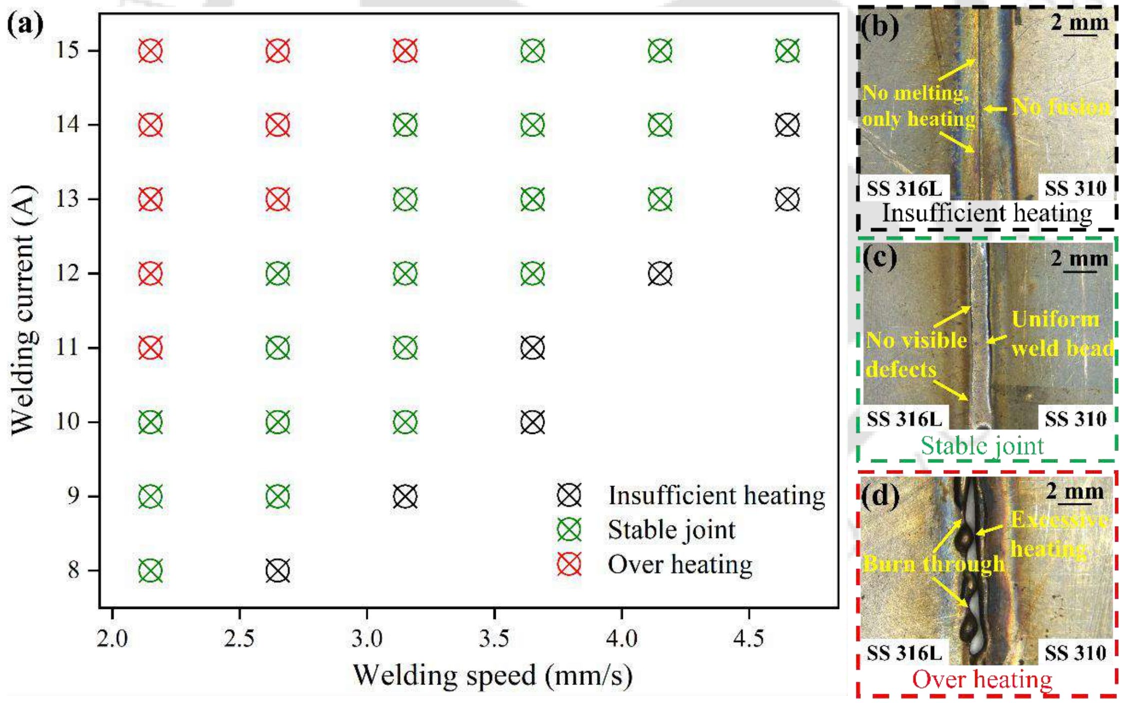

Fig. 3.13 Depicts (a) M-PAW welding process window and (b-d) images of joints under different process parameters.

Weldments fabricated at 52 J/mm (L_{52}), 63 J/mm (M_{63}), and 77 J/mm (H_{77}) values of heat input are further subjected to different characterization techniques. The sample preparation for optical and electron microscopy is conducted as per the ASTM E407 standard, wherein samples extracted from the dissimilar joints are subjected to microscopic, elemental, and X-ray diffraction (XRD) analysis. Mechanical evaluation is executed to determine the joint strength using a uniaxial tension test following the ASTM E8 standard; microhardness measurement along the different sections in the fusion zone is performed as per the ASTM E384 standard; potentiodynamic polarization test is done as per the ASTM G59 standard to measure corrosion resistance in 3.5 wt. % NaCl solution followed by elemental analysis to determine the alteration of chemical composition in the weld joints. Further, an advanced non-destructive test (X-ray CT) is used to determine the presence of internal defects. Finally, residual stress is measured using the XRD technique, and a coordinate measuring machine (CMM) is used to measure the longitudinal and out-of-plane distortion of the dissimilar joints.

Table 3.11 Heat supplied for the full-factorial combination of welding current and speed.

W_s (mm/s) →	2.15	2.65	3.15	3.65	4.15	4.65
W_c (A) ↓	⟵ Heat Input (J/mm) ⟶					
8	🟩 61.40	🟦 49.81	🟦 41.90	🟦 36.16	🟦 31.81	🟦 28.39
9	🟩 69.07	🟩 56.04	🟦 47.14	🟦 40.68	🟦 35.78	🟦 31.94
10	🟩 **$76.74^{H}{}_{77}$**	🟩 62.26	🟩 52.38	🟦 45.21	🟦 39.76	🟦 35.48
11	🟧 84.42	🟩 68.49	🟩 57.62	🟦 49.73	🟦 43.73	🟦 39.03
12	🟧 92.09	🟩 74.72	🟩 **$62.86^{M}{}_{63}$**	🟩 54.25	🟦 47.71	🟦 42.58
13	🟧 99.77	🟧 80.94	🟩 68.10	🟩 58.77	🟩 **$51.69^{L}{}_{52}$**	🟦 46.13
14	🟧 107.44	🟧 87.17	🟩 73.33	🟩 63.29	🟩 55.66	🟦 49.68
15	🟧 115.12	🟧 93.40	🟧 78.57	🟩 67.81	🟩 59.64	🟩 53.23
	🟦 'Under-weld'		🟩 'Stable-weld'		🟧 'Over-weld'	

Table 3.12 Heat input selected for the joining of SS316L and SS310.

Sl. No.	W_c (A)	W_s (mm/s)	Heat input (J/mm)	Nomenclature
1.	13	4.15	51.69 (~52)	L_{52}
2.	12	3.15	62.86 (~63)	M_{63}
3.	10	2.15	76.74 (~77)	H_{77}

The microscopic analysis uses a field emission scanning electron microscope (FESEM) to identify the presence of lathy/skeletal ferrite in the austenitic matrix. The relative amount of $\delta_{ferrite}$ in the austenite matrix is calculated. The elemental analysis helps to get an idea regarding the resulting composition of the different regions of the fusion zone, which aids in determining the solidification mode by calculating $Cr_{eq.}/Ni_{eq.}$ ratio using the Schaeffler diagram. Also $Cr_{eq.}$ and $Ni_{eq.}$is marked on the Fe-Ni-Cr ternary diagram (70 wt. % Fe). Further, EBSD analysis provides average grain size and misorientation angle distribution and allows understanding grain orientation in the fusion zone. Fig. 3.14 illustrates the macrograph (transverse section) of weld bead fabricated at different values of heat input (L_{52}, M_{63}, and HI_{77}).

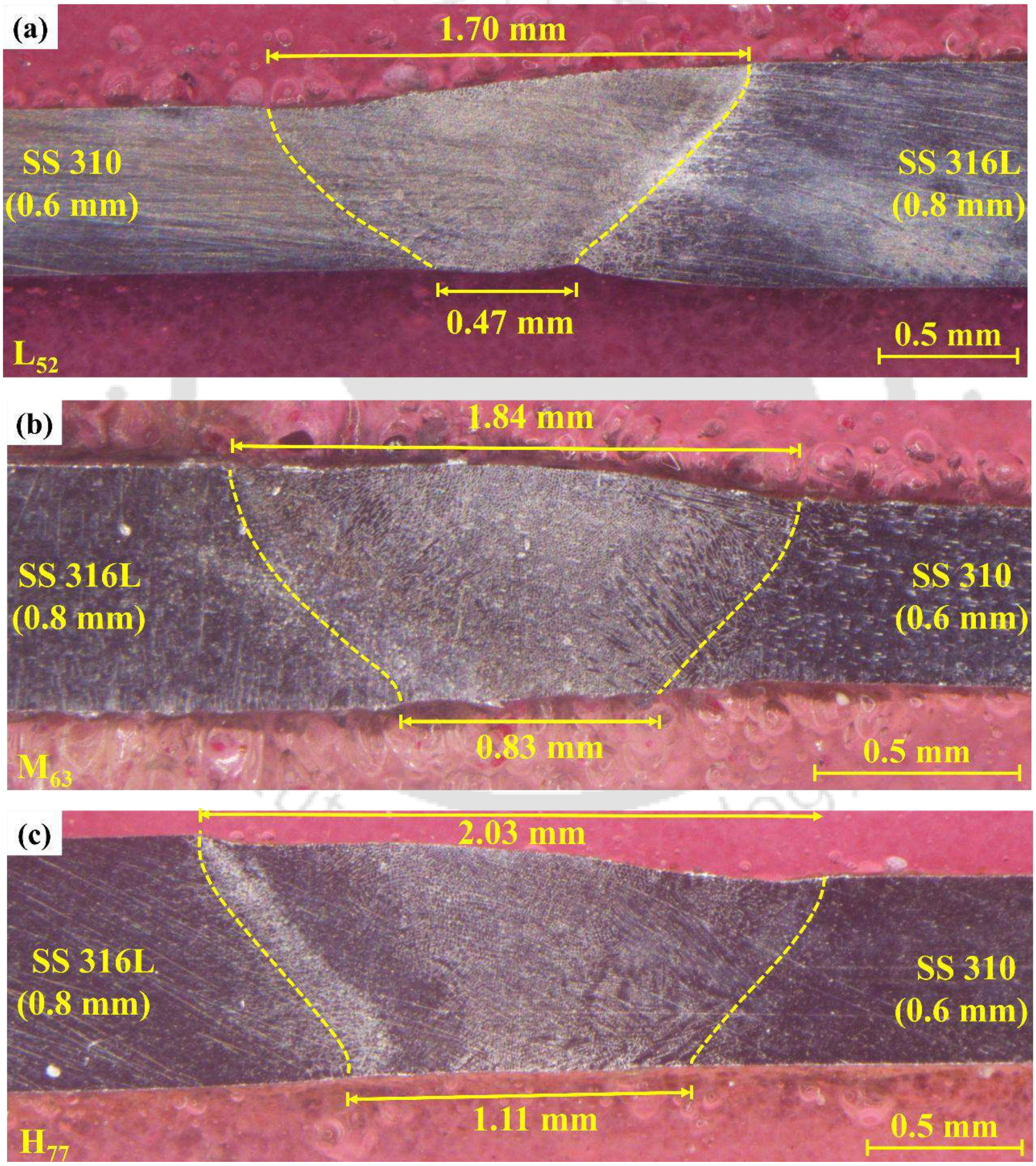

Fig. 3.14 Macrograph (transverse section) of weld bead with increasing value of heat input from (a) L_{52}, (b) M_{63}, and (c) HI_{77}.

3.6 Characterization of the welded joints

To quantify the joint properties, the welded joints are subjected to a wide range of testing methods that include metallurgical analysis, non-destructive testing, chemical stability, and followed by mechanical evaluation. The testing procedure starts with metallurgical characterization (ASTM E407 standard), for which the test coupons are extracted across the joints. The test coupons undergo mandatory metallographic practices and are then analyzed under optical (*Make: Leica S6D, Leica MC 120 HD, and Make: Carl Zeiss, Germany*) and electron microscopy (*Zeiss, Sigma*), which provides only qualitative information regarding the occurrence of different morphology. To quantify the compositional distribution, elemental (point, line, and area) analysis is carried out on the welded specimens. To estimate the grain's properties and texture, the joints are subjected to EBSD analyses (*TSL-EDX*^{TM}) after electrochemical polishing. Further, the X-ray diffractometers (*XRD*, *Rigaku Technologies, Smartlab*) technique is utilized to quantify the occurrence of different phases.

The measurement of residual stress (using XRD technique) at the surface of the weld joints is achieved by *Bruker D8-Discover*^{TM} system. Bragg's law evaluates the magnitude of residual strain between atomic planes. Further, the stress value is evaluated by the $sin^2\psi$ method, which relies on the variation of the peak location of the diffraction for different inclinations (tilt angle) of the sample (Mousavi and Miresmaeili, 2008). The expression used for calculating of stress by the $sin^2\psi$ method is given by Eq. (3.4) (Kohli et al., 2014),

$$\sigma = \frac{Y}{(1+\upsilon)} \times \frac{1}{sin^2\psi} \times \left(\frac{d^{\psi}}{d^{o}} - 1\right) \tag{3.4}$$

where Y: elastic modulus, υ: Poisson's ratio, ψ: angle between the bisector of the incident and diffracted rays, d^o: unstrained lattice spacing, and d^{ψ}: strained lattice spacing. The process condition for the measurement of stress by the XRD technique is represented in Table 3.13.

Table 3.13 Process condition for the measurement of residual stress by XRD technique.

Plane	Target	Aperture (mm)	Wavelength (Å)	Voltage (kV)	Current (mA)
{311}	Cu	Square	1.54	45	14

To identify the internal imperfections, X-ray computed tomography (*GE Phoenix® V/TOME/ 120XS*), a non-destructive testing method, is utilized for determining defects by positioning the sample in a rotary stage in the middle of an X-ray origin and a matrix identifier. The schematic of the experimental setup for X-ray CT is illustrated in Fig. 3.15(a, b). X-ray CT testing and evaluation consists of two units, i.e., (a) testing unit and (b) analysis unit. The testing unit comprises a rotary plate on which the specimen is placed. The sample is revolved one step at a time, acquiring projected images at every rotated position. The projected picture is consecutively re-constructed into a 3-D figure in the analysis unit (Kastner and Heinzl, 2018; Rezghi Maleki et al., 2019). The specimen is scanned using a cone type X-ray beam due to its shorter scan time, improved resolution, and enhanced contrast as compared to fan type X-rays beam. X-ray CT scanning parameters used in the present study are 100 kV/80 µA with an exposure time of 1000 ms and 1000 no. of projection images taken for each angular location with a voxel size of 8 µm.

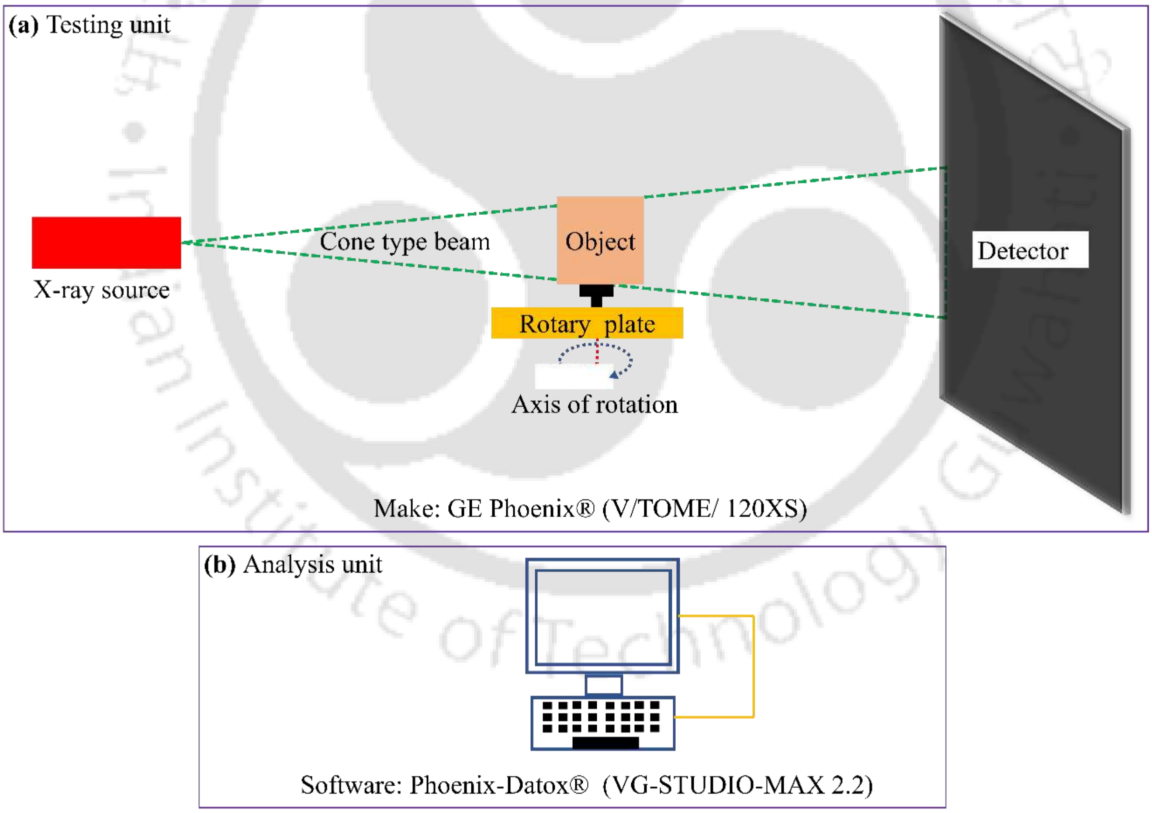

Fig. 3.15 Displays (a) testing unit and (b) analysis unit used for X-ray CT testing and evaluation.

Metallurgical and mechanical properties do not provide the complete picture regarding joint stability. The affinity of the joints when exposed to corrosive environments determines

Indian Institute of Technology Guwahati

the chemical stability, which is accomplished using a traditional 3-electrode arrangement (fusion zone is considered as the working electrode, Ag/AgCl is used as reference electrode, and Platinum is used as counter electrode) system to perform the potentiodynamic polarization evaluation (ASTM G59) in a 3.5 wt. percentage NaCl solution (*Make: Autolab PGSTAT302N, Netherlands*).

The characterization techniques (metallurgical evolution, grain properties, and X-ray CT, chemical stability) presented above do not show any quantified values regarding the joint strength. Hence, to estimate the joint properties (joint strength and percentage elongation), tensile specimens are extracted (using a wire-electrical discharge machine, *Make: Fostex, Model no. FDK 7735, Berlin*) in the transverse direction (perpendicular to weld direction) as per ASTM E8 guidelines. Fig. 3.16 illustrates a tensile specimen tensile specimen prepared as per ASTM E8 standard. To accomplish the tensile testing, a 250 kN-UTM (*Make: BISS Model: MEDIAN 250*) is employed at a constant cross-head speed of 0.5 mm/min. Failed tensile samples are further analysed to identify the failure characteristics. Failure characteristics provide much information about the joints, including the failure location, the site for crack initiation, and failure mode. The first two characteristics can be evaluated using a low-magnification optical microscope (macro-fractography analysis), but the third feature can be explored only by Field Emission Scanning Electron Microscope (micro-fractography analysis).

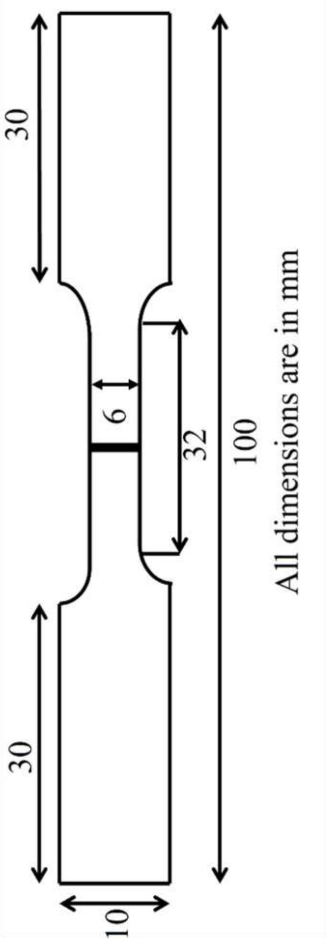

Fig. 3.16 A tensile specimen prepared as per ASTM E8 standard.

Microhardness evaluation remains a routine but extremely vital procedure to judge the indentation resistance of a material, which confirms the presence of finer/coarser morphology and allows to understand the variation across the different regions (FZ, HAZ, and BM). To achieve an error-free result, the ASTM E384 standard is followed determining microhardness using the Vickers hardness test (*Micro Vickers hardness tester, Omni Tech*), which yields the Vickers Hardness Number (VHN). Fig. 3.17 depicts the schematic of an indent caused by the Vickers test, wherein the Vickers hardness number (VHN) formula is used to determine the VHN. Test coupons extracted across the weld direction are mirror polished and subjected to 200-500 gf force with a dwell interval of 10 s.

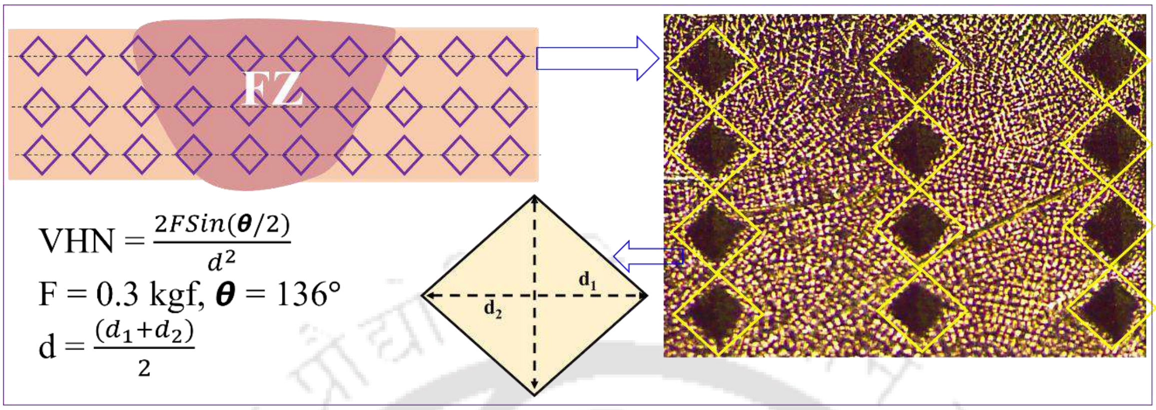

Fig. 3.17 Schematic representation of Vickers microhardness indentation and the formula for calculating VHN.

Metallurgical, mechanical, and chemical analysis do not guarantee the sound performance of a weld joint. The occurrence of deflection has a detrimental influence on the welded component. Hence, estimating deflection becomes an integral part of any welded structure. Deflection (distortion) is extremely common in the welding of thin sheets and possess a list of negative effects on the resulting joints, including (i) dimensional variance (reduced quality), (ii) unstable component, and (iii) added cost (due to post-processing). Hence, quantification of the amount of distortion presents a clear knowledge regarding the robustness of the joints, for which a coordinate-measuring machine (CMM, *Make: Accurate Spectra, Model: Spectra, Accuracy: 0.5 micron*) (shown in Fig. 3.18(a)) is utilized. On the base table of the CMM, the welded sample is placed on a clamping stand, and the probe tip (attached to the probe head via the probe stem) is used to measure the X, Y, and Z coordinates for a selected point. In the welded sample, data is acquired along the several points marked on the sheets. Fig. 3.18(b-d) schematically represents the occurrence of deflection across (transverse) and along (longitudinal) the welds, wherein the dotted lines represent the as-received sheets and the solid lines depict the as-welded component.

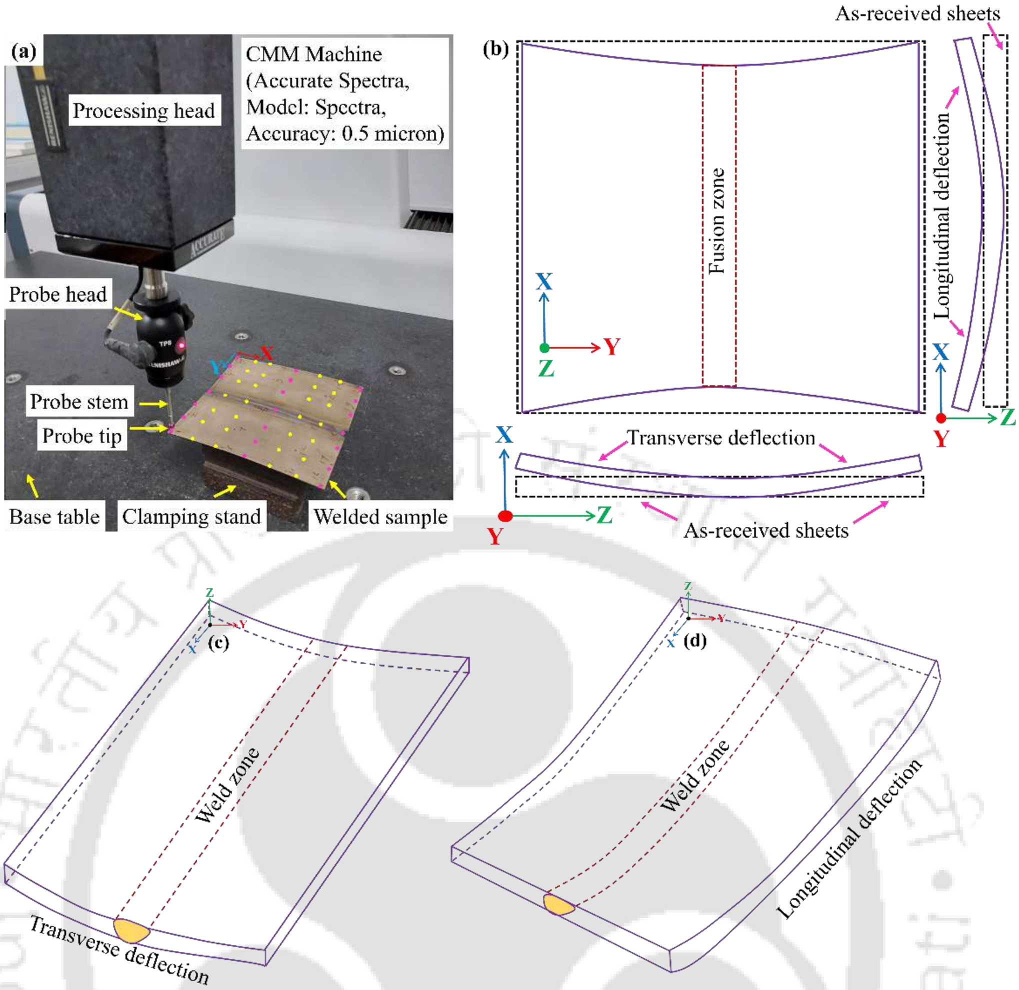

Fig. 3.18 Illustrates (a) measurement of distortion using CMM and (b-d) schematic of the distortion pattern.

Fig. 3.19(a-g) depicts the overall testing methods used for the current experimentation. Fig. 3.19(a) represents the weld specimen from which standard coupons are extracted to study the microstructural, mechanical, electrochemical behaviour, and NDT as per ASTM standards. Fig. 3.19(b) depicts the sample considered for metallography analysis to reveal the different regions (fusion zone: FZ and heat-affected zone: HAZ) of the specimen. Fig. 3.19(c) shows the standard tensile coupon carried out at 0.5 mm/min to quantify the joint strength. Further, the failed tensile coupons are investigated to identify the failure mode of the joints, shown in Fig. 3.19(d). Along with metallurgical and mechanical properties, the electrochemical behaviour of the joints is also conducted to measure the corrosion behaviour of the joints under a selected corrosion media, as predicted in Fig. 3.19(e). Fig. 3.19(f) demonstrates an X-ray CT machine to identify the internal defects, and Fig. 3.19(g) shows evaluation of microhardness using ASTM E384 standard.

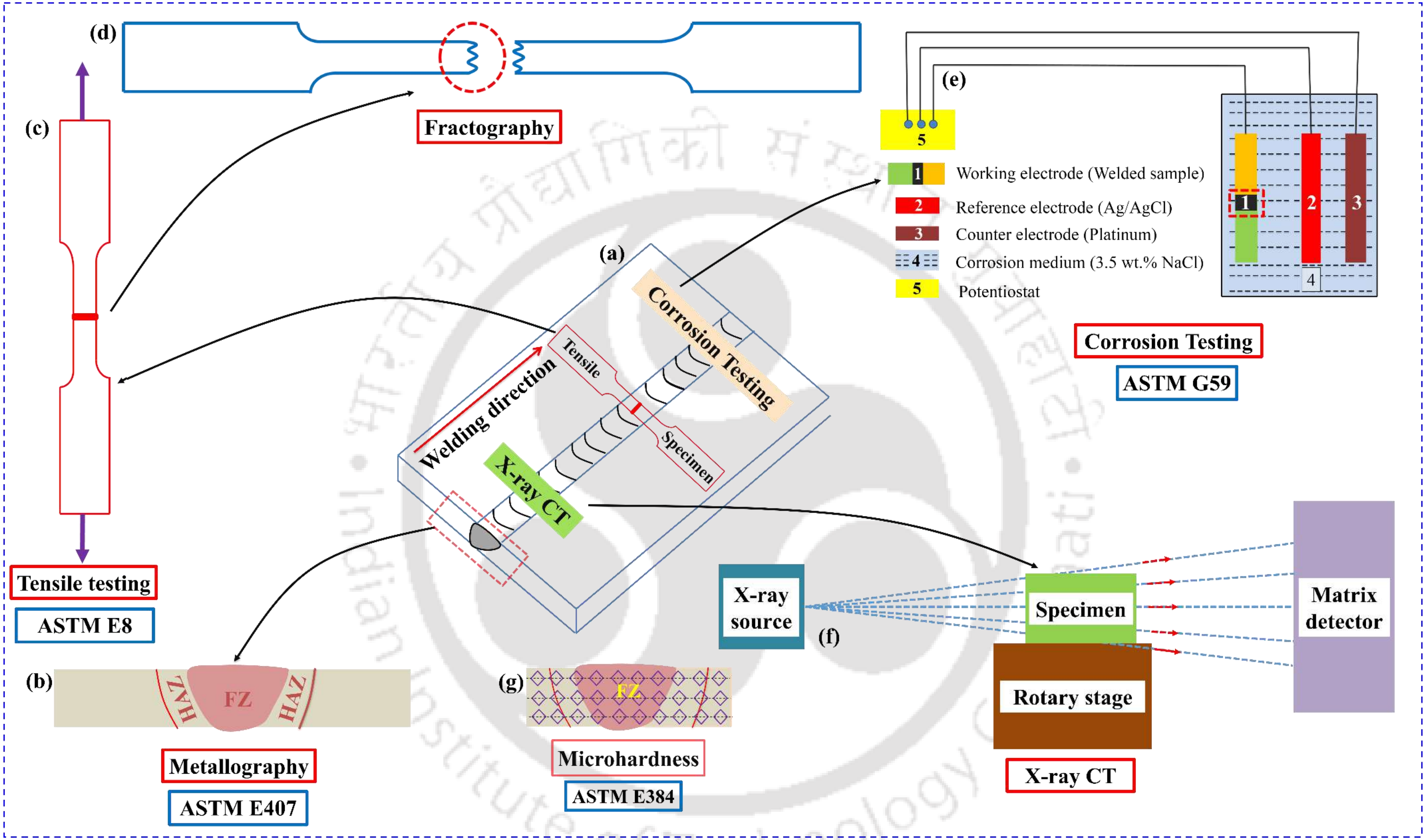

Indian Institute of Technology

Fig 3.19 The different testing methods implemented to characterize the welded joints and the corresponding ASTM standards.

3.7 Summary

In this present chapter, an experimental study is conducted to explore the joining process for similar and dissimilar combinations of materials. M-PAW process is utilized to join 700 µm-thick cupronickel alloy using continuous as well as pulse current mode. Further, the GTAW process is employed to join a pair of 1-mm thick dissimilar ferrous (SS304) and non-ferrous (Cu(T2)) materials. Finally, the joining capability of dissimilar austenitic stainless steels (800 µm-thick SS316L and 600 µm-thick SS310) is also realized by the M-PAW process. Feasible process parameters are bracketed, and the joints are tested using a wide range of methods. Different testing methods employed to identify the microstructural characteristics are optical microscope, field emission scanning electron microscope, energy dispersive X-ray analysis, and Electron Backscatter Diffraction evaluation. The microstructural characteristics are carried out to identify fusion zone (FZ), fusion boundary (FB), and key microstructural features. Further, corrosion analysis is accomplished to determine the chemical stability of the joints. Distortion in the joints is measured using a coordinate-measuring machine, and surface topology is identified using a non-contact surface profilometer. In addition, an advanced NDT (X-ray computed tomography: X-ray CT) is carried out to identify internal defects. The welded joints are also subjected to uniaxial tensile test using universal testing machine, microhardness testing using Vickers microhardness tester, and facture analysis. X-ray diffraction technique is also utilized to confirm the presence of different phases.

भारतीय प्रौद्योगिकी संस्थान गुवाहाटी • Indian Institute of Technology Guwahati •

Chapter 4

Theoretical Formulation

4.1 Introduction

Due to the complexity involved in a welding process, precise quantification of temperature variation in the weld pool is cumbersome. A finite element (FE) based numerical model often helps to overcome the experimental limitations by estimating temperature in the weld pool and determining solidification parameters. The current chapter deals with the theoretical formulation that has been implemented while developing a sequentially coupled thermo-mechanical and thermo-metallurgical-mechanical (TMM) model to investigate the welded joints using a finite element method. The thermal analysis is executed to estimate the temperature-time data by applying a suitable volumetric heat source as a part of Fourier heat conduction model. The obtained result from the thermal analysis is deployed as an input for the mechanical analysis. The accomplished thermal model helps to predict the temperature-time data and the weld dimensions. Meanwhile, the mechanical model provides necessary information regarding the value of residual stress and distortion. However, for the TMM model, the metallurgical model is incorporated by considering solid-state phase transformation through the addition of extra strain component (phase transformation component). The behaviour of the material is assumed to follow elastic-plastic in nature, wherein the plasticity model adheres to the isotropic hardening, von Mises yield criterion, and rate-independent flow rule. The FE-based numerical simulation uses a self-developed Fortran-based DFLUX subroutine in commercial software ABAQUS. For cupronickel, where phase transformation strain is negligible, the thermo-mechanical model is sufficient to estimate the distortion and residual stress. However, for dual-phase materials (austenitic stainless steel), the TMM model is significant in influencing phase transformation on residual stress and distortion.

4.2 Conduction mode heat transfer analysis

The current analysis utilizes a conduction-based heat transfer model, neglecting the impact of fluid flow. To perform the numerical analysis, a Gaussian distributed volumetric heat source is deployed to substitute for the plasma heat source in the model. The transient non-linear thermal analysis is attempts to predict the temperature field in the melt-pool. The thermal analysis is completed in two phases: first, the volumetric heat source is applied to the base materials to provide the necessary heat for melting, which is followed by the second phase, wherein the welded sample is allowed to cool down after removal of the heat source to reach a steady-state condition. The cooling time depends on the welding process, and in the present case, the cooling time is assumed to be twice the welding time. If the heat source is considered to be moving in the x-direction (welding direction), the governing for energy conservation in a 3D Cartesian coordinate system is given by Eq. (4.1),

$$\frac{\partial}{\partial x_i}\left(k_{ij}\,\frac{\partial T}{\partial x_j}\right) + \dot{h}_{generation} = \rho \times C_p \times \left(\frac{\partial T}{\partial t} - W_s\,\frac{\partial T}{\partial x}\right) \tag{4.1}$$

where ρ indicates density, k_{ij} refers to thermal conductivity, $\dot{h}_{generation}$ implies volumetric heat generation, C_p implies specific heat, W_s is the welding velocity vector, T stands for temperature, and t indicates time, $\frac{\partial T}{\partial t}$ implies a rate of change of temperature, $\frac{\partial T}{\partial x}$ highlights temperature gradient. The LHS and RHS of Eq. (4.1) denote the 3D heat conduction equation and transient heat transfer process, respectively. The developed numerical model is based on the following theoretical assumptions:

- The welded thin sheet is assumed to be solid deformable body with ideal geometry and no pre-existing stresses.
- The influence of shielding gas on the top surface of the melt pool is neglected and presumed to be flat, which reduces computational complexity.
- Only half of the entire geometry is considered owing to symmetry.
- Temperature-dependent thermal properties are implemented to accurately predict the thermal distribution, including the effect of latent heat.
- The initial temperature is considered ambient, and heat loss is through all modes of heat transfer.

- Enthalpy of fusion is considered while enthalpy heat of vaporization is neglected and the mass transfer is neglected during computation. Hence, material depletion is neglected.

The solution domain and boundary conditions used for the thermal analysis are represented schematically in Fig. 4.1—4.3. The zone in between the T_{Liquidus} and T_{Solidus} is the mushy zone, where both solid and liquid phase exist together. The top surface of the base metal is subjected to the heat flux, and the remaining surfaces lose heat in the form of convection and radiation. The boundary conditions imposed for thermal analysis are given by Eq. (4.2—4.4),

- Dirichlet boundary conditions, wherein the temperature is presumed to be room temperature at time $t = 0$.

$$\mathrm{T}\,(\mathrm{x}, \mathrm{y}, \mathrm{z}, 0) = \mathrm{T}_{\mathrm{initial}} \tag{4.2}$$

- At the symmetric surface, the temperature gradient is assumed to be zero in the normal direction, i.e.,

$$\frac{\partial \mathrm{T}}{\partial \mathrm{y}} = 0 \tag{4.3}$$

- $$\dot{\mathrm{Q}}_{\mathrm{flux}} = \mathrm{k}\,\frac{\partial \mathrm{T}}{\partial \mathrm{t}} + \mathrm{h}_{\mathrm{convection}}\,(\mathrm{T}_{\mathrm{surface}} - \mathrm{T}_{\mathrm{initial}}) + \sigma\varepsilon\left(\mathrm{T}_{\mathrm{surface}}^{4} - \mathrm{T}_{\mathrm{initial}}^{4}\right) \tag{4.4}$$

where $\dot{\mathrm{Q}}_{\mathrm{flux}}$ denotes volumetric heat flux, $\mathrm{T}_{\mathrm{surface}}$ represents surface temperature, $\mathrm{T}_{\mathrm{initial}}$ symbolizes initial temperature, σ represents Stefan-Boltzmann constant, and ε denotes emissivity of the base materials. $\mathrm{h}_{\mathrm{convection}}$ represents heat transfer coefficient. $\frac{\partial \mathrm{T}}{\partial \mathrm{t}}$ implies rate of change of temperature, $\frac{\partial \mathrm{T}}{\partial \mathrm{x}}$ highlights temperature gradient. Surfaces directly in contact with air are assigned to convective heat transfer coefficient of air. Meanwhile, the surfaces in contact with high conductivity copper fixture and backing plate are assumed to have a higher value of heat transfer coefficient.

For cupronickel alloy, the value of heat transfer coefficient is assigned as 25 W/m^{2}K on the top surface, and the emissivity value is used as 0.65 for similar joining of cupronickel alloy (Ferro et al., 2005). For the joining dissimilar ASSs, the heat transfer coefficient values are assumed as 30 W/m^{2}K (SS316L) and 15 W/m^{2}K (SS310) on the top surface. The emissivity values are used as 0.7 for SS316L and 0.75 for SS310 (Saida et al., 2015; Rong et al., 2017).

Due to the highly conductive fixture (made of copper), a higher value of heat transfer coefficient (1000 W/m^{2}K) is assumed on the bottom surface (Baruah and Bag, 2016).

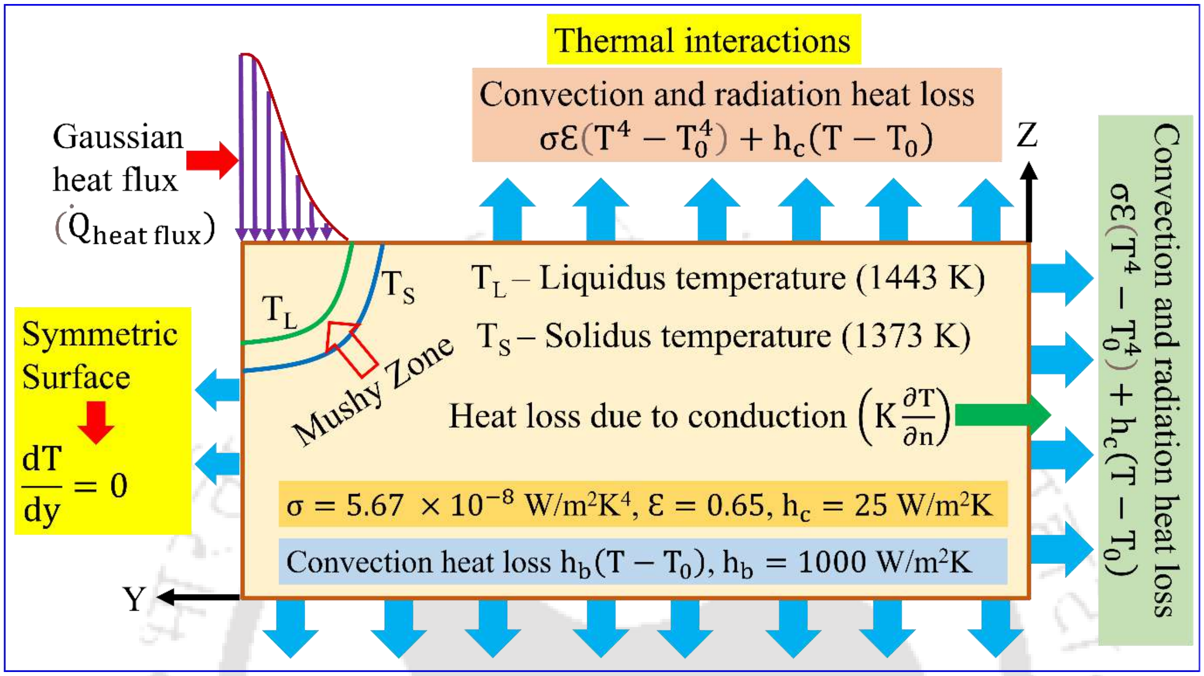

Fig. 4.1 The solution domain and boundary conditions used for thermal analysis.

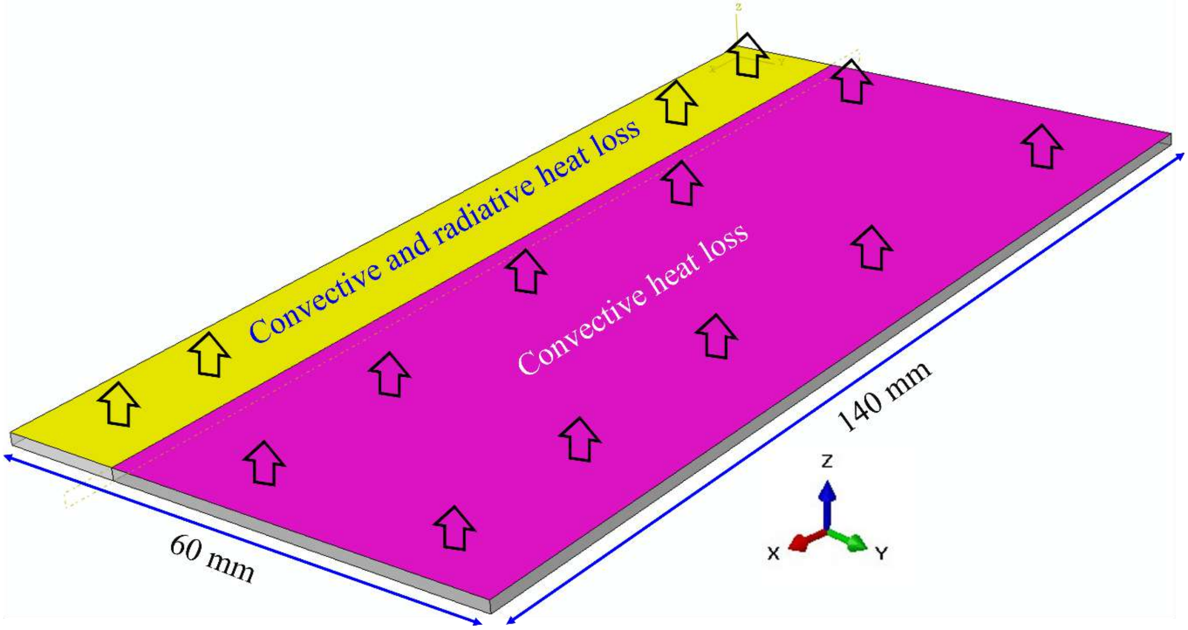

Fig. 4.2 The solution geometry and thermal boundary interactions for the similar joining of cupronickel alloy.

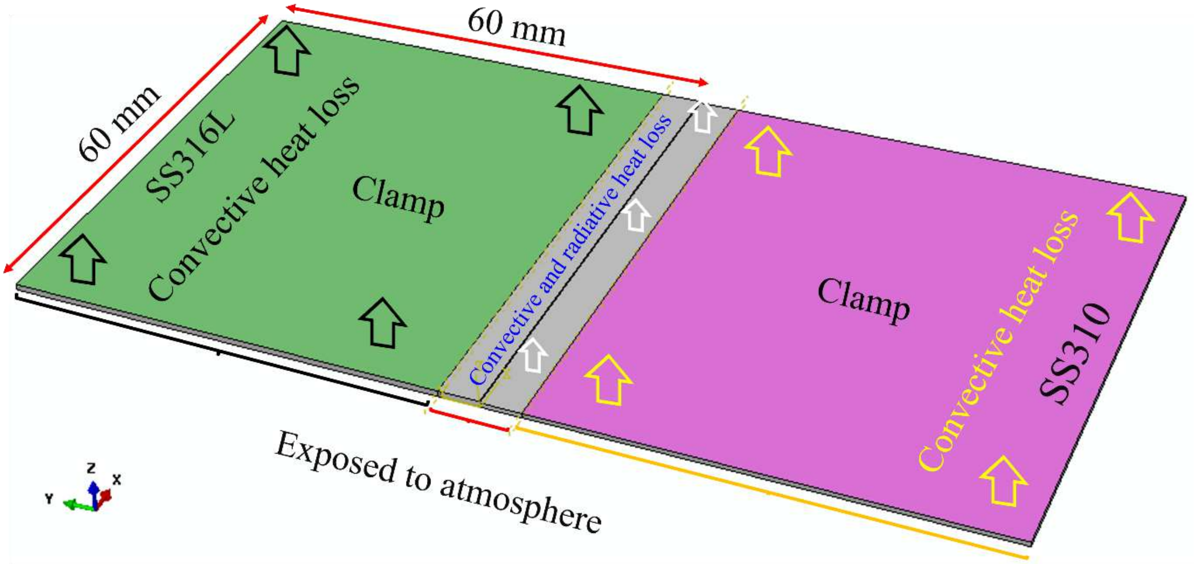

Fig. 4.3 Illustrates solution geometry and boundary interactions for joining dissimilar austenitic stainless steels.

4.3 Heat source model

The heat source model aids in reliably predicting the temperature fields in the weld pool and weld bead dimensions. Due to the constricted plasma arc heat source, the surface heat source lacks complete penetration, hence, a body/volumetric heat source is applicable. A double-ellipsoidal heat source model is implemented to predict the thermal characteristics precisely for the thermal analysis of similar joining of cupronickel alloy. Fig. 4.4 illustrates the double-ellipsoidal volumetric heat source schematic and the optimized parameters used for the numerical analysis. The volumetric heat source (double-ellipsoidal) equations are given by Eq. (4.5) and Eq. (4.6) (Goldak et al., 1984),

$$\dot{q}_f\,(x,y,z) = \frac{6\sqrt{3}\times \mathrm{f_f}\times \mathrm{Q}}{\mathrm{a_f}\times \mathrm{b}\times \mathrm{c}\times \pi\sqrt{\pi}}\times \exp\left(-\frac{3\mathrm{x}^2}{\mathrm{a_f^2}}\right)\exp\left(-\frac{3\mathrm{y}^2}{\mathrm{b}^2}\right)\exp\left(-\frac{3\mathrm{z}^2}{\mathrm{c}^2}\right) \tag{4.5}$$

$$\dot{q}_r\,(x,y,z) = \frac{6\sqrt{3}\times \mathrm{f_r}\times \mathrm{Q}}{\mathrm{a_r}\times \mathrm{b}\times \mathrm{c}\times \pi\sqrt{\pi}}\times \exp\left(-\frac{3\mathrm{x}^2}{\mathrm{a_r^2}}\right)\exp\left(-\frac{3\mathrm{y}^2}{\mathrm{b}^2}\right)\exp\left(-\frac{3\mathrm{z}^2}{\mathrm{c}^2}\right) \tag{4.6}$$

where $\dot{q}_f$ and $\dot{q}_r$ explains the volumetric generation of heat at the front and rear ellipsoids. Q refers to the total power input; $\mathrm{f_f}$, $\mathrm{f_r}$ implies a portion of the heat flux delivered corresponding to front and rear ellipsoids, and $\mathrm{a_f}$, $\mathrm{a_r}$ corresponds to heat source from center to the front and rear ellipsoids, b represents half weld width, c denotes penetration depth; x, y, and z details coordinates with a heat source at the origin.

The intensity of heat responsible for providing the necessary heat to melt the base materials is given in Eq. (4.7),

$$Q = V \times I \times \eta \tag{4.7}$$

where, V, I, and η denotes voltage, welding current, and welding process efficiency. The cycle fluctuation of current between the peak current (I_p) and base current (I_b) results in temporal variation of the flux. Therefore, the current pulsation effect is incorporated in Eq. (4.7) by substituting the value of I_p and I_b. Therefore, modified Eq. (4.7) is represented by Eq. (4.8),

$$Q(t) = \begin{cases} V \times I_P \times \eta, \text{ if } \quad \mathrm{t} \leq \mathrm{t_{on}} \\ \qquad or \\ V \times I_b \times \eta, \text{ if } \quad \mathrm{t} > \mathrm{t_{on}} \end{cases} \tag{4.8}$$

wherein I_p is applied during pulse-on time (t_{on}) and I_b is applied during pulse-off time (t_{off}).

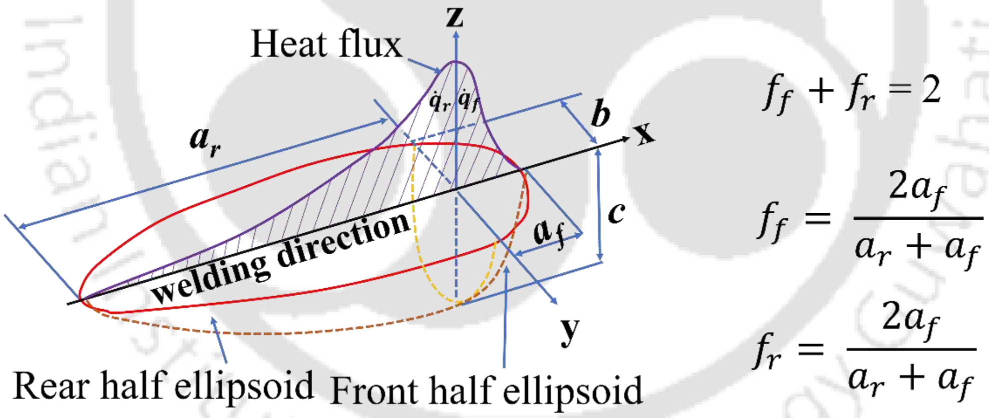

$$f_f + f_r = 2$$

$$f_f = \frac{2a_f}{a_r + a_f}$$

$$f_r = \frac{2a_f}{a_r + a_f}$$

Heat source parameter	a_f	a_r	b	c	f_f	f_r
Optimized value (mm)	1.5	3.0	0.58, 0.77, 0.90	0.7	1.33	0.67

Fig. 4.4 Depicts the double-ellipsoidal volumetric heat source schematic implemented for thermal analysis.

For the joining of dissimilar ASSs, a Gaussian volumetric heat source with decreasing intensity in the thickness direction is selected and given by Eq. (4.9) (Baruah and Bag, 2016).

$$\dot{Q}_{\mathrm{flux}}\,(x, y, z, t) = \frac{p\eta V W_c}{\pi r_{\mathrm{eff}}^2 d_p} e^{\left[-p\frac{(x-W_s t)^2+y^2}{r_{\mathrm{eff}}^2}\right]} e^{(t-z)} \qquad (4.9)$$

where $\dot{Q}_{\mathrm{flux}}$ is the volumetric heat source, (x, y, z) is the position connected with the dynamic heat source, p is the power intensity factor, V is measured voltage, η is the welding process efficiency, W_c is the welding current, r_{eff}^2 is the radius (effective) of the plasma arc, d_p is the penetration depth, W_s is the welding speed, and *t* is the thickness.

4.4 Mechanical analysis

During the joining process, heating (expansion) followed by subsequent cooling (contraction) and results in intense deformation where the deflection and stresses are determined by thermo-elastic-plastic analysis. The small deformation principle is incorporated to predict the values of deflection, wherein strain and displacement are correlated linearly. The elastic properties are employed by using Hooke's law, and the plastic properties are implemented through the rate-independent yield criterion (von Mises) and hardening (isotropic) principle, in which temperature-dependent yield stress and plastic strain values are considered. For simplifying the mechanical modeling, the following types of strain are neglected: impact of creep (because FZ remains at high temperature for a small duration), viscoelasticity (because temperature-dependent data is considered, not time-dependent), and phase transformation (because $Cu_{90}Ni_{10}$ is a single-phase material). No inertia exists during the joining process; thus, the stress analysis is considered static.

Fig. 4.5 illustrates the BCs employed for the mechanical analysis wherein the degrees of freedom (DOF) are restricted at different edges of the sheet: edge-1 (c-d) ($U_{(z)} = 0$), edge-2 (e-f) ($U_{(x)}$, $U_{(y)}$, $U_{(z)} = 0$), edge-3 (g-h) ($U_{(y)}$, $U_{(z)} = 0$), due to symmetry (a-b-c-d) ($\partial T/\partial y = 0$), and bottom surface (b-d-f-h) ($U_{(x)}$, $U_{(y)} = 0$). Similarly, Fig. 4.6 illustrates the constraint applied for mechanical analysis of dissimilar ASSs welded joints. For mechanical analysis, the static equilibrium and thermo-elastic-plastic models are considered. The equilibrium equation used for mechanical analysis and the cumulative strain factor ($\varepsilon_{ij}^{\mathrm{total}}$) is represented by Eq. (4.10) and Eq. (4.11) (Liang et al., 2024), respectively.

$$\frac{\partial \mathrm{Stress}_{ij}}{\partial x_j} + b_i^f = 0 \qquad (4.10)$$

Wherein Stress_{ij} represents Cauchy stress (tensor) and b_i^f denotes body force (vector). The incremental nature of the elastic-plastic analysis is evident from the fact that total strain increment (ε_{ij}^{total}) (Li et al., 2021) is denoted as the sum of the strain components represented by Eq. (4.11),

$$\Delta\varepsilon_{ij}^{total} = \Delta\varepsilon_{ij}^{e} + \Delta\varepsilon_{ij}^{thm} + \Delta\varepsilon_{ij}^{p} + \Delta\varepsilon_{ij}^{pt} + \Delta\varepsilon_{ij}^{trip} \tag{4.11}$$

where the components of the elastic strain ($\Delta\varepsilon_{ij}^{e}$), the thermal strain ($\Delta\varepsilon_{ij}^{thm}$), the plastic strain ($\Delta\varepsilon_{ij}^{p}$), and the phase transformation-induced strain ($\Delta\varepsilon_{ij}^{pt}$) are all listed. The present study incorporated yield stress and associated plastic strain as a function of temperature. The plasticity model adheres to the isotropic hardening, related rate-independent flow rule, and von Mises yield criterion. For similar joining of cupronickel alloy (single-phase material), no phase transformation occurs. Meanwhile, for dissimilar joining of ASSs (dual-phase material), phase transformation occurs. However, strain accompanied by other factors, including TRIP, is ignored because it shows an insignificant effect on residual stress, particularly for stainless steel (Sun et al., 2014).

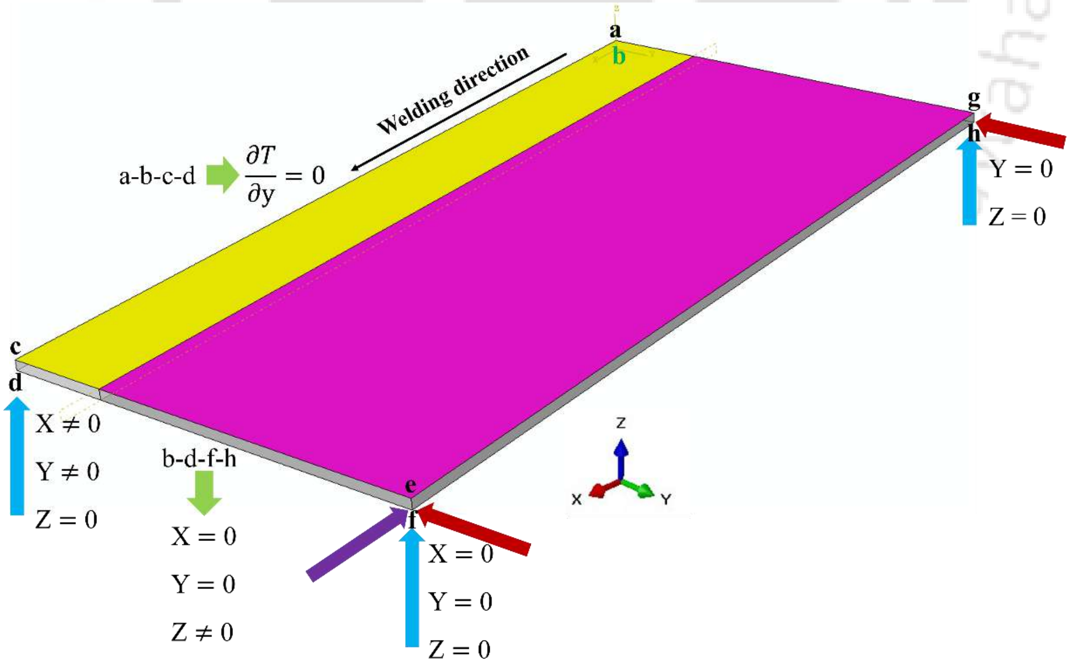

Fig. 4.5 The boundary condition employed for the mechanical analysis of similar cupronickel welded joints (Deng et al., 2013).

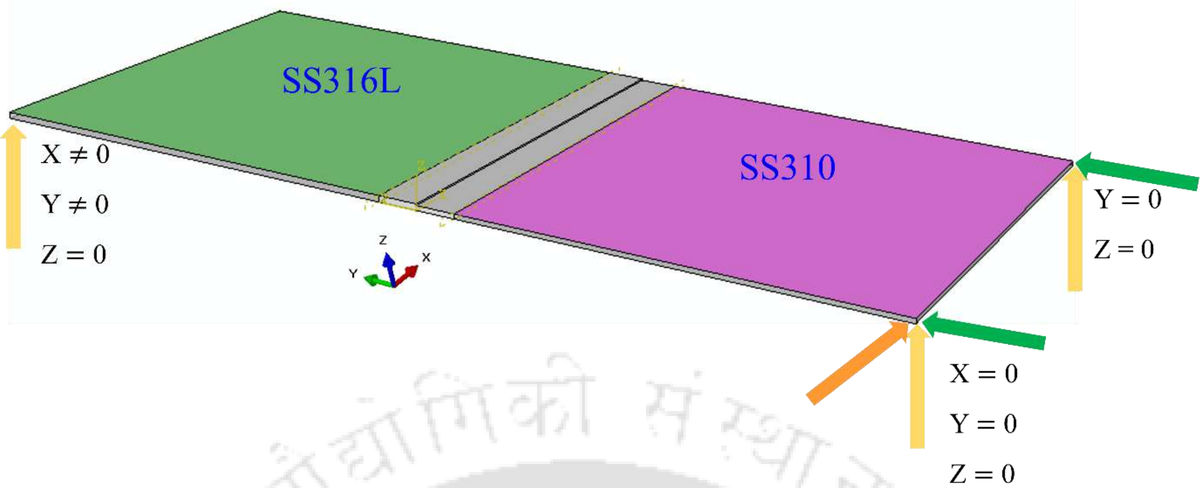

Fig. 4.6 The boundary condition employed for the mechanical analysis of dissimilar joining of ASSs (Deng et al., 2013).

4.5 Solid-state phase transformation (SSPT)

The phase transformation kinetics is controlled by non-homogeneous alloying element distribution. SSPT plays a key role in the residual stress distribution within the weld pool, which governs the overall mechanical behaviour of the welded joints (Homporova et al., 2011). During any fusion welding process, factors that play a significant role in modifying the residual stress distribution are melting, followed by solidification and solid-state phase transformation. It is to be noted that the strain caused as a result of phase transformation can alter the state of residual stress. Phase transformation usually occurs during the cooling phase and can significantly contribute towards residual stress and distortion of the resulting structure. Temperature variations during the welding process modify the lattice parameters (due to thermal expansion and contraction), due to which volumetric changes occur, leading to phase transformation. Generally, two different types of phase transformation are considered: diffusional and diffusionless transformation. For ASS, phase transformation is negligible during the heating phase. However, during the cooling phase, ASSs undergo a diffusional transformation from $\delta_{\text{ferrite, BCC}}$ to $\gamma_{\text{austenite, FCC}}$ within a narrow range of temperatures. The next sections describe the transformation kinetics, volumetric strain, and implementation of thermo-mechanical and thermo-metallurgical-mechanical (TMM) model.

4.5.1 Transformation kinetics in the cooling cycle

The Schaeffler and pseudo-binary illustration of the Fe-Cr-Ni ternary system accurately depicts the phase transformation behaviour of FZ evolved in the dissimilar joint under various process conditions. The material under investigation undergoes a eutectic reaction that produces liquid, $\gamma_{\text{austenite}}$, and δ_{ferrite} phases at temperatures between solidus ($T_{\text{solidus}} \sim 1648$ K) and liquidus ($T_{\text{Liquidus}} \sim 1728$ K). The present work does not consider the phase change dynamics from liquid to solid. The isopleth of the ternary Fe-Ni-Cr system (with 70 wt.% Fe) states that on the verge of SSPT, the austenitic steel comprises $\gamma_{\text{austenite}}$ and δ_{ferrite} at T_{solidus}. M-PAW is categorized as a rapid cooling-assisted welding technique due to its highly collimated and coherent plasma arc. $\gamma_{\text{austenite}}$ (Ni) has a comparatively high solubility at elevated temperatures, while δ_{ferrite} is extremely stable at high temperatures. The initial phase fractions of $\gamma_{\text{austenite}}$ and δ_{ferrite} at solidus temperature are arbitrarily considered in the current work to be 4-5% and 95-96%, respectively (Lippold and Kotecki, 2005). It is assumed that the SSPT between $\delta_{\text{ferrite}} \rightarrow \gamma_{\text{austenite}}$ adheres to the John-Mehl-Avrami-Kolmogorov (JMAK) equation (Avrami, 1940), which is written as,

$$f'_{\gamma}(T_{(t)}) = [1 - e^{(-k_{\delta\rightarrow\gamma}(\tau)^{n_{\delta\rightarrow\gamma}})}] \times f_{\gamma}^{eq.} \qquad (T_{\gamma s} \geq T \geq T_{\gamma f}) \qquad (4.12)$$

where $k_{\delta\rightarrow\gamma}$ specifies the nucleation and growth rate, which primarily depends on temperature, and $f'_{\gamma}(T_{(t)})$ represents the phase proportion of the austenitic phase at a temperature (T) and time (t). $n_{\delta\rightarrow\gamma}$ is the Avrami coefficient to account for the nucleation, followed by growth, and $f_{\gamma}^{eq.}$ indicates the maximum value of the phase proportion of the γ-phase at the equilibrium stage. Further, $T_{\gamma s}$ and $T_{\gamma f}$ signifies δ_{ferrite} dissolution starts (1673 K) and finish temperature (1273 K), respectively. Based on the Temperature-Time-Transformation (TTT) diagram, the highest value of transformation is assumed to be 98%, and as a result, $n_{\delta\rightarrow\gamma}$ and $k_{\delta\rightarrow\gamma}$ are estimated as 2.65 and 0.01, respectively (Feujofack Kemda et al., 2021).

4.5.2 Conversion into non-isothermal domains

The aforementioned empirical relation is applicable only for calculating phase proportion growth about transformation under isothermal conditions. However, Scheil's additivity rule is used to account for non-isothermal characteristics (Feujofack Kemda et al., 2021). It signifies that the total amount of time required to attain a specified fraction of a particular phase during continuous cooling is calculated by adding several incremental isothermal steps corresponding to instantaneous temperature changes. For the incorporation of the non-isothermal behaviour of phase transformation, the term fictitious time (τ_f^*) is introduced. τ_f^* is the time required for the transformation to arbitrary volume fraction, i.e., $\mathrm{f}_{\delta\to s}$ at temperature $\mathrm{T_o}$, considering an isothermal transformation at temperature $\mathrm{T_o} + \Delta\mathrm{T}$. Thus, τ_f^* (Kumar et al., 2021, 2020) is evaluated using Eq. (4.13).

$$\tau_f^* = \left\{\frac{1}{-\mathrm{k}_{\delta\to s}} \times \ln\left(1 - \frac{{\mathrm{f}_{\delta\to s}}^{\mathrm{eqb.}} \times (\mathrm{T_o})}{{\mathrm{f}_{\delta\to s}}^{\mathrm{eqb.}} \times (\mathrm{T_o} + \Delta\mathrm{T})}\right)\right\}^{(\mathrm{N}_{\delta\to s})^{-1}} \tag{4.13}$$

Using the Avrami model, the phase proportion at equilibrium for the transformation is plotted against temperature (Ahn et al., 2017; Avrami, 1940) to determine the γ-phase proportion at equilibrium at a specific temperature, T_t and $T_{t+\Delta t}$. Thus, by using fictitious time, Eq. (4.12) is modified to Eq. (4.14).

$$\mathrm{f'}_\gamma(\mathrm{t} + \Delta\tau, \mathrm{T} + \Delta\mathrm{T}) = \begin{cases} [1 - e^{\{-\mathrm{k}_{\delta\to\gamma}(\tau_0{}^* + \Delta\tau)\}^{\mathrm{n}_{\delta\to\gamma}}}] \times {\mathrm{f}_\gamma}^{\mathrm{eq.}} & (1273\ \mathrm{K} \leq \mathrm{T} < 1673\ \mathrm{K}) \\ 5 \times 10^{-2} & (\mathrm{T} > 1673\ \mathrm{K}) \end{cases} \tag{4.14}$$

4.5.3 Volumetric strain

The thermal strain components are algebraically added to the volumetric expansion that takes place during instantaneous phase fraction evolution corresponding to SSPT. Overall strain is composed of a thermal and a phase-transition component (Kumar et al., 2021, 2020) and is represented as

$$\begin{aligned} \Delta\varepsilon^{\mathrm{thm}} + \Delta\varepsilon^{\mathrm{pt}} &= \alpha(\mathrm{T}) \times \Delta\mathrm{T} + \alpha_{\mathrm{pt}}(\mathrm{T}, \mathrm{t}) \times \Delta\mathrm{T} = \\ &\Delta\mathrm{T}[\alpha(\mathrm{T})] + \{\varepsilon^{\Delta\mathrm{vt}} \times (\mathrm{T}(\mathrm{t})) \times \Delta\mathrm{f'}_\gamma(\mathrm{T}, \mathrm{t})\} \end{aligned} \tag{4.15}$$

where $\varepsilon^{\Delta\mathrm{vt}}$ is the change in volumetric strain brought on by SSPT during the cooling stage, and $\Delta\mathrm{f'}_\gamma$ is the instantaneous change in the phase fraction of the austenite phase. The expansion coefficient corresponding to SSPT is denoted by the symbol α_{pt}. The interaction of ferrite and austenite lattice characteristics is used to estimate the volumetric strain (Kumar et al., 2021, 2020), which is denoted as

$$\varepsilon^{\Delta vt}(T) = \frac{1}{3}\frac{\Delta V}{V} = \frac{(V_{\delta'})^{1/3} - (V_{\gamma'})^{1/3}}{(V_{\gamma'})^{1/3}} = \frac{A_{\delta'} - A_{\gamma'}}{A_{\gamma'}} \tag{4.16}$$

where $A_{\delta'}$ and $A_{\gamma'}$ represent the lattice constant of δ- and γ-phases, respectively. The $A_{\delta'}$ and $A_{\gamma'}$ (Kumar et al., 2021, 2020) are evaluated using Eq. (4.17).

$$A_{\delta',\gamma'}(T) = \begin{cases} 0.28863 \times \{1 + 17.55 \times 10^{-6} \times (T - 1073\ K)\} \\ \{0.36308 + (0.00075 \times C\%)\} \times [1 + \{24.92 - (0.61 \times C\%)\} \times 10^{-6} \times (T - 1273\ K)] \end{cases} \tag{4.17}$$

Eq. (4.17) is implemented to approximate the temperature-related austenite's lattice parameter, which is dependent on the percentage of carbon (Onink et al., 1993). Carbon is a strong austenitic stabilizer, and its concentration highly influences the lattice constant. Overall, the volumetric strain component is used to alter the thermal strain component in structural analysis to account for the SSPT effect.

4.6 Model geometry, meshing, and material properties

The calibration of the FE model requires a lot of trials, including the selection of elements, extent of solution geometry, and unknown properties like convective heat transfer coefficient and mesh size. However, the selection of mesh size, element type, and time step plays an important role in accurately predicting the thermal, metallurgical, and mechanical characteristics from the developed numerical model. Initially, all variables are fixed except mesh size, and the model is calibrated for thermal analysis. A trade-off between mesh size and computational time is maintained to reach the optimum mesh size, which is decided to reach a constant value of peak temperature at the center of the heat source for a particular mesh size.

The meshing and element type details used for the similar joining of cupronickel alloy are illustrated in Fig. 4.7. The thermo-mechanical analysis is performed using a fine mesh ($0.1 \times 0.1 \times 0.1$ mm^3) near the region of interest (fusion and heat-affected zone) and a coarse mesh ($0.1 \times 0.3 \times 0.1$ mm^3) away from the fusion zone/heat-affected zone. The element types DC3D8 (eight-noded diffusive heat transfer linear brick element) and C3D8R (brick element accompanied by reduced integration) are used for the thermal and mechanical analysis, respectively. The number of elements and nodes utilized for performing the thermo-mechanical modeling are 1,95,300 and 2,26,352, respectively. For the thermo-mechanical analysis, half (owing to symmetry) of the sheet dimension (140 × 60 × 0.7 mm^3) is assessed with respect to the weld direction. Temperature-dependent thermal properties (Ferro et al., 2005) are implemented to accurately predict the thermal profile, including the effect of latent heat. The time-temperature data is extracted from the thermal analysis and is used as input onto the mechanical analysis for which temperature-dependent properties (Jenkins et al., 1957; Ledbetter, 1982) [coefficient of thermal expansion (α), elastic properties (Young's modulus, Poisson's ratio) and plastic properties (yield stress)] are applied.

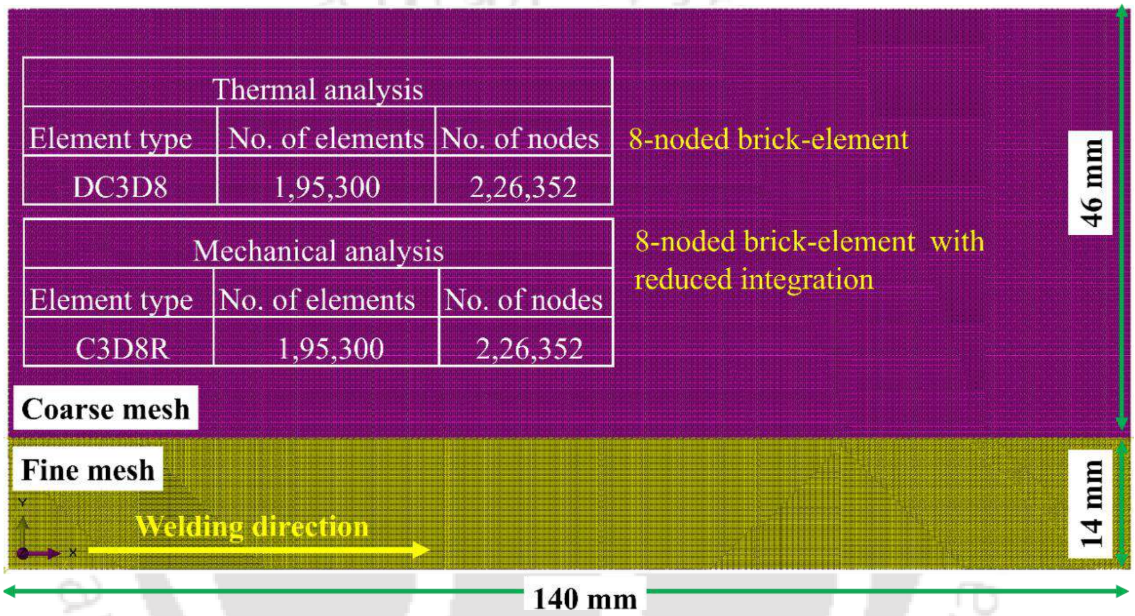

Thermal analysis		
Element type	No. of elements	No. of nodes
DC3D8	1,95,300	2,26,352

Mechanical analysis		
Element type	No. of elements	No. of nodes
C3D8R	1,95,300	2,26,352

Fig. 4.7 Illustrates the meshing details used for the similar joining of cupronickel alloy.

Similarly, the meshing and element type details used for the dissimilar joining of austenitic stainless steels are illustrated in Fig. 4.8. In the present case, a mesh size of 0.2 mm is used in the area of interest (fusion zone/heat-affected zone). The elements used for the thermal-metallurgical-mechanical analysis are DC3D8 (eight-noded diffusive heat transfer linear brick element) and C3D8R (brick element accompanied by reduced integration), respectively. The number of elements and nodes selected for the present analysis are 2,73,600 and 3,06,493 respectively. Temperature-dependent thermal and mechanical properties (SS310 (Saida et al., 2015) and SS316L (Rong et al., 2017)) are implemented to accurately predict the required thermal, metallurgical, and mechanical characteristics.

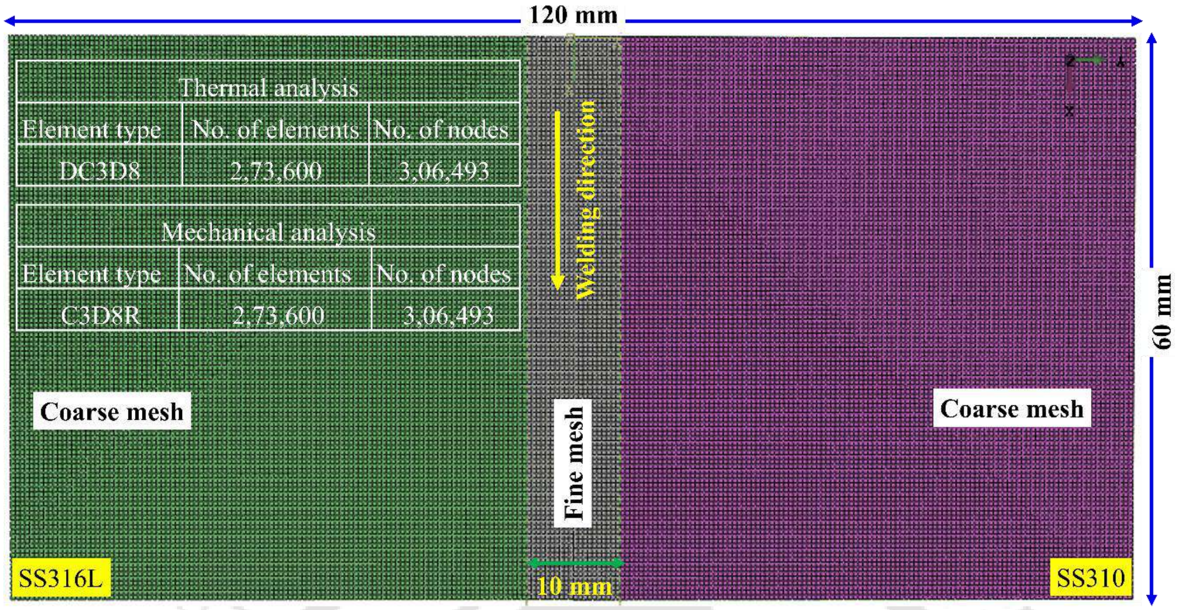

Thermal analysis		
Element type	No. of elements	No. of nodes
DC3D8	2,73,600	3,06,493

Mechanical analysis		
Element type	No. of elements	No. of nodes
C3D8R	2,73,600	3,06,493

Fig. 4.8 Illustrates the meshing details used for the joining of dissimilar ASSs.

4.7 Implementation of thermo-mechanical and thermo-metallurgical-mechanical (TMM) model

For the similar joining of cupronickel ($Cu_{90}Ni_{10}$) alloy, the sequentially coupled thermo-mechanical model is employed using commercial software ABAQUS. The heat source model is implemented through the DFLUX subroutine. However, the TMM model is employed for the dissimilar joining of ASSs. The development of a numerical model is accomplished using two separate phases. Phase I comprises a heat transfer model to extract temperature variation concerning time using the DFLUX subroutine in ABAQUS. Further, different temperature ranges are defined as $T < T_{solidus}$, $T_{solidus} \leq T_{melting}$, $T > T_{\delta \rightarrow f}$, and $T_{\delta,f} \leq T_{solidus}$, where $T \longrightarrow$ desired temperature, $T_{solidus} \longrightarrow$ solidus temperature, $T_{melting} \longrightarrow$ melting temperature, $T_{\delta \rightarrow f} \longrightarrow$ ferrite finish temperature. The mentioned temperature ranges are stated under subroutine USDFLD as state-dependent (Kumar et al., 2021; Kumar and Bag, 2019). The dT/dt is evaluated for the cooling phase for each node, and the node that complies with dT/dt criteria and its peak temperature corresponds to the SSPT temperature scale. This satisfying criterion displays volumetric dilation and goes through phase transformation phenomena. The output of Phase I of the numerical simulation is used as input to Phase II, in which the UEXPAN subroutine is implemented to predict the time and temperature-dependent percentage growth of $\gamma_{\text{austenite}}/\delta_{\text{ferrite}}$. After predicting the fraction of $\gamma_{\text{austenite}}/\delta_{\text{ferrite}}$, ε^{pt} is added to ε^{thm}. Further, the $\Delta\varepsilon^{\text{total}}$ is used to evaluate residual stresses in the dissimilar ASSs joints.

4.8 Summary

With the recent advancement in the computation field, the estimation of temperature distribution, distortion, and residual stress can be achieved effectively. The FE-based computational tool enables the necessary measurement of thermal, metallurgical, and mechanical characteristics that would have been challenging otherwise by experimentation. However, to achieve the aforementioned characteristics, the establishment of the heat transfer model with the proper selection of heat source becomes inherently necessary. Hence, the present chapter outlines the theoretical formulation of thermal, metallurgical, and mechanical analysis incorporated in fusion welding of similar and dissimilar materials.

The conduction-based heat transfer model is well-suited to predict the temperature distribution and weld-bead dimensions in pulse and continuous current modes. After the validation of the numerical model, the temperature-time history distribution is utilized to approximate the values of solidification parameters. The values of solidification parameters aid in determining the cooling rate of the welding process, which governs the resulting microstructural morphology of the welded joints, thus impacting the mechanical behaviour of the joints. Further, a sequentially-coupled thermo-mechanical and thermo-metallurgical-model aids in precisely predicting the value of distortion and residual stress. It is noteworthy that for cupronickel alloy, where the phase transformation effect is insignificant, only thermo-mechanical model is sufficient for process analysis. However, for dual-phase materials (ASS), the thermo-metallurgical-mechanical model is most suitable for estimating the phase fraction and precise estimation of distortion and residual stress.

भारतीय प्रौद्योगिकी संस्थान गुवाहाटी • Indian Institute of Technology Guwahati •

Chapter 5

Results and Discussion

5.1 Introduction

The current work focuses on controlling defect formation in the joining of $Cu_{90}Ni_{10}$ alloy via optimum heat supplied in continuous mode, and application of the least heat supplied is recommended in compliance with full penetration depth. Further enhancement in joint features is attained by better control over the average heat supplied using pulse mode. The pulse current provides better results in terms of the least depletion of metal, fine equiaxed morphology with reduced secondary dendritic arm spacing, and the lowest number of internal pores.

Further investigation focuses on the bimetallic joint between ferrous (SS304) and non-ferrous (Cu-T2) metals fabricated using the gas tungsten arc welding (GTAW) process. Thus, an effort has been made to realize the importance of arc offset and joining mode in the performance of Cu-SS bimetallic joints. The critical findings suggest that with an increased arc offset, the joint demonstrates a variation from welding mode to a weld-brazing mode, where the failure mode deviates from ductile to brittle fracture. A drastic decrement in strength and elongation is experienced with an increase in arc offset value. The primary factor governing the reduction in the joint properties positively correlates with the increasing percentage of copper in the fusion zone.

The present experimentation also aims to join a different combination of austenitic stainless steels (ASSs) (SS316L and SS310) using the M-PAW process and to establish a correlation linking the influence of heat input on the formation of different microstructural morphology, variation in joint strength, mode of failure, pore formation and to determine the optimal level of heat input that ensures weld joint remains free from internal defects, hot-cracking, and sensitization/weld-decay. The role of microstructure developed in dissimilar welding on residual stress generation is also established in the present work. Further, estimating residual stress in dissimilar austenitic steels is highly complicated, where the solidification behaviour and morphology are predominant. A significant lack of substantial work on dissimilar joints with the incorporation of solid-state phase transformation (SSPT), which has yet to be explored. Hence, the present study aims to investigate the mitigation of residual stress by controlling microstructural morphologies that can elude the failures of a welded joint. Thus, an attempt is made to understand the solidification behaviour of the weld metal as well as its correlation with microstructural features and residual stress distribution. The phase fraction and residual stresses are computed employing a finite element (FE) based thermal-metallurgical-mechanical (TMM) model, which includes the effect of SSPT. The key findings indicate that a lower level of heat input promotes the formation of a high amount of δ_{ferrite}, which generates comparatively more compressive stress due to the disparity in thermal expansion coefficient ($\alpha_{\text{Ni}} \sim 1.6\ \alpha_{\text{Cr}}$) and aids in the reduction of residual stress.

5.2 Micro-plasma arc welding of cupronickel alloy

Porosity is one of the most prevalent defects associated with the fusion welding of copper-nickel alloys. The presence of porosity and non-metallic inclusions reduced $Cu_{90}Ni_{10}$ joint properties fabricated using the flux-cored arc welding (FCAW) process (Devletian et al., 2006). Undercut and porosity defects were common in all the laser beam welded $Cu_{70}Ni_{30}$ joints, which caused the joints to fail in the FZ (fusion zone)/HAZ (heat-affected zone). However, all the fabricated joints were independent of surface cracks (Cao and Nolting, 2019). Due to the increased applied power, Ferro et al. (Ferro et al., 2005) observed a decline in the FZ properties, attributed to thermal softening and a larger secondary dendritic arm spacing (SDAS). Chakravarthy et al. (Chakravarthy et al., 2014) identified that finer equiaxed morphology with uniform distribution enhanced the joint properties of $Cu_{70}Ni_{30}$ joints fabricated by the LBW process. However, the weld joints showed undercuts, and no surface cracks were reported.

Munro (Munro, 2013) observed a significant decline in the impact energy of the welded joint, where cold working was the prime reason for the reduction in joint quality. However, annealing between 650-825°C aided in regaining the lost impact energy for the joints welded multiple times. Reutzel et al. (Reutzel et al., 2007) explored joining CuNi alloys using both LBW and hybrid welding (LBW + GMAW) processes. The authors reported complete penetration without porosity using LBW for a 0.25-inch plate. However, defects like sagging and undercutting were reported for welding speeds that were less than 30 inches per minute.

The hybrid welding technique to join $Cu_{70}Ni_{30}$ and $Cu_{90}Ni_{10}$ produced many porosities. The authors attempted to tackle porosity by (i) adjusting the power and speed, (ii) acid dipping (before/after performing the joining), and (iii) back purging but failed to achieve any positive results. The authors stated that reactive elements at elevated temperatures resulted in pore formation, which were not allowed to get away due to the high rate of solidification during LBW. Xing et al. (Xing et al., 2023) examined the corrosion properties of gas tungsten arc welded (GTAW) $Cu_{90}Ni_{10}$ and HSCuNi joints in flowing seawater. The authors reported a higher corrosion rate for the HAZ because of galvanic corrosion.

The literature highlights various welding techniques (FCAW, GTAW, M-PAW, SAW, USW, LBW + GMAW, and LBW) employed to join CuNi alloys (Cao and Nolting, 2019; Chakravarthy et al., 2014; Das et al., 2019; Devletian et al., 2006; Ferro et al., 2005; Munro, 2013; Reutzel et al., 2007; Straight et al., 1988; Xing et al., 2023). Among these, micro-plasma as a heat source allows the usage of a controlled and constricted arc with higher power density. Available at a lower magnitude of power, allowing minimal deterioration to the weldments, thus enabling high-quality joints. In addition, M-PAW is a relatively economical technique compared to LBW and EBW joining methods for producing joints in the order of 100-1000 microns. Therefore, the M-PAW is an economically viable option to produce superior-quality weldments with minimal defects (Haldar and Pal, 2024).

The present investigation aims to understand the weldability of 0.7 mm-thick $Cu_{90}Ni_{10}$ alloy by controlling defect formation via optimum heat supplied in continuous mode. Further enhancement in joint properties is attempted by application of pulse mode. The weld joints are subjected to destructive and non-destructive testing (NDT) to judge the feasibility of the fabricated joints. The destructive testing includes microstructural analysis (optical, electron microscopy, and EBSD), microhardness evaluation, tensile testing, micro-and macro-fractography analysis. Further, corrosion analysis is accomplished to determine the chemical stability of the joints. The NDT used in the present investigation aims to assess residual stress and distortion in the joints. In addition, an advanced NDT (X-ray computed tomography: X-ray CT) is carried out to identify internal defects. A finite element (FE) model is also incorporated to predict the peak temperature, weld dimension, residual stress, and distortion on the fabricated joints. In the present study, three selected values of heat input ($HI_{35.80}$, $HI_{66.67}$, and $HI_{96.03}$) used for the similar joining of cupronickel alloy ($Cu_{90}Ni_{10}$) are highlighted in Table

3.3 of Chapter 3 and the implementation of the thermo-mechanical model is detailed in Section 4.7 of Chapter 4.

5.2.1 Temperature distribution and validation of the numerical model

The accomplished thermal model helps to predict the temperature-time data and the weld dimensions. It is to be noted that the current FE model assumes the top surface of the weld to be flat (neglecting the flow of fluid/molten material). Fig. 5.1(a) illustrates the temperature-time data extracted from the flat surface of the weld centerline for the three different cases ($HI_{35.80}$, $HI_{66.67}$, and $HI_{96.03}$). The thermal profile, which consists of the heating and cooling periods, aids in identifying the heating/cooling rate. The peak temperature attained for the cases $HI_{35.80}$, $HI_{66.67}$, and $HI_{96.03}$ turns out to be 1708, 2011, and 2331 K, respectively. The rise in the value of peak temperature with heat provided is self-evident because higher heat supplied by the heat source allows a larger engagement duration, leading to more melting and a rise in peak temperature. Macrographs showing the cross-sectional view of the joints are depicted in Fig. 5.1(b-d), in which the weld size shows a positive relationship with the peak temperature. The yellow dotted lines representing the fusion boundary (FB) demarcate the FZ from the HAZ and BM. To validate the thermal model, a K-type thermocouple attached at a distance of ~2.0 mm from the weld centerline is used to extract the temperature data, wherein the operating temperature of the thermocouple is between 73-1533 K for single usage. Fig. 5.1(b-d) depicts the variation in weld width for different weld cases, where an increase in heat provided ($HI_{35.80}$, $HI_{66.67}$, $HI_{96.03}$) leads to a corresponding rise in weld width (1.16, 1.54, 1.80 mm) but up to a certain extent. Beyond which (~96 J/mm) insignificant effect is noted, and further rise (~105 J/mm) in heat provided results in irregular weld/burn-through. A vital aspect noted from Fig. 5.1(b-d) is the 'concave shape crater defect,' in which the metal loss is observed near the weld cap region, and the resulting shape becomes upward concave. The influence of heat input on the weld width and metal depletion is illustrated earlier in Fig. 3.9 of Chapter 3.

Fig. 5.2(a-c) presents validation of the numerically extracted thermograph (right) with the experimentally obtained macrograph (left), along with the temperature legend (NT11, K) shown alongside. The peak temperature is represented with the grey color band (which represents the FZ), followed by the red color band (which depicts the mushy zone, MZ). The FZ is demarcated by the liquidus temperature ($T_{Liquidus}$, 1443 K), the HAZ is indicated below 1373 K (solidus temperature, $T_{Solidus}$) to 1163 K, and the phases of solid and liquid co-exist in the MZ ($T_{Liquidus}-T_{Solidus}$). The different color bands represent isotherm contours, which demarcate the FZ (grey), MZ (red), and HAZ (yellow). With the rise in the heat provided, the width of FZ and HAZ increases, along with the loss of metal in the form of a crater. With the rise in heat input, metal loss from the weld top increases (0.14, 0.18, 0.25 mm; marked with green color arrows in Fig. 5.2(a-c)), directly impacting the joint properties. The maximum error percent in predicting the bead dimensions at the weld cap and root is calculated as 6.89% and 10.63%, respectively. It is evident that the numerical results show acceptable agreement with the experimental values. Another way to check the reliability of the developed model is to validate the experimentally obtained temperature values with the numerically predicted values. Fig. 5.2(d) compares the peak temperature achieved for the numerical and experimental values for the different weld conditions with a maximum error of 5.87%, which authenticates the reliability of the applied numerical model.

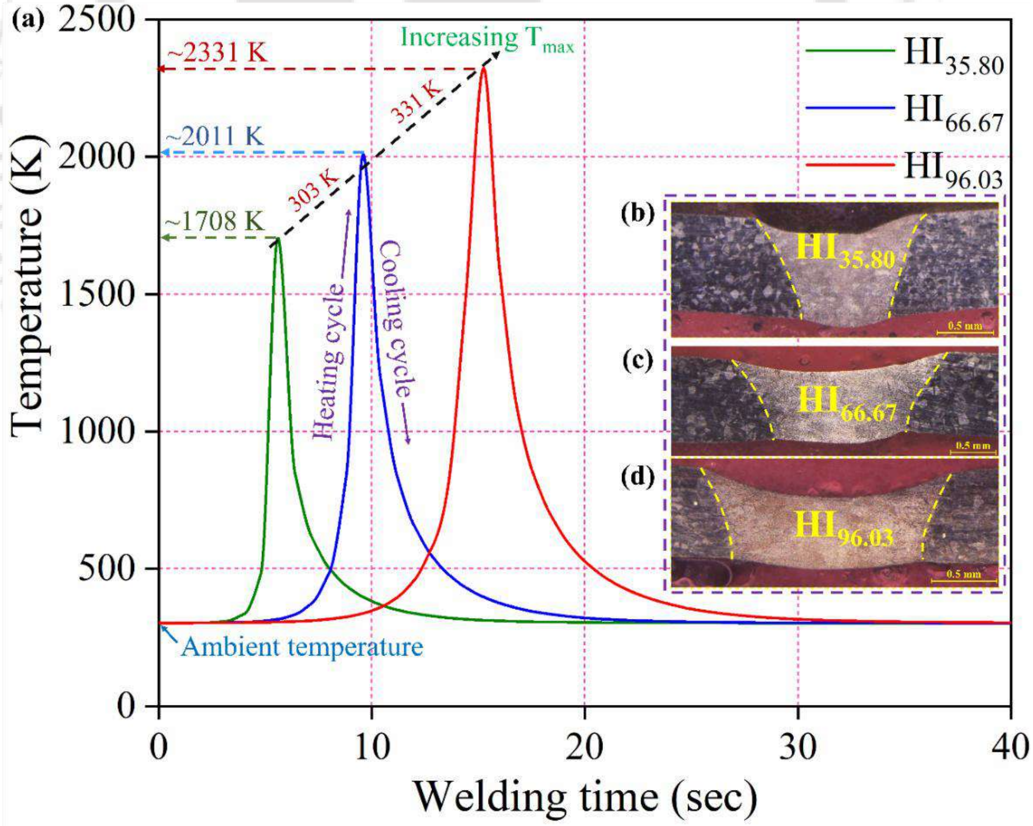

Fig. 5.1 Illustrates (a) temperature-time curve and (b-d) macrographs of the fabricated joints at different heat input values ($HI_{35.80}$, $HI_{66.67}$, and $HI_{96.03}$).

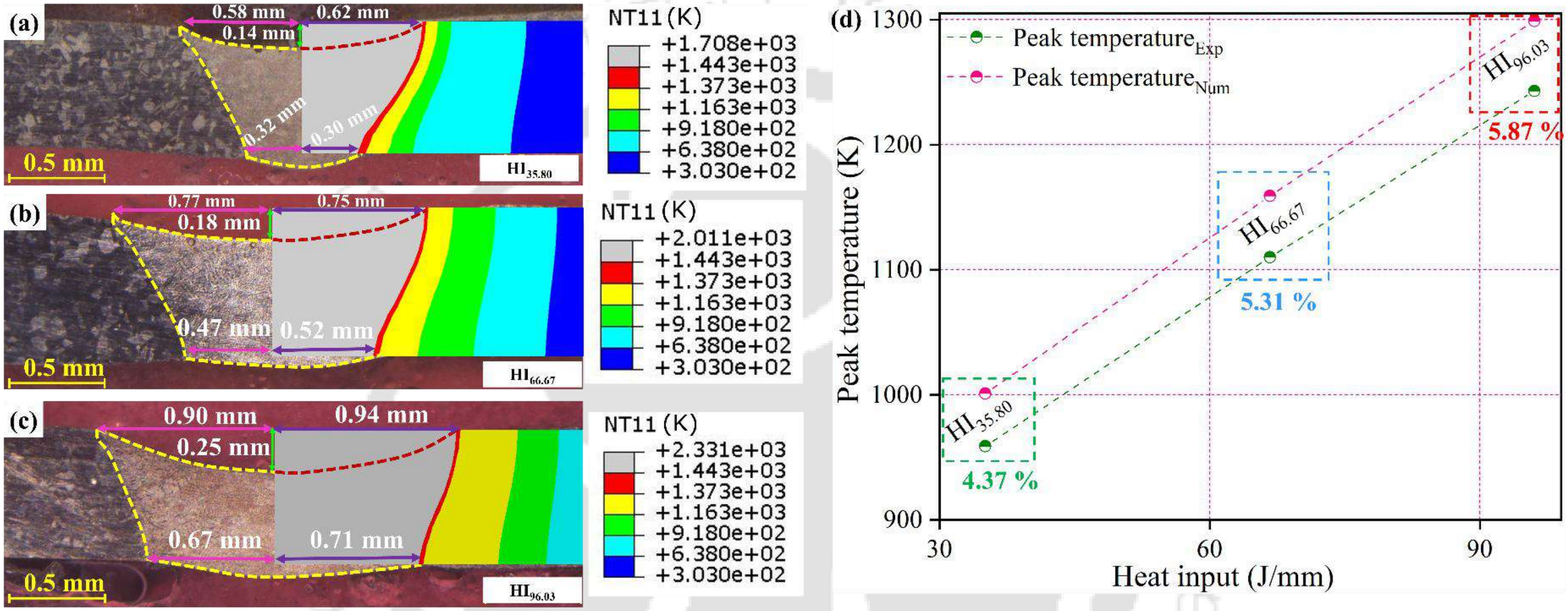

Fig. 5.2 Depicts the validation of numerically extracted data with experimental values for (a-c) weld dimensions and (d) peak temperature at different weld conditions ($HI_{35.80}$, $HI_{66.67}$, and $HI_{96.03}$).

5.2.2 Materials microstructure and solidification behaviour

Test coupon (10 mm × 5 mm) extracted in the transverse direction from the weld joint is put through a sequential mechanical and chemical cleaning process. To distinguish the FZ from the HAZ and the unaffected base material (BM), an etchant solution comprising $FeCl_3$ (5 g), HCl (50 ml), and H_2O (100 ml) is applied for a duration of 15 s to the test coupon. Fig. 5.3(a-c) illustrates the top view of the weld joints, illustrating the FZ, FB, and HAZ for the case $HI_{35.80}$. In Fig. 5.3(a-c), the pink dotted line represents the weld centerline, the red dotted line represents the FB, which demarcates the FZ and HAZ, and the yellow dotted line represents the HAZ, which demarcates the HAZ and the BM. The enlarged version on either side of the weld centerline is shown in Fig. 5.3(b, c). Fig. 5.4(a-i) depicts optical micrographs of the joints assembled at different heat inputs. In Fig. 5.4(b, e, h), the blue dotted lines demarcate the columnar and equiaxed structure formed in the FZ. The micrographs indicate the columnar structure near the FB growing in the direction perpendicular to the applied heat flux direction (Cao and Nolting, 2019) and equiaxed structure in the weld centerline, with complete DOP for all the weld cases. Fig. 5.4(a, c), Fig. 5.4(d, f), and Fig. 5.4(g, i) depicts the magnified view near the FB for the weld conditions $HI_{35.80}$, $HI_{66.67}$, and $HI_{96.03}$, respectively, wherein the growth of columnar grains can be easily spotted. The higher power density of M-PAW and a high thermal conductivity (40 W/mK) of $Cu_{90}Ni_{10}$ restricts the coarsening of grains in the HAZ (Ferro et al., 2005).

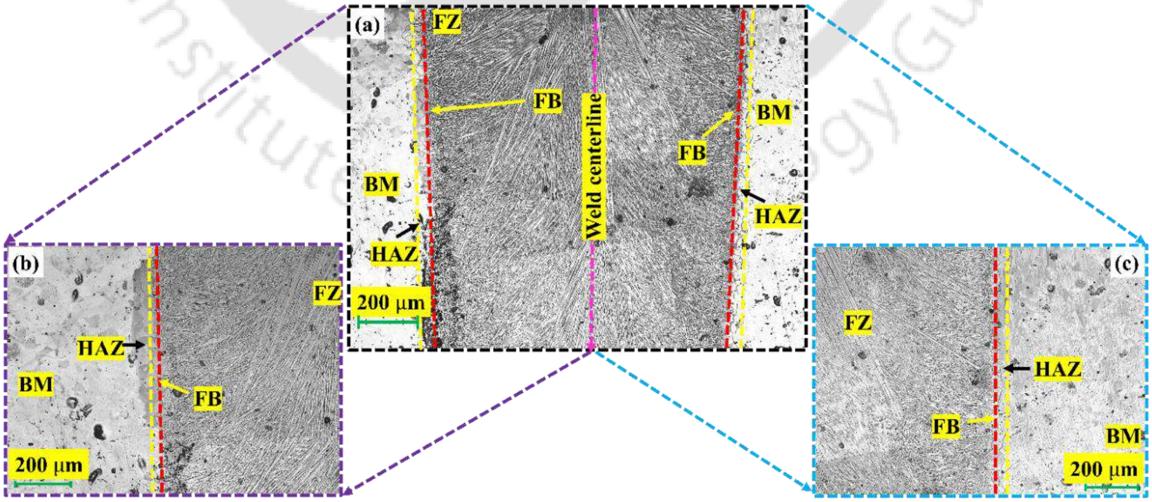

Fig. 5.3 (a-c) Top view of the weld joint illustrating fusion zone, fusion boundary, and heat-affected zone for the $HI_{35.80}$ weld joint.

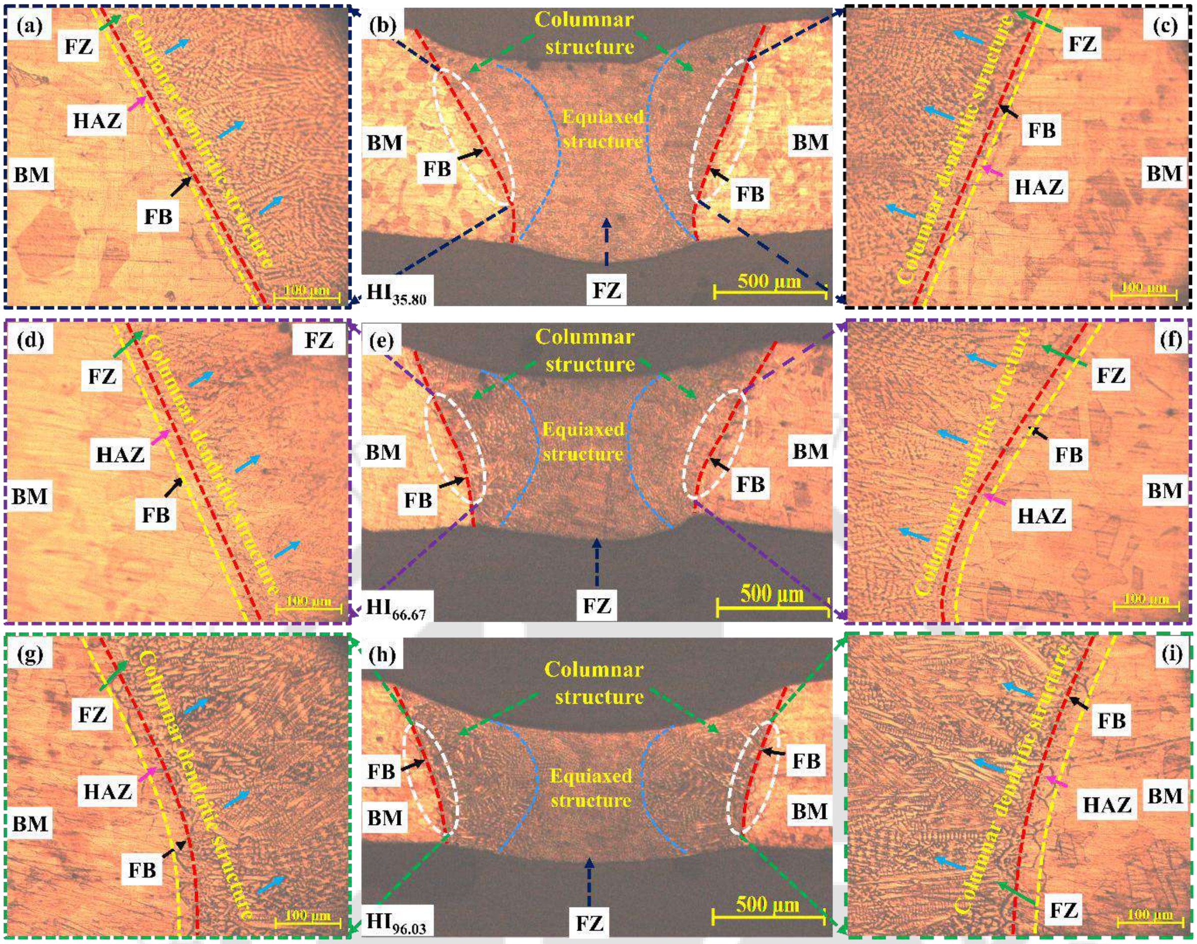

Fig. 5.4 Transverse view of the weld joints illustrating fusion zone, fusion boundary, and heat-affected zone for (a-c) $HI_{35.80}$, (d-f) $HI_{66.67}$, and (g-i) $HI_{96.03}$.

The solidification parameter G (temperature gradient, K/mm) is evaluated from dT/dt data using Eq. (5.1) (Sahu and Bag, 2021), and R (crystallization velocity) is acquired from the experimental condition (welding speed). Numerical values of $G \times R$ and G/R correspond to the size and type of morphology formed (Sahu and Bag, 2021). The $G \times R$ for the different weld conditions are evaluated as 1434 K/s ($HI_{35.80}$), 1179 K/s ($HI_{66.67}$), and 886 K/s ($HI_{96.03}$). Fig. 5.5(a-f) represents the microstructure evolved in the fusion zone, illustrating the dendritic arms for different weld conditions. Cu and Ni are completely soluble, and the only structure of the alloy is single-phase (α) FCC. The dendritic arms contain high Ni content, and the space in between contains Cu. It is noteworthy that during solidification, CuNi alloys are prone to cracking (Devletian et al., 2006). With the reduction in heat input, the rate of solidification increases, which allows finer dendritic structure in the resulting weld joints, leading to enhanced properties. The extent of refining of the resulting structure is measured in terms of SDAS, as presented in Eq. (5.2) (Ferro et al., 2005). With the increasing heat input value ($HI_{35.80}$, $HI_{66.67}$, $HI_{96.03}$), the solidification rate decreases, increasing the SDAS value (5.42, 5.69, 6.12 μm).

$$G(\mathrm{K/mm}) = \frac{T_{\text{weld center}}(\mathrm{K}) - T_{\text{solidus}}(\mathrm{K})}{\text{Distance between nodes (mm)}} \tag{5.1}$$

$$\text{SDAS } (\mu\text{m}) = 33.683 \times \text{ Cooling Rate } (\mathrm{K/s})^{-0.2512} \tag{5.2}$$

Due to the variation in G/R ratio, the solidification deviates from columnar (near the FB) to equiaxed (weld center). For the different weld conditions, contrasting morphology (equiaxed in the center of the FZ and columnar near the FB) is observed with the fine equiaxed and columnar structure for $HI_{35.80}$ joints shown in Fig. 5.5(a, b); coarse equiaxed and columnar structures for $HI_{66.67}$ joints shown in Fig. 5.5(c, d). Meanwhile, coarser equiaxed and columnar structures, along with solidification cracks, are observed for $HI_{96.03}$ joints, as shown in Fig. 5.5(e, f). The principal aspect that leads to cracking (solidification) in CuNi alloys are (i) broad mushy zone (70 K), (ii) impurities, and (iii) adequate stress (tensile) in the course of solidification (Devletian et al., 2006). The joints fabricated at $HI_{35.80}$ and $HI_{66.67}$ show no evidence of cracking, which confirms reasons (i) and (ii) cited above are not responsible for the presence of cracks in $HI_{96.03}$ joints. At $HI_{96.03}$, the molten pool remains at a high temperature for a longer duration (due to the low cooling rate, 886 K/s). Afterward, during the solidification, stress generation (tensile) occurs, and when the generated stress exceeds the yield stress of the base metal, cracks are observed in the FZ. Due to relatively lower heat input values (35.80, 66.67 J/mm), the stress generated must be lower than the YS_{BM} (~130 MPa). Meanwhile, for the 96.03 J/mm joints, the stress must have exceeded the YS_{BM} for which cracking occurs. The quantitative establishment (experimentally and numerically) of the stress generated in the joints is accomplished in the residual stress section (section 5.2.7).

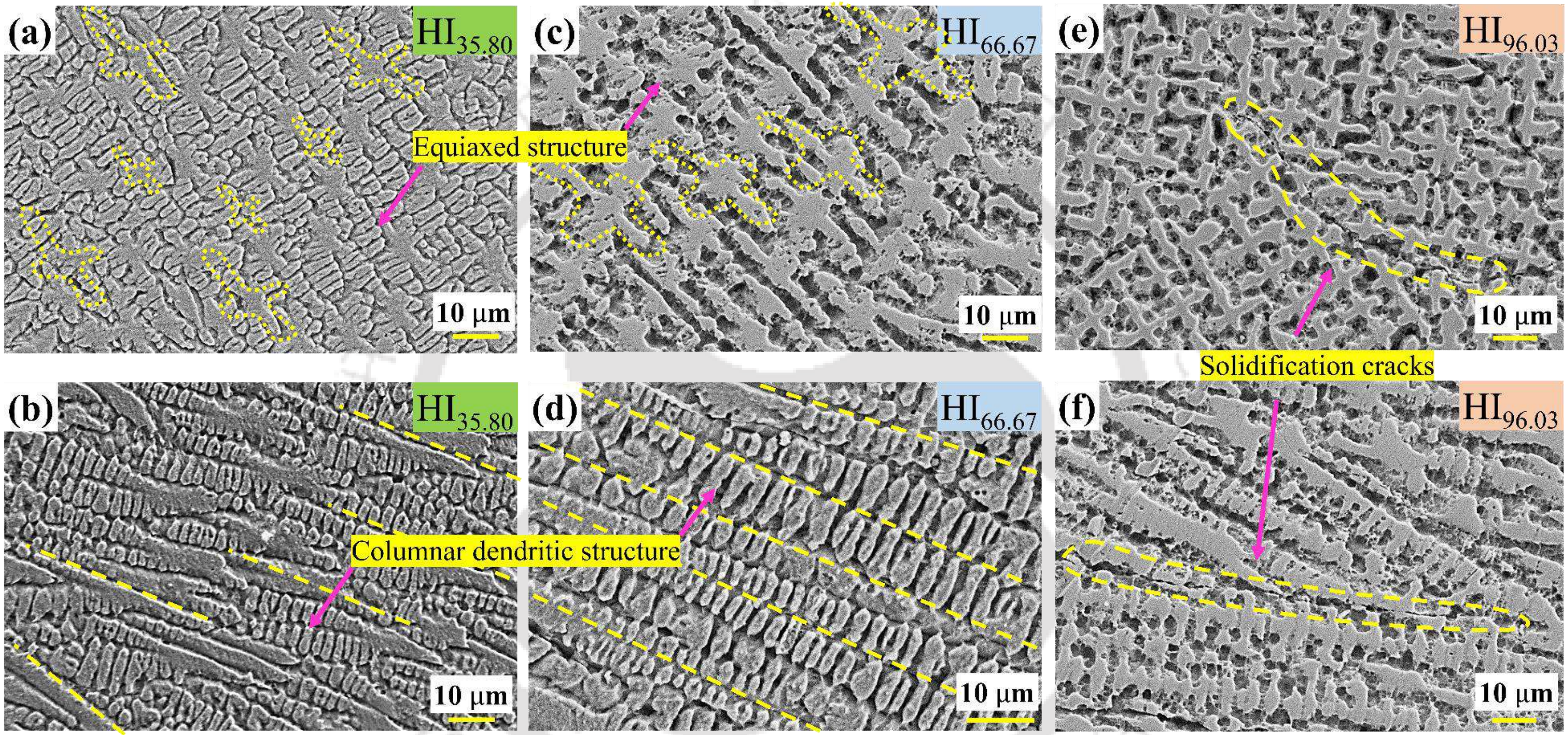

Fig. 5.5 Illustrates the evolution of microstructure within the fusion zone due to changes in the local cooling rate and temperature gradient for (a, b) $HI_{35.80}$, (c, d) $HI_{66.67}$, and (e, f) $HI_{96.03}$ joints.

Institute of Technology

5.2.3 EBSD evaluation

To estimate the grain's texture and properties, the joints are subjected to EBSD analyses after electrochemical polishing. Fig. 5.6(a-c) represents the inverse pole figure (IPF) color map and grain details of the as-received $Cu_{90}Ni_{10}$ alloy. The average grain size (AGS) (~4.73 µm), low-angle (< 15°), and high-angle (≥ 15°) grain boundaries (LAGBs⟶ 84.77 %, HAGBs⟶ 15.23 %) are determined using EBSD results. Fig. 5.6(d) represents the color legend of the inverse pole figure map (IPF). During the liquid-state joining process, the involvement of a temperature higher than the melting temperature of the base metal forces the fusion zone to undergo microstructural changes involving phase transformation, growth of grains, different microstructural morphology, and variation in the LAGBs and HAGBs (Kangazian and Shamanian, 2019a; Shamanian et al., 2020). Cu and Ni are completely soluble, and the only structure of the CuNi alloy is single-phase (α) FCC. Hence, no phase transformation occurs during solidification. Fig. 5.6(e-g) illustrates the phase map for the $HI_{35.80}$, $HI_{66.67}$, and $HI_{96.03}$ joints with red color representing the existence of a single-phase FCC structure. Fig. 5.6(h-j) illustrates the IPF color map of the fusion zone, which signifies the grain size, orientation, and morphology of the grains. Increasing the heat supplied allows a longer cooling time, which promotes grain growth. Thus, increased heat input $HI_{35.80}$, $HI_{66.67}$, and $HI_{96.03}$ results in a visible increase in average grain size values ~39.52, ~44.23, and ~49.26 µm, respectively. With respect to the base metal (AGS ~4.73 µm), a significant increase in the average grain size can be observed for $HI_{35.80}$, $HI_{66.67}$, and $HI_{96.03}$ weld conditions.

The LAGBs and HAGBs show an increase (25.94, 38.91, 52.96 %) and decrease (83.87, 74.06, 47.04 %), respectively, with the rise in the value of heat provided ($HI_{35.80}$, $HI_{66.67}$, $HI_{96.03}$). It results from a sharp temperature gradient and a high cooling rate (1434, 1179, 886 K/s). Such conditions lead to a state of non-equilibrium solidification (due to prolonged thermal exposure), favouring the formation of a high percentage of LAGBs. As a known fact, a higher percentage of HAGBs corresponds to better stability of weld joints by preventing the occurrence of cracks (Jiang et al., 2020; Shamanian et al., 2019) because dislocation motion slows down when a high percentage of HAGBs prevails, and low AGS exists, thus enhancing strength and ductility (Reyaz et al., 2024). Hence, $HI_{35.80}$ fabricated joints show better weld properties, which will be quantified in the joint strength section (section 5.2.5). Another probable reason for the variation in the LAGBs might be linked to the magnitude of residual stresses for the different weld conditions (Shamanian et al., 2020). A lower percentage of LAGBs corresponds to minimum residual stress, and its value will be discussed in the residual stress section (section 5.2.7).

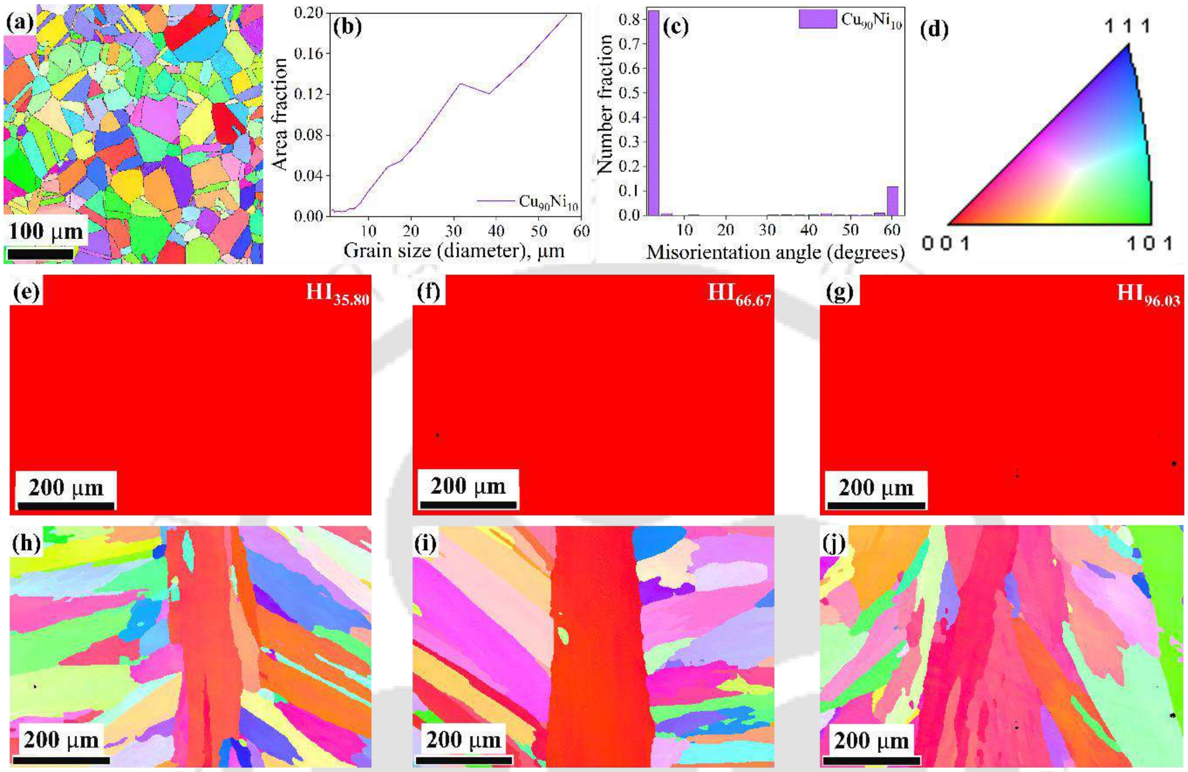

Fig. 5.6 Illustrates EBSD results for BM (a) IPF color map, (b) GS distribution, (c) misorientation angle distribution, (d) legend of IPF color map; phase map and IPF color map joints fabricated at (e, h) HI$_{35.80}$, (f, i) HI$_{66.67}$, and (g, j) HI$_{96.03}$.

The variation in the heat input values corresponds to different temperature gradients for the HI$_{35.80}$, HI$_{66.67}$, and HI$_{96.03}$ joints, resulting in the formation of equiaxed (weld center) and columnar (near the FB) microstructural morphology. Thus, the difference in heat input value contributes to the evolution of texture in the fusion zone (Kangazian and Shamanian, 2019b). Fig. 5.7(a-c) depicts the (001), (110), and (111) pole figures (PFs) for the joints HI$_{35.80}$, HI$_{66.67}$, and HI$_{96.03}$, which helps to determine the texture evolved in the FZ. As marked in the color scale bar, the magnitude of maximum texture density (MTD) increases (3.660, 6.888, 10.876) with heat supplied (HI$_{35.80}$, HI$_{66.67}$, HI$_{96.03}$), which suggests the presence of fine and consistently dispersed grains with minimal texture orientation. HI$_{96.03}$ joints exhibit the highest MTD (texture strengthening), indicating a higher extent of grain orientation (higher anisotropy). This results from a lower cooling rate (886 K/s), severely impacting the mechanical properties (Chen et al., 2024; Zhang et al., 2024). Table 5.1 summarizes the results obtained from EBSD analyses for the different weld conditions.

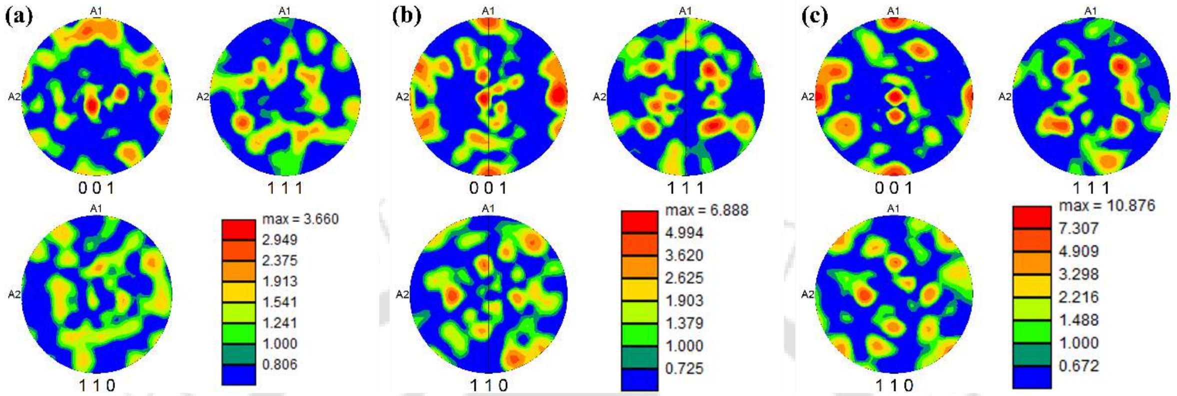

Fig. 5.7 Pole figures for joints fabricated at (a) $HI_{35.80}$, (b) $HI_{66.67}$, and (c) $HI_{96.03}$.

Table 5.1 Summarizes the EBSD results at different weld conditions.

Heat input	LAGBs (%)	HAGBs (%)	AGS (µm)	MTD
$HI_{35.80}$	25.94	74.06	39.52	3.660
$HI_{66.67}$	38.91	61.09	44.23	6.888
$HI_{96.03}$	52.96	47.04	49.26	10.876
BM: LAGBs (84.77 %), HAGBs (15.23 %), AGS (~4.73 µm)				

5.2.4 X-ray CT analysis

The optical images confirm the absence of root sagging, spatter, undercut, and lack of fusion; however, the major issue lies within the joints, for which an NDT technique is being explored. The X-ray CT scanning parameters used in the present study include 100 kV/80 µA with an exposure time of 1000 ms and a set of 1000 projection images taken for each angular location with a voxel size of 8 µm. Pore size (minimum: P_{min} and maximum: P_{max}) and the total number of pores (N_{pores}) are assessed for the joints assembled at different heat inputs. Pores of varying sizes (colors) are presented in Fig. 5.8(a-c), illustrating re-constructed 3D transparent images along the longitudinal section of the joints. The X-Y-Z coordinates correspond to the longitudinal, transverse, and thickness directions. Fig. 5.8(d-f) represents the legend corresponding to the defects shown in Fig. 5.8(a-c), where the defect volume legend shows a constant rise with heat input. The pore characteristics for the joints are represented in Table 5.2, wherein an increase in the value of the N_{pores} (16, 77, 89) and pore size (P_{min}: 8.05, 16.54, 19.87 µm/ P_{max}: 30.21, 170.92, 221.23 µm) is observed with increasing value of heat input. The emergence of pores may occur due to (a) entrapped gases, or/and (b) shrinkage cavities, or/and (c) instability of the weld region. Due to full penetration, the 'instability' criterion is eliminated; due to the spherical shape of the pores, 'shrinkage cavities' are also not a possible cause. Therefore, gas entrapment is the most predictable justification for the emergence of porosity. At a higher value of heat input ($HI_{96.03}$), chances of emergence and enhancement of pores by the coalition are increased. Meanwhile, at a lower value of heat input, the emergence of pores is restricted, resulting in minimum pore quantity and size.

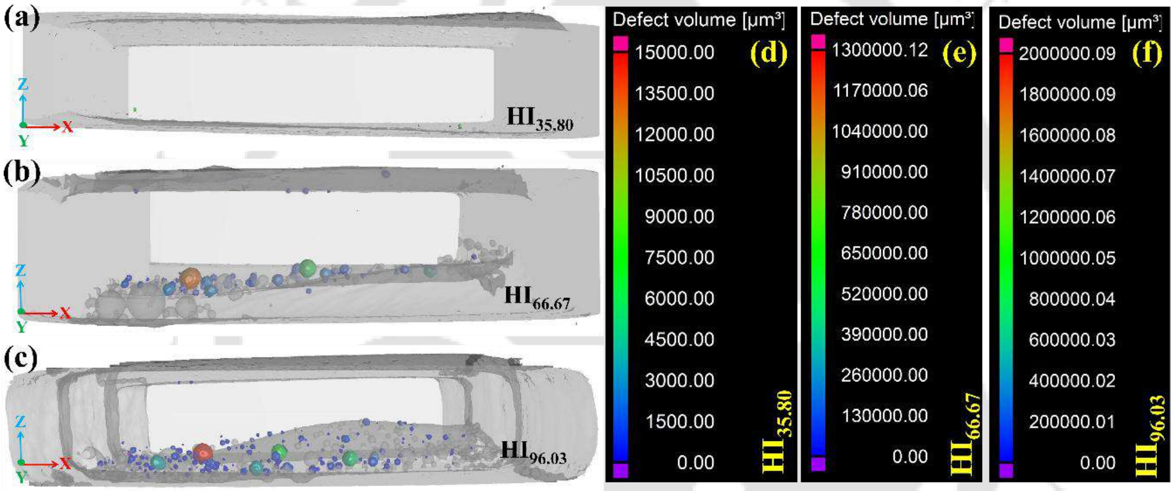

Fig. 5.8 Illustrates (a-c) re-constructed 3D transparent images along the longitudinal section and (d-f) legend illustrating the volume of defects (pores) corresponding to weld joints assembled at different weld conditions ($HI_{35.80}$, $HI_{66.67}$, and $HI_{96.03}$).

Table 5.2 Presents complete details about the pores formed at different weld conditions.

Heat input	Total number of pores	Minimum pore size (µm)	Maximum pore size (µm)
$HI_{35.80}$	16	8.05	30.21
$HI_{66.67}$	77	16.54	170.92
$HI_{96.03}$	89	19.87	221.23

5.2.5 Mechanical characterization

The characterization techniques (metallurgical evolution, grain properties, and X-ray CT) presented above do not show any quantified values regarding joint strength. Hence, a uniaxial tensile test is executed to acquire the joint properties. The tensile test is performed on test coupons (ASTM E8 standard) at 0.5 mm/min cross-head speed under ambient conditions on a universal testing machine (UTM). To ensure repeatability in the reported results, three transverse tensile coupons are tested for each weld condition, and the average value is reported. Fig. 5.9(a) represents the engineering stress-strain curve, wherein a drastic reduction in the UTS (~58 MPa) and %EL (~30 %) is observed with an increase in heat input from 35.80 J/mm ($HI_{35.80}$) to 96.03 J/mm ($HI_{96.03}$). The joint efficiency and percentage elongations are displayed in Fig. 5.9(b) and Table 5.3, which shows a reduction in the values with increased heat supplied.

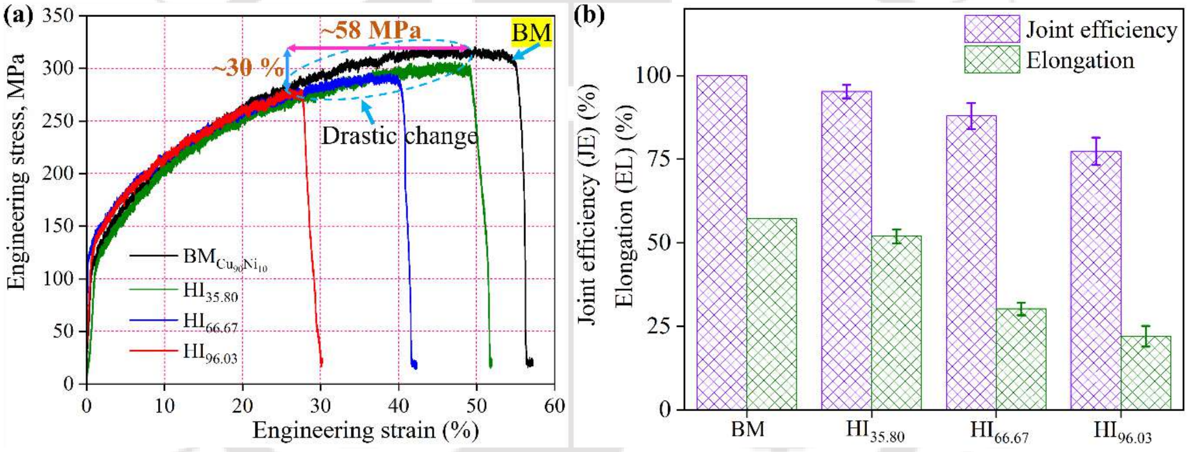

Fig. 5.9 Illustrates (a) engineering stress-strain curve and (b) joint properties for the joints fabricated at different weld conditions ($HI_{35.80}$, $HI_{66.67}$, and $HI_{96.03}$).

Table 5.3 Transverse tensile test results for the joints fabricated at different weld conditions.

Heat input	YS (MPa)	UTS (MPa)	Ductility (%)	Joint efficiency (%)
$HI_{35.80}$	124.83	306.51	51.95	95.18
$HI_{66.67}$	121.22	283.10	30.21	87.91
$HI_{96.03}$	116.46	249.20	22.02	77.39
BM: UTS (~322 MPa), YS (130 MPa), Ductility (~57.16 %)				

The decrease in the values of joint efficiency and elongations is a function of crater defect, SDAS, and porosity. An increase in the magnitude of heat supplied results in (i) more amount of metal loss (crater loss), which results in a reduction of the weld area, leading to diminished joint strength, (ii) increased SDAS values diminish the joint properties, and (iii) higher percentage of porosity present in the joints leads to sudden failure. Also, the occurrence of cracks drastically reduces the joint strength. Hence, lower heat supplied results in favourable conditions or minimizes the negative impact stated earlier. Thus, due to the presence of the least crater loss, fine and equiaxed morphology (with the least SDAS value), and minimum porosity, the joints fabricated at $HI_{35.80}$ exhibit maximum joint efficiency (~95.18 %) and highest elongation (~51.95 %).

Failure characteristics provide a lot of information about the joints, including (i) the location of the failure, (ii) the site for crack initiation, and (iii) the mode of failure. The first two (i) and (ii) characteristics can be evaluated using macro-fractography analysis, but the third feature (iii) can be explored by micro-fractography analysis. Fig. 5.10(a-c) shows the optical macro-fractography images of the joints assembled at different weld conditions, wherein the pink dotted lines show the weld centerline and the yellow lines (representing the FB) demarcate the FZ from the HAZ/BM. Failure occurs in the FZ for all weld conditions, which suggests that FZ is the weakest site for the fabricated joints. Further, the site for the crack initiation region is highlighted (green/blue/red color) in Fig. 5.10(a-c), and the enlarged version is depicted in Fig. 5.10(d-f). Fig. 5.11(a-f) corresponds to the fracture surface (FESEM images) of the joints assembled at different weld conditions ($HI_{35.80}$, $HI_{66.67}$, and $HI_{96.03}$). In Fig. 5.11(a, b), several dimples of varying depth and size can be observed for the $HI_{35.80}$ joints, which corresponds to a ductile mode of fracture that symbolizes the absorption of large deformation before failure. Fig. 5.11(c, d) characterizes the weld joint assembled at $HI_{66.67}$, showing the presence of dimples and a few micro/macro pores. Finally, Fig. 5.11(e, f) is identified with a large number of micro/macro pores for $HI_{96.03}$ joints, resulting in the lowest joint efficiency and elongation among the joints assembled at different weld conditions.

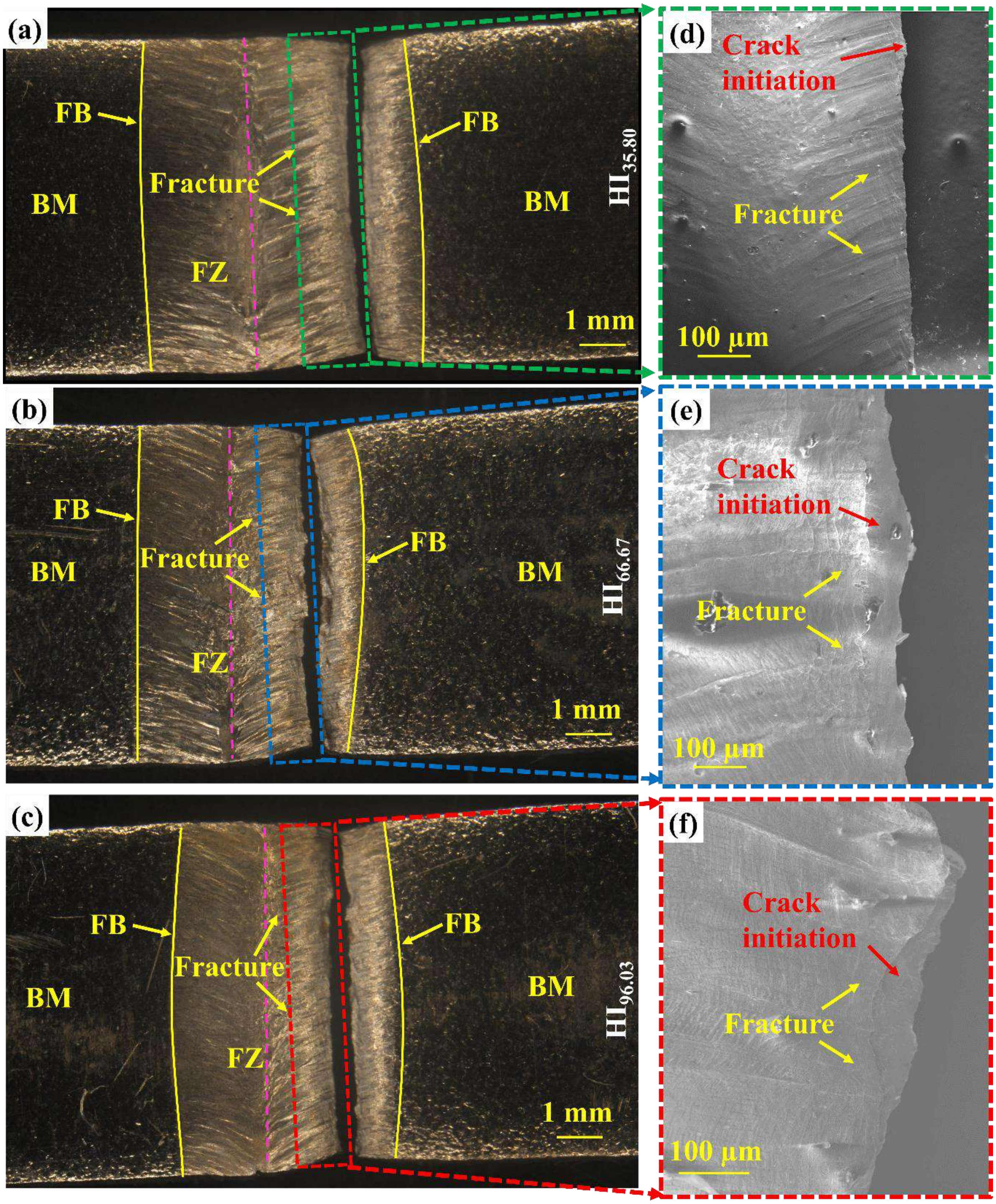

Fig. 5.10 Illustrates (a-f) failed tensile specimens for the joint assembled at different heat inputs ($HI_{35.80}$, $HI_{66.67}$, and $HI_{96.03}$).

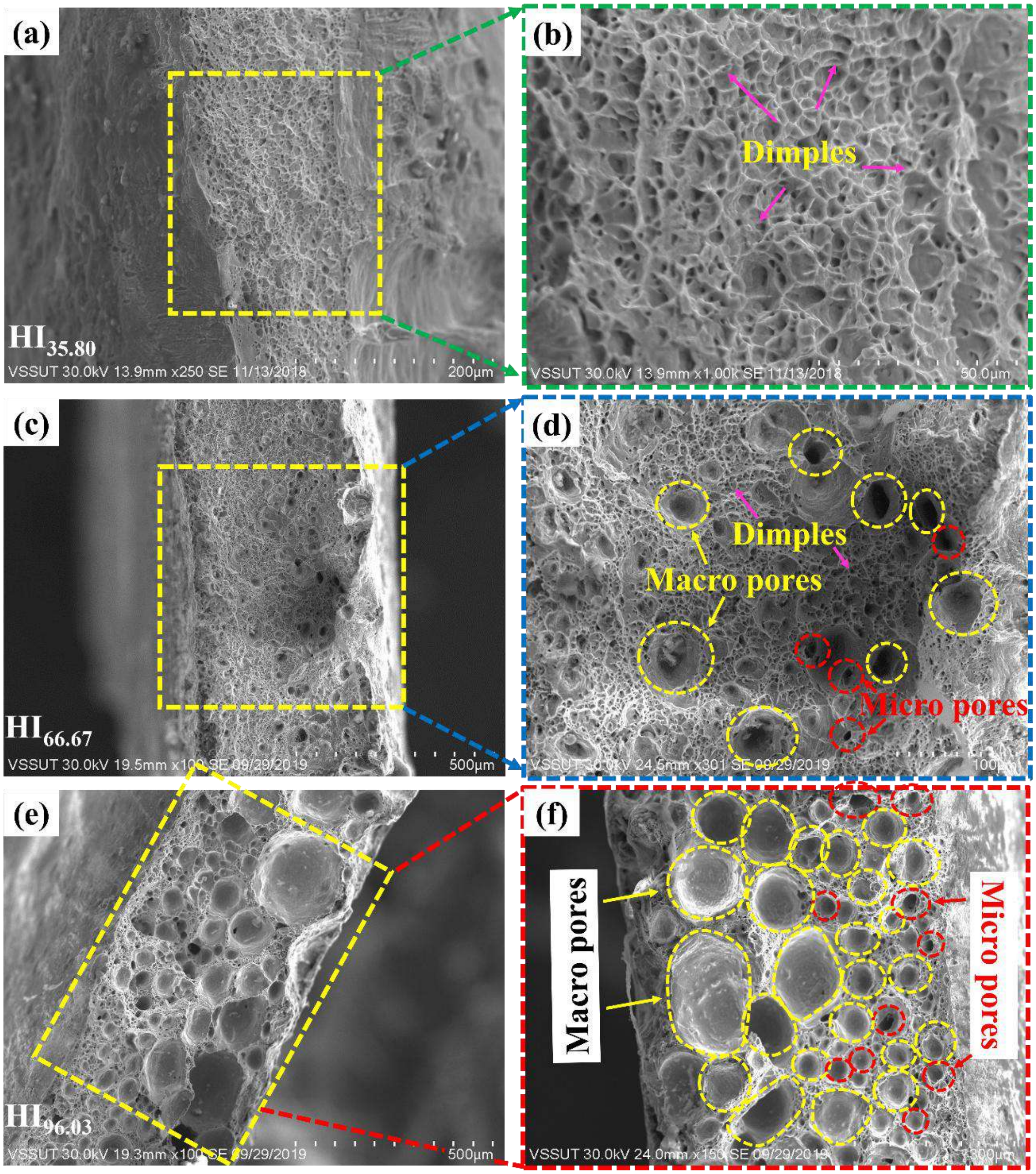

Fig. 5.11 Illustrates the fracture surface for the joints assembled at different weld conditions (a, b) $HI_{35.80}$, (c, d) $HI_{66.67}$ and (e, f) $HI_{96.03}$.

The ASTM E384 standard is followed for determining microhardness using the Vickers hardness test. Test coupons extracted across the weld direction are mirror-polished and subjected to 300 gf force with a dwell interval of 10 s. Microhardness testing is carried out to obtain the Vickers Hardness Number (VHN) for the entire joint, and the obtained data results are plotted as shown in Fig. 5.12. The VHN follows the sequence in decreasing order as BM

> FB > FZ > HAZ. The lowest VHN values are obtained in the HAZ due to deformed grains, while the FZ exhibits higher VHN values due to fine equiaxed grains. Due to the higher cooling rate, the value of VHN near the FB is greater than the FZ. The magnitude of the VHN in the BM remains highest because it is unaffected by the heat flux. The average VHN value obtained for the different regions varies as 122-130 $HV_{0.3}$ (FZ), 130-136 $HV_{0.3}$ (FB), and 117-121 $HV_{0.3}$ (HAZ). For easy understanding, the VHN values of the BM, FZ, HAZ, and FZ for the joints ($HI_{35.80}$, $HI_{66.67}$, $HI_{96.03}$) are highlighted in boxes of different colors in Fig. 5.12. The overall VHN profile shows a 'sinking effect' in the FZ (Ferro et al., 2005), which leads to deteriorated properties in the FZ compared to the BM. The VHN value in the FZ and FB is found to be highest for least heat-supplied welds ($HI_{35.80}$) due to finer morphology produced as a result of high cooling rate (1486 K/s), whereas $HI_{96.03}$ joints comprise coarser morphology due to low cooling rate (886 K/s). The VHN value in the HAZ decreases with the increase in heat supplied. Such observation is due to higher heat input, leading to a lower cooling rate and allowing a longer grain growth duration. Past researchers have reported a similar trend in the VHN for CuNi alloys (Chakravarthy et al., 2014; Ferro et al., 2005).

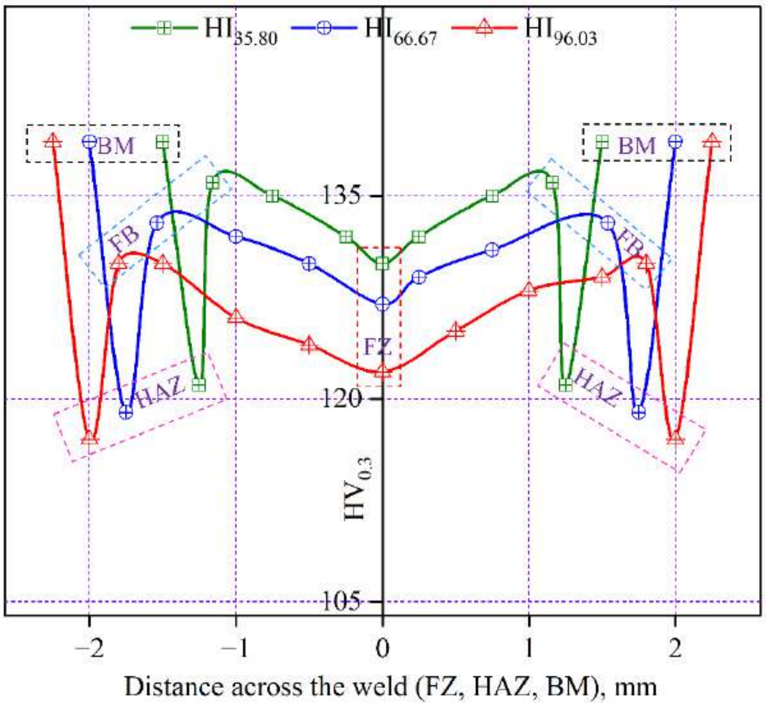

Fig. 5.12 Represent VHN variation for the joints fabricated at $HI_{35.80}$, $HI_{66.67}$, and $HI_{96.03}$.

5.2.6 Corrosion assessment

The affinity of the joints when exposed to corrosive environments determines the chemical stability, which is accomplished using a 3-electrode arrangement (FZ of $Cu_{90}Ni_{10}$ joints is considered as the working electrode, Ag/AgCl is used as reference electrode, and Platinum is used as counter electrode) system to perform the potentiodynamic polarization evaluation (PPE) in a 3.5 wt. percentage NaCl solution (corrosion test environment). The data extracted from the PPE is used to generate the Tafel plot, which provides vital information (E_{corr} denotes potential (V), I_{corr} represents symbolizes current density ($A.cm^{-2}$), E_p signifies passivation voltage (V), and I_p stands for passivation current density ($A.cm^{-2}$)). Generally, I_{corr} governs the corrosion rate, and E_{corr} suggests the tendency for the occurrence of corrosion. However, for the materials where the formation of a passive layer occurs, the value of I_p should be considered to judge the corrosion resistance (Sahu et al., 2024), wherein I_p reflects the current value at which the passive layer attains stability. A lower value of I_p signifies a reduction in the dissolution rate of the passive layer (enhanced corrosion properties) (Sichani et al., 2024).

Fig. 5.13(a) illustrates the Tafel plot for the $HI_{35.80}$, $HI_{66.67}$, and $HI_{96.03}$ joints, wherein the lower part (potential: -1.22 to 0.44 V) of the curve shows an active behaviour, in which the corrosion proceeds without any hindrance. However, the top part (potential: 0.45 to 0.95 V) of the curve (highlighted in a black dotted box) demonstrates a passive response. The passive response is linked to the formation of the passive layer, which is associated with the deposition of corrosion products. As the potentiodynamic polarization test begins, the corrosion accelerates due to the absence of any obstruction or passive (protective) layer. As time goes by, corrosion products form and accumulate on the exposed weld surface. These accumulated corrosion products act as a passive (protective) layer, which restricts the corrosive environment from direct contact with the exposed surface, and further corrosion is restricted. However, for different materials, a similar effect of corrosion products acting as a passive (protective) layer has also been reported in the past literature (Rahimi et al., 2021). The basic idea of a passive layer is that with the application of the potential, the variation in the current density is negligible. From the passive layer, the value of I_p shows a constant rise (0.411, 0.851, 1.445 $\mu A.cm^{-2}$) with increasing heat supplied ($HI_{35.80}$, $HI_{66.67}$, $HI_{96.03}$), which conveys $HI_{96.03}$ joints to be the least and $HI_{35.80}$ joints to be utmost chemically stable. The above discussion does provide the basic idea behind the stability of the passive layer (formed due to the deposition of corrosion products), but the physics of the process can better be realized by understanding the influence of surface roughness (R_a) on the passive layer stability.

The corrosion behaviour of metals relies on several factors, such as electrolyte, temperature, impurities, and surface roughness (Toloei et al., 2013). However, for CuNi alloys, the corrosion behaviour can be better understood by examining the stability of the passive layer (Ezuber and Al Shater, 2016). For the metals where a passive layer exists, a smooth surface (low R_a value) allows the formation of a stable passive layer (deposition of corrosion products), which obstructs the corrosive environment with the unreacted material (Toloei et al., 2015). As the amount of heat provided increases, the magnitude of surface roughness ($R_{a,}$ µm) at the weld surface also shows an upward trend with values ~0.399 ($HI_{35.80}$), ~2.76 ($HI_{66.67}$), and ~5.01 µm ($HI_{96.03}$). The rise in the value of R_a is linked with intense disturbance (agitation) arising as a result of extended exposure during the heating period. As the amount of heat provided increases, the heating period exists for a longer duration, allowing more surface disparities to form, due to which the value of R_a shows a constant rise. As a result of an increase in the value of R_a (~0.399, ~2.76, ~5.01 µm), the chances of forming a stable passive (protective) layer decrease. Thus, the joints fabricated at $HI_{96.03}$ condition demonstrate the least corrosion resistance. A smooth surface (low R_a value) allows the formation of a stable passive layer (deposition of corrosion products), leading to the highest corrosion resistance. Hence, it can be concluded that the passive layer formed at low heat input conditions is more protective than that of high heat input conditions. Also, with increased heat supplied value, E_{corr} approaches towards a more negative value (−236.6, −298.1, −342.5 mV), and I_{corr} also follows an increasing trend (1.147, 1.165, 2.959 $\mu A.\,cm^{-2}$). The values of E_{corr} and I_{corr} suggest a decrease in corrosion resistance with increased heat supplied. Fig. 5.13(b-d) depicts the corrosion products forming a protective layer on the surface of the exposed region for the different weld conditions ($HI_{35.80}$, $HI_{66.67}$, and $HI_{96.03}$), whereas Fig. 5.13(d) exhibits corrosion products formed around the crack formed during solidification. Table 5.4 details the extracted corrosion test results (I_{corr}, E_{corr}, and I_p) from Fig. 5.13(a) for different weld conditions.

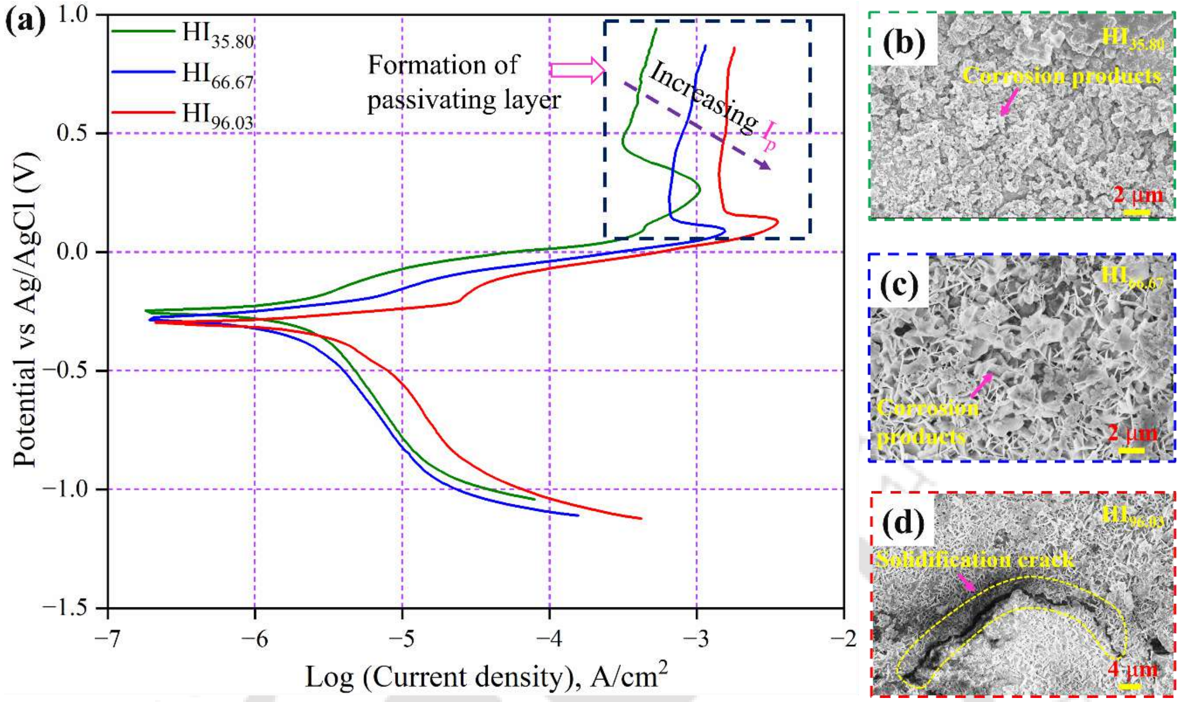

Fig. 5.13 Represents (a) the Tafel plot and (b-d) corrosion products formed in the joints fabricated at different weld conditions (HI$_{35.80}$, HI$_{66.67}$, and HI$_{96.03}$).

Table 5.4 Presents the corrosion test results for different weld conditions.

Weld conditions ⟶	HI$_{35.80}$	HI$_{66.67}$	HI$_{96.03}$
I$_{corr}$ (μA. cm^{-2})	1.147	1.165	2.959
E$_{corr}$ (mV)	−236.6	−298.1	−342.5
I$_p$ (μA. cm^{-2})	0.411	0.851	1.445
Working electrode: FZ of Cu$_{90}$Ni$_{10}$ joints, Reference electrode: Ag/AgCl, Counter electrode: Platinum, Corrosion media: 3.5 wt. percentage NaCl solution			

5.2.7 Residual stress and distortion analysis

The generation of residual stress and distortion has a detrimental influence on the welded component. Generally, the value of the S22 component of stress is significantly lower than the S11 component. Hence, the present study focuses on the S11 stress component in the longitudinal and transverse directions. The magnitude of stress (S11) along the weld (top surface) for the different weld conditions (HI$_{35.80}$, HI$_{66.67}$, and HI$_{96.03}$) is depicted in Fig.

Indian Institute of Technology Guwahati

5.14(a). The stress value remains constant (evenly distributed) between X ~17 to ~123 mm for all the weld cases except at the start and finishing points, where the stress value is negative/compressive. Compressive stress is observed because the FZ remains in a tensile stress state (during the heating cycle), and afterward (during the cooling cycle), the FZ encounters contraction. Thus, the fusion zone remains plastically deformed to retain the initial linear dimension. It is essential to mention that the maximum value of the S11 stress component shows an increase (101.4, 126.4, and 185.2 MPa) with the rise in the heat supplied ($HI_{35.80}$, $HI_{66.67}$, and $HI_{96.03}$). The justification lies in the fact that higher heat flux corresponds to greater melting of the BM, followed by extensive contraction ($\alpha \sim 16 \times 10^{-6}\ K^{-1}$), resulting in higher magnitude of stresses. The value of the S11 stress component for the $HI_{35.80}$ and $HI_{66.67}$ lies within the YS_{BM} (~130 MPa, yield strength of base metal). Meanwhile, for the $HI_{96.03}$ joints, the S11 stress value is significantly higher than the YS_{BM}. As a known fact, residual stress enhances the crack susceptibility (Liu et al., 2023), leading to cracking in the fusion zone during solidification. The stress distribution (S11 represents longitudinal/along the weld/x-direction stress) for the $HI_{35.80}$ welded component is highlighted in Fig. 5.14(b). From the legend color bar (S11), the different types/natures of the stress can be observed that exist near (tensile) and away (compressive) from the FZ. The co-existence of the tensile and compressive stresses in the welded component ensures the structural stability.

The magnitude of stress (S11) across the weld for the different weld conditions ($HI_{35.80}$, $HI_{66.67}$, and $HI_{96.03}$) is depicted in Fig. 5.14(c). S11 (FZ) values are predicted numerically, measured experimentally, and the percentage error is determined as 101.4 MPa, ~107±6 MPa, 5.23% ($HI_{35.80}$); 126.4 MPa, ~129±8 MPa, 2.01% ($HI_{66.67}$); and 185.2 MPa, ~192±9 MPa, 3.54% ($HI_{96.03}$). The magnitude and nature of the stress vary from a maximum value in the FZ (tensile) to a minimum value (compressive) away from the FZ. The S11 (across the weld) shows a gradual decrease with increasing distance from the FZ with values of 53.25, 65.20, 84.64 MPa (~3 mm from weld centerline), and −22.79, −40.35, −92.25 MPa (~10 mm from weld centerline) for the $HI_{35.80}$, $HI_{66.67}$, and $HI_{96.03}$ joints. After a certain distance (~20 mm), the value of S11 remains constant (−30 MPa) for all the weld cases. Thus, the above data suggests a sudden decline in the stress value near the FZ (~3 mm) and remains constant far away (~20 mm) from the FZ. The presence of a tensile type of stress near the FZ results from a constricted plasma arc falling in a narrow region, which causes a low-temperature gradient.

It is to be noted that a wide gap exists in the magnitude of tensile and compressive stress types, which suggests that stress remaining in a welded component is predominantly due to longitudinal stress and the primary cause for the generation of deflection in the thin sheets.

The amount of distortion present in a joint is measured using a coordinate-measuring machine (CMM). Fig. 5.14(d, e) illustrates the image of the welded sample ($HI_{96.03}$), where deflection (transverse deflection shows an upward V-shape and longitudinal deflection follows an inward concave shape) is prominently noticeable, and the measured values of deflection along with numerical data is compared in Fig. 5.14(f, g). Fig. 5.14(f) illustrates the comparison between the experimental and numerical values for the deflection across the weld direction ($U_{(y)}$). As the shape of the distorted structure resembles a V-shape, it's evident that the minimum and maximum deflection occur at the edge and center of the weld component, respectively. Fig. 5.14(g) depicts the deflection along the weld direction ($U_{(x)}$). The contour of the distorted component corresponds to an inward concave/outward convex shape, which causes the minimum and maximum deflection to occur at the edge and center of the weld component, respectively. The maximum value of deflection is predicted as −1.06, −1.27, and −1.45 mm for the joints $HI_{35.80}$, $HI_{66.67}$, and $HI_{96.03}$, respectively, and the maximum percentage error is calculated as 5.91 %, 4.29 %, 6.44 % for $U_{(y)}$ and 10.96 %, 8.48 %, 7.42 % for $U_{(x)}$, which is highlighted in Fig. 5.14(f, g). A maximum error of ~10.96 % achieved implies the reliability of the FE model.

In Fig. 5.14(f, g), the critical feature to be noted is the obtained value of deflection for the joints is in the negative direction (Z-axis), and an insignificant magnitude of deflection is reported towards the extreme edge of the sheets. The above situation arises due to BC's implementation (shown in Fig. 4.5 of Chapter 4), wherein movement in the thickness direction is restricted ($Z = 0$) at the edges but not at the start of the welding ($Z \neq 0$). Hence, it deforms without restriction to release the stress during the cooling cycle. It is essential to recognize that the value of distortion (across the weld) is identified to be maximum for the highest heat-supplied condition ($HI_{96.03}$). The possible explanation is that extensive induction of plastic/permanent strain exists due to high heat supplied, which stays even after the cooling cycle. Further, with the withdrawal of clamps, the strain modifies to permanent distortion.

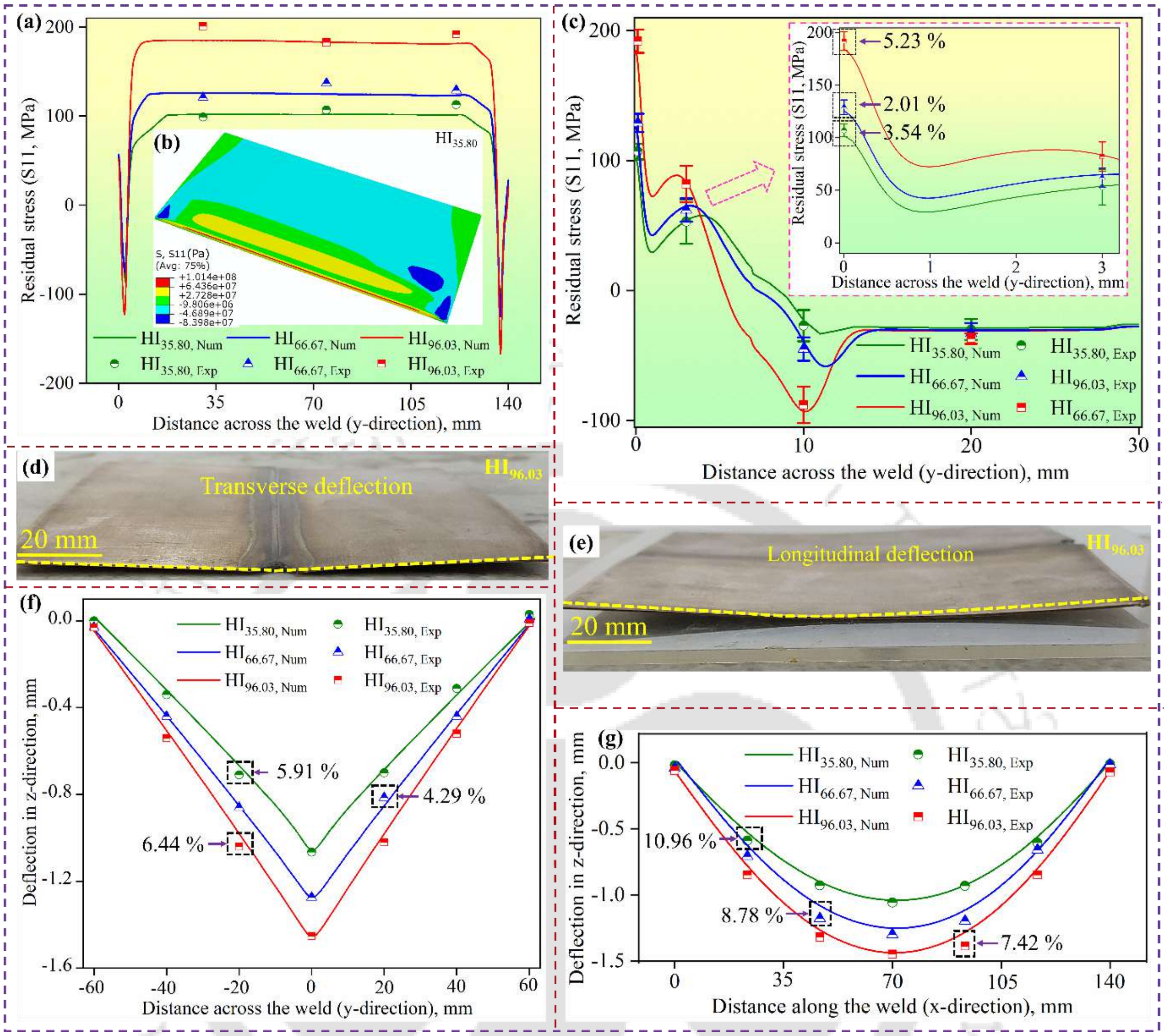

Fig. 5.14 Illustrates (a) S11 stress along the joints, (b) S11 stress distribution for HI$_{35.80}$ joint, (c) S11 stress across the joints; (d, e) actual distortion pattern, and validation of distortion data (f, g) across and along the weld joints for HI$_{35.80}$, HI$_{66.67}$, and HI$_{96.03}$ weld conditions.

5.2.8 Discussion on the effect of current pulsation

The above discussion on the impact of heat supplied to fabricate Cu$_{90}$Ni$_{10}$ joints recommends the application of low heat input (HI$_{35.80}$), which provides several positive effects on the joints. Hence, implementing pulsed current (PC) can further enhance the joint properties. A PC-M-PAW with parameters I_p (peak current) ~ 21.5 A, I_b (base current) ~ 29 % of I_p, t_{on} (arc on time) ~ 0.39 s, t_{off} (arc off time) ~ 0.89 s are combined to supply a 35.50 J/mm heat (HI$_{35.50,\ PC}$) to join Cu$_{90}$Ni$_{10}$ thin sheets. To understand the improvement in joint properties using pulsed current, a comparison is made between the lowest heat supplied in continuous and pulse conditions, i.e., $HI_{35.80,\ CC}$, and $HI_{35.50,\ PC}$, respectively.

The impact of pulsed current is illustrated in Fig. 5.15(a-g). Fig. 5.15(a) depicts the IPF map, which signifies the grain details with different orientations and morphology. Grain refinement is achieved from 39.52 ($HI_{35.80,\ CC}$) to 35.53 µm ($HI_{35.50,\ PC}$), which adds to one of the factors responsible for the increase in joint strength. Fig. 5.15(b) illustrates the PFs for the $HI_{35.50,\ PC}$ joints with an MTD value of 2.140, lower than $HI_{35.80,\ CC}$ (3.660), which improves the joint properties. With the use of a pulsed current, the value of the cooling rate increases from 1434 to 1543 K/s, resulting in finer SDAS (as per Eq. (5.2)), leading to enhanced weld characteristics. The orientation of the grains in the fusion zone can be understood by the 'crystal rain' mechanism, in which implementation of pulsed current corresponds to intermittent variation in the Lorentz force, which leads to intermittent agitation in the weld pool. During the cooling (solidification) phase, the newly generated grains have no preferential orientations. Thus, the crystal rain mechanism contributes towards the evolution of texture in the fusion zone of $HI_{35.50,\ PC}$ joints (Kangazian and Shamanian, 2019b). Fig. 5.15(c-f) presents the microstructural features with relatively smaller equiaxed and columnar structures due to a limited time available for growth (due to a higher cooling rate, 1543 K/s). Fig. 5.15(g) compares the stress-strain curve for the $HI_{35.80,\ CC}$, and $HI_{35.50,\ PC}$ joints, wherein grain refinement and finer SDAS are the primary reasons for the improvement in joint efficiency from 95.18 to 99.44 % (~100 %).

The above-discussed benefits of PC can better be reviewed by understanding the mechanics of the process. The basic theory is based on the fact that the I_p is applied for a specific duration (t_{on}), and for the rest of the part (t_{off}), the arc does not provide any heating effect (I_b). Due to the discontinuous application of the arc, pulsed current promotes reduced heat input, enhanced solidification properties, which result in detachment and re-melting of dendrites, and improved metal flow, leading to grain refinement.

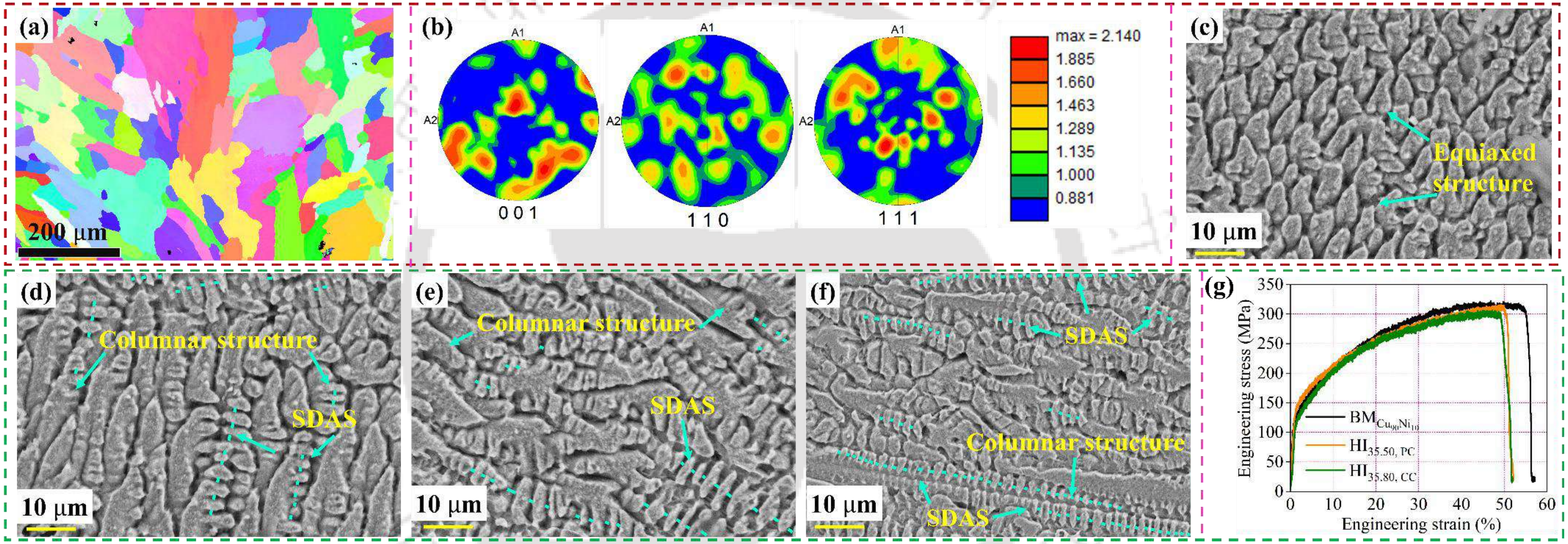

Fig. 5.15 Presents the influence of pulse current on $Cu_{90}Ni_{10}$ joints, illustrating (a) IPF map, (b) PF map, (c-f) microstructure in the FZ, and (g) engineering stress-strain curve.

5.3 Gas tungsten arc welding of dissimilar ferrous and non-ferrous metals

The difficulties in dissimilar joining include differences in their melting point, thermal conductivity, coefficient of thermal expansion, specific heat capacity, and limited solubility (Gavrish and Perig, 2020). Materials having a wide variation in the coefficient of thermal expansion value (α_{Cu}: 2.4 × 10^{-5} K^{-1}, α_{SS304}: 1.8 × 10^{-5} K^{-1} (Singh et al., 2020)) fail during solidification (crack formation (Meng et al., 2019)) or in the course of service usage (thermal fatigue). Differences in the melting point and thermal conductivity value (MP_{Cu}: 1357 K (Zhu et al., 2024), MP_{SS304}: 1727 K (Diegel et al., 2023, p. 304)) results in the prior melting of one material compared to another (Magnabosco et al., 2006). A higher thermal conductivity value of copper (398 W/mK (Zhu et al., 2024)), compared to SS304 (16.3 W/mK (ElSheikh et al., 2022)), hinders reaching the melting point temperature of copper (Kar et al., 2018). Also, poor solid solubility between Cu (13 wt. % in γ-Fe at 1420 ℃; 2 wt. % in α-Fe at 860 ℃ (Tosto et al., 2003)) and Fe (3.5 wt. % in Cu at 1085 ℃ (Tosto et al., 2003)) always remains an additional concern that promotes liquid separation at the steeper cooling rate (Kar et al., 2016). Due to compositional differences of the materials, macro-segregation (solute segregation) may materialize near the fusion boundary (FB) or away from the FB (in the fusion zone, FZ). Macro-segregation corresponds to degradation of the weld properties, including corrosion resistance, stress-corrosion cracking, reduction in toughness, and hydrogen cracking (Soysal et al., 2016). Contrary to the joining of titanium-aluminium, copper-aluminium, and steel-titanium, copper-steel joining is considered less complicated due to the non-existence of intermetallic compounds (IMCs) (Kuryntsev and Shiganov, 2018). Thus, researchers prioritize the copper-steel combination.

Beam offset (towards the SS-side) assists in modifying the joining mode from fusion welding to weld brazing. The weld-brazing mode involved limited melting (dilution) of Cu in the FZ, along with the occurrence of solidification cracks (Joshi and Badheka, 2019). Joints fabricated at optimum offset value (0.5-1.0 mm, towards Cu-side) led to defect-free Cu-SS joints, with failure occurring in the Cu-base metal. The offset value lower than 0.5 mm contributed to a decline in joint properties (Meng et al., 2019). Joints fabricated with beam oscillation demonstrated better weld properties with minimum defects (64 pores) in contrast to joints assembled without beam oscillation (115 pores). Implementing beam oscillation allowed enhanced mixing of copper and steel, which also aided in the backfilling of microcracks (Kar et al., 2016, 2018). Copper plates were subjected to pre-heating, and the joint was suitably designed to compensate for the differences in the thermal properties of Cu and SS (Shiri et al., 2012). Beam offset was identified as the most dominant factor (among laser power, speed, and beam offset) that governs the joint strength of the fabricated bimetallic joints. Joint properties illustrated maximum (261 MPa) and minimum strength (66 MPa) for the welds prepared with beam offset towards the Cu-side and SS-side, respectively (Sahul et al., 2020). Arc offset (0-3 mm, towards Cu) was implemented to join Cu and SS in the butt configuration. At 1.25 mm arc offset, joint strength of 194 MPa and 83.62 % elongation was achieved. In contrast, the melting of copper was restricted with smaller offset values (0-0.75 mm), and defects (hot cracks, porosity, and LOF) were reported for the arc offset values beyond the optimal range (1.0-2.50 mm) (Singh et al., 2020, 2021). Implementation of modest beam offset (0.2 mm SS to 1 mm Cu) resulted in enhanced joint performance due to restricted HAZ and limited defects in the FZ. Meanwhile, increased beam offset led to a deterioration in joint quality (Guo et al., 2016).

Despite significant differences in the melting points of Cu and SS, the application of high-power density of laser and electron beam enables the instant melting of materials (Magnabosco et al., 2006). In contrast, implementation of EBW requires an inherent vacuum environment (Joshi and Badheka, 2019), which narrows down its application (RK et al., 2018) and the likelihood of beam deflection (due to electromagnetic surroundings (Phanikumar et al., 2005)) causes difficulty in maintaining consistent beam offset (Joshi and Badheka, 2019). Similarly, the high reflectivity of copper corresponds to an increase in the energy utilization for the LBW process (Cheng et al., 2019). On the other hand, arc-based joining techniques employ an un-constricted heat source for a longer duration, leading to an ungovernable composition of the weld joints (Cheng et al., 2020). Overall, the GTAW process remains inferior to LBW and EBW processes in terms of welding speed, penetration depth, weld quality, and productivity. Despite that, the GTAW process is widely utilized because of joint tolerance, the cost of the welding equipment, and the ease of equipment portability (Dwibedi and Bag, 2024). Additionally, the GTAW process is widely accepted for joining dissimilar materials (Rafiei and Mostaan, 2019) and is readily available compared to LBW/EBW processes (Soysal et al., 2016). Hence, the GTAW process is deemed suitable for producing defect-free Cu-SS bimetallic joints for the present experimentation. The current experimental work aims to fabricate a bimetallic joint (T2-Cu and SS304) with minimum metallurgical inhomogeneities that enhance the joint characteristics. Thus, an effort has been made to realize the importance of arc offset and joining mode in the performance of Cu-SS bimetallic joints. In the current experimentation, the three selected values of arc offset (CS_1: 1.3 mm, CS_2: 2.0 mm, CS_3: 2.7 mm) considered for the dissimilar joining of ferrous (SS304) and non-ferrous (T2-Cu) metals are highlighted in Table 3.7 of Chapter 3.

5.3.1 Cu-Fe binary phase equilibrium diagram

In the Cu-Fe binary phase diagram (Fig. 5.16), two peritectic reactions occur, one on the Cu-rich side ($L + \gamma_{Fe} \rightarrow \varepsilon_{Cu}$ at 1096 °C) and the other on the Fe-rich side ($L + \delta_{Fe} \rightarrow \gamma_{Fe}$ at 1485 °C), wherein poor solid solubility between Cu in Fe (α) and Fe in Cu (ε) exists. The solid solubility of Cu in Fe (11.5 wt. %) is greater than Fe in Cu (3.5 wt. %). Accordingly, the bimetallic joint exhibits only two major phases, i.e., α_{phase} (rich in Fe-Cr-Ni) and $\varepsilon_{\text{phase}}$ (rich in Cu) (Debin et al., 2020). No intermetallic phases exist between Cu and SS (Magnabosco et al., 2006), but intermetallic compounds (IMCs) may occur in the form of oxides (Rajendran et al., 2024). By stating the Fe-rich matrix, it is inherently understood that it is Fe-Cr-Ni-rich; hence, the Fe-rich matrix will be stated throughout the present investigation. Due to the unavailability of sufficient time for the proper mixing of Cu and SS; Cr, and Ni do not redistribute during the joining process. Therefore, the Fe-rich region is also Cr and Ni-rich (Rajendran et al., 2024). Also, as a

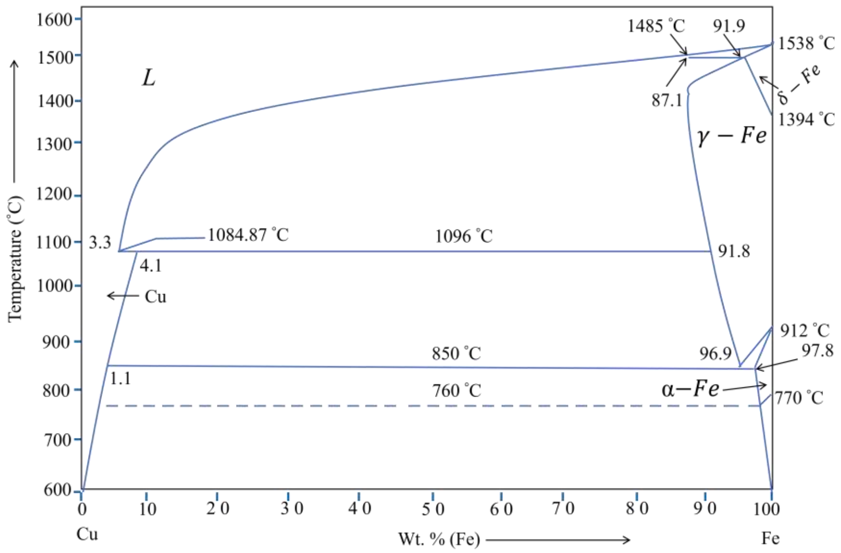

Fig. 5.16 Illustrates Cu-Fe binary phase equilibrium diagram (Guo et al., 2016).

result of color contrast, it becomes simple to distinguish between Fe-Cr-Ni rich and Cu-rich phases.

5.3.2 Microstructural analysis of CS_1 joint

At CS_1 weld condition (1.3 mm arc offset, towards Cu-side), Cu(T2) and SS304 melt completely, with the majority of the regions rich in Fe; and Cu can be observed only in the form of Cu-globules or lamellae. Fig. 5.17(a) presents the macrograph of the entire CS_1 weld joint, representing the FZ, FB, and key microstructural features (Fe-rich Island, Cu-embedded in Fe-rich Island, and fish-hook structure). Fig. 5.17(b-q) illustrates the optical and FESEM images of the Cu-SS joint fabricated under CS_1 weld conditions. Fig. 5.17(b, f, j, n, n_1) shows the SS-side FB of the Cu-SS bimetallic joints, wherein the FB (depicted in a red dotted line) serves as a partition between the FZ and the SS-base metal. Fig. 5.17(f) shows the occurrence of δ_{ferrite} (delta ferrite) dendritic structure within $\gamma_{\text{austenite}}$ (austenite) matrix in the partially melted zone (PMZ) towards the SS-side (highlighted in Fig. 5.17(n_1)), and Cu embedded in the Fe-rich matrix can be observed in the FZ near the SS-side FB. The PMZ near the SS-side FB comprises the dual-phase region ($\delta_{\text{ferrite}} + \gamma_{\text{austenite}}$). Fig. 5.17(c, g) highlights the enlarged version of a part of Fig. 5.17(f), wherein Cu embedded in the Fe-rich matrix is distinctly visible. The contrasting thermal conductivities of Cu and SS304 result in varying cooling rates near the FB of both metals, leading to primary liquid separation. As a result of primary liquid separation, Cu-rich globules (spherical phases/spherical segregation/droplet) are formed within a Fe-rich matrix (Joshi and Badheka, 2020). Fig. 5.17(d) represents the macrograph of the FZ, in which the development of Fe-rich Island (macro-segregation) can be seen. The formation of the Fe-rich Island occurs when $T_{\text{Liquidus (weld)}} < T_{\text{Liquidus (SS304)}}$ (Soysal et al., 2016). Fig. 5.17(e, h) illustrates the Cu-side FB of the bimetallic joints, in which the FB demarcates the FZ from the Cu-base metal. The molten metal penetrates the Cu-side FB, wherein the noticeable microstructural features observed are fish-hook and jagged/teeth-like structures. It may be noted that the Cu-side FB does not demonstrate a planar morphology, signifying proper metallurgical bonding between the base materials. An enlarged version of the fish-hook structure is depicted in Fig. 5.17(i). Fig. 5.17(k, l, o, p, q) demonstrates various regions in the FZ, where the distribution of Cu-particles within the Fe-rich matrix can be observed in Fig. 5.17(k), and the occurrence of long Cu-lamellae can be seen in Fig. 5.17(o-q).

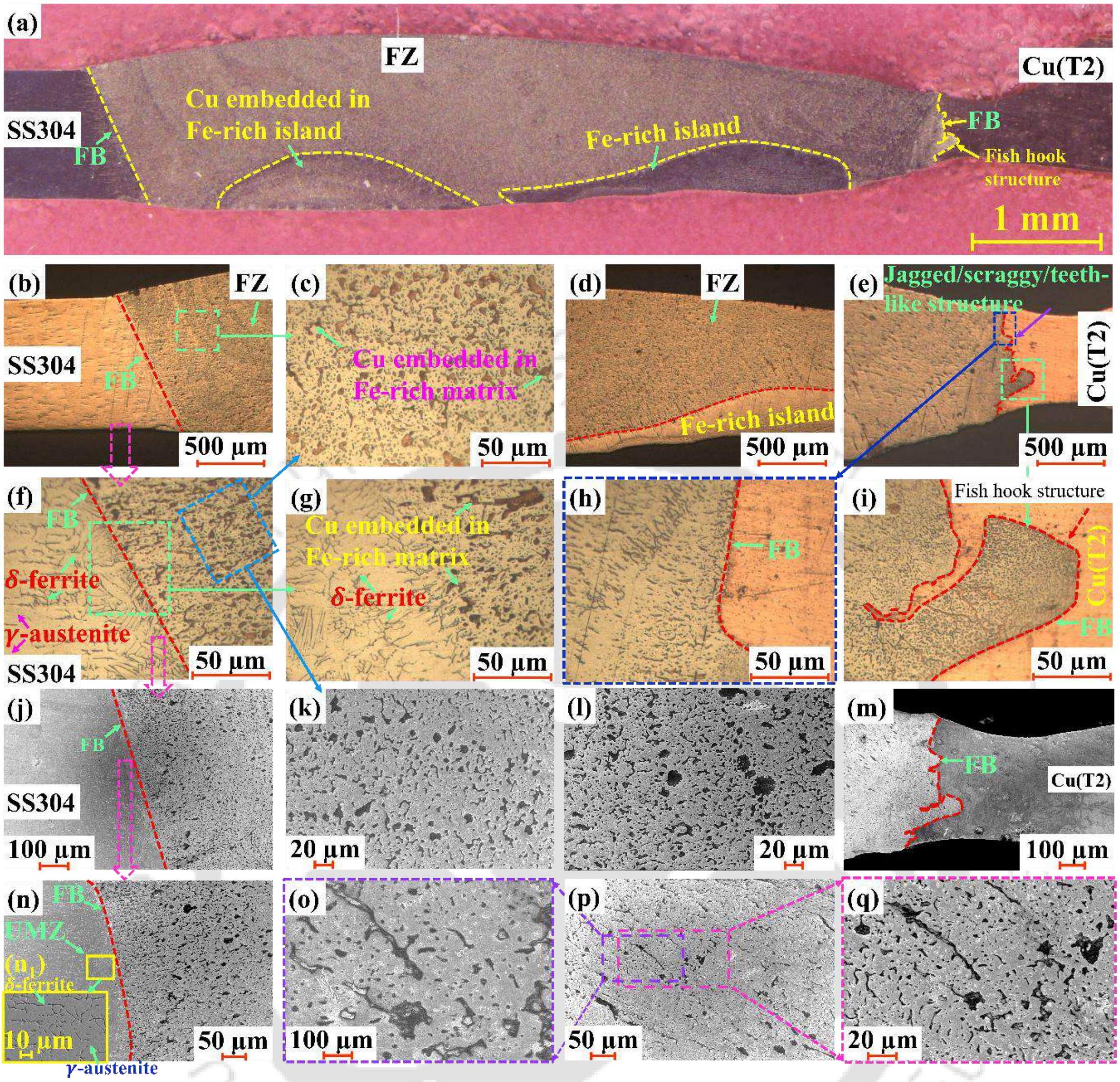

Fig. 5.17 Illustrates (a) macrograph, (b-i) optical, and (j-q) electron micrographs near the fusion boundary (SS-side, Cu-side) and fusion zone for the joints fabricated at CS_1 weld condition.

5.3.3 Elemental analysis of CS_1 joint

To identify the elemental variation within the various regions of the joint, point, line, and area mapping is carried out and represented in Fig. 5.18(a-a_5, b-b_3, c-c_5, d-d_4). Fig. 5.18(a-a_2) represents the area mapping of the FB region towards the SS-side, wherein the difference between the presence of Cu (yellow color) and Fe (cyan color) can be distinctly seen. Fig. 5.18(a_3-a_5) depicts the line EDX pattern across the FB, in which a sharp peak (Fig. 5.18(a_4)) and simultaneous decline (Fig. 5.18(a_5)) can be observed at the locations where it encounters the Cu-rich phase. Fig. 5.18(b-b_2) demonstrates area elemental analysis in the FZ, wherein Cu-rich globules (varying dimensions) can be observed in the Fe-rich matrix. Moreover, Fig. 5.18(b_3) depicts the variation of elements at three selected points (marked in Fig. 5.18(b)). The elemental composition of Cu-rich globule shows a higher wt. percentage of Cu (85.1%) at point 2, whereas higher wt. percentage of Fe is observed in the Fe-rich matrix at point 1 (Fe: 61.8%, Cr: 16.2%, Ni: 5.8%) and point 3 (Fe: 63.5%, Cr: 16.7%, Ni: 5.7%).

Fig. 5.18(c-c_3) reveals the area elemental distribution across the FB (Cu-side). The distribution of Cu and Fe can be observed with a Fe-rich region (cyan color) near the FB, followed by Cu-base metal (yellow color). Fig. 5.18(c_3-c_5) depicts line elemental variation across the FB, wherein sudden peaks and decline represent Cu (Fig. 5.18(c_4)) and Fe (Fig. 5.18(c_5)) elements, respectively. Fig. 5.18(d-d_2) represents a Cu-rich globule within a Fe-rich matrix. The majority of the Cu-globule comprises Cu (yellow color), but the presence of Fe-rich globules as secondary precipitated phases (cyan color) can be observed within the Cu-rich globule. Thus, primary and secondary liquid separation phenomena are responsible for forming Cu-rich globules and Fe-rich globules within Cu-rich globules, respectively (Haglon et al., 2024). Fig. 5.18(d_3) shows the Cu and Fe percentages in two selected points (within and outside the Cu-rich globule). Points within the Cu-rich globule comprise a higher percentage of Cu (66.5, 44.1 %), whereas point outside the Cu-globule contains a higher amount of Fe (61.5 %). However, the solubility of Cu in Fe is 11.5 wt. % and Fe in Cu is 3.5 wt. % (Debin et al., 2020), the elemental analysis results (Fig. 5.18(b_3, d_3)) exceed the theoretical value indicated in the phase diagram. The possible explanation is that an over-saturated solid solution is formed of Cu in Fe-matrix and Fe in Cu-matrix (Haglon et al., 2024).

Due to the greater melting of SS304 (on account of less arc offset), the microstructural morphology for the CS_1 joints primarily comprises the Fe-rich region throughout the FZ and near the FB (Cu-side and SS-side). Meanwhile, Cu is identified (in a low percentage) as globules, lamellae, and dendritic structures. Overall, the microstructural morphology illustrates no significant inhomogeneities except the formation of Cu-embedded in Fe-rich Island and Fe-rich Island in the FZ. The wt. percentage of Fe-Cr-Ni remains above 75% throughout the FZ (76.12 % near the SS-side FB, 77.81 % in the weld center, and 88.99 % near the Cu-side FB).

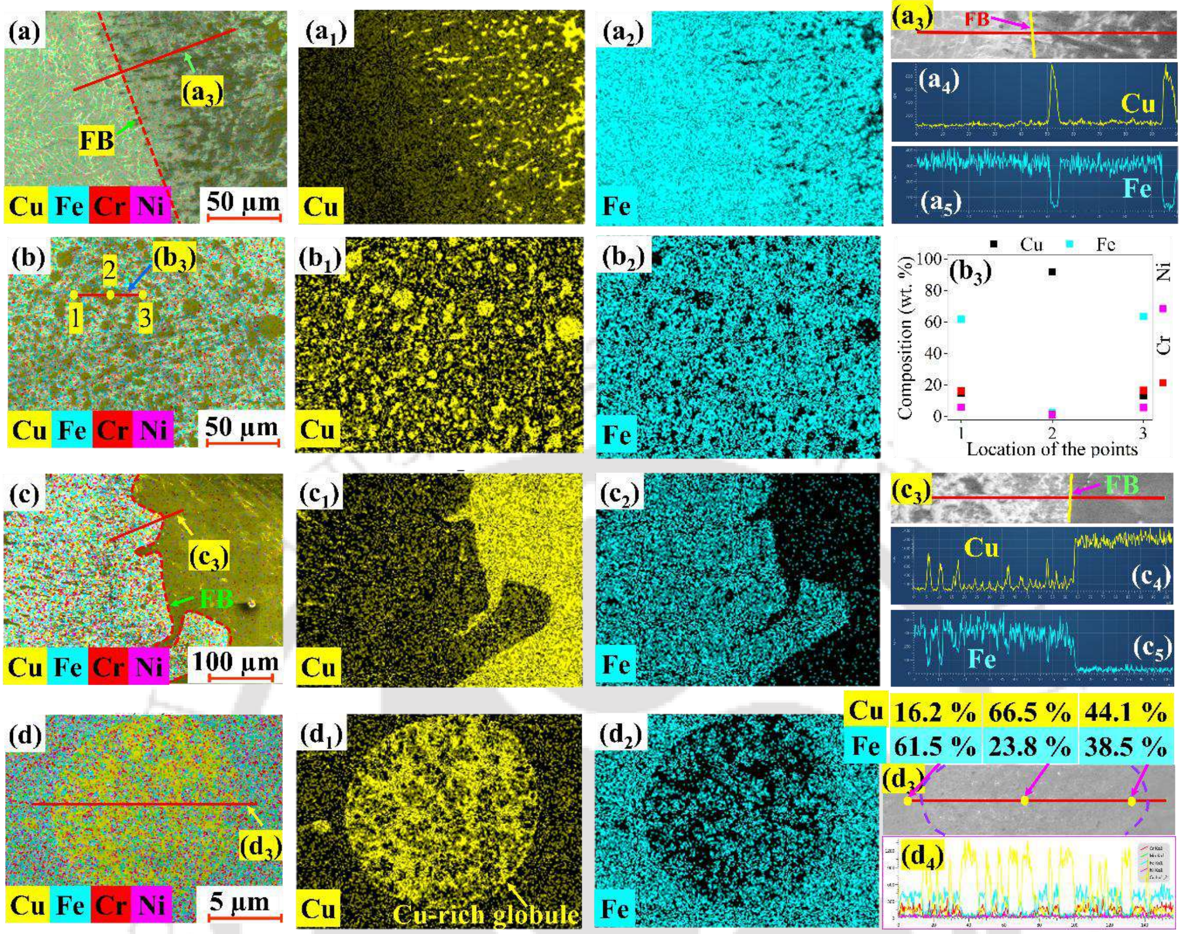

Fig. 5.18 (a-a_5, b-b_3, c-c_5, d-d_4) Illustrates elemental analysis near the fusion boundary (SS-side, Cu-side) and fusion zone for the joints fabricated at CS_1 weld condition.

5.3.4 Microstructural analysis of CS_2 joint

As the arc offset increases towards the Cu-side (2.0 mm, CS_2), it results in higher melting of Cu compared to CS_1 weld conditions. Also, the microstructural morphology displays completely different features compared to CS_1. Fig. 5.19(a) presents an overview of the macrograph of the entire CS_2 weld joint that would aid in interpreting the optical images represented in Fig. 5.19(b-m). Fig. 5.19(b-m) illustrates the optical images of the CS_2 joints near the FB (SS-side and Cu-side) and in the FZ center. Fig. 5.19(b, c, f, g) depicts the SS-side FB of the CS_2 joints, wherein features like Fe-rich globules, Fe-rich dendritic structures, and Fe-rich peninsula (macro-segregation) are formed. Formation of the Fe-rich peninsula occurs when $T_{\text{Liquidus (weld)}} < T_{\text{Liquidus (SS304)}}$ (Soysal et al., 2016). Fig. 5.19(d, h, j-l) represents the different regions in the FZ, which comprises microstructural attributes like Fe-rich globules, Fe-rich globules containing Cu-rich particles, and Fe-rich dendritic structure. Due to contrasting thermal conductivities (Cu and SS304), primary liquid separation occurs, which leads to the formation of Fe-rich globules. Whereas secondary liquid separation contributes to the formation of Fe-rich globules containing Cu-rich globules/particles (Haglon et al., 2024). Fig. 5.19(e, i, m) shows the optical images of the joints towards the Cu-side FB, in which Fe-rich globules and Fe-rich particles can be observed, but the difference lies in the size and number of Fe-rich globules. Fe-rich globules near the SS-side FB are quite large compared to Cu-side FB.

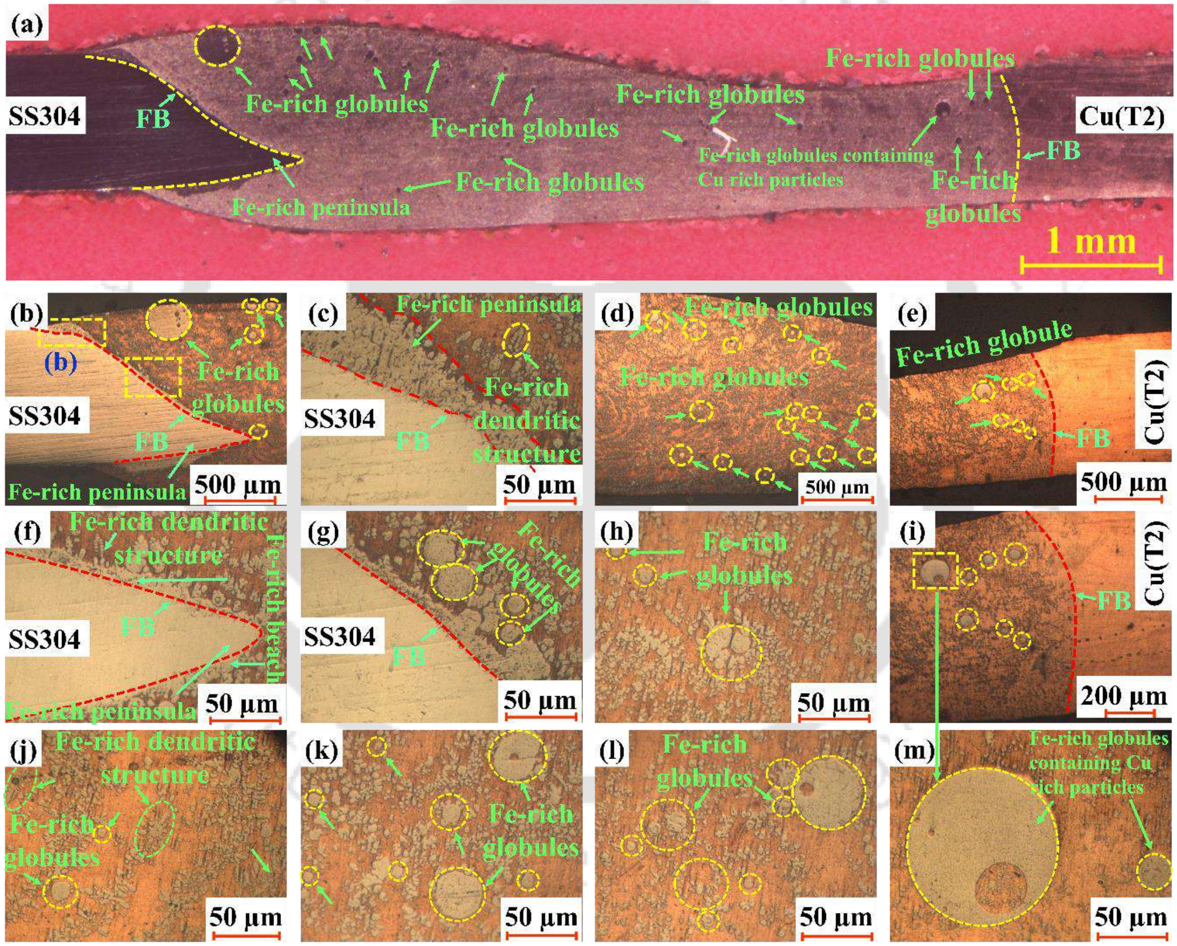

Fig. 5.19 Depicts optical (a) macrograph, (b, c, f, g) micrographs near the SS-side fusion boundary, (e, i) near the Cu-side fusion boundary, and (d, h, j-m) fusion zone center for the joints fabricated at CS_2 weld condition.

5.3.5 Elemental analysis of CS_2 joint

Fig. 5.20(a-a_5, b-b_5, c-c_3, and d-d_5) details the distribution of elemental composition in different parts of the CS_2 weld joints. Fig. 5.20(a-a_2) displays the area mapping of a Fe-rich globule (cyan color) present within the Cu-rich (yellow color) matrix. Within the Fe-rich globule, Cu-rich particles can also be observed. A line elemental analysis is represented in Fig. 5.20(a_3-a_5) to identify the elemental variation within the Fe-rich globule. It can be observed that a continuous variation (peak followed decline) exists in Cu and Fe elemental composition, which confirms the occurrence of Cu-rich particles within the Fe-rich globule. Fig. 5.20(b-b_2) depicts the area mapping of two coupled Fe-rich globules within the Cu-rich matrix. Line elemental analysis shows (Fig. 5.20(b_3-b_5)) continuous fluctuation along the entire line, thus confirming the presence of Cu-rich particles in the Fe-rich globules. Fig. 5.20(c-c_3) illustrates area mapping analysis of a Fe-rich dendritic structure within a Cu-rich matrix, wherein the wt. percentage comes out as 79.4 % (Cu) and 14.4 % (Fe). Fig. 5.20(d-d_2) shows area elemental distribution in the FZ, in which the occurrence of Fe-rich globules and Fe-rich particles can be identified within the Cu-rich matrix. To identify the Fe-rich globules within the Cu-rich matrix, the line elemental spectrum is depicted in Fig. 5.20(d_3-d_5), in which the line spectrum representing Cu (Fig. 5.20(d_4)) shows a sharp decline as it crosses the Fe-rich globule. Due to the increase in the arc offset value (2.0 mm), the amount of melting increases for Cu(T2) and decreases for SS304, respectively. Consequently, the microstructural features for the CS_2 weld condition comprise Fe-rich globules and Fe-rich dendritic structure in a Cu-rich matrix. The wt. percentage of Cu remains above 55 % throughout the FZ (61.78 % near the SS-side, 57.45 % in the weld center, and 87.26 % near the Cu-side). Both Cu and SS, melt completely, hence the joining mode for CS_2 weld conditions remains the same as CS_1 (i.e., welding).

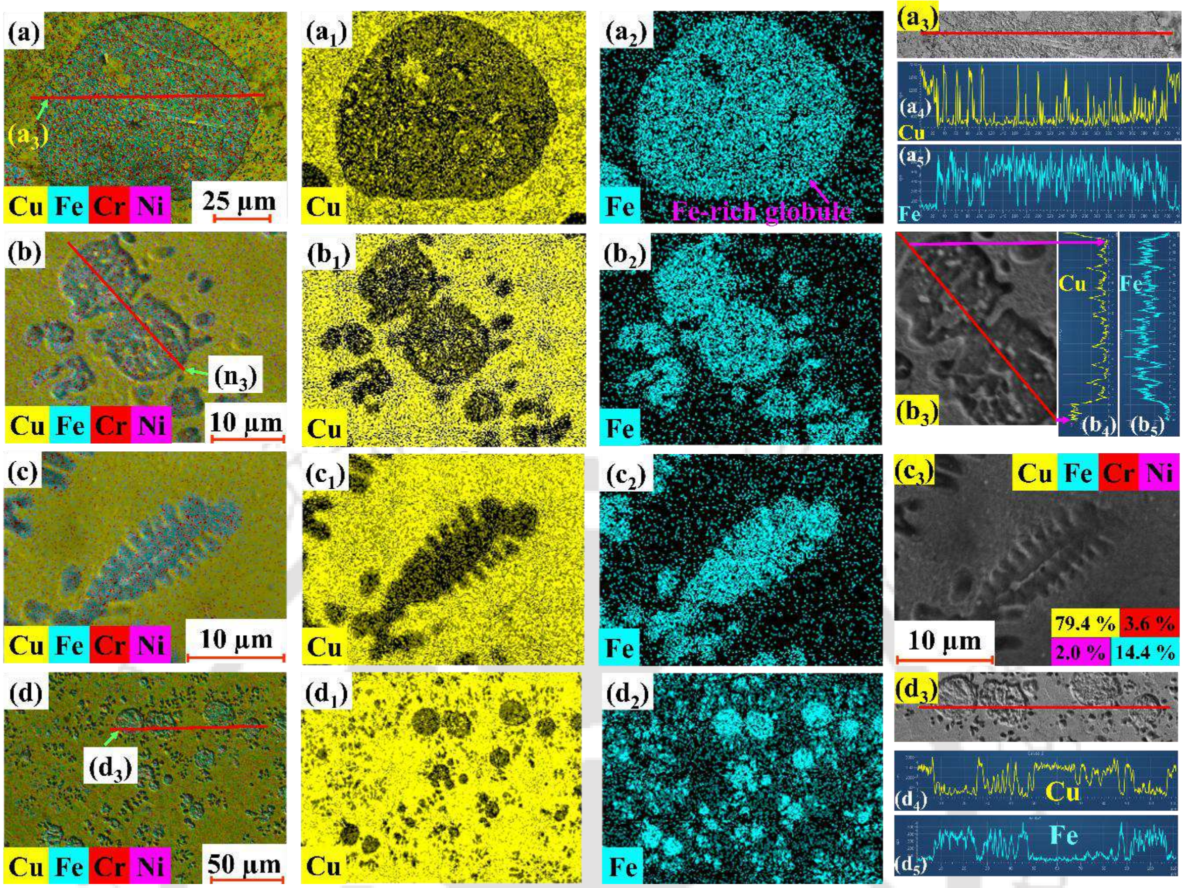

Fig. 5.20 Elemental analysis within the fusion zone illustrating (a-a_5, b-b_5) Fe-rich globule, (c-c_3) Fe-rich dendritic structure, and (d-d_5) Fe-rich globules present within Cu-rich matrix for the joints fabricated at CS_2 weld condition.

5.3.6 Microstructural and elemental analysis of CS_3 joint

As the arc offset is further increased towards the Cu-side (2.7 mm, CS_3), it results in limited melting of SS304 compared to CS_1 and CS_2 weld conditions. On account of the limited melting of SS304, the joining mode changes from welding (CS_1 and CS_2) to weld-brazing mode. A similar weld-brazing mode has been reported during the fabrication of Cu-SS bimetallic joints (Cheng et al., 2019). Also, the microstructural morphology for CS_3 joints displays completely different features compared to CS_1 and CS_2. Fig. 5.21(a) illustrates the macrograph of the CS_3 weld joint, which would aid in interpreting the micrographs represented in Fig. 5.21(b-e). It can be observed that complete melting occurs towards the Cu-side FB, whereas, near the SS-side, the FB root (bottom) region remains unmelted, and the weld cap (top) region forms a melted-unmixed zone (MUZ). Fig. 5.21(b) displays the Cu-base metal, FB, and FZ for the CS_3

joints. Fig. 5.21(b_1) provides comprehensive evidence that only melted and solidified Cu exists near the Cu-side FB, along with porosities.

Fig. 5.21(c, d) illustrates three different zones: (i) FZ, which mainly comprises solidified Cu, with Fe-rich globules and dendritic structure towards the SS-side FB, (ii) Melted-unmixed zone (MUZ, comprises melted SS304 within which Cu-rich particles and lamellae can be observed), and (iii) SS304 base metal. The MUZ (between red and yellow color dotted lines) is also described as a Fe-rich beach with Cu-rich particles and remains a part of the FZ. Fig. 5.21(e) represents the SS-side FB, wherein a planar interface corresponds to a weld-brazing mode. The upper part of the SS04 melts and forms a MUZ, whereas the root region remains unmelted, leading to weld-brazing mode. Fig. 5.21(f-j) represents the FESEM images of the microstructural features formed near the SS-side FB. Fig. 5.21(f) illustrates a Fe-rich globule within a Cu-rich matrix near the MUZ. Fig. 5.21(k-k_2) depicts the area elemental mapping of the Fe-rich globule (cyan color) surrounded by a Cu-rich matrix (yellow color). The formation of the Fe-rich beach occurs when $T_{\text{Liquidus (weld)}} < T_{\text{Liquidus (SS304)}}$ (Soysal et al., 2016).

To evaluate the percentage of Cu and Fe within and outside the Fe-rich globule, point elemental analysis is carried out. Outside the Fe-rich globule, it comprises 87.1 % Cu and 6.5 % Fe, whereas the point within the Fe-rich globule consists of 1.5 % Cu and 70.2 % Fe. Fig. 5.21(g) represents a unique microstructural feature identical to the rib cage of humans. A similar rib cage-type microstructural feature has also been reported in the past literature (Siddiquee et al., 2023). Fig. 5.21(l-l_2) confirms the presence of a Fe-rich (cyan color) rib cage structure within the Cu-rich (yellow color) matrix. Fig. 5.21(h, i) represents the MUZ formed near the SS-side FB. Some part of the MUZ resembles a unique feature identical to a cow hump. The corresponding area elemental analysis is depicted in Fig. 5.21(m-m_2) and Fig. 5.21(n-n_2), in which the MUZ primarily comprises a Fe-rich matrix containing Cu-rich particles and lamellae. Fig. 5.21(j) depicts the FESEM images near the bottom part of the SS-side FB, wherein brazing mode prevails. Area elemental analysis is shown in Fig. 5.21(o-o_2) to confirm the occurrence of brazing mode. It can be distinctly observed from Fig. 5.21(o_1-o_2) that no inter-mixing occurs between Cu(T2) and SS304. Cu(T2) melts completely and gets solidified, whereas no melting occurs in the SS-side root (bottom) region.

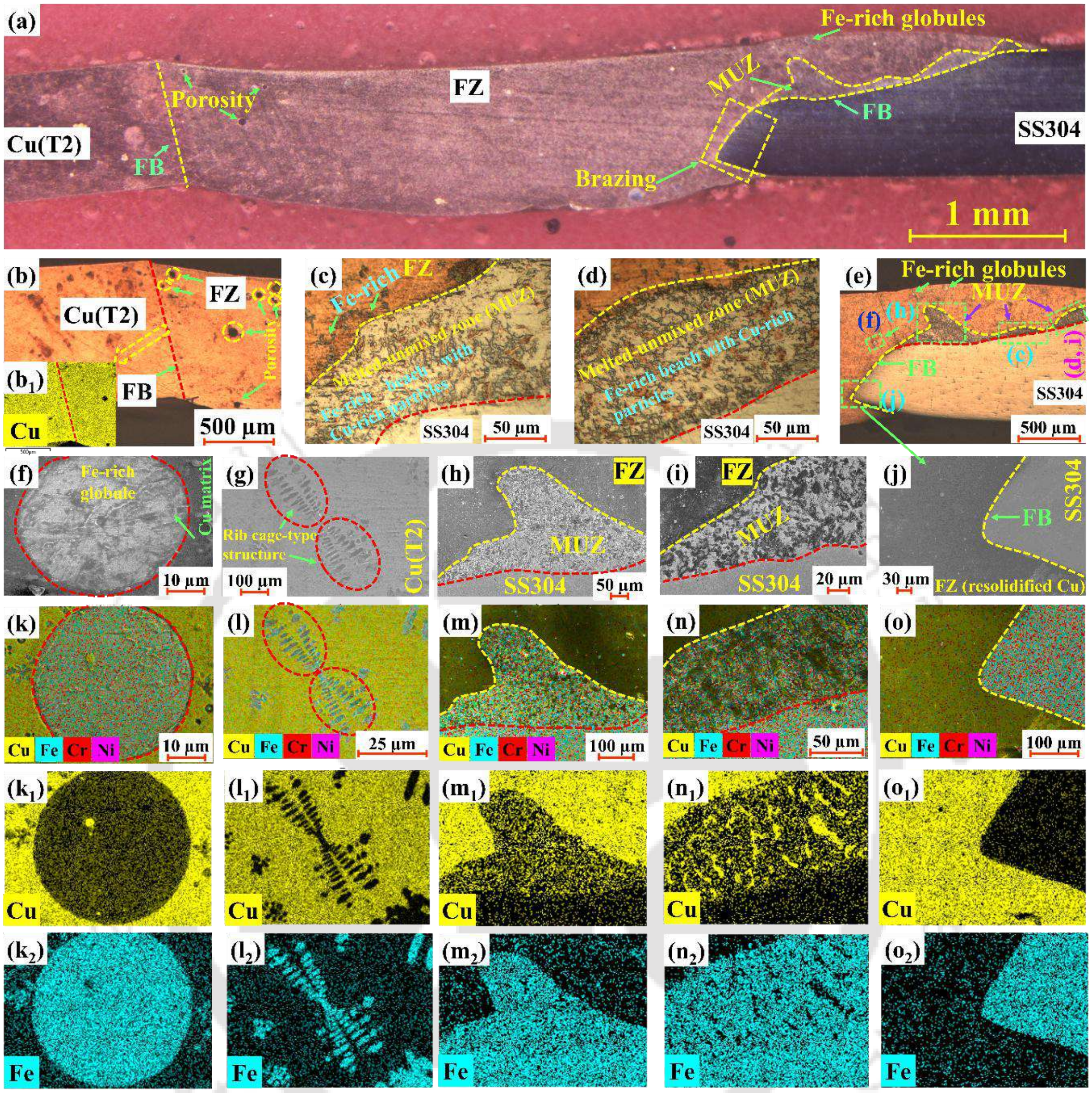

Fig. 5.21 Illustrates optical (a) macrograph, (b-e) micrographs near the fusion boundary (SS-side, Cu-side) and MUZ; (f-j) electron micrographs near the fusion boundary (SS-side), and (k-k_2, l-l_2, m-m_2, n-n_2, o-o_2) elemental area mapping for the joints fabricated at CS_3 weld condition.

Due to a higher arc offset (2.7 mm) value, the FZ comprises solidified Cu and minimal Fe-rich region. Except in the melted-unmixed zone (MUZ) and areas near it, there exist limited Fe-rich regions in the FZ. As a result, the microstructural analysis demonstrates no inhomogeneities except the formation of MUZ near the SS-side FB. The wt. percentage of Cu remains above 87 % throughout the FZ (87.62 % near SS-side FB, 93.51 % in the weld center, and 95.91 % near Cu-side FB).

It can be inferred that as the arc offset value increases (1.3, 2.0, 2.7 mm), the amount of Cu percentage also increases, and the mode of joining modifies from welding (CS_1, CS_2) to weld-brazing mode (CS_3). The occurrence of dissolved gases (O & H) also increases (0.48, 0.96, 2.12 wt. %) with arc offset/Cu percentage. The increase in the Cu content negatively impacts the Cu-SS bimetallic joints, which will be discussed later under porosity assessment (section 5.3.8) and strength analysis (section 5.3.9) sections. Microstructural features reported in the present study have also been reported in the past literature (MUZ (Cheng et al., 2019), Cu-rich globules in Fe-rich matrix (Chen et al., 2013; Magnabosco et al., 2006; Mannucci et al., 2018; Siddiquee et al., 2023), Fe-rich globules in copper matrix (Cheng et al., 2019; Magnabosco et al., 2006), Fe-rich Island, Fe-rich peninsula (Meng et al., 2019; Soysal et al., 2016), Cu-rich dendritic structure, Fe-rich dendritic structure, PMZ (Joshi and Badheka, 2020), fish hook structure (Siddiquee et al., 2023), and rib cage type structure (Siddiquee et al., 2023)). However, some parts of the MUZ resemble a cow hump-type feature, which has yet to be reported to date. Table 5.5 explains the key microstructural characteristics, and Table 5.6 details the elemental composition of major elements for the joints fabricated at CS_1, CS_2, and CS_3 weld conditions.

Table 5.5 Key microstructural characteristics obtained for the CS_1, CS_2, and CS_3 weld joints.

Sl. No.	Key features	CS_1	CS_2	CS_3
1.	Mode of joining	Welding	Welding	Weld-brazing
2.	Cu-rich globules in Fe-rich matrix	FZ center	-	-
3.	Cu-rich flakes in the Fe-rich matrix	Near the SS-side FB and FZ center	-	-
4.	Fe-rich globules in Cu-rich matrix	-	Near FB (SS and Cu-side) and FZ center	Near the SS-side FB
5.	Fe-rich Island	Bottom of the FZ	-	-
6.	Fe-rich peninsula	-	Near the SS-side FB	
7.	Fish-hook structure	Near the Cu-side FB	-	-
8.	Melted un-mixed zone (MUZ)	-	-	Near the SS-side FB
9.	Fe-rich dendritic structure	-	Near the SS-side FB and FZ center	Near the SS-side FB
10.	Cu-rich dendritic structure	FZ center	-	-

Table 5.6 Details the composition of major elements present (by wt. %) in the FZ of the CS_1, CS_2, and CS_3 weld joints.

Weld condition	Near SS-side FB		FZ center		Near Cu-side FB	
	Cu	Fe -Cr-Ni	Cu	Fe-Cr-Ni	Cu	Fe-Cr-Ni
CS_1	23.41	76.12	21.68	77.81	10.55	88.99
CS_2	61.78	37.27	57.51	41.51	87.26	11.81
CS_3	87.62	10.23	93.51	4.46	95.91	1.91

5.3.7 Quantification of Cu and Fe phases

XRD is among the top characterization techniques utilized in materials science (Omar, 2016), and for the current analysis, it is employed to quantify the occurrence of different phases. Process variables (200 mA, 45 kV) are utilized to generate and allow X-ray to pass through a square shape slit of 2 mm size. The data is extracted for a range of 40-90° with a step size of 0.02°. XRD analysis identifies the peak position for Cu and Fe for the different weld conditions. The change in the elemental composition influences the intensity counts, position of 2θ, and X-ray spectrum shape (Omar, 2016). As the proportion of phases available is directly correlated with the intensity counts (Kumar et al., 2021a), comparing the intensity counts of the joints confirms the presence of different phases.

The entire FZ is extracted from the welded samples, and X-ray exposure is centered on the FZ for XRD analysis. The reference Intensity ratio (RIR) method is utilized to quantify the phases, wherein the obtained XRD pattern is compared with the available standard database (ICSD code from JCPDS files). In the past literature, a similar analysis was performed to quantify phases of Cu-SS bimetallic joints (Rajendran et al., 2024). Fig. 5.22(a-c) demonstrates the XRD patterns for the joints fabricated at CS_1, CS_2, and CS_3 weld conditions. The five prominent peaks depicted in Fig. 5.22(a, b) correspond to the planes (111), (110), (200), (220), and (222). Similar peaks have also been reported in the past literature (Xu et al., 2021). Amongst these, peaks occurring at (111), (200), and (220) belong to Cu, and peaks developed at (110) and (222) represent Fe. Furthermore, the intensely high peak at the (111) plane corresponds to pure Cu. The intensity (counts) for the (111) plane shows a continuous rise with increasing arc offset values (CS_1: 1792, CS_2: 2074, CS_3: 4033). Also, (200) and (220) planes demonstrate an amplification ($CS_1 \longrightarrow CS_2 \longrightarrow CS_3$) in their intensity (counts), with values $969 \longrightarrow 1602 \longrightarrow 2832$ and $588 \longrightarrow 841 \longrightarrow 2052$, respectively.

The escalation in the intensity (counts) for (111), (200), and (220) planes resulted in an increasing amount of Cu (wt. %) (21.68 % for CS_1, 57.45 % for CS_2, and 94.54 % for CS_3) in the FZ. The (110) and (222) planes representing Fe illustrate a decrease in the intensity (counts) due to decreasing Fe content (wt. %) in the center of the FZ (77.81 % for CS_1, 41.51 % for CS_2, and 4.46 % for CS_3). Instead of five, only three peaks exist for the CS_3 weld joints. The reason for the absence of the (110) and (222) planes in Fig. 5.22(c) is due to the weld-brazing mode, leading to the complete fusion of Cu(T2) base metal and limited melting of SS304.

Thus, the FZ center comprises 93.51 % Cu, leading to the absence of peaks for the (110) and (222) planes. Hence, the XRD results reinforce the findings in the section 5.3.2—5.3.6, in which the CS_1 joints primarily comprise a Fe-rich matrix wherein Cu globules are identified in the FZ center. As the arc offset increases (2.0 mm for CS_2), the melting of Cu increases, resulting in a Cu-rich matrix comprising Fe-rich globules. Whereas, for CS_3 joints, on account of the minimal melting of SS304, the FZ center predominantly includes Cu. Fig. 5.22(d) details the intensity (counts) achieved in the center of the FZ, wherein an increase and decrease in the intensity is achieved for Cu and Fe, respectively.

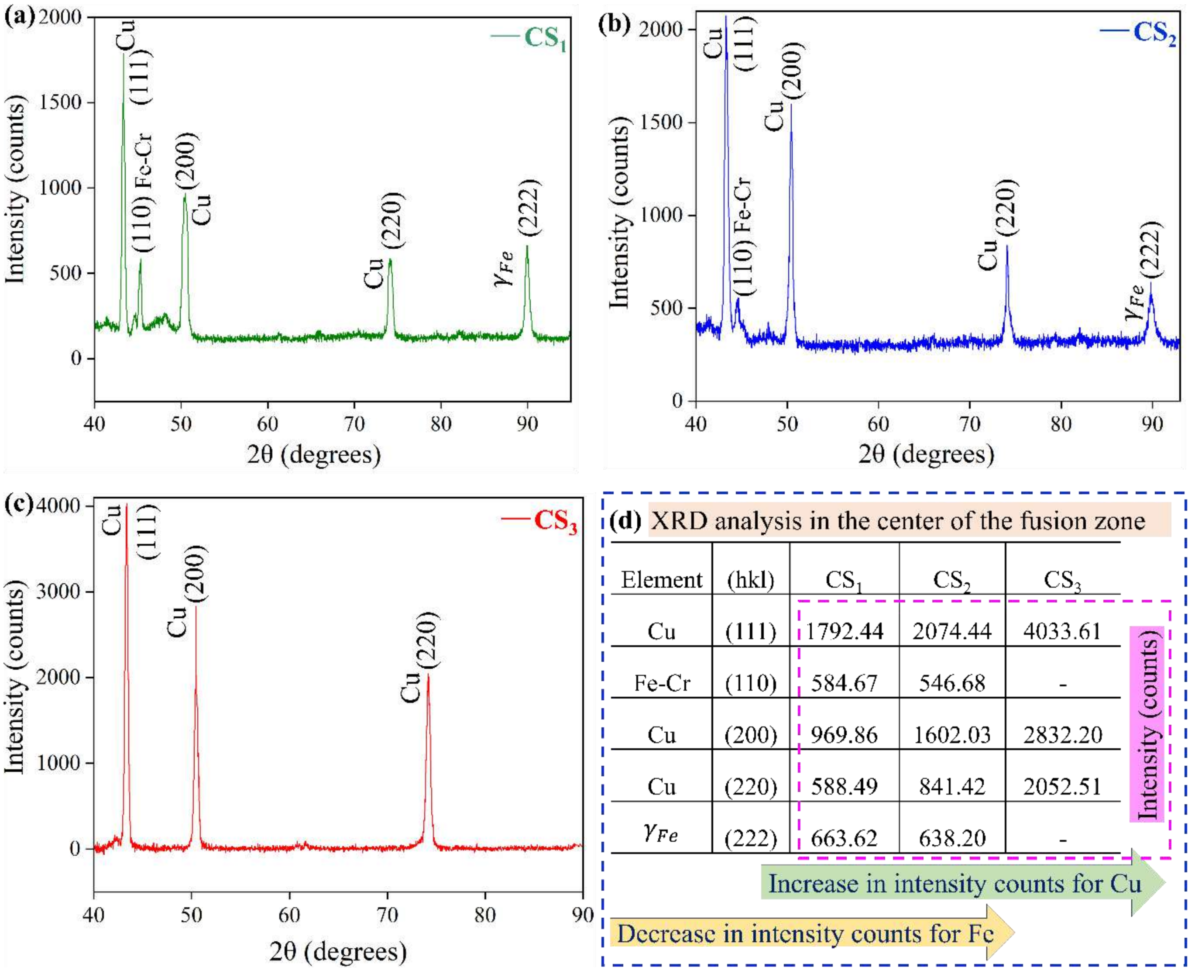

(d) XRD analysis in the center of the fusion zone

Element	(hkl)	CS_1	CS_2	CS_3
Cu	(111)	1792.44	2074.44	4033.61
Fe-Cr	(110)	584.67	546.68	-
Cu	(200)	969.86	1602.03	2832.20
Cu	(220)	588.49	841.42	2052.51
γ_{Fe}	(222)	663.62	638.20	-

Fig. 5.22 XRD patterns for the joints fabricated at (a) CS_1, (b) CS_2, and (c) CS_3 weld conditions, and (d) detail the results obtained from the XRD analysis.

5.3.8 Porosity analysis

Based on the visual inspection, Cu-SS bimetallic joints fabricated at CS_1, CS_2, and CS_3 weld conditions (~308 J/mm) are selected for quantitative analysis. Further, macro-structural analysis confirms the absence of hot cracks, undercut, and lack of fusion in the joints. However, identifying porosity (internal flaw) requires special attention, for which an NDT (X-ray CT) is employed. The scanning parameters utilized for the detection of porosities are 100 kV (voltage), 90 µA (current), 1000 ms (exposure time), 1000 projection images, and 8 µm (voxel size). Fig. 5.23(a-c) represents reconstructed images (2D, top view) for the joints fabricated at CS_1, CS_2, and CS_3 weld conditions. The heavier metal (Cu) looks brighter, whereas the lighter metal (SS304) looks dark. It is evident that the pores primarily form towards the Cu-side. Fig. 5.23(d-f) demonstrates the reconstructed 3D images along the weld (longitudinal, side view) direction, which aids in clearly identifying the size and position of the pores. It is to be noted that the different colors of pores correspond to varying volumes. The X-Y-Z coordinates represent the longitudinal, transverse, and thickness directions. The legend bar illustrated in Fig. 5.23(g-i) shows an increase in the maximum defect volume (μm^3) from CS_1 to CS_3. Accordingly, the pore diameter (considered spherical) shows an enlargement in pore size. Fig. 5.24(a) demonstrates pore diameter and its occurrence rate for the Cu-SS bimetallic joints. Maximum pore size and total number of pores are extracted from Fig. 5.24(a) and represented in Fig. 5.24(b), wherein the total number of pores (13, 19, 136) and maximum pore size (194.82, 445.14, 580.63 µm) increases with increasing arc offset (CS_1, CS_2, CS_3).

The probable reasons for the occurrence of porosities in the FZ might be due to (i) shrinkage cavities, (ii) instability in the FZ, (iii) occurrence of volatile elements (Zn, Mg), and (iv) the presence of dissolved gases (Hydrogen and Oxygen) in the base materials. The spherical geometry of the pores eliminates the possibility of shrinkage cavities, whereas instability in the FZ is excluded because of complete penetration. The absence of volatile elements in the base metals confirms the presence of dissolved gases as the only possible option for forming porosities (Kar et al., 2018). As the magnitude of arc offset increases, the percentage of Cu increases in the FZ, leading to more pore formations. Another critical point is that porosities tend to form predominantly in Cu-rich regions. Such observation is due to the occurrence of Oxygen and Hydrogen as dissolved gases in Cu-base metal, leading to the creation of porosities. A similar trend in the inter-dependence of porosity and Cu content has also been reported in the past literature (Kar et al., 2018).

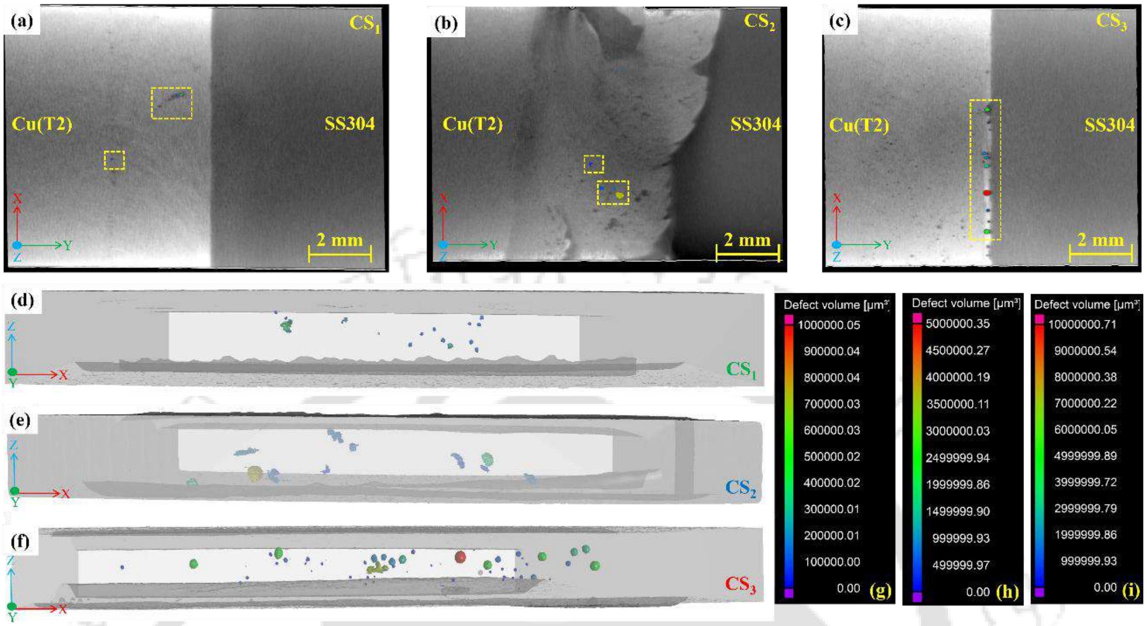

Fig. 5.23 Depicts (a-c) reconstructed images (2D, top view), (d-f) reconstructed transparent images (3D) along the weld (longitudinal) direction, and (g-i) legend bar demonstrating the volume of the pores formed at CS$_1$, CS$_2$, and CS$_3$ weld conditions.

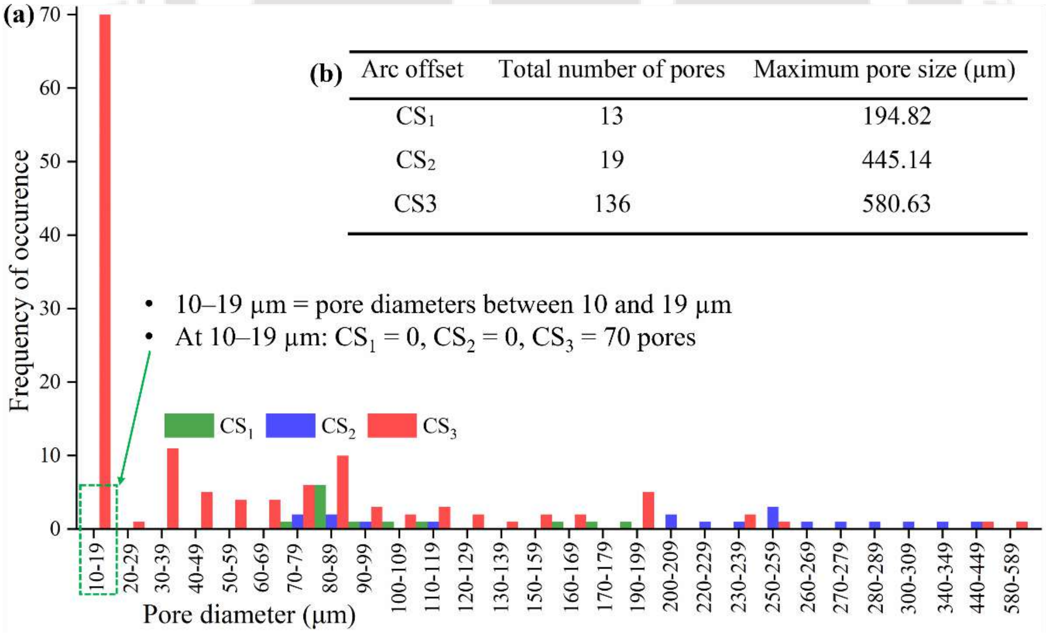

Arc offset	Total number of pores	Maximum pore size (µm)
CS$_1$	13	194.82
CS$_2$	19	445.14
CS3	136	580.63

- 10–19 µm = pore diameters between 10 and 19 µm
- At 10–19 µm: CS$_1$ = 0, CS$_2$ = 0, CS$_3$ = 70 pores

Fig. 5.24 Depicts (a) pore diameter vs frequency count and (b) pore size vs number of pores for the joints fabricated at CS$_1$, CS$_2$, and CS$_3$ weld conditions.

For CS_1 joints, limited melting of Cu-base metal occurs, corresponding to Fe-rich regions (minimum 75 wt. % Fe-Cr-Ni) throughout the FZ. Wherein Cu is distributed within the Fe-rich matrix. Meanwhile, for CS_3 joints, minimal melting of SS304 occurs, hence, the FZ primarily comprises melted and solidified Cu (minimum 89 wt. % Cu). The formation of porosity in the Cu-SS bimetallic joints negatively impacts the strength and ductility (to be discussed in section 5.3.9). Hence, utmost care should be implemented to avoid internal defects and enhance joint properties. In the present case, careful consideration is required to ensure the presence of a Fe-rich matrix with limited melting of Cu-base metal.

5.3.9 Joint strength and fracture behaviour

To estimate the joint properties, tensile specimens are extracted in the transverse direction as per ASTM E8 guidelines. Fig. 5.25(a-c) illustrates tensile specimens for the CS_1, CS_2, and CS_3 welded joints. As the reliability of dissimilar joints remains a prime concern, three specimens are tested for each weld condition, and the mean magnitude is stated. A 250 kN-UTM is employed at a constant cross-head speed of 0.5 mm/min to accomplish the tensile test. Fig. 5.25(d) depicts the stress-strain curve for the joints prepared under varying arc offset values (1.3, 2.0, 2.7 mm). The evaluated values of UTS (ultimate tensile strength) and %EL (percentage elongation) follow a decreasing trend with increasing arc offset values: ~222 MPa and 28 % (1.3 mm), ~211 MPa and 22 % (2.0 mm), ~183 MPa and 16 % (2.7 mm).

As the arc offset value increases from 1.3 mm (CS_1) to 2.7 mm (CS_3), a significant reduction in the UTS (39 MPa) and %EL (12 %) is noted. The reduction in the UTS values directly correlates with the percentage of Cu and the occurrence of porosity within the joints. The joints (CS_1) with the least Cu content (10-23 %) and a minimum number of pores (13) demonstrate the best joint properties. Also, on account of better joint properties of SS304 (UTS_{SS304} ~743 MPa, $\%EL_{SS304}$ ~ 54 % and $UTS_{Cu(T2)}$ ~209 MPa, $\%EL_{Cu(T2)}$ ~33.91 %), the presence of Fe-rich region throughout the FZ tends to enhance the strength and ductility of CS_1 joints. In addition to the Fe-rich region, microstructural features such as fish-hook and jagged-teeth structures at the Cu-side interface also offer an interlocking at the Cu-side interface during the tensile test, providing further resistance to the applied tensile force and enhance the CS_1 joint properties. As the arc offset increases (CS_2), the FZ comprises Cu-rich region throughout the matrix, resulting in reduced joint properties compared to the CS_1 weld condition, where a Fe-rich matrix exists. Hence, it can be inferred that microstructural non-uniformities and unique morphology like fish-hook and jagged-teeth structures significantly contribute to the joint properties of Cu-SS bimetallic joints. As the arc offset further increases to 2.7 mm (CS_3), the joining mode changes from welding to weld-brazing, wherein the FZ is primarily composed of melted and solidified Cu with increased pore formation. Though the CS_3 joint shows no microstructural non-uniformities, except Melted-unmixed zone (MUZ) near the Cu-side; due to the weld-brazing mode of joining, the joint properties show a drastic reduction. The joint efficiency for dissimilar joints is evaluated with reference to the weaker base material, which, in this case, is Cu(T2), and given by using Eq. (5.3). Fig. 5.25(d_1) depicts the stress-strain curve for Cu(T2)-base material, wherein the value of the UTS is evaluated as 209 MPa with 33.91 % ductility.

$$\eta_{\text{weld joint}} = \frac{\text{UTS}_{(\text{Cu-SS, bimetallic joints})}}{\text{UTS}_{\text{Cu(weaker base material)}}} \times 100\% \qquad (5.3)$$

The failed tensile specimens assist in identifying the location of failure (macro-fractography) and failure pattern (micro-fractography). Fig. 5.25(e-e_2) illustrates the failed specimens (CS_1) after the tensile test, wherein the FZ is demarcated from the base metals with a cyan color. It is to be noted that the CS_1 joints fail far away from the FZ towards the Cu-side. Meanwhile, for CS_2 joints, the failure location moves closer toward the FZ, as shown in Fig. 5.25(f-f_2). Unlike CS_1 and CS_2; CS_3 weld joints demonstrated failure within the FZ, which implies that FZ is the weakest. Fig. 5.25(g-g_2) provides clear evidence regarding the failure location for CS_3 joints, which occurs within the FZ, specifically towards Cu-side FB. It is evident that as the arc offset increases (1.3, 2.0, 2.7 mm), the weld joints display a continuous decline in the joint properties.

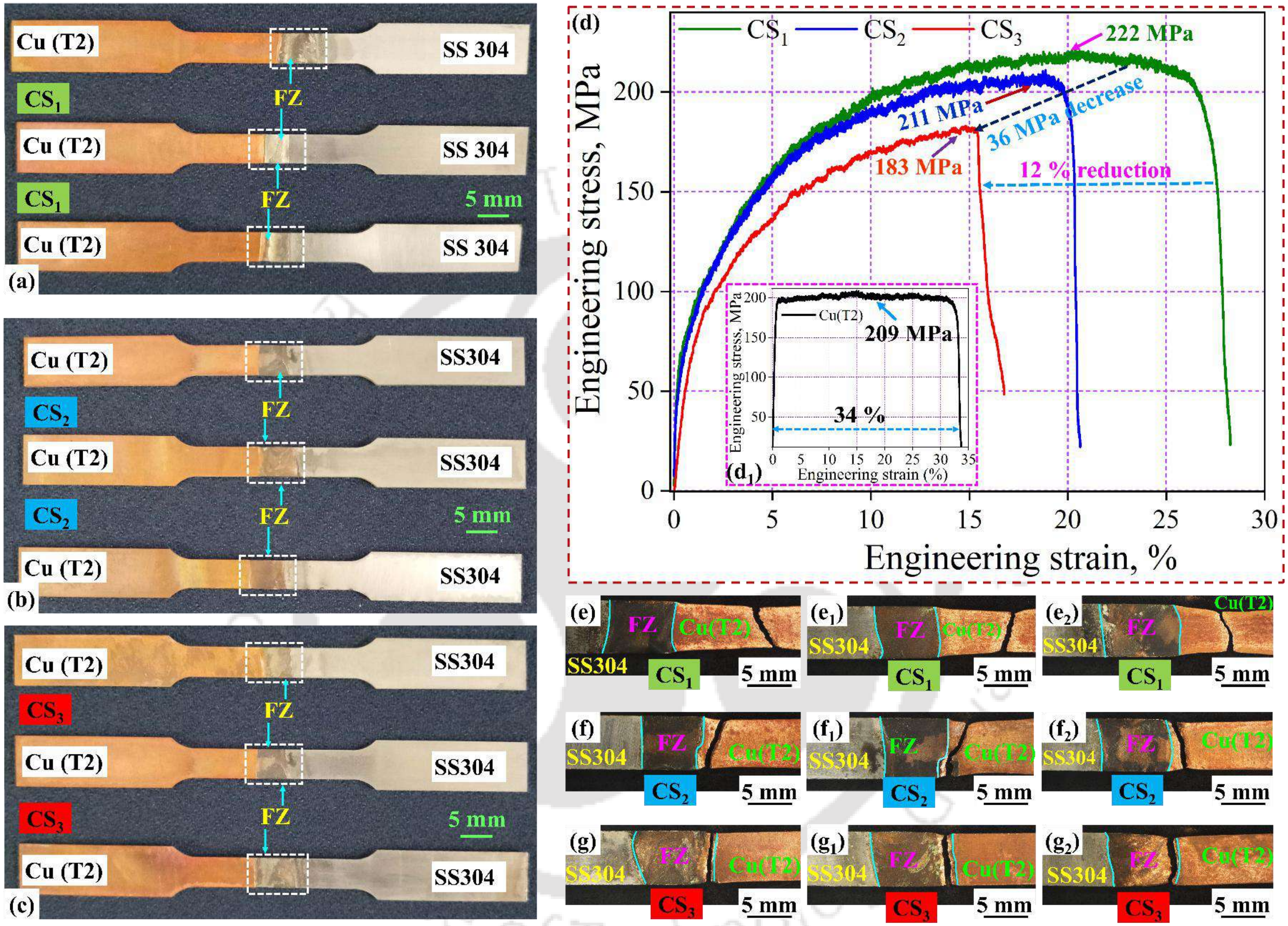

Fig. 5.25 Displays (a-c) tensile-test coupons, (d-d$_1$) engineering stress-strain plots, and (e-e$_2$, f-f$_2$, g-g$_2$) failed tensile specimens for the joints fabricated at CS$_1$, CS$_2$, and CS$_3$ weld conditions.

To reveal the failure pattern, micro-fractography analysis is carried out on the failed tensile samples shown in Fig. 5.25(e, f, g). Fractured samples are subjected to an electron microscope, and the captured FESEM images are illustrated at different magnifications (1500, 2500, 5000 ×). Fig. 5.26(a-a_2) and Fig. 5.26(b-b_2) depicts the micro-fractography images for CS_1 and CS_2 weld conditions. Fig. 5.26(a-a_2) reveals fine fibrous dimples throughout the fracture region, whereas coarse dimples and a few pores are identified in Fig. 5.26(b-b_2). The occurrence of fine dimples (CS_1) indicates higher deformation capacity compared to coarse dimples (CS_2). Thus, the CS_1 joints possess higher strength and %EL compared to CS_2. Fig. 5.26(c-c_2) illustrates the micro-fractography images of CS_3 joints, wherein pores of varying sizes (micro and macro pores) can be recognized. As a result, the CS_3 joints demonstrate the least strength and %EL among the joints fabricated at different arc offset values (1.3, 2.0, 2.7 mm).

Fig. 5.27 explains the dependence of arc offset and Cu content on the mechanical properties. As the arc offset increases (1.3, 2.0, 2.7 mm), the melting of Cu-base material increases, leading to a change in the joining mode (welding for CS_1, CS_2, and weld-brazing for CS_3). Due to the change in the joining mode, the failure mode changes from ductile to brittle, and a decrease in the joint properties (UTS and %EL) is observed. Consequently, the joint efficiency decreases with increasing arc offset (106.14 % for CS_1, 101.01 % for CS_2, and 87.56 % for CS_3). Hence, a lower arc offset corresponds to enhanced joint properties. A similar positive impact of arc offset (towards the Cu-side) on joint properties has also been reported in the past literature (Meng et al., 2019; Singh et al., 2020, 2021; Tanmay and Panda, 2023). Table 5.7 details the tensile test results, fractography analysis, the mode of joining, and failure mode for the fabricated Cu-SS bimetallic joints.

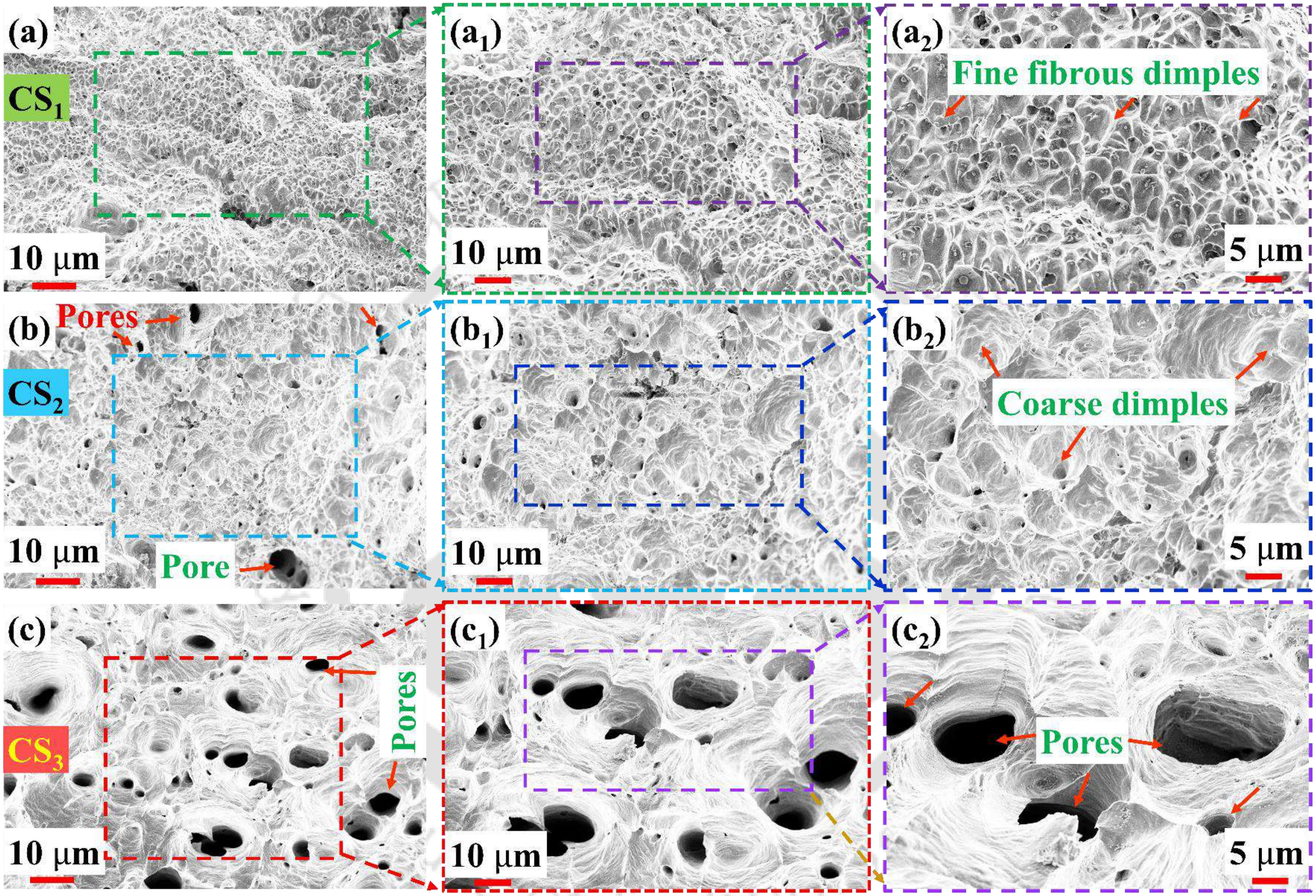

Fig. 5.26 Micro-fractographs for the failed tensile specimens fabricated at (a-a$_2$) CS$_1$, (b-b$_2$) CS$_2$, and (c-c$_2$) CS$_3$ weld conditions.

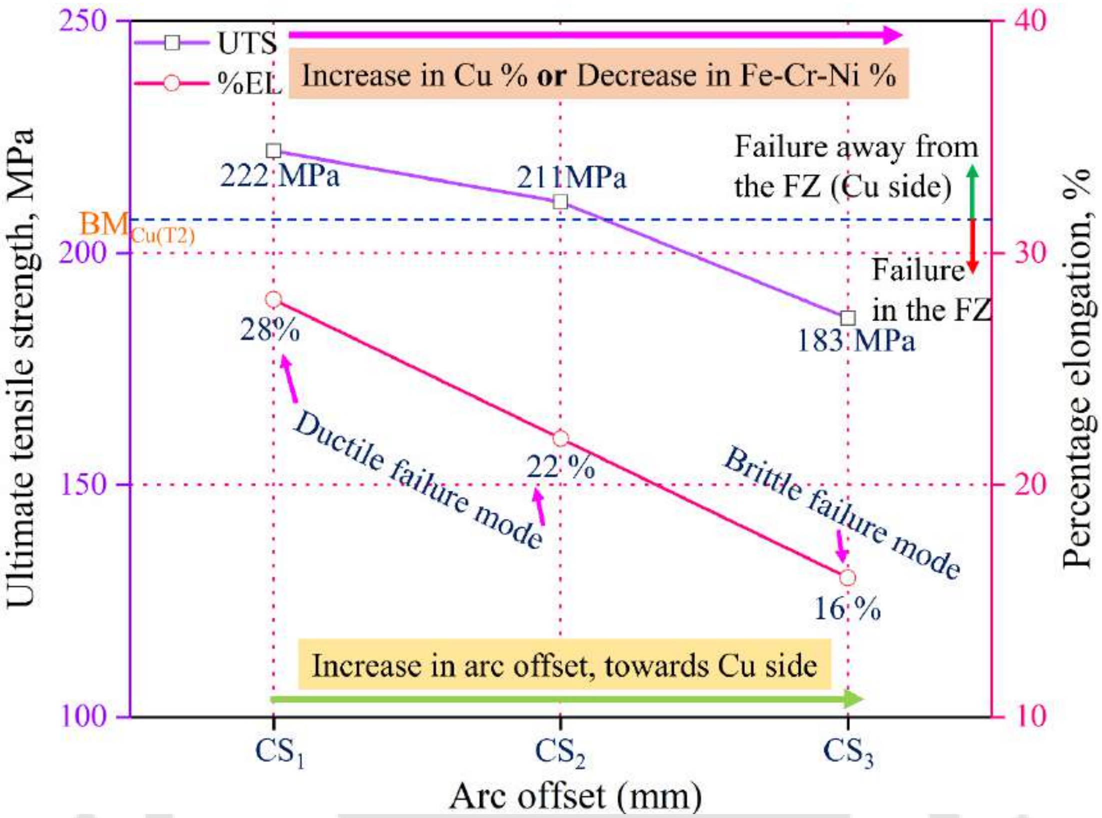

Fig. 5.27 Illustrates the variation of joint strength and percentage elongation with increasing arc offset.

Table 5.7 Summarizes the tensile test results and fractography analysis.

Weld condition	UTS (MPa)	% EL at break	η_{joint} (%)	Mode of joining	Fracture location	Mode of failure
CS_1	221.84	28.25	106.14	Welding	Cu-side	Ductile
CS_2	211.13	21.61	101.01	Welding	Cu-side	Ductile
CS_3	183.01	16.15	87.56	Weld-brazing	FZ	Brittle
Cu(T2) base metal: 209 MPa (UTS), 33.91 % (%EL)						

5.3.10 Microhardness plot

Vickers microhardness measurement is carried out using ASTM E384 guidelines by employing a 200 gf load with a hold time of 10 s. The test coupons are extracted perpendicular to the welding direction and meticulously polished to remove scratches and achieve a mirror-like surface finish. Microhardness measurements are cautiously made to ensure no overlapping of indentation occurs. Fig. 5.28(a-c) illustrates the microhardness variation across the CS_1, CS_2, and CS_3 welded joints.

The microhardness values represented by the Vickers hardness number (VHN) show inhomogeneities within the FZ for the fabricated bimetallic joints. Fig. 5.28(a) depicts variation in the VHN across the CS_1 joints, wherein the VHN order follows SS304-BM (210 $HV_{0.2}$) > FZ > Cu(T2)-BM (71 $HV_{0.2}$). Within the FZ, a VHN of 196-203 $HV_{0.2}$ is achieved due to the occurrence of a Fe-rich matrix. However, the appearance of Cu-rich globules in a Fe-rich matrix and Cu-rich dendritic structure corresponds to reduced VHN of 70-170 $HV_{0.2}$. Fig. 5.28(b, c) illustrates the VHN fluctuation for the joints fabricated at CS_2 and CS_3 joints, wherein the VHN order follows a similar pattern (SS304-BM > FZ > Cu(T2)-BM) as identified for CS_1 joints.

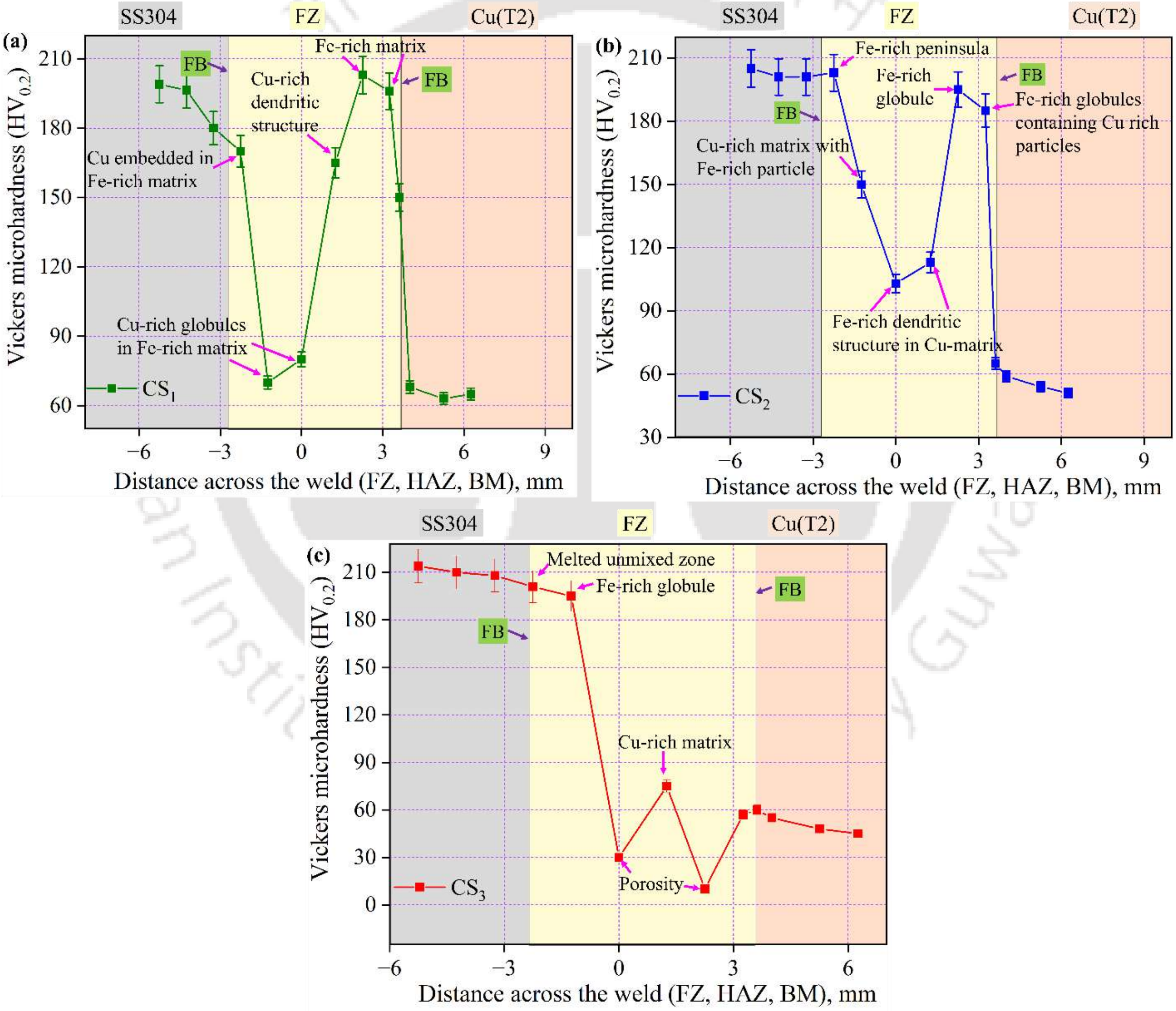

Fig. 5.28 Microhardness variation across the joints fabricated at (a) CS_1, (b) CS_2, and (c) CS_3 weld conditions.

The difference lies in the value of VHN within the FZ. For the CS_2 joints, the occurrence of Fe-rich peninsula, Fe-rich globules containing Cu-rich particles, and Fe-rich globules correspond to the higher values of VHN (185-203). Meanwhile, the presence of a Cu-rich matrix with Fe-rich particles and a Cu-rich matrix with a Fe-rich dendritic structure reduces the VHN (103-150 $HV_{0.2}$). For CS_3 joints, primarily comprising Cu-rich matrix in the center of the FZ, the VHN varies in the range 57-75 $HV_{0.2}$. A marked reduction in the VHN is spotted where the indenter meets porosity of varying dimensions. The VHN recorded near the SS-side FB attained a value of 195-201 $HV_{0.2}$. Such a high value of VHN is achieved due to the occurrence of a Fe-rich beach comprising Cu-particles (Melted-unmixed zone, MUZ).

5.3.11 Influence of heat input on solidification cracking

The critical findings of the arc offset suggest that the CS_1 (1.3 mm) process condition yields the least number of pores (13) and the highest joint efficiency (106.14 %). Further, to study the influence of heat input on joint properties, a comparison is made between CS_1 and CS_4 weld joints. Cu-SS bimetallic joints fabricated at ~339 J/mm (CS_4, 1.3 mm arc offset) undergo cracking during solidification, significantly decreasing the joint properties. The primary reason for solidification cracks is controlled by the amount of inter-mixing of the base metals, which is directly regulated by the supplied heat input (Joshi and Badheka, 2019). The increase in the value of heat input from CS_1 to CS_4 (308⟶ 339 J/mm) corresponds to (i) enhanced solubility and (ii) promotes turbulent flow, which results in higher microstructural non-uniformities within the FZ of the CS_4 joints. At a higher value of heat input (~339 J/mm, CS_4), SS304 melts first and solidifies last, leading to solidification cracks. Fig. 5.29(a) illustrates the entire macrograph of the CS_4 weld joint, representing the FZ, FB, and key microstructural features (Fe-rich peninsula, Cu-rich globules, Cu-rich and Fe-rich Islands). Fig. 5.29(b-j) illustrates the optical and FESEM images of the CS_4 joints. Fig. 5.29(b) illustrates the SS-side FB of the Cu-SS bimetallic joints, wherein the FB (yellow dotted line), Cu-rich Island, Cu-rich globules, and solidification crack are highlighted. Fig. 5.29(c) depicts the FZ center, highlighting Fe-rich Island, Cu-rich Island, and Fe-rich globules. Fig. 5.29(d) exhibits the Cu-side FB, where the FB demarcates the FZ and Cu-side base metal. Fig. 5.29(e) highlights the Cu-rich globules within the Fe-rich matrix, Fe-rich globules within the Cu-rich matrix, Fe-rich Island, Cu-rich Island, and cracks formed at the weld surface. Fig. 5.29(f, g) depicts the enlarged version of Cu-rich and Fe-rich Islands. Wherein Fe-rich particles and Fe-rich chunks are observed within the Cu-rich Island. Fig. 5.29(h) highlights the Cu-rich globules within the Fe-rich matrix, in which Fe-rich particles are observed within Cu-rich globules. Due to contrasting thermal conductivities (Cu and SS304), primary liquid separation occurs, which leads to the formation of Cu-rich and Fe-rich globules. Whereas secondary liquid separation contributes to the formation of Cu-rich islands containing Fe-rich globules/particles (Haglon et al., 2024). Fig. 5.29(h, i) highlights the backfilling of copper into the cracks. When the crack remains unfilled, the crack appears within the FZ. The self-healing effect positively impacts the joint properties, wherein the molten Cu re-fills the crack produced. The re-filling of crack is also termed a 'self-healing crack,' which has also been reported in the past literature (Chen et al., 2015, 2013; Li et al., 2020). Fig. 5.29(j) illustrates the FESEM image near the crack region, highlighted in red dotted line. Line and area elemental analysis is carried out to understand the reason for crack generation.

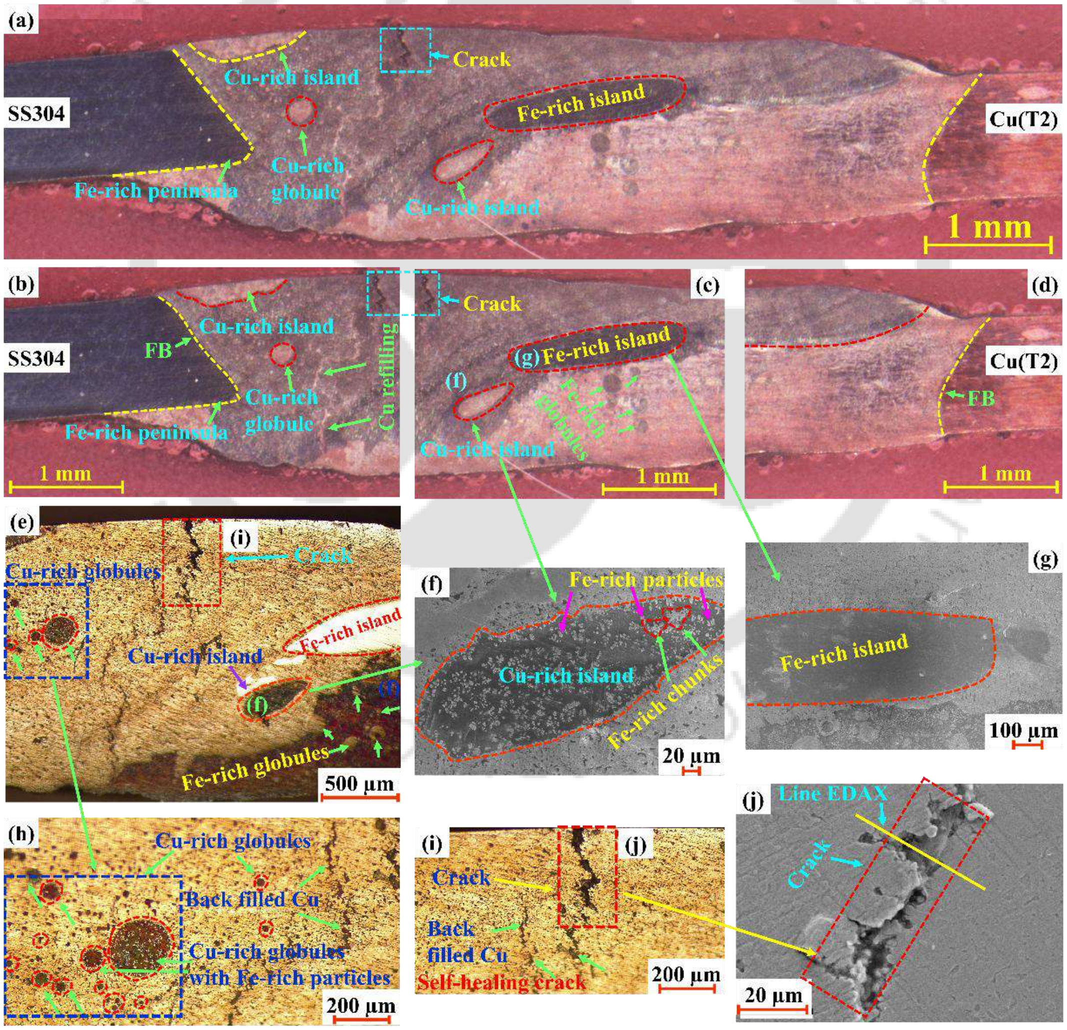

Fig. 5.29 Illustrates (a-c) macrograph, (d-i) micrograph, and FESEM images of the Cu-SS joints fabricated at ~339 J/mm (CS_4) weld condition.

Fig. 5.30(a-a$_5$) details the area elemental analysis of Fig. 5.29(j), in which the crack region primarily consists of Si (orange color). Fig. 5.30(b, b$_1$) highlights the line elemental analysis across the crack formed (marked in yellow color in Fig. 5.29(j)), wherein all the elements (Cu, Fe, Cr, and Ni) except Si show a sudden dip. A sudden spike is noted at the crack position, which is Si. At the crack position, the wt. percentage of the elements is evaluated as Cu (8.8 %), Fe (6.5 %), Si (84.4 %), Cr (0.3 %), and Ni (0.4 %). Elemental analysis aids in identifying the occurrence of IMCs in the form of impurities for the fabricated CS$_4$ bimetallic joint. Silicon combines with Oxygen to form silicon dioxide (SiO_2, an IMC), which is brittle and leads to the development of cracks. IMCs severely deteriorate the quality of the fabricated joints, which corresponds to a reduction in joint strength (Rajendran et al., 2024). Fig. 5.30(c) compares the joint properties of CS$_1$ (~308 J/mm) and CS$_4$ joints (~339 J/mm). Due to the presence of a solidification crack (CS$_4$), a drastic reduction in UTS (CS$_1$: 221.84⟶ CS$_4$: 172 MPa) and %EL (CS$_1$: 28.25⟶ CS$_4$: 10 %) is observed. A similar negative impact of higher heat input has also been reported in the past literature, wherein higher weld speed contributed to a reduction in pore and crack formation (Nguyen et al., 2020). Thus, it's appropriate to mention that the lower heat input provides a more stable environment for fabricating the Cu-SS bimetallic joint. Hence, welding parameters such as arc offset and heat input need careful attention to obtain a Cu-SS bimetallic joint with minimum microstructural non-uniformities and defect formation.

Table 5.8 summarizes the critical microstructural and mechanical characteristics obtained for the fabricated joints (CS$_1$, CS$_2$, and CS$_3$). Further, a comparison is made in Table 5.9 with respect to defects reported, energy utilized, and joint properties in joining Cu-SS by different fusion welding processes. Despite the occurrence of porosity and macro-segregation, the outcome of the present experimental investigation displays an exceptional joining capability at CS$_1$ weld condition (~308 J/mm, 1.3 mm arc offset). Compared to the joint efficiency reported in the past literature on the GTAW process for fabricating Cu-SS bimetallic joints (85-96 % (Tanmay and Panda, 2023), 96 % (Shiri et al., 2012), 83.62 % (Singh et al., 2020), 92.1 % (Saranarayanan et al., 2019), 76.02-79.10 % (Joshi and Badheka, 2020)), the present investigation exhibits the highest value (106.14 %).

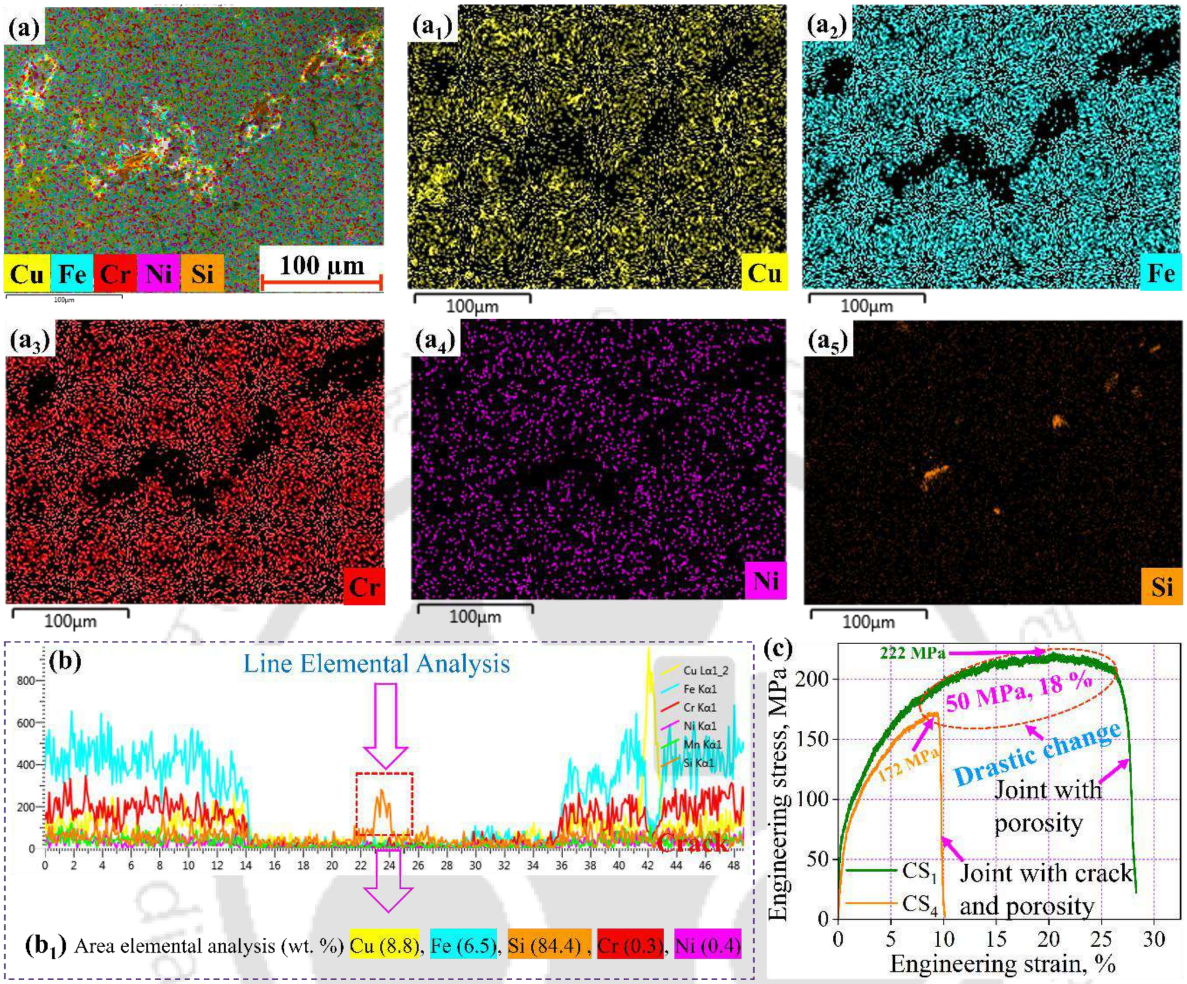

Fig. 5.30 Illustrates (a, a$_1$-a$_5$) area mapping, (b, b$_1$) line and area elemental analysis of the crack formed, and (c) comparison of tensile properties at different heat inputs (308 J/mm-CS$_1$, 339 J/mm-CS$_4$).

Institute of Technology

Table 5.8 Summarizes the key microstructural and mechanical characteristics obtained for the CS$_1$, CS$_2$, and CS$_3$ weld joints.

Key features	Different weld conditions (~308 J/mm, arc inclination 6°, arc offset towards Cu 1.3, 2.0, 2.7 mm)			
	CS$_1$ (1.3 mm arc offset)		CS$_2$ (2.0 mm arc offset)	CS$_3$ (2.7 mm arc offset)
Mode of joining	Welding		Welding	Weld-brazing
Microstructural features	FB (Cu-side)	Fish hook structure, Jagged or scraggy or teeth-like structure	Fe-rich globules in Cu matrix	Fe-rich dendritic structure, Melted un-mixed zone, Fe-rich globules in Cu matrix
	FZ-Center	Cu-rich globules in the steel matrix, Cu-rich dendritic structure, Fe-rich and Cu-rich Island	Fe-rich dendritic structure, Fe-rich globules in Cu matrix	Cu matrix
	FB (SS-side)	Cu-rich globules in steel matrix	Fe-rich peninsula, Fe-rich dendritic structure, Fe-rich globules in Cu matrix	Cu matrix
Major elements present, wt. %	SS-side FB	Cu (23.41), Fe-Cr-Ni (76.12)	Cu (61.78), Fe-Cr-Ni (37.27)	Cu (87.62), Fe-Cr-Ni (10.23)
	FZ-Center	Cu (21.68), Fe-Cr-Ni (77.81)	Cu (57.51), Fe-Cr-Ni (41.51)	Cu (93.51), Fe-Cr-Ni (4.46)
	Cu-side FB	Cu (10.55), Fe-Cr-Ni (88.99)	Cu (87.26), Fe-Cr-Ni (11.81)	Cu (95.91), Fe-Cr-Ni (1.91)
Joint strength, MPa	221.84		211.13	183.01
Percentage elongation, %	28.25		21.61	16.15
Joint efficiency, %	106.14		101.01	87.56
Location of failure	Away from FZ (Cu-side)		Away from FZ (Cu-side)	FZ
Mode of failure	Ductile		Ductile	Brittle
Total pores, max. pore size (µm)	13, 194.82		19, 445.14	136, 580.63

Indian Institute of Technology Guwahati

Table 5.9 Compares the defects formed, energy utilized, and joint properties in joining Cu-SS by different fusion welding processes.

(Reference)	Materials (Process)	Defects reported	Energy utilized	Strength (Efficiency), %EL
(Cheng et al., 2019)	Pure Cu, SS304 (3 mm) (Hybrid)	Microcracks	281, 354, 486 J/mm	226 MPa (83 %), 19.4 %, 229 MPa (84 %), 20.6 %, 224 MPa (81.7 %), 25.6 %
(Moharana et al., 2016)	Pure Cu, SS304 (3 mm) (LBW)	Macro-segregation	(3, 3.5 kW), (2, 3 m/min)	190 MPa (-), 10.3 %; 201 MPa (-), 19.1 %; 195 MPa (-), 10.7 %; 192 MPa (-), 13.7 %
(Joshi and Badheka, 2019)	ETP Cu, SS304L (3 mm) (LBW)	Solidification cracks	(900, 1000 kW), (205, 300 m/min)	210 MPa (92.5 %), 20 %; 224 MPa (98.7 %), 25 %; 197 MPa (86.8 %), 12 %
(Ramachandran and Lakshminarayanan, 2020)	C21000 and SS304 (2 mm) (LBW)	Porosity	4 kW, 1.5 m/min	236 MPa (84.28 %), 5 %
(Moharana et al., 2020)	CP-Cu, SS304 (1 mm) (LBW)	Cracks	3.5 kW, 2 mm/sec	105, 124, 146 MPa (-), -
(Kar et al., 2018, 2016)	C10300, SS304 (3 mm) (EBW)	Microcracks, porosity	60 kV, 73 mA, 1000 mm/min	249 MPa (> 95 %), 17 %; 250 MPa (> 95 %), 18 %; 252 MPa (> 95 %), 19 %,
(Singh et al., 2020, 2021).	Cu (C10200), SS304 (1 mm) (GTAW)	Hot cracks, porosity, LOF	90 A, 11 V, 1.44 mm/s	194 MPa (83.62 %), -
(Shiri et al., 2012)	CP-Cu, SS304 (3 mm) (GTAW)	Solidification crack, voids, LOF	200 A, 50 mm/min	- (96 %), 44 %
(Joshi and Badheka, 2020)	Cu (ETP), SS304L (3 mm) (GTAW)	Defect-free	(125, 150, 200) A, 50 mm/min	172.56 (76.02 %), 5.81 %; 179.49 MPa (79.1 %), 4.77 %; 178.5 (78.63 %), 4.77
Present work	Cu(T2), SS304 (1 mm) (GTAW)	Macro-segregation, porosity, hot cracks	~308 J/mm	221.84 MPa (106.14 %), 28.25 %

5.4 Micro-plasma arc welding of dissimilar austenitic stainless steels

The joining of dissimilar materials inherently involves complexity concerned with variations in thermal, metallurgical, and mechanical properties. Micro-segregation, solidification cracking, and porosity formation in the fusion zone are some predominant drawbacks that are mostly attained by dissimilar joints (Casalino et al., 2018; Jahanzeb et al., 2017). Therefore, increased utilization of dissimilar metals with built-in complexities demands significant consideration to achieve reliable joints with adequate strength (Chaudhari and Ingle, 2019). Austenitic stainless steels (ASSs) are reasonably ductile and can undergo considerable shrinkage, but the joints are sensitive to cracking during the cooling cycle (Soltani and Tayebi, 2018). Difficulties associated with the ASS weld joint are compounded with the formation of carbides along the grain boundary (GB), leading to sensitization/weld-decay (Singh and Slathia, 2016). However, with low specific heat and thermal conductivity, high thermal expansion coefficients of ASS often exhibit inferior mechanical properties of welded joints owing to (a) the development of high residual stresses and structural deformation propensity and (b) ignorance of the role of microstructural attribute in residual stress evolution (Lin and Chou, 1995). The accurate prediction of residual stress is always of great interest as it paves the road to eliminate or mitigate it.

The majority of examination in the joining of dissimilar ASSs is conducted using gas tungsten arc welding (GTAW) or laser beam (LB) or electron beam (EB) welding process. Considering a cost-effective method providing high-quality joints, micro-plasma arc welding (M-PAW) offers an incredible opportunity to take both these advantages (Saikia et al., 2019). Also, it is obvious from the literature that thermal stability, mechanical features, and residual stress of dissimilar ASS welding are controlled by the distribution and quantity of δ_{ferrite} in the fusion zone. Further, the estimation of residual stress in dissimilar austenitic steels is highly complicated, where the solidification behaviour and morphology are predominant. Hence, the objective of the present study is to investigate the mitigation of residual stress by controlling microstructural morphologies that can elude the failures of a welded joint. Therefore, an attempt is made to understand the solidification behaviour of the weld metal as well as its correlation with microstructural features and residual stress distribution. A sequentially coupled thermal-metallurgical-mechanical model (TMM) is developed and implemented using an in-house developed code through the subroutine of available commercial software. Further, numerically obtained residual stress values are validated with the experimentally measured data. The role of microstructure developed in dissimilar welding on residual stress generation is also established in the present work. An attempt is made to understand the dependence of cooling rate on phase transformation and its effect on the generation of compressive residual stress in dissimilar welding. In this study, three selected values of heat input (52 J/mm: L_{52}, 63 J/mm: M_{63}, and 77 J/mm: H_{77}) used for the dissimilar joining of ASSs are highlighted in Table 3.12 of Chapter 3 and the implementation of the thermo-metallurgical-mechanical model is detailed in Section 4.7 of Chapter 4.

5.4.1 Validation of the numerical model and temperature distribution

Validation of the developed model is carried out by comparing the experimentally obtained macrograph with the numerically computed weld dimensions. Fig. 5.31(a-f) depicts the comparison of a computed thermo-graph with an experimental macro-graph for all different values of heat input. The weld geometry shows neither crater defect at the weld top nor root sagging at the bottom/root of the weld. Isotherms distinctively demarcate the FZ, mushy zone, and HAZ. The FZ is specified by the liquidus temperature ($T_{Liquidus}$) of SS310 (1728 K), i.e., the largest out of SS316L/SS310. The HAZ is specified below the solidus temperature ($T_{Solidus}$) of SS316L (1648 K), i.e., least out of S S316L/SS310, wherein solid-state phase transformation prevails. The zone in between the isotherm formed by the $T_{Liquidus}$ and $T_{Solidus}$ is the mushy zone, where both solid and liquid phase exist together. Solidus temperature ($T_{Solidus}$) for SS316L ~1648 K, SS310 ~1673 K and liquidus temperature ($T_{Liquidus}$) for SS316L ~1673 K and SS310 ~1728 K are considered for the present numerical computation. With a rise in the magnitude of heat input from L_{52} to H_{77}, the weld width value increases; subsequently, the weld pool size also increases. Fig. 5.31(g-i) depicts the temperature range corresponding to Fig. 5.31(a, c, e).

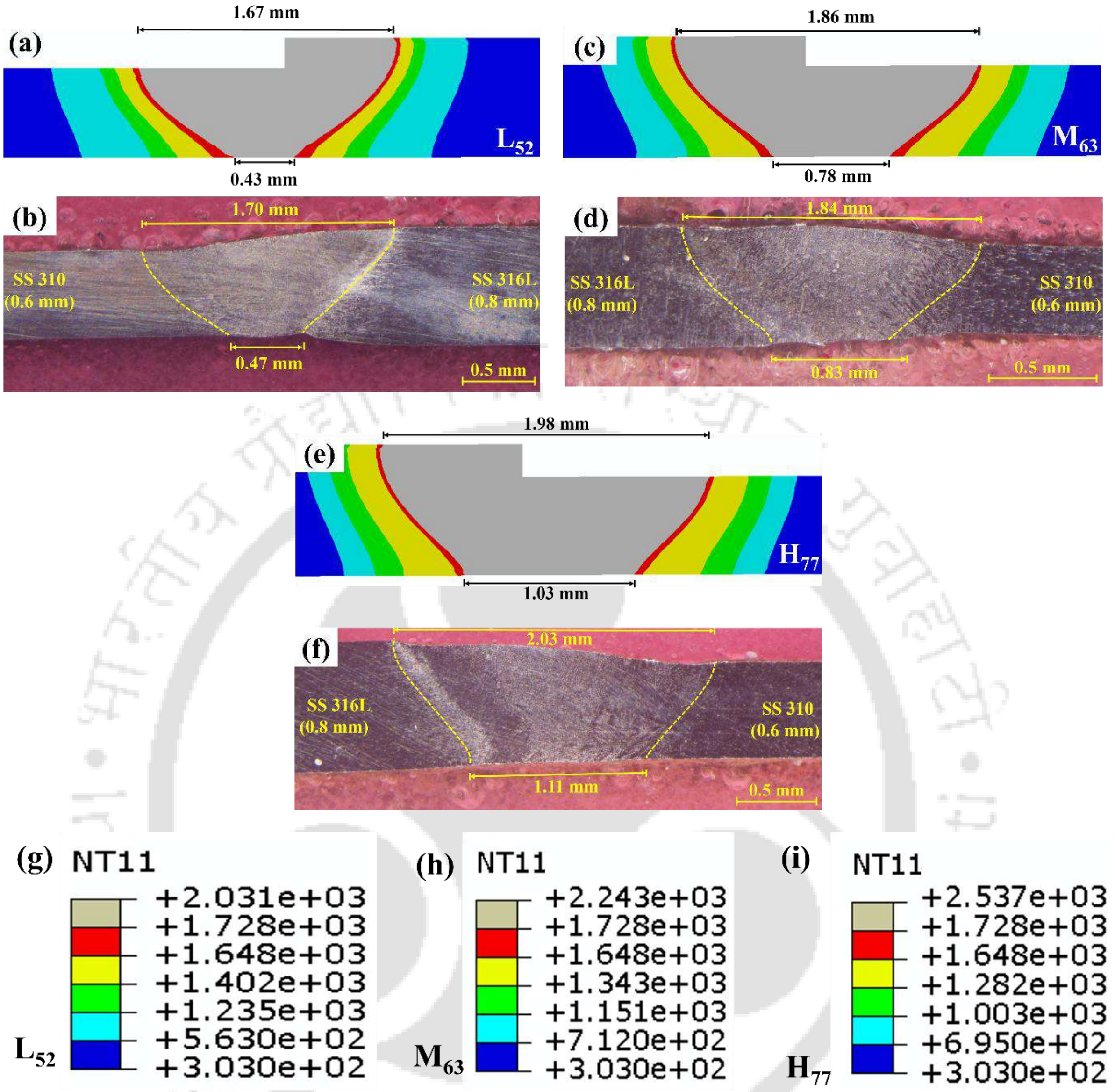

Fig. 5.31 (a-f) Comparison of numerical and experimental weld dimensions, and (g-i) depicts the temperature range for weld joints fabricated at different weld conditions (L_{52}, M_{63}, and H_{77}).

Fig. 5.32 shows a graphical comparison of the numerically computed weld dimensions with the experimentally derived data for all three cases of heat input at the weld cap and weld root of the fusion zone, which demonstrates fair agreement with an error percentage of ~2 %, ~9 % for L_{52}, ~1 %, ~6 % for M_{63} and ~3 %, ~7 % for H_{77}.

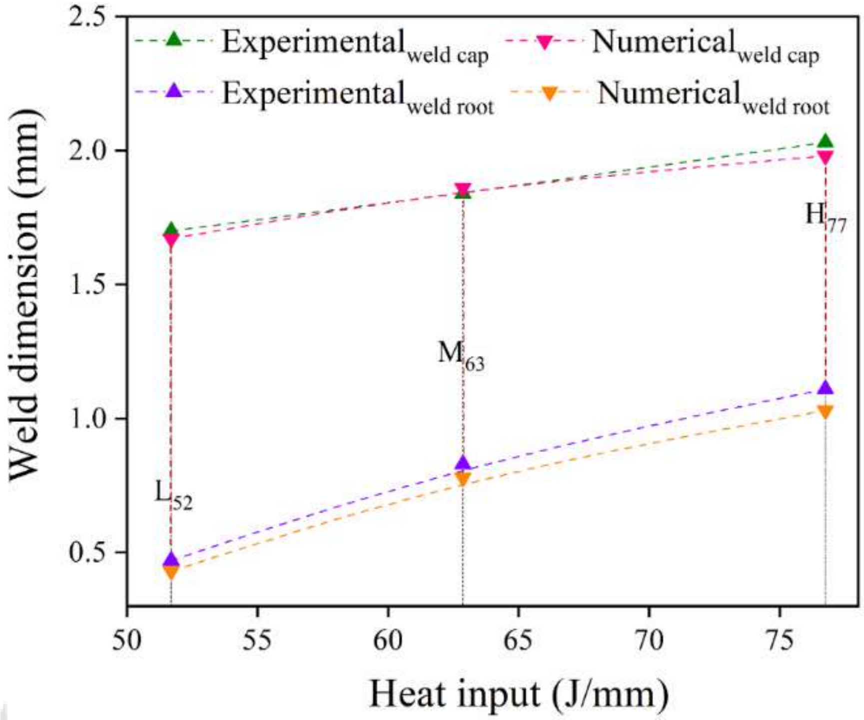

Fig. 5.32 Comparison of numerical and experimental weld dimensions for L_{52}, M_{63}, and H_{77} weld conditions.

The reliability of the developed numerical model is verified by comparing the dimensions of the top (W_{top}) and root (W_{root}) portion of the FZ. Additionally, the peak temperature obtained during the simulation is validated with the measured values by a K-type thermocouple where the limits of the inaccuracy of the thermocouple are as per ASTM E230 standard. Fig. 5.33(a, b) compares the peak temperature for L_{52} and M_{63} conditions on either side of the dissimilar joints at a distance of 1.6 mm from the weld centerline. The error (absolute value) for the temperature data yields ~5.17%, ~5.28% (L_{52} condition), and ~7.43%, ~5.31% (M_{63} condition) on the SS316L and SS310 sides of the FZ. Fig. 5.33(c) allows us to understand the variation of temperature at the top, middle, and root regions at the weld centerline for L_{52}, M_{63}, and H_{77} conditions. The peak temperature values extracted from the numerical model turn out as ~2032 K, ~2243 K, and ~2537 K for the cases L_{52}, M_{63}, and H_{77}, respectively. It shows a rise in the value from $L_{52} \longrightarrow M_{63} \longrightarrow H_{77}$, which is understandable due to the increasing amount of heat input. As the heat source moves away from a particular space, the value of peak temperature decreases. The maximum and minimum temperatures are seen at the W_{top} and W_{root}, respectively. As the heat source is in close contact at the top surface, the maximum temperature is seen at the W_{top}, whereas the minimum temperature is observed at the W_{root}, which is in contact with a highly conductive copper fixture. The time-temperature curve consists of two phases: heating and cooling. Once peak temperature is achieved, the heating phase is over, and the cooling phase begins. The cooling rate is evaluated by using the parameters G (temperature gradient) and R (growth rate). The value of G (K/mm) is extracted from the numerical model, and the value of R (mm/s) is substituted as the welding speed (Lee et al., 2014). The value of the cooling rate ($G \times R$) is evaluated as 1063 K/s for L_{52}, 832 K/s for M_{63}, and 583 K/s for H_{77}.

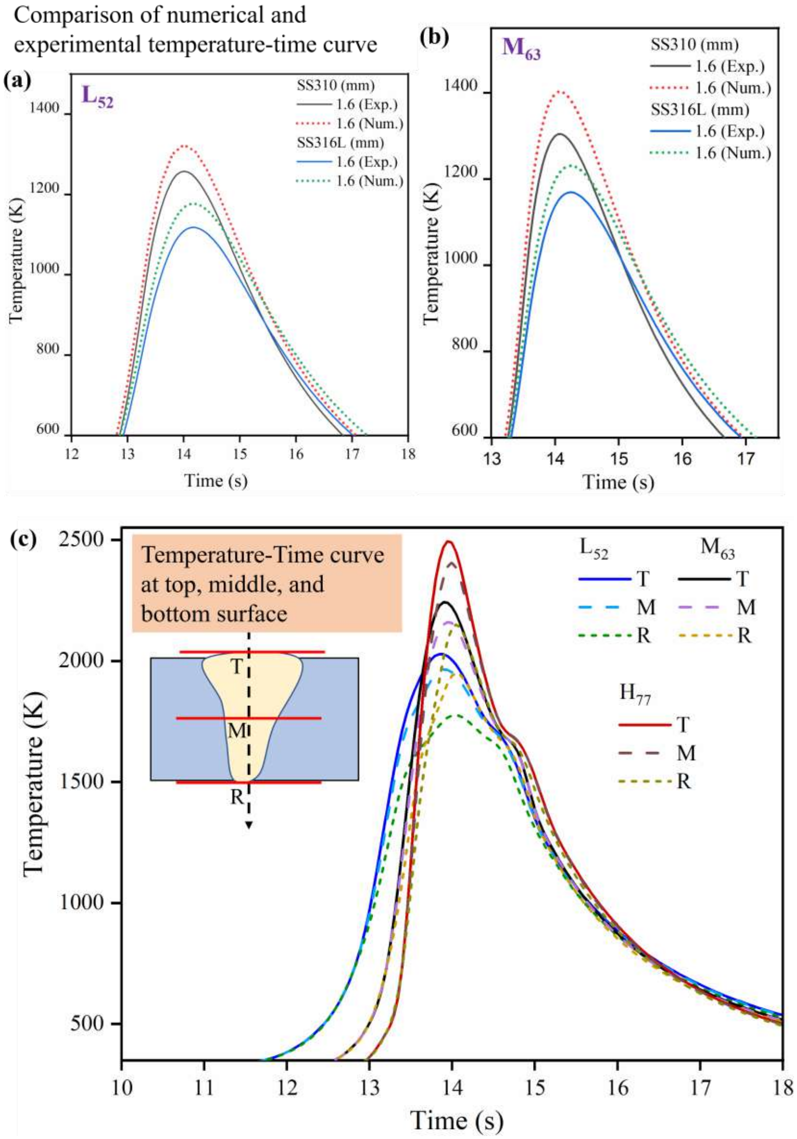

Fig. 5.33 (a, b) Compares the temperature-time history of numerical results with experimental data for L_{52}, M_{63} process conditions and (c) temperature-time profile at the top, middle, and bottom surface for L_{52}, M_{63}, H_{77} process conditions.

5.4.2 Microstructural analysis

Specimens of dimensions 10 mm × 5 mm taken out in transverse orientation are cold mounted, followed by subsequent polishing using varying SiC abrasive paper grades ranging from 400 to 2500 grit size. Specimens are further subjected to polishing using diamond paste on velvet cloth to achieve the mirror-like surface finish. Further, weld specimens are chemically etched using Glyceregia (HNO_3: Glycerol: HCl in the ratio 1:2:3) as an etchant and are observed under an optical macro/microscope and electron-microscope. The optical micrograph reveals the absence of root-sagging, cracks, undercut, or unfused region for the weldments fabricated under 'stable-weld' conditions. Fig. 5.34(a-d) depicts the different microstructural morphology and the weld joint's fusion boundary fabricated at 52 J/mm (L_{52}) weld condition. Due to a sharp thermal gradient in the direction normal to the fusion interface (indicated with arrows), the fusion interface promotes columnar dendritic structure, wherein the growth increases from the fusion interface to the FZ, as shown in Fig. 5.34(b, d).

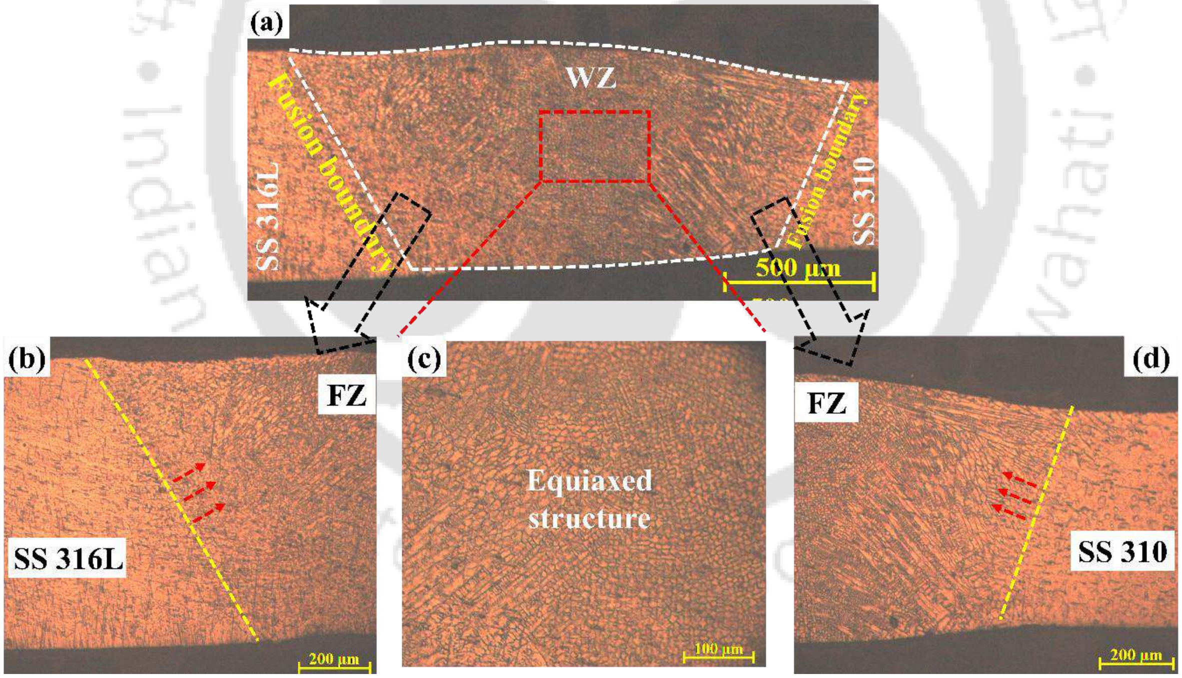

Fig. 5.34 (a-d) Optical micrographs for the L_{52} weld condition.

The FESEM images of the fusion zone for the dissimilar joints at the L_{52} condition are shown in Fig. 5.35(a-f). Fig. 5.35(a, b) depicts the fusion boundary and FZ at the two different interfaces near the SS310 and SS316L sides. Further, in the FZ, due to variations in the local cooling rate, different microstructural morphologies are observed. Due to the variation in G/R ratio, the solidification deviates from the FB to weld center (cellular in the fusion boundary, then columnar, and finally equiaxed in the weld center). In Fig. 5.35(c-f), different areas of the FZ are shown in magnified view for clear visibility of the microstructural evolution. An equiaxed structure is evident at the weld center, followed by a columnar, and cellular structure at the fusion boundary. The FZ comprises δ_{ferrite} within the $\gamma_{\text{austenite}}$ region, and the presence of both δ_{ferrite} and $\gamma_{\text{austenite}}$ (both phases) is related to the incomplete diffusional phase transformation of $\delta_{\text{ferrite}} \longrightarrow \gamma_{\text{austenite}}$ within the FZ. The specimen associated with the high heat input condition (H_{77}) results in skeletal ferrite, whereas lathy δ_{ferrite} is observed for the lowest heat input condition (L_{52}). The cooling rate ($G \times R$) controls the transformation of the phase from δ_{ferrite} to $\gamma_{\text{austenite}}$. The lower amount of heat supplied corresponds to a higher cooling rate, which offers limited duration for phase transformation, therefore restricts phase transformation from δ_{ferrite} to $\gamma_{\text{austenite}}$ in the fusion zone at lower heat input (L_{52}) (Saha and Pal, 2019). Thus, the weldments assembled at the least value of heat input (L_{52}) correspond to a higher content of δ_{ferrite} in the FZ (Huang, 2010).

A few more significant characteristics associated with the rise in the value of heat supplied are (i) an increase in the size of the equiaxed structure and (ii) an increase in dendritic length, primary, and secondary dendritic arm spacing (PDAS, SDAS) (Ragavendran and Vasudevan, 2020). Inter-relation between PDAS, SDAS, and CR is indicated in Eq. (5.4) and Eq. (5.5) (Yan et al., 2019), where CR represents the cooling rate, a, b, and c are constant values. The influence of heat input on microstructural morphology is observed in Fig. 5.36(a-d). Irrespective of the heat input, lathy and skeletal shape pattern δ_{ferrite} are identified. However, the relative amount of lathy δ_{ferrite} is directly proportional to the cooling rate. In Fig. 5.36(a, b), the lath size for the dendritic arms is shown in blue color, the δ_{ferrite} is represented in maroon color arrows, and the $\gamma_{\text{austenite}}$ matrix is shown in yellow color arrows for L_{52} and H_{77} weld conditions. The figure also depicts inter-dendritic or PDAS and SDAS. Fig. 5.36(c) depicts the FZ, fusion boundary, and the heat-affected region for the L_{52} condition; Fig. 5.36(d) shows the enlarged view in the FZ, wherein the presence of lathy δ_{ferrite} can be observed. The measurement (average value) of δ_{ferrite} lath size reveals 412 nm (L_{52}), 723 nm (M_{63}), and 1040 nm (H_{77}). It is to be noted that the low heat input (high cooling rate) condition allows limited time for the overall growth of lath size, whereas high heat input allows sufficient time for the growth of dendrites; a similar trend has been reported earlier (Kumar and Shahi, 2011). The inter-dendritic spacing (average) measures ~10 µm (L_{52}), ~15 µm (M_{63}), and ~20 µm (H_{77}). It is to be noted that the value of inter-dendritic spacing also shows an increasing trend with an increase in heat input (Yan et al., 2019).

$$\mathrm{PDAS} = a \times (\mathrm{CR})^{-b} \tag{5.4}$$

$$\mathrm{SDAS} = a \times (\mathrm{CR})^{-c} \tag{5.5}$$

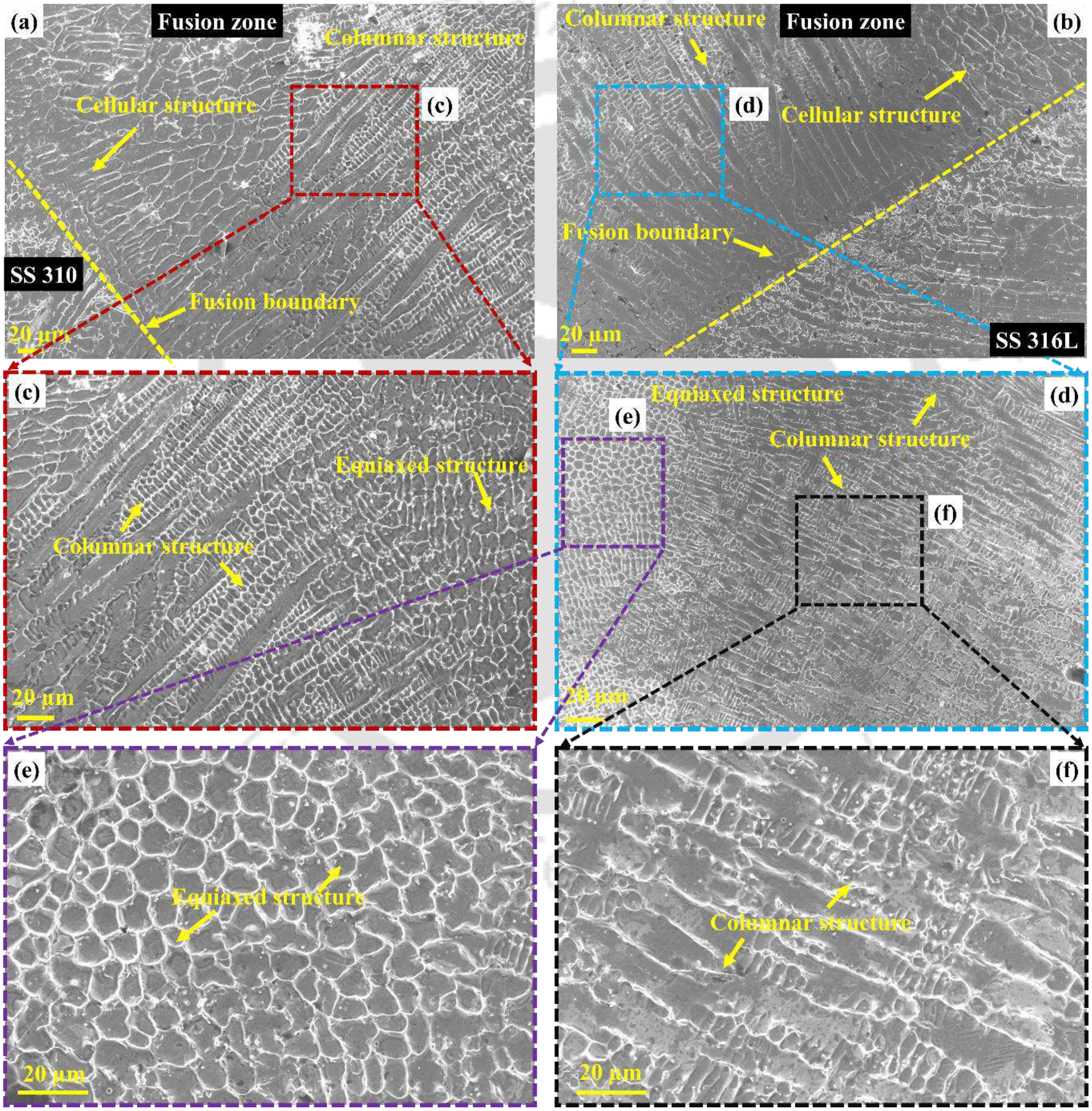

Fig. 5.35 (a-f) Illustrates the presence of various microstructural morphology near the fusion boundary and in the fusion zone for L_{52} weld condition.

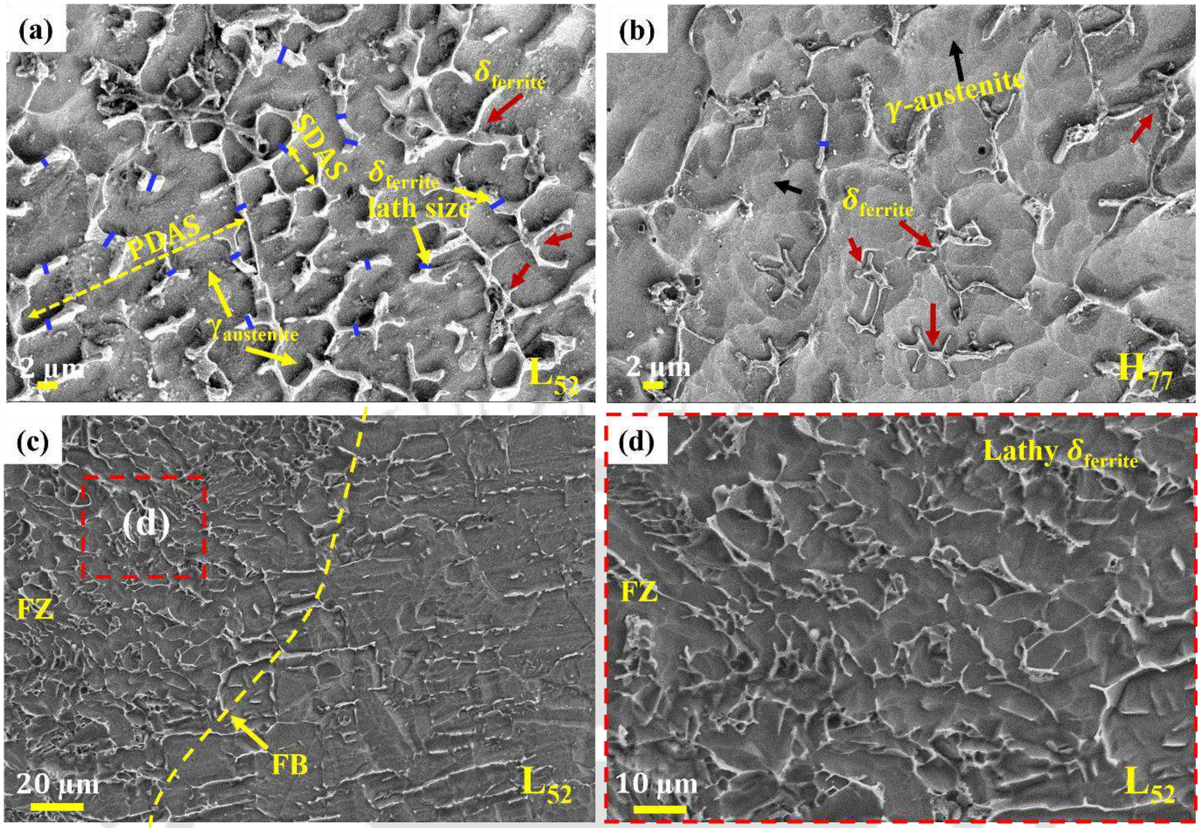

Fig. 5.36 Illustrates microstructural morphology for different process conditions (a) L_{52}, (b) H_{76}, and (c, d) L_{52}.

5.4.3 Mode of solidification

Different morphologies of the ferrite phase evolved due to the localized cooling rate variation in the solidified molten pool. Solidification of the melt pool governs the resulting metallurgical evolution in the dissimilar joints. To identify the mode of solidification, it becomes inherently necessary to calculate equivalent chromium $\left(Cr_{eq.}\right)$ and nickel equivalent $\left(Ni_{eq.}\right)$ content. An elemental analysis is carried out in the FZ, and the corresponding results are shown in Fig. 5.37(a-c). The values of $Cr_{eq.}$ and $Ni_{eq.}$ are evaluated from the elemental analysis for L_{52}, M_{63}, and H_{77} conditions. The $Cr_{eq.}/Ni_{eq.}$ ratio corresponds to the mode of solidification as austenitic (A) < 1.37, austenitic-ferritic (AF) 1.37-1.5, ferritic-austenitic (FA) 1.5-2, and ferritic (F) > 2 (Ragavendran and Vasudevan, 2020). The estimated $Cr_{eq.}/Ni_{eq.}$ ratio is evaluated as 1.77 for L_{52}, 1.65 for M_{63}, and 1.54 for H_{77}, which is marked in the Schaeffler diagram to identify the ferrite no. and also highlighted in the pseudo phase diagram of ASS

Indian Institute of Technology Guwahati

(Fig. 5.37(d, e)). Thus, from the obtained $Cr_{eq.}/Ni_{eq.}$ ratio, it is confirmed that the FZ of the dissimilar joints undergoes FA solidification mode for all three cases, leading to a dual-phase structure of ferrite (lathy) and austenite. Once the liquid melt pool starts to solidify, after 1728 K, the molten pool comprises liquid metal (L) and $\delta_{ferrite}$ (δ). On reaching 1648 K, along with L and δ, it also shows γ-phase. On complete solidification, L completely transforms into δ and γ phases. After solidification, the retained $\delta_{ferrite}$ ranges from 7-12 % for the conditions L_{52}, M_{63}, and H_{77}.

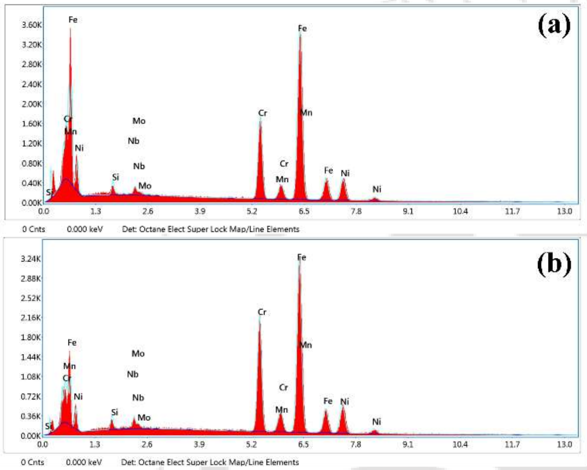

(c)

Element (wt. %)	L_{52}	M_{63}	H_{77}
Cr	23.33	21.9	19.5
Mo	1.2	1.6	2.1
Si	0.8	1.5	1.9
Nb	0.4	0.4	0.8
Ni	13.9	14.8	15.7
Mn	1.8	1.5	0.5
Fe	Bal.	Bal.	Bal.
$Cr_{eq.}/Ni_{eq.}$	1.77	1.65	1.54

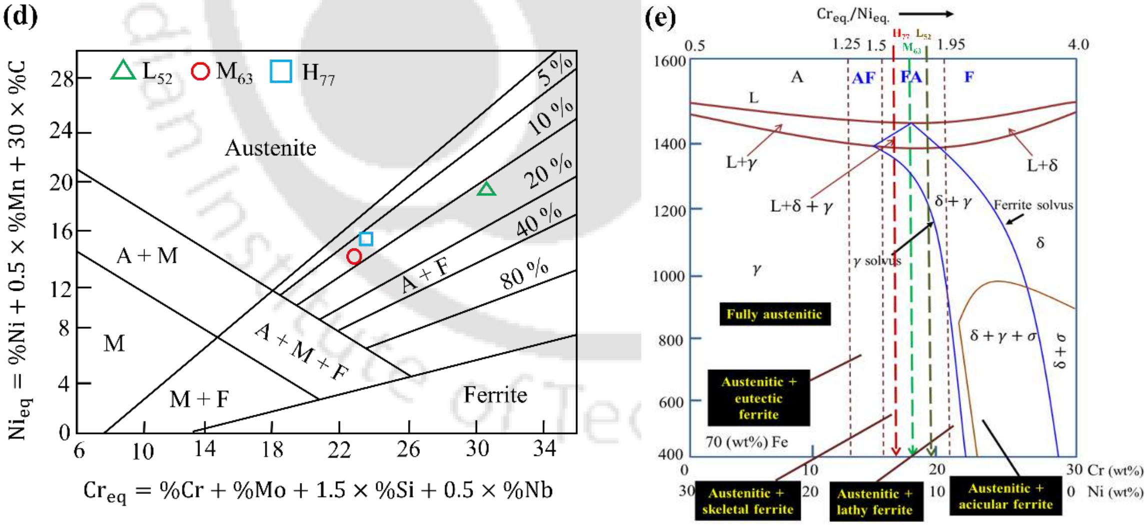

Fig. 5.37 Depicts (a, b) elemental analysis, (c) chromium and nickel equivalent calculation, the composition of dissimilar joints represented on (d) Schaeffler diagram; (e) pseudo phase diagram of ASS (Lippold and Kotecki, 2005).

The elements Cr and Ni act as ferritic and austenitic stabilizers, respectively. An increase in Cr and a decrease in Ni content is related to the rejection of Cr and absorption of Ni in the austenitic region. Thus, complete transformation fails to occur at a high cooling rate during the solidification process. This incomplete transformation forces δ_{ferrite} to be partially transformed into $\gamma_{\text{austenite}}$. The complete physics of the process is explained in Fig. 5.38(a-d).

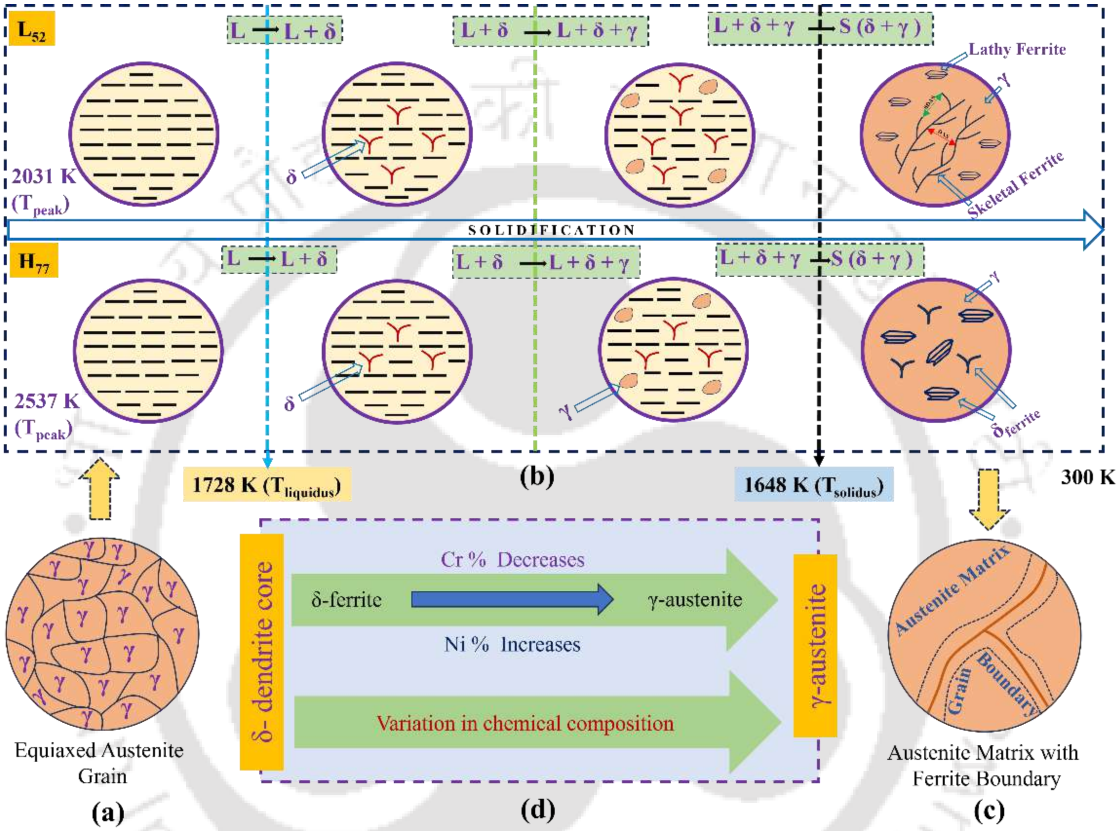

Fig. 5.38 Illustrates (a) equiaxed γ-grains, (b) schematic representation of microstructural changes for L_{52} and H_{77} process conditions, (c) austenitic matrix with ferrite-enriched dendritic core, and (d) shows the variation of Cr and Ni in the austenitic and dendritic region.

The process starts with the equiaxed grain structure of the base metal (Fig. 5.38(a)). The process follows the heating, solidification, and cooling stages. Fig. 5.38(b) illustrates solidification stages for L_{52} and H_{77} conditions, wherein FA solidification prevails. The solidification stages for L_{52} and H_{77} conditions can be stated as: $L \rightarrow L + \delta \rightarrow L + \delta + \gamma \rightarrow \delta + \gamma$. During the $L + \delta$ stage, a high cooling rate (1063 K/s) results in the formation of more amount of δ_{ferrite} in the L_{52} condition compared to a low cooling rate (583 K/s) in the H_{77} condition. Just before T_{solidus}, $L + \delta + \gamma$ a mixture exists together for a short-lived period.

The formation of $\gamma_{austenite}$ results from the complete transformation of $\delta \longrightarrow \gamma$. As shown in Fig. 5.38(b), the transformation of $\delta \longrightarrow \gamma$ is caused by the combination of Cr in the dendritic region and the dissociation of Ni from the austenitic matrix. In the final stage, the temperature reaches from $T_{solidus}$ to T_{room}, which results in a microstructure comprising both phases ($\delta + \gamma$). Here, the lathy and skeletal shape pattern $\delta_{ferrite}$ is identified. Fig. 5.38(c) shows the completely transformed austenitic matrix with enriched dendritic core ferrite boundary. Fig. 5.38(d) illustrates the complete transformation ($\delta \longrightarrow \gamma$) and the existing variation in the elemental composition of the dendritic core and austenitic region. Due to the presence of $\delta_{ferrite}$ in the dendritic core region, the percentage of Cr is high, whereas in the austenitic region, Ni content is high.

5.4.4 Elemental analysis of fusion zone and weld interface

Fig. 5.39(a-c), Fig. 5.40(a, b), and Fig. 5.41(a-f) illustrate point, line, and area mapping analysis for selected regions in the FZ for sample L_{52} weld condition. In Fig. 5.39(a), point elemental analysis is carried out for two spectrums: the first point (spectrum 1, shown in Fig. 5.39(b)) is selected inside the austenitic region, and the second (spectrum 5, shown in Fig. 5.39(c)) is selected in the dendritic ferrite region. Ni is an austenitic stabilizer, and Cr is a ferritic stabilizer; therefore, the elemental analysis indicates the predominant variation of Cr and Ni in the austenitic and dendritic regions. The austenitic region shows higher Ni content, whereas the dendritic region shows higher Cr content. It is observed that phase transformation from $\delta_{ferrite} \longrightarrow \gamma_{austenite}$ relies on diffusion, with pct. of Cr increasing from ~19% (austenitic region) to ~25% (dendritic region), and percentage of Ni decreasing from ~14% (austenitic region) to ~9% (dendritic region). Fig. 5.40(a, b) illustrates the line elemental analysis for a selected length of 100 µm, in which the variation of all the elements can be observed, especially Cr and Ni. A peak in the Cr line (pink color) can be observed as it crosses the dendritic region, whereas a peak in the Ni line (cyan color) can be seen as it passes through the austenitic matrix. Iron (Fe) is present in maximum percentage; thus, red (color) remains at the top.

Fig. 5.41(a-f) shows the FESEM image and area elemental analysis, in which the presence of major elements such as Fe (60.9%), Cr (23.2%), and Ni (12.8%) can be observed. As oxygen is not visible in any of the elemental analysis, it can also be concluded that the FZ is free from oxidation. Due to Cr being ferritic and Ni being an austenitic stabilizer, an increase, and decrease in Cr and Ni content is related to the rejection of Cr and absorption of Ni in the austenitic region. Thus, it can be confirmed that complete transformation fails to occur during the solidification process due to a high cooling rate. Due to this incomplete transformation, $\delta_{ferrite}$ is transferred to $\gamma_{austenite}$.

Fig. 5.42(a, b, e, f) illustrates the base metals (BM) (SS310, SS316L), HAZ, FB, and FZ and Fig. 5.42(c, d, g, h) presents the line spectrum at the interface of the weld joints for a better understanding of the elemental diffusion across the FZ, HAZ, and BMs. The line spectrum shows consistency in the elemental analysis with no significant rise/sudden drop in the major elements like Fe, Cr, and Ni.

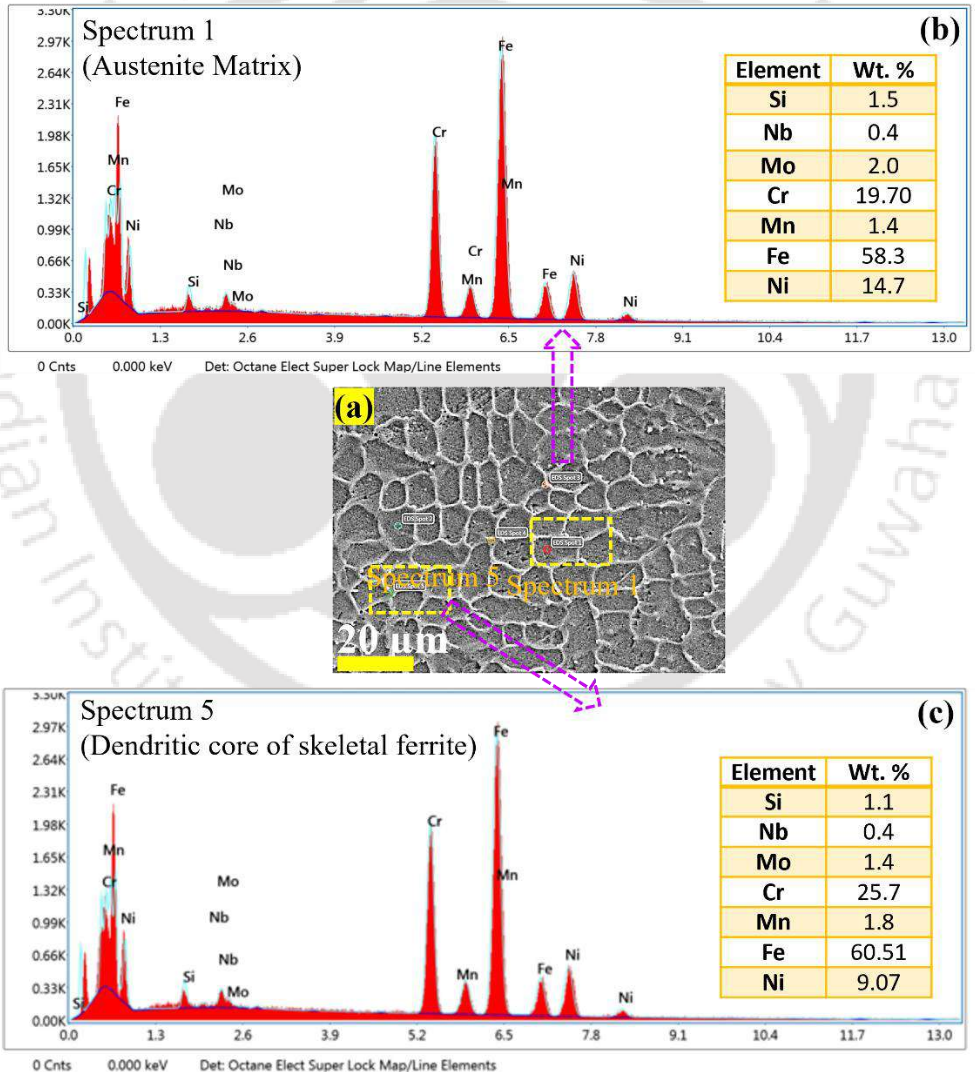

Element	Wt. %
Si	1.5
Nb	0.4
Mo	2.0
Cr	19.70
Mn	1.4
Fe	58.3
Ni	14.7

Element	Wt. %
Si	1.1
Nb	0.4
Mo	1.4
Cr	25.7
Mn	1.8
Fe	60.51
Ni	9.07

Fig. 5.39 (a-c) Illustrates the point spectrum in the weld center of the fusion zone for the L_{52} weld condition.

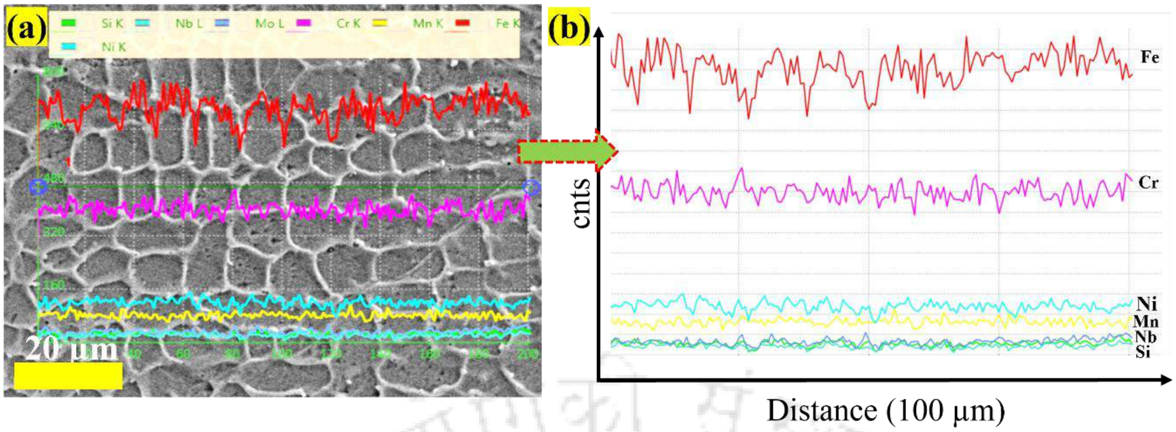

Fig. 5.40 (a, b) Illustrates the point spectrum in the weld center of the fusion zone for the L_{52} weld condition.

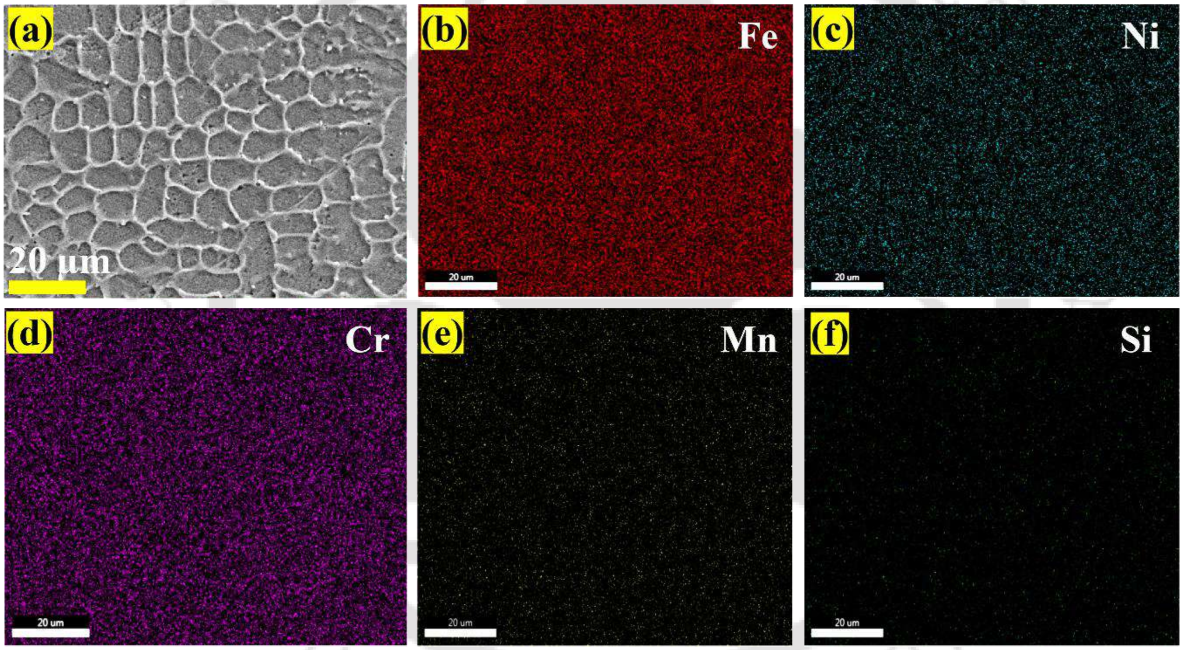

Fig. 5.41 Illustrates (a) FESEM image and (b-f) area mapping in the weld center of the fusion zone for the L_{52} weld condition.

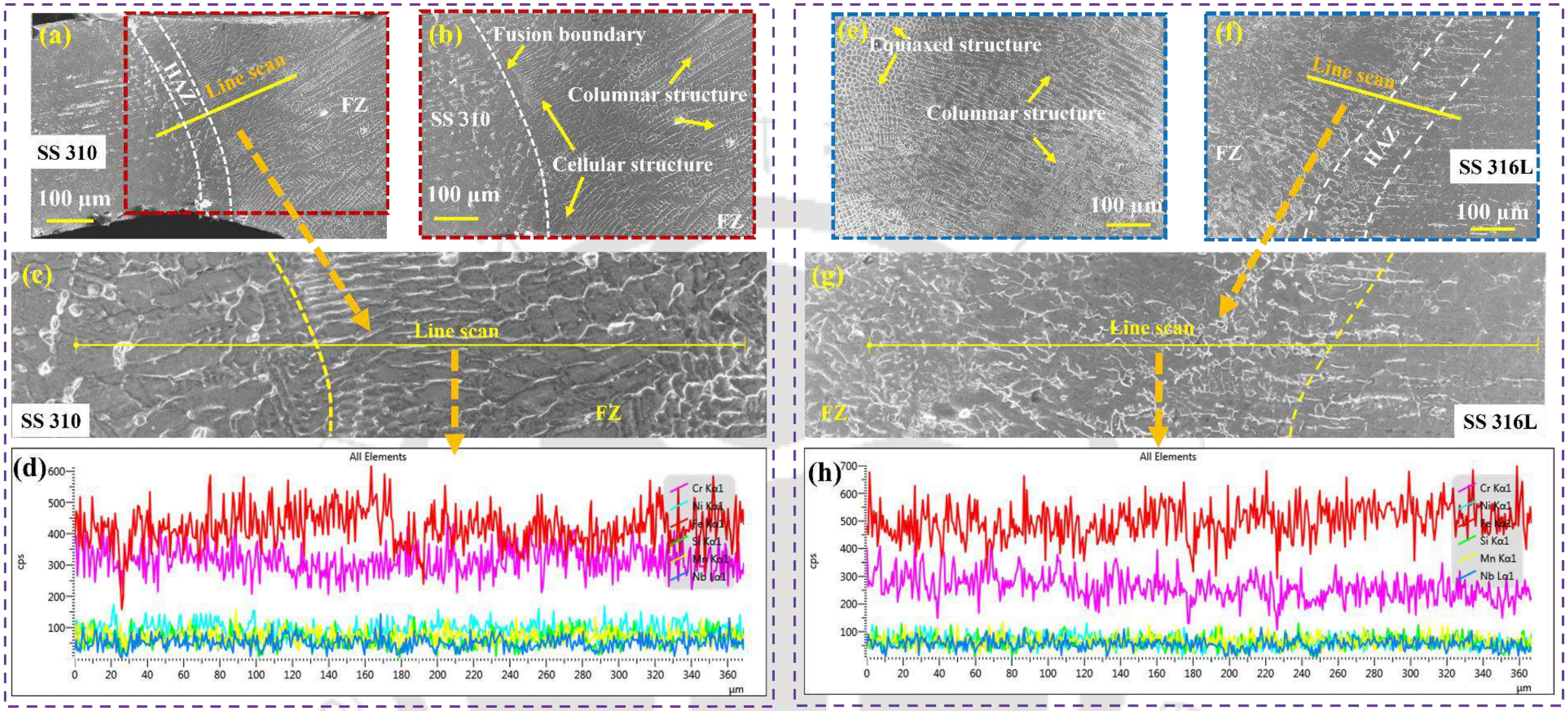

Fig. 5.42 Illustrates (a, b, e, f) microstructure of base metals: HAZ, fusion boundary, and fusion zone; (c, d, g, h) represents the line spectrum at the interface of the weld joint for the L_{52} process condition.

5.4.5 Prediction of phase fraction

During the cooling phase, the initial phase fractions of $\gamma_{austenite}$ and $\delta_{ferrite}$ at $T_{solidus}$ are arbitrarily considered as 4-5% and 95-96%, respectively (Lippold and Kotecki, 2005). During solidification, once the temperature falls below $T_{solidus}$, unstable $\delta_{ferrite}$ goes into the $\gamma_{austenite}$ matrix due to elemental diffusion, wherein the crystal structure changes from BCC ($\delta_{ferrite}$) to FCC ($\gamma_{austenite}$). The BCC ⟶ FCC transformation corresponds to volumetric enlargement; thus, the proportion of ferrite decreases, and the amount of austenite increases. The complete phase transformation ($\delta_{ferrite} \longrightarrow \gamma_{austenite}$) fails to occur below 1273 K (γ finish temperature), and some ferrite content is retained in the FZ, which remains as retained ferrite. Fig. 5.43(a-c) illustrates the transformation of $\delta_{ferrite}$ to $\gamma_{austenite}$ and retained ferrite concerning temperature and time.

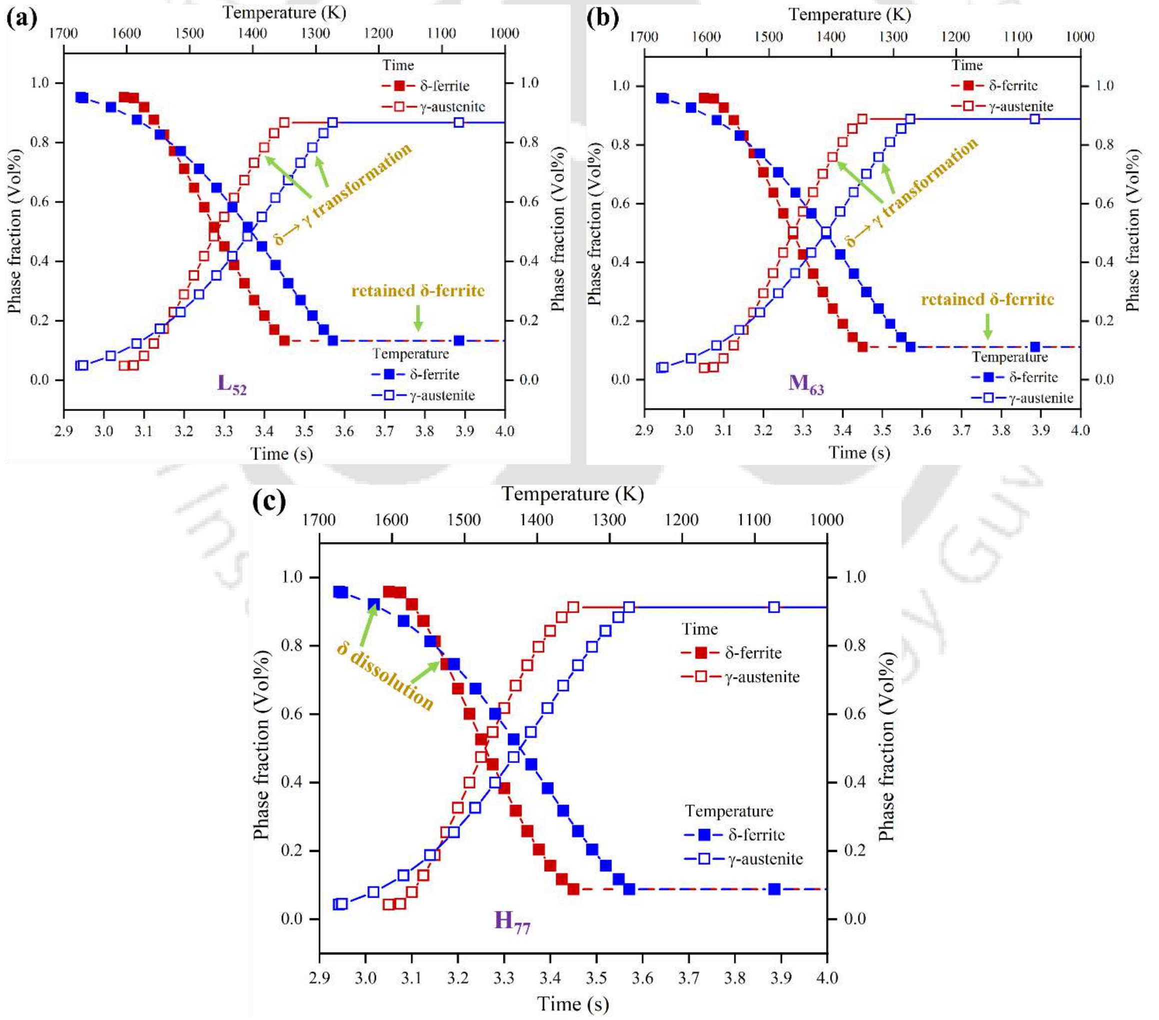

Fig. 5.43 Illustrates $\delta_{ferrite} \rightarrow \gamma_{austenite}$ transformation for different process conditions (a) L_{52}, (b) M_{63}, and (c) H_{77}.

The slope of the phase diagram for the experimental and numerical conditions shows a considerable variation due to the high cooling rate achieved in the FZ. The percentage of retained ferrite using the numerical model is predicted as ~13.1% for L_{52}, ~11.2% for M_{63}, ~8.8% for H_{77}, and the remaining fraction comprises an austenite matrix in the FZ. Fig. 5.44 shows a satisfactory comparison between numerical results and the data determined from the Seferian relation (Lippold and Kotecki, 2005).

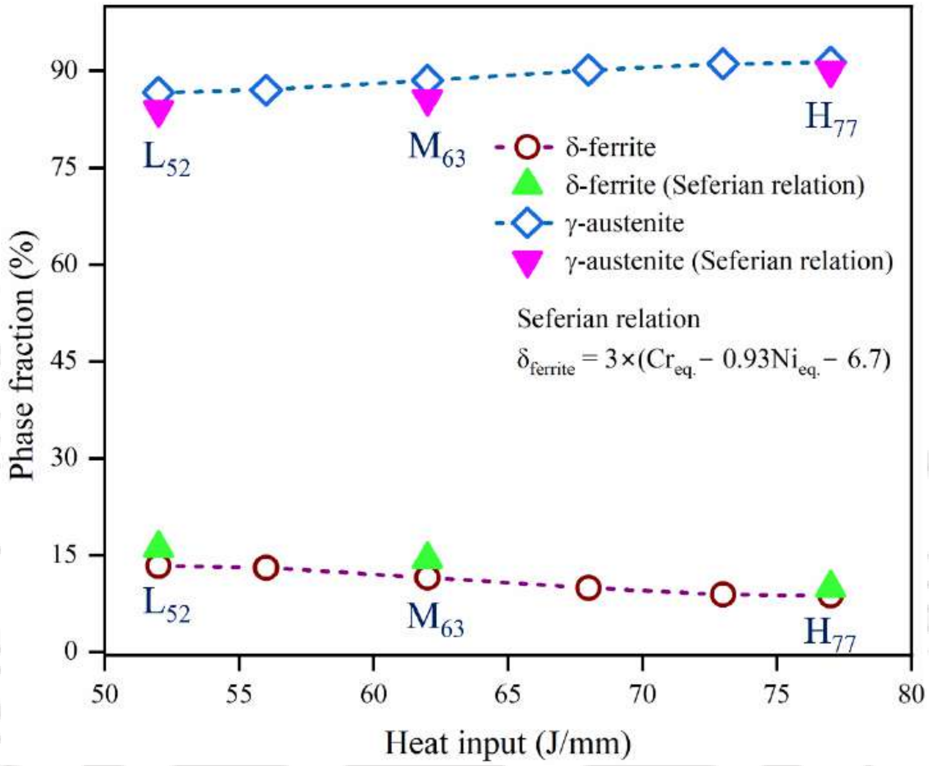

Fig. 5.44 Compares $\delta_{ferrite}$ and $\gamma_{austenite}$ fraction numerical results with Seferian relation.

Fig. 5.45(a-d) depicts the FESEM spectrum of the solidified fusion zone along with calculated $\delta_{ferrite}$ volume fraction at three different heat inputs. A Gaussian blur is applied before applying a manual threshold to determine the volume percentage of the $\delta_{ferrite}$ phase. This comprises converting an unprocessed image (RGB) to a greyscale (8-bit) image, which is then thresholded to generate a binary (black and white) image. Accordingly, the $\delta_{ferrite}$ is identified as white-branched skeletons in the black region (matrix), as depicted in Fig. 5.45(b). The fraction measurements are performed using the standard manual point count method (ASTM, 2011), in which a grid of points is superimposed on the microstructural images illustrated after thresholding using ImageJ software. The ratio of the total number of points occurring in the phase that is of interest to the total available number of grid points is obtained, and this ratio yields the estimated statistical value of the phase in volume fraction. The dual-phase microstructure clarifies the incomplete phase transformation from $\delta_{ferrite}$ to $\gamma_{austenite}$. Fig. 5.45(c, d) displays dampening of skeletal-structured $\delta_{ferrite}$ phase fraction from 11.2% → 7.9% upon increasing heat input from 52 → 77 J/mm. Higher heat input provides the platform for the dissolution of $\delta_{ferrite}$ into the $\gamma_{austenite}$ matrix, which leads to the diffusional transformation of $\delta_{ferrite}$ to $\gamma_{austenite}$. The error in the numerically predicted values of $\delta_{ferrite}$ compared to the experimental values is evaluated as ~16% for L_{52}, ~15% for M_{63}, and ~11% for H_{77} process conditions.

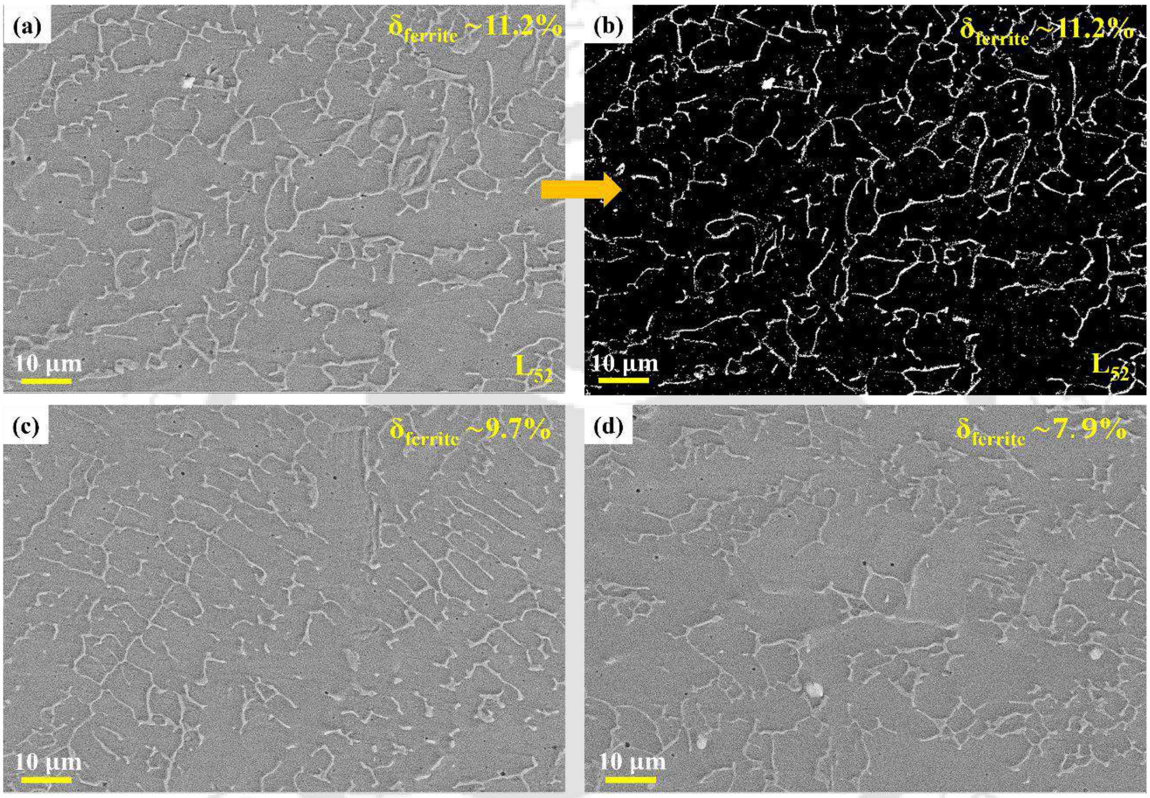

Fig. 5.45 Illustrates retained percentage of $\delta_{ferrite}$ at different process conditions (a, b) L_{52}, (c) M_{63}, and (d) H_{77}.

5.4.6 XRD analysis

Fig. 5.46(a) illustrates the XRD pattern of the FZ, and the intensity counts are depicted in Fig. 5.46(b). The planes (111), (200), (220), and (222) represent $\gamma_{austenite}$ peaks, and the plane (110) corresponds to $\delta_{ferrite}$ peak. Intensity counts (intensity peak) directly relate to the quantity of phases available in the inspected region (Bansal et al., 2016). The intensity counts of the γ (111), γ (200), γ (220), γ (222), and δ (110) show a decreasing trend as the heat input increases. The decreasing intensity of the γ-phase is related to incomplete transformation ($\delta_{ferrite} \longrightarrow \gamma_{austenite}$), which is elaborated under the mode of solidification (section 5.4.3) in Fig. 5.38. The case of δ (110) also shows a decreasing trend with increasing heat input. The highest count is observed for the L_{52} (~ 1063 K/s) weld condition. A higher cooling rate reduces the time available for the conversion of $\delta_{ferrite}$ to $\gamma_{austenite}$. Therefore, an increase in the cooling rate leads to a higher amount of $\delta_{ferrite}$ (Kumar et al., 2021b).

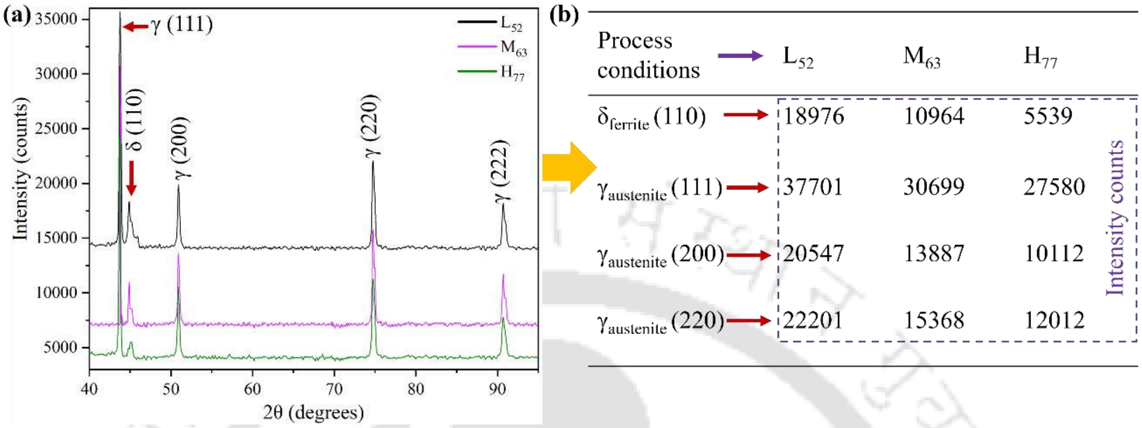

Process conditions →	L_{52}	M_{63}	H_{77}
$\delta_{ferrite}$ (110) →	18976	10964	5539
$\gamma_{austenite}$ (111) →	37701	30699	27580
$\gamma_{austenite}$ (200) →	20547	13887	10112
$\gamma_{austenite}$ (220) →	22201	15368	12012

Fig. 5.46 Illustrates (a) XRD pattern in the FZ for L_{52}, M_{63}, and H_{77} process conditions and (b) intensity counts for $\delta_{ferrite}$ and $\gamma_{austenite}$.

5.4.7 EBSD analysis and misorientation angle distribution

EBSD analysis for the base metals and the fusion zone at different process conditions is conducted, and the grain size variation with inverse pole figure (IPF) maps is depicted in Fig. 5.47. The IPF maps of the base metals are shown in Fig. 5.47(a). It provides the grain size variation throughout the area fraction, from 1.39 μm to 37.06 μm for SS316L and from 1.39 μm to 45.89 μm for SS310. The average grain size for the base metals is 7.42 μm for SS316L and 9.63 μm for SS310. Fig. 5.47(b) depicts the fluctuation in grain size with heat input, where a rise in heat input results in increased grain size. An increase in heat input leads to a slower cooling rate, which provides more time for the grains to grow. The increase in grain size can be observed from the IPF maps, where the grain diameter varies from 3.55 μm to 211.71 μm for L_{52}, 2.87 μm to 247.22 μm for M_{63}, 5.65 μm to 426.27 μm for H_{77}. The average grain size is evaluated as 28.68 μm for L_{52}, 42.57 μm for M_{63}, and 58.53 μm for H_{77}. Fig. 5.47(b) also illustrates the IPF maps for all three cases, L_{52}, M_{63}, and H_{77}. Further, the enlarged view of IPF maps for L_{52}, M_{63}, and H_{77} conditions is shown in Fig. 5.47(c-e). Fig. 5.47(f) represents the color legend of the IPF map. Fig. 5.47(g, h) denotes the misorientation angle and the frequency with which it occurs. It enables us to understand the presence of low-angle grain boundaries (LAGBs, $2^{\circ} < \theta < 15^{\circ}$), and high-angle grain boundaries (HAGBs, $15^{\circ} < \theta < 65^{\circ}$). The LAGB and HAGB are relatively similar for the base materials, whereas LAGB and HAGB vary with heat input. The percentage of LAGBs increased (23.64 ⟶ 38.16 ⟶ 48.99%), and HAGBs decreased (76.36 ⟶ 61.48 ⟶ 51.01%) with increased heat input value. Thus, it can be concluded that an increase in heat input value leads to a decrease in HAGBs. The relative decline in HAGBs or increase in LAGBs results from a high cooling rate. As the solidification rate decreases, the FZ is in a state of extreme non-equilibrium, corresponding to the formation of high-density LAGBs (Jiang et al., 2020, 2016). Also, fatigue resistance positively correlates with residual stress value; in other words, low-density LAGBs lead to a lower value of stresses developed (Zhang et al., 2021a, 2021b).

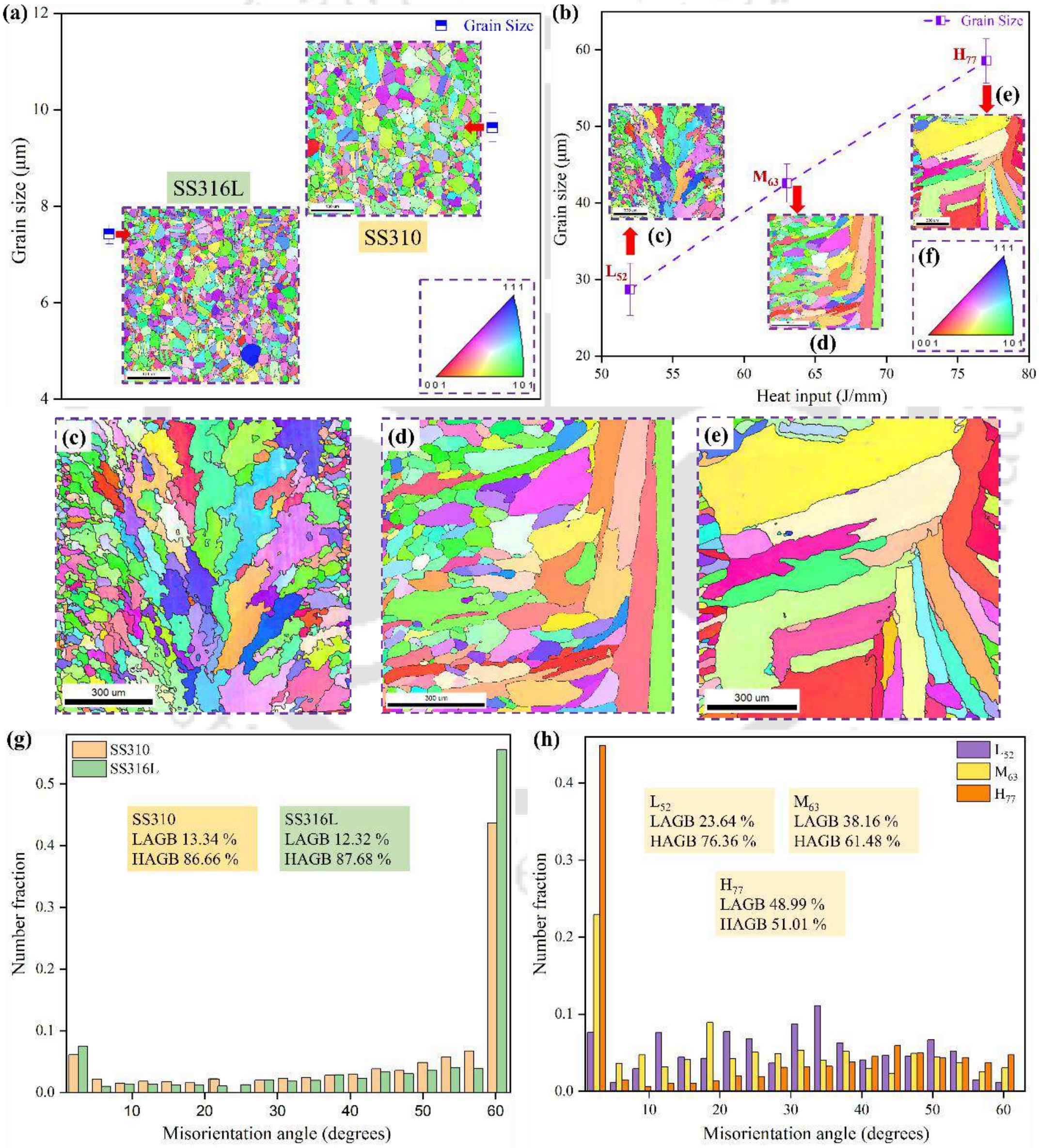

Fig. 5.47 Grain size and IPF maps for (a) base metals, (b) at different heat inputs L_{52}, M_{63}, and H_{77}, (c-e) IPF maps for L_{52}, M_{63}, and H_{77}, (f) IPF color coding, and (g, h) misorientation angle distribution.

5.4.8 X-ray CT analysis

To identify the internal defects in the weld joints in 3D, X-ray computed tomography (X-ray CT) equipment is employed. X-ray CT testing and evaluation consists of two units, i.e., the testing unit and an analysis unit. The testing unit comprises a rotary plate on which the specimen is placed. The sample is revolved one step at a time, acquiring projected images at every rotated position. The projected picture is consecutively re-constructed to a 3-D figure in the analysis unit (Kastner and Heinzl, 2018). Porosity in weld joints leads to a significant deterioration in joint strength; therefore, to analyze the effect of heat input on pore formation, the weld joints are subjected to X-ray CT analysis. Fig. 5.48(a-c) depicts reconstructed transparent images for the weld joints fabricated at different weld conditions (52 J/mm-L_{52}, 63 J/mm-M_{63}, and 77 J/mm-H_{77}), illustrating pores of different volume. Fig. 5.48(a-c) illustrates reconstructed images at a voxel size of 8 µm, which indicates that pores having a diameter of 8 µm or more can be detected by the X-ray CT machine. Fig. 5.48(d-f) shows the defect volume (µm^3) corresponding to pores for different weld conditions. From Fig. 5.48(d-f), the defect volume can be identified, and further quantification of the number of pores and their corresponding sizes is done using the software package Phoenix-Datox®.

Fig. 5.49(a) shows the pore diameter and their corresponding frequency of occurrence. Formation of pores results due to (i) dissolved/entrapped gases or/and (ii) shrinkages cavities in the weldments. As the pores are spherical, the most probable justification for pores' emergence is likely to dissolve/entrapped gasses (Kar et al., 2019). Fig. 5.49(b, c) represents the influence of heat input on pore formation. The number of pores along with the largest pore size follows an increasing trend with values (6, 18.25 µm) for L_{52}, (53, 181.82 µm) for M_{53}, and (90, 374.92 µm) for H_{77}. Weld joints formed at a higher value of heat input (H_{77}) result in a lower cooling rate, which benefits the formation and development of pores by propagation and merging pores of smaller size, leading to larger dimensions. Whereas weldments fabricated at a lower value of heat input (L_{52}) prevent the pores' growth, resulting in a limited number and size of pores. As per ISO 13919-2, related to the acceptable limit of the pore size, the maximum gas porosity in the joints should be less than the maximum value of 600 µm (Chen et al., 2018). In the present analysis, the maximum pore diameter is 374.92 µm, which is within the acceptable limit.

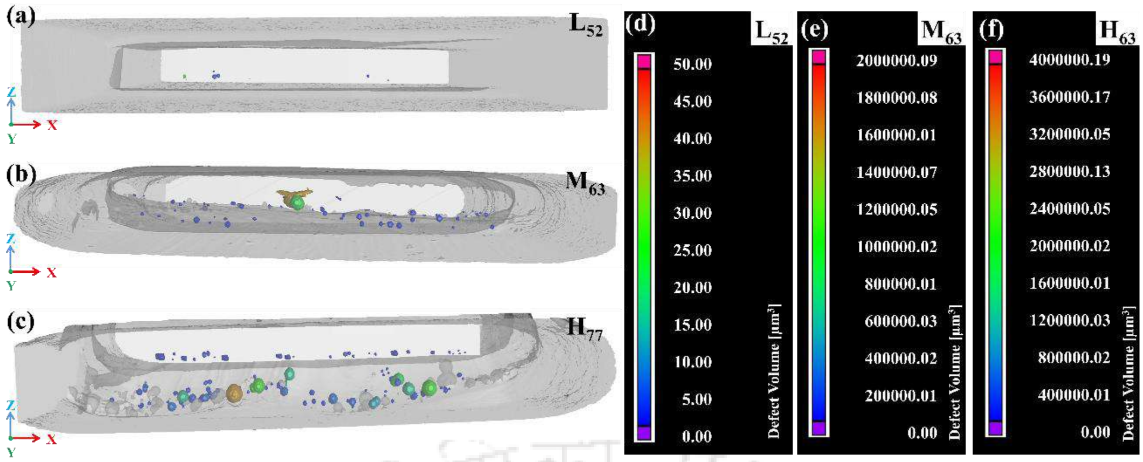

Fig. 5.48 Illustrates (a-c) reconstructed transparent images (longitudinal direction) and (d-f) defect volume corresponding to pores formed at different weld conditions (L_{52}, M_{63}, and H_{77}).

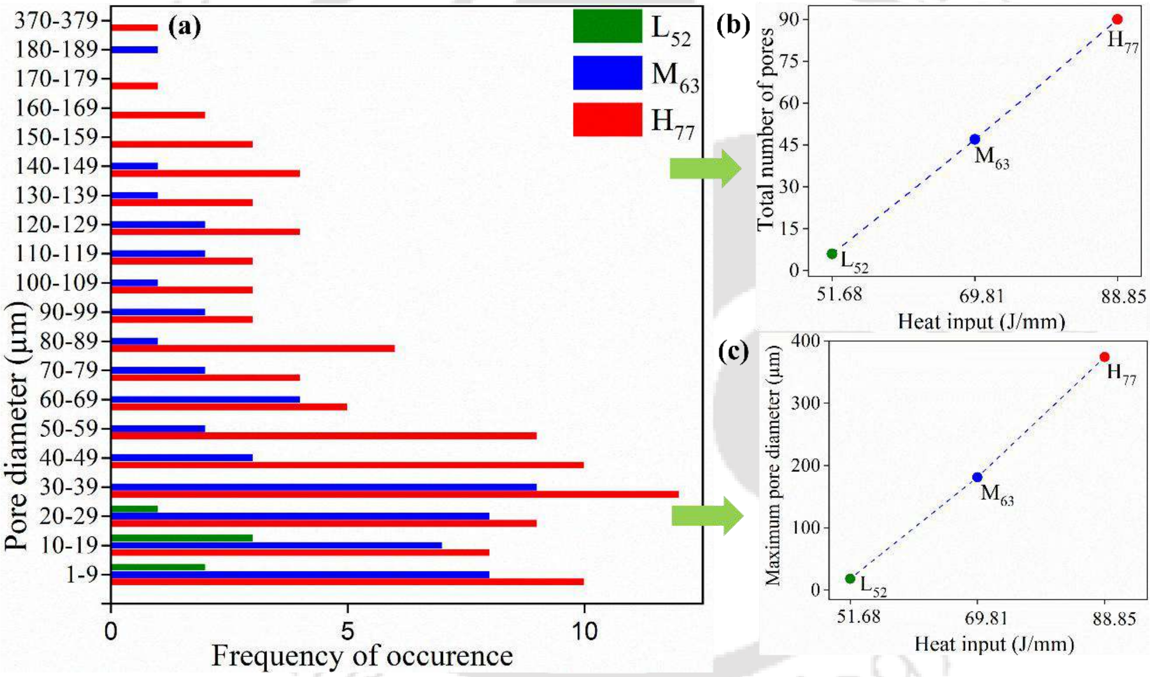

Fig. 5.49 Illustrates (a) pore size vs frequency of occurrence and (b, c) the total number of pores and maximum pore size variation with heat input.

5.4.9 Evaluation of mechanical properties

Tensile coupons are taken out in a transverse direction for the dissimilar ASSs weld joint fabricated at varying heat input values and subjected to uniaxial tension tests. Fig. 5.50(a) represents a sub-size tensile specimen as per the ASTM E8 standard with 25 mm gauge length and 6 mm width. The tensile test is accomplished at ambient temperature using a uniform rate of 0.5 mm/min. Fig. 5.50(b) illustrates the engineering stress-strain curve, and the images explaining the location of the failure are shown in Fig. 5.50(c). Failure is identified in the fusion zone and a similar situation is observed in all three weld conditions, i.e., failure occurring in the fusion zone. As repeatability is a concern in the welding process, primarily when a new process is being evaluated for a new combination of materials, three repetitions for each set of experiments are performed, and the average values are reported.

The ultimate tensile strength (UTS) value of the base materials SS316L and SS310 are 610 MPa and 540 MPa. The determined average UTS values for different weld joints are 618 MPa (L_{52}), 577 MPa (M_{63}), and 542 MPa (H_{77}). The corresponding joint efficiency is determined, which is evaluated as $\mathrm{UTS}_{\text{weld joint}}/\mathrm{UTS}_{\text{base material}}$, wherein the UTS of the base material is taken as the minimum value, i.e., SS310. Evaluated values of joint efficiency are identified as ~115 % (L_{52}), ~107 % (M_{63}), and ~101 % (H_{77}), which shows a decreasing trend with the rise in heat input. The decreasing trend in strength is due to the extended PDAS and SDAS in the fusion zone (Kumar and Shahi, 2011). The variation in joint strength is related to the microstructural evolution of finer equiaxed dendritic morphology for L_{52}, followed by M_{63} and H_{77}. The joint efficiency value for all the weld joints suggests that the fabricated weldments exhibit an efficiency of more than one hundred percent for all welding conditions. As the failure occurs in the fusion zone, therefore the fusion zone is marked as the weakest region in the resulting joints. The fracture surfaces are subjected to SEM analysis for further evaluation to identify the mode of failure and presence of foreign particles.

Fig. 5.50(d-f) displays the electron microscopic images of the fracture surface for the weld joints fabricated at different heat input values (52 J/mm- L_{52}, 63 J/mm- M_{63}, and 77 J/mm-H_{77}). Prominent features visible on the fracture surface include dimples and micro/macro-pores. The occurrence of micro/macro-pores displays an increasing nature with the rise in heat input. The joint assembled with a lower amount of heat input is identified with a large number of dimples of different dimensions, indicating a significant amount of energy absorbed before failure, leading to ductile fracture (Kumar and Shahi, 2011). In contrast, micro/macro-pores presence modifies the fracture manner to mixed-mode failure (Devendranath Ramkumar et al., 2015). The absence of any form of contamination in the weldments is confirmed by elemental (energy dispersive x-ray analysis) examination of the fracture surfaces.

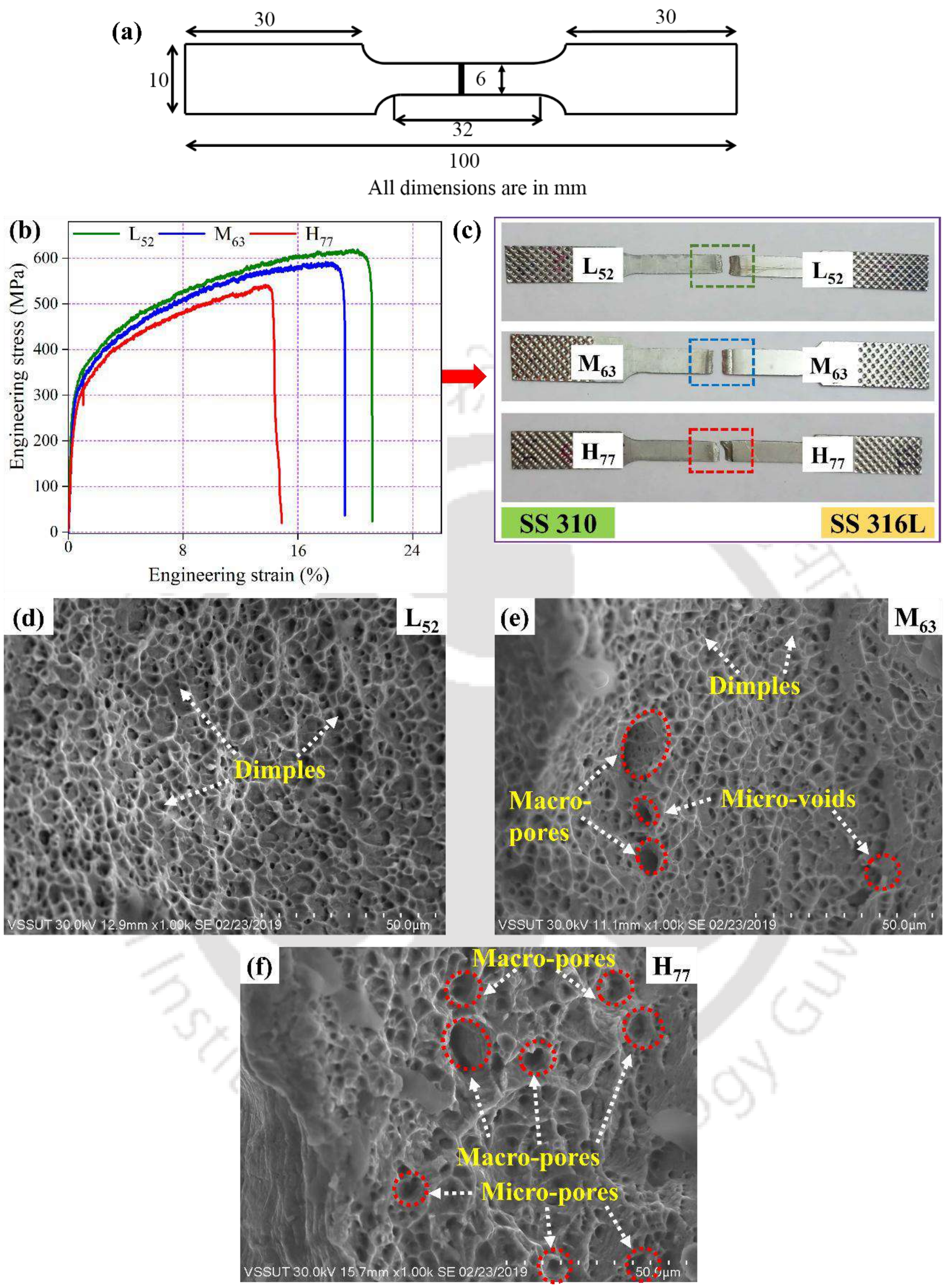

Fig. 5.50 Depicts (a) tensile specimen as per ASTM E8 standard, (b) engineering stress-strain curve, (c) photograph of failed tensile test specimens, (d-f) electron microscopic images of the fracture surface for the weld joints fabricated at different process conditions (L_{52}, M_{63}, and H_{77}).

Microhardness determination is carried out in two different orientations, i.e., perpendicular (top to bottom) and parallel (across) to the weld joint. Measurement is carried out with a load of 500 g for a dwell duration of 10 s. Fig. 5.51 displays the resulting Vickers hardness number (VHN) values plotted across the weld joint. In Fig. 5.51, the x-axis represents the location at which Vickers microhardness is measured, i.e., the fusion zone and the distance on either side of the fusion zone, and the y-axis represents the value of VHN. In the measurement of VHN in the perpendicular direction, the values of VHN measured close to the upper surface of the weld is identified to be comparatively higher and moderately reduces as the indenter head towards the weld center, such variation in VHN results due to non-uniform cooling in the FZ. As the upper surface of the fusion zone is exposed to the atmosphere, all three heat transfer modes prevail, which corresponds to a higher amount of heat losses; hence, a higher cooling rate is achieved for the upper surface compared to the weld center. Meanwhile, in evaluating VHN across the weld, the value of VHN increases from the weld center to the fusion boundary and then decreases. The value of VHN varies from weld center-weld interface-HAZ (SS316L/SS310) as 157-168-158 VHN (SS316L side) and 157-196-188 VHN (SS310 side) for L_{52}, 142-152-147 VHN (SS316L side) and 142-182-177 (SS310 side) for M_{63}, 130-142-135 (SS316L side) and (130-172-167) (SS310 side) for H_{77}.

The increase in the VHN value from the weld-center to the fusion boundary is justified by the high cooling rate achieved in the weld interface compared to the weld center. Further, the value of VHN decreases due to the existence of coarser grain in the HAZ, resulting from the low cooling rate. Significant findings achieved from the microhardness analysis reveals that (i) the value of microhardness shows an increasing trend following the sequence as fusion zone, HAZ, and weld interface for the weld joints fabricated at different values of heat input; (ii) for L_{52} (52 J/mm), the value of microhardness is found to be the highest than the weld joints assembled with higher heat input values (M_{63}/H_{77}), which is as a result of a high rate of cooling leading to the formation of finer equiaxed dendritic morphology. In Fig. 5.51, variation in Vickers hardness is shown in the (i) fusion zone, (ii) weld interface, and (iii) the HAZ. It should be noted that the value of hardness is shown up to the HAZ, because beyond the HAZ (i.e., in the base materials), the hardness value remains constant across for all three weld conditions.

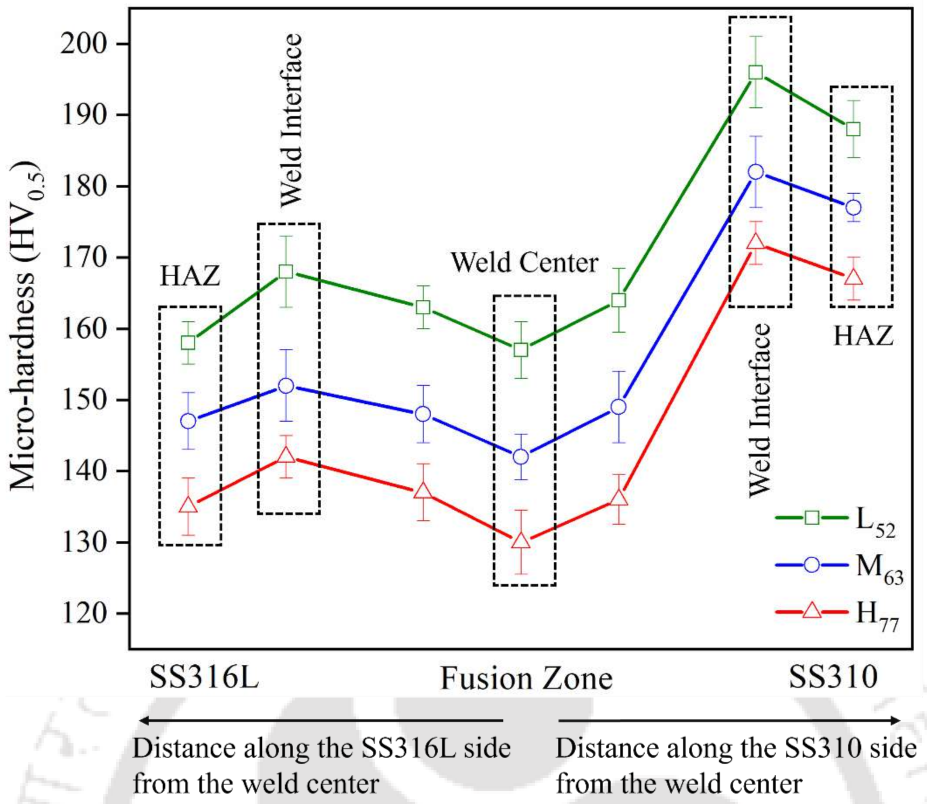

Fig. 5.51 Depicts VHN variation along the different zones for the weld joints fabricated at different process conditions (L_{52}, M_{63}, and H_{77}).

5.4.10 Potentiodynamic polarization evaluation

Base materials and weld joints prepared at different heat input values are individually subjected to a potentiodynamic polarization test inside an experimental setup shown in Fig. 5.52(a) that yields the potentiodynamic polarization graph or Tafel plot, presented in Fig. 5.52(b). Using the Tafel slope computed from the Tafel curve, I_{corr} (corrosion current density); E_{corr} (current potential) are identified and presented in Table 5.10. Tafel plot reveals that corrosion resistance is highest for the joints assembled with the least heat input (L_{52}), and the joints fabricated with the highest heat input (H_{77}) shows the least corrosion resistance. It is a well-known fact that resistance to corrosion increases with a higher level of chromium. A lower amount of heat supplied corresponds to the evolution of (i) a high level of retained $\delta_{ferrite}$ (11.2 %), which contains higher chromium content than the austenitic phase (Valiente Bermejo, 2012) and (ii) limited formation of chromium carbide, leading to higher chromium content (Devendranath Ramkumar et al., 2015). The decrease in corrosion resistance is due to inter-granular corrosion (IGC) phenomena, illustrated in Fig. 5.52(c). During service operation, the temperature reaches around 450-650 °C, and if maintained for a longer duration, chromium carbide nucleates along the grain boundaries.

The region surrounding the grain boundary is depleted with chromium, surrounded by a part having sufficient chromium content. Thus, the area with the lowest percentage of chromium is more susceptible to corrosion, leading to IGC. Fig. 5.52(d) illustrates the variation of chromium percentage with heat input, which is estimated using Energy Dispersive X-ray Analysis (EDX). The reason for such a difference in the percentage of chromium is the high cooling rate for L_{52}, resulting in a high level of $\delta_{ferrite}$ and a limited formation of chromium carbide (Devendranath Ramkumar et al., 2015; Gil et al., 1988). Also, as the heat input increases, the chances of melting a greater amount of SS316L are higher compared to SS310, due to the lower liquidus temperature of SS316L ($T_{Liquidus}$ for SS316L ~1673 K and SS310 ~1728 K). Additionally, since SS316L contains a lower percentage of chromium than SS310, the overall chromium content decreases as the heat input increases.

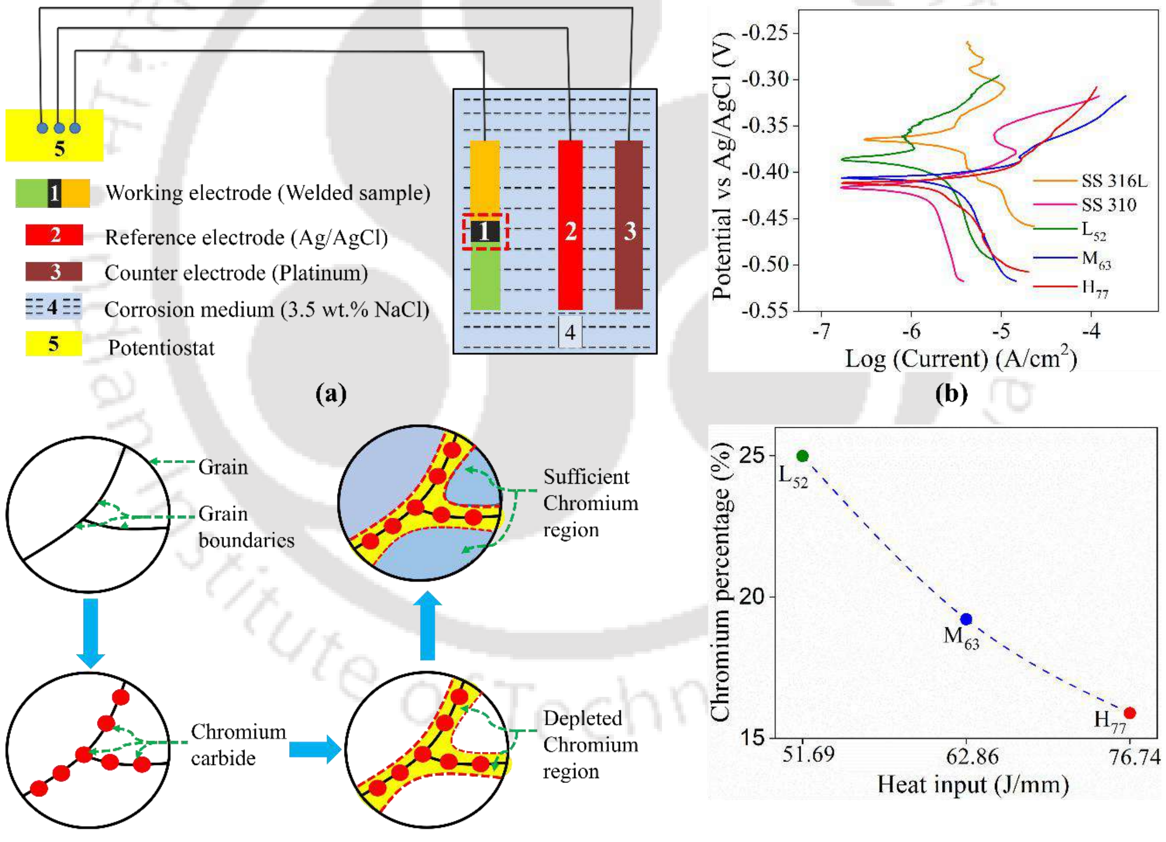

(a) (b)

(c) (d)

Fig. 5.52 (a) Schematic of the experimental setup for corrosion testing, (b) Tafel plot for base materials and weld joints, (c) picturization of IGC, and (d) variation of chromium percentage with heat input.

Table 5.10 Corrosion test results for base metals and joints fabricated at L_{52}, M_{63}, and H_{77}.

	SS 316L	SS 310	L_{52}	M_{63}	H_{77}
E_{Corr} (mV)	−364.6	−416.3	−385.8	−401.4	−417.9
I_{Corr} (µA/cm^2)	8.3	4.5	2.5	2.4	1.3

5.4.11 Residual stress analysis

The estimated residual stress obtained from the numerical results is validated with the experimental values measured at the surface, and a comparison is made in Fig. 5.53(a, b) for L_{52}, M_{63}, and H_{77} weld conditions. The longitudinal component (S11) of residual stresses against the distance across the weld cross-section is presented in Fig. 5.53(a). The numerically calculated S11 stress values are 212 MPa, 239 MPa, and 280 MPa, with the percentage error in predicting the S11 stress value is evaluated as ~17% for L_{52}, ~11% for M_{63}, and ~15% for H_{77} process conditions. As the heat input increases from L_{52} to H_{77}, a high rise of 147.3 MPa is observed because high heat input (H_{77}) leads to more melting of the base materials, leading to larger contraction, and higher values of residual stresses. In contrast, low heat input corresponds to lower melting of the base materials, which confines the FZ to a narrower region, thus leading to a lower residual stress value. The S11 stress changes from positive (tensile) at the weld center line and nearby location to negative (compressive) at a faraway location i.e., at a distance of ~5 mm from the weld center line for the L_{52} condition. As the heat source moves away, the heated region starts to cool down and regain its length, wherein positive (tensile) stresses are developed (Baruah and Bag, 2017).

The maximum magnitude of the longitudinal stress field (S11) is measured at the fusion line whereas it is obtained as ~181± 38 MPa, ~266 ± 34 MPa and ~328 ± 20 MPa for specimens L_{52}, M_{63} and H_{77}, respectively. The localization in the distribution of tensile residual stress is also seen by a highly collimated micro-plasma arc, which resulted in relatively low cooling rate and less temperature gradient at distant locations across the weld region for the lowest heat input condition (L_{52}). The maximum compressive residual stress (S11) of 88± 30 MPa (SS310 side) and 94 ± 33 MPa (SS316L side) at location ~11 mm is seen for case L_{52}; however, it is measured as 144 ± 35 MPa (SS316L side) and 122 ± 34 MPa (SS310 side) for M_{63} sample and 165 ± 34 MPa (SS310 side) and 183 ± 28 MPa (SS316L side) for case H_{77}. The tensile stress at the nearby location of the weld region is compromised by successive compressive stress at a distant location to maintain the neutrality of the structural stress field or to accommodate structural equilibrium.

Fig. 5.53(b) illustrates the comparison in the residual stress values along the transverse direction (perpendicular to the weld direction, S22). The S22 stress (transverse) value is relatively smaller than the S11 component. The S22 stress values also show a similar trend as S11 stress, wherein, residual stresses also increase with the increase in the heat input value. The value of S22 stress is experimentally determined as -19.5 ± 10 MPa, 67.3 ± 23 MPa, and 124.6 ± 32 MPa for L_{52}, M_{63}, and H_{77} conditions, respectively. The S22 stress value primarily relies on the size of the FZ, i.e., a smaller width of the FZ achieved under low heat input conditions lowers the stress value alongside changing the nature of stress (Ishigami et al., 2017). The S22 value for L_{52} weld condition changes from negative (compressive) at the weld center line to zero at the outer edges. The highest value of S11 (328.6 ± 20 MPa) and S22 (124.6 ± 32 MPa) stress components correspond to the maximum heat input condition (H_{77}), whereas the minimum heat input condition (L_{52}) results in relatively low stress (S11 and S22) value.

The fusion zone for the L_{52} weld condition comprises 11.2% δ_{ferrite} and 88.8% $\gamma_{\text{austenite}}$, and for the H_{77} condition comprises 7.9% δ_{ferrite} and 92.1% $\gamma_{\text{austenite}}$. Fig. 5.53(c) presents the stress generation in the $\gamma_{\text{austenite}}$ and δ_{ferrite} core regions in a tabular format. The presence of higher δ_{ferrite} involves more amount of Cr and less Ni content. Also, it is to be noted that the austenitic matrix comprises higher Ni and less Cr content, whereas δ_{ferrite} contains higher Cr and less Ni content, and the coefficient of thermal expansion (α), for Ni is ~1.6 times that of Cr (Karunaratne et al., 2016; Kumar et al., 2021b). Due to the difference in the value of α, the γ-region (containing more amount of Ni) contracts more as compared to the δ-region (containing more amount of Cr), which corresponds to compressive stresses in the dendritic core region and tensile stresses in the γ-region.

Fig. 5.53(d) illustrates the tensile and compressive stress behaviour associated with the γ-region and δ_{ferrite} core region, respectively. The reduction of tensile stresses in the FZ is observed for L_{52} and M_{63} conditions. Under the high heat input condition (H_{77}), lower δ_{ferrite} content restricts compressive stresses in the FZ. Also, the deformation of δ_{ferrite} is restricted by the surrounding hard phase austenite, which restricts the development of back stress due to δ_{ferrite}, thus resulting in a lower stress level for L_{52} than the H_{77} condition. It suggests that residual stress distribution changes primarily due to volumetric changes during phase transition, which significantly reduces the cumulative longitudinal stress. Fig. 5.54 shows the inter-relationship between $\delta_{ferrite}$ lath size and retained $\delta_{ferrite}$ on the resulting S11 stress value.

Comparison of numerical results with experimental data

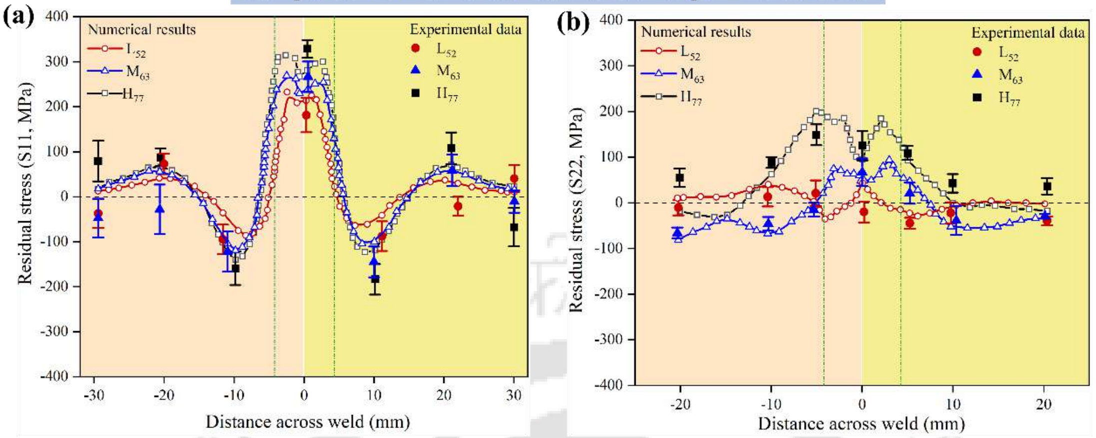

(c) Stress generation associated with microstructural evolution

$\gamma_{austenite}$ matrix	$\delta_{ferrite}$ rich dendritic core
α_{Ni} ~ (15-17.5) × $10^{-6}\ K^{-1}$	α_{Cr} ~ (9-11) × $10^{-6}\ K^{-1}$
More Ni, Less Cr	More Cr, Less Ni
Tensile stress ✚✚✚✚	Compressive stress – – – –

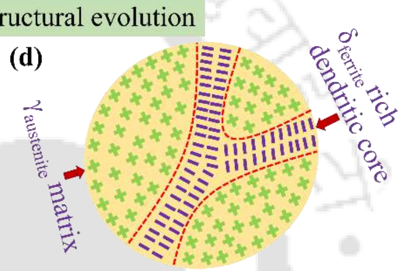

Fig. 5.53 Illustrates (a, b) comparison of residual stresses developed along the longitudinal (S11) and transverse direction (S22) and (c, d) tensile/compressive stress generation.

Inter-relationship between $\delta_{ferrite}$ lath size, retained $\delta_{ferrite}$, and longitudinal stress (S11)

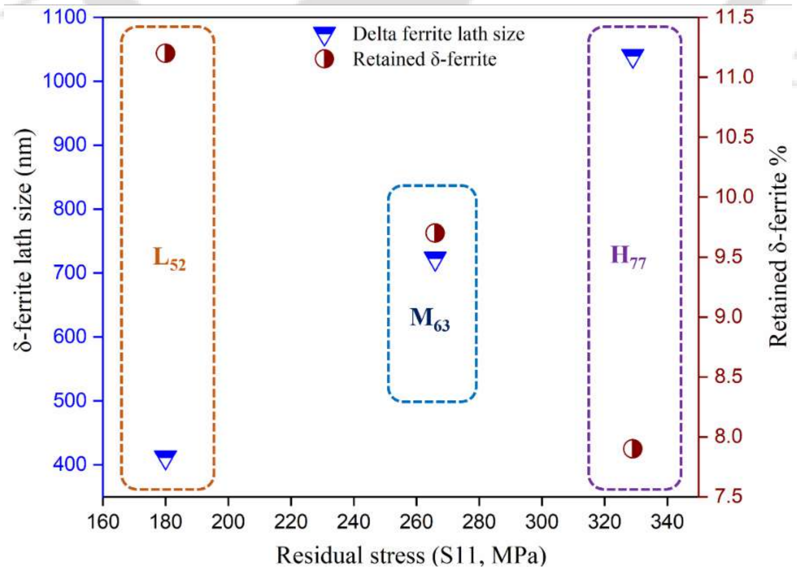

Fig. 5.54 Depicts inter-relation between lath size, longitudinal stress, and retained $\delta_{ferrite}$ percentage for L_{52}, M_{63}, and H_{77} conditions.

Hence, the increase in lath size (412 nm for L_{52} to 1040 nm for H_{77}) and the increase in inter-dendritic spacing (10 µm for L_{52} to 20 µm for H_{77}) also contribute to the overall enhancement of the locked-in stress value. It is observed that a lower value of lath size (412 nm) and higher retained $\delta_{ferrite}$ percentage (11.2 %) leads to a minimum S11 value (181.3 ± 38 MPa). Overall, a low heat input value, higher retained $\delta_{ferrite}$, fine lath size, and reduced inter-dendritic spacing lead to minimum residual stress value (Chen et al., 2019; Hsieh et al., 2014; Kianersi et al., 2014).

Fig. 5.55(a-c) represents the longitudinal (S11) stress distribution for L_{52}, M_{63}, and H_{77} conditions. The presence of tensile stress near the weld region for all the cases is obvious. Further, to maintain structural equilibrium, the tensile (positive) nature of the stress changes to compressive (negative) for the region away from the fusion zone. The maximum value of residual stress for L_{52} and M_{63} cases is identified as 235.7 MPa and 269.7 MPa, respectively, which falls within the yield strength value of the base metals (277 MPa for SS310 (Hosseini et al., 2011) and 376 MPa for SS316L (Kumar and Das, 2021)). However, residual stress is estimated as 315.7 MPa for the H_{77} condition, which is on the higher side with reference to the base material SS310. It indicates a severe chance of structural failure on the SS310 side.

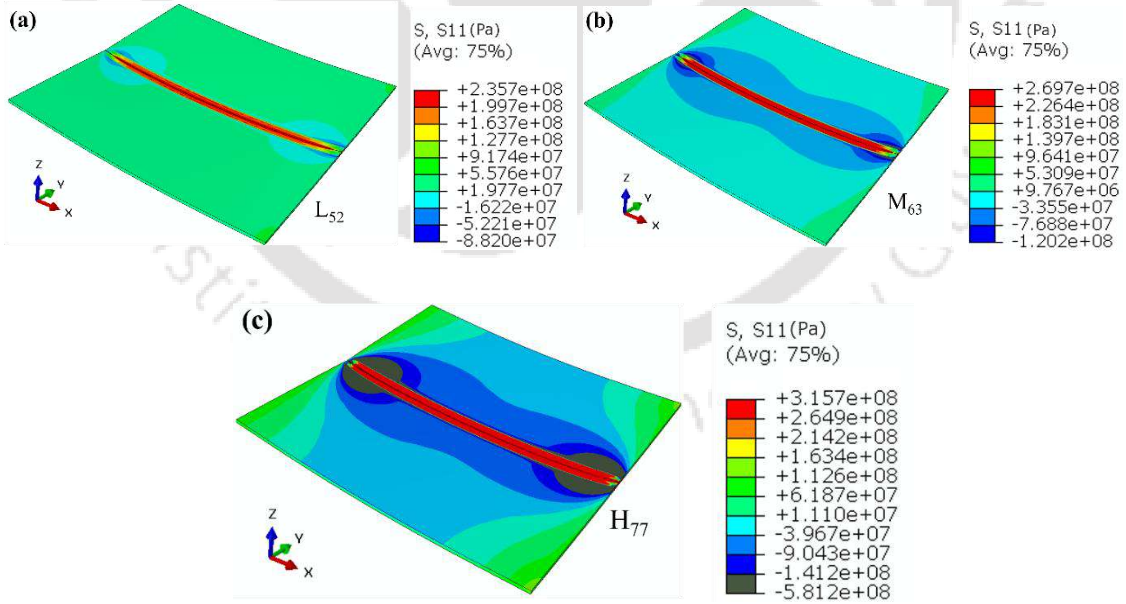

Fig. 5.55 Residual stress distribution along the longitudinal direction (S11) for different process conditions (a) L_{52}, (b) M_{63}, and (c) H_{77}.

5.4.12 Distortion analysis

The effect of phase transformation is also observed in the resulting distortion value of the welded joints. To evaluate the influence of phase transformation, the distortion value is analysed for dissimilar joints fabricated at maximum heat input conditions (H_{77}). Fig. 5.56(a, b) illustrates distortion along the weld direction and out-of-the-plane distortion for the H_{77} condition. An outward convex-type shape along the weld (longitudinal, U_x) direction indicates that the maximum and minimum deflection occurs near the weld center and the edges, respectively. The maximum deflection (U_x) with and without consideration of phase transformation is measured as 1.17 and 1.54 mm, respectively. The experimental value determined from the CMM is 1.23 mm. Thus, the error in predicting U_x for the H_{77} process condition is evaluated as ~5% and ~25% with and without consideration of phase transformation, respectively. The significant error of U_x implies that incorporating phase transformation immensely aids in accurately predicting the value of distortion. Notably, the value of U_x is found to be highest for the H_{77} process condition. The probable reason for such a scenario is the involvement of a high amount of plastic strain induced in the joints. Fig. 5.56(b) illustrates the out-of-the-plane distortion (U_z) for H_{77} weld condition, wherein the maximum value of the deflection with and without phase transformation is identified as 0.654 mm and 0.8 mm, respectively. The experimental data is measured as 0.68 mm, and the corresponding error in predicting the value of U_z is evaluated as ~4% and ~17% with and without phase transformation, respectively. Similar to U_x, the value of U_z is found to be highest for the high heat input process condition (H_{77}).

Fig. 5.56(c-f) represents the comparison between the transverse deflection (U_y) and out-of-plane distortion (U_z) distortion contour for the H_{77} weld condition. It is observed that the magnitude of U_y is maximum without consideration of the phase transformation effect, and the value of U_y is lowered with consideration of the phase transformation effect. The out-of-the-plane distortion is shown in Fig. 5.56(d, f), where the deflection is the highest at the edges, and reduces with consideration of the phase transformation effect. The incorporation of phase transformation prevents overestimating stress value due to consideration of compressive stresses created by δ_{ferrite} enriched core. Similarly, a reduction in deflection value is observed due to partial cancelation of deflection in U_x and U_z directions. A similar trend is reported in the martensitic transformation of medium carbon steel, resulting in a considerable reduction in distortion by incorporating the phase transformation effect (Deng, 2009).

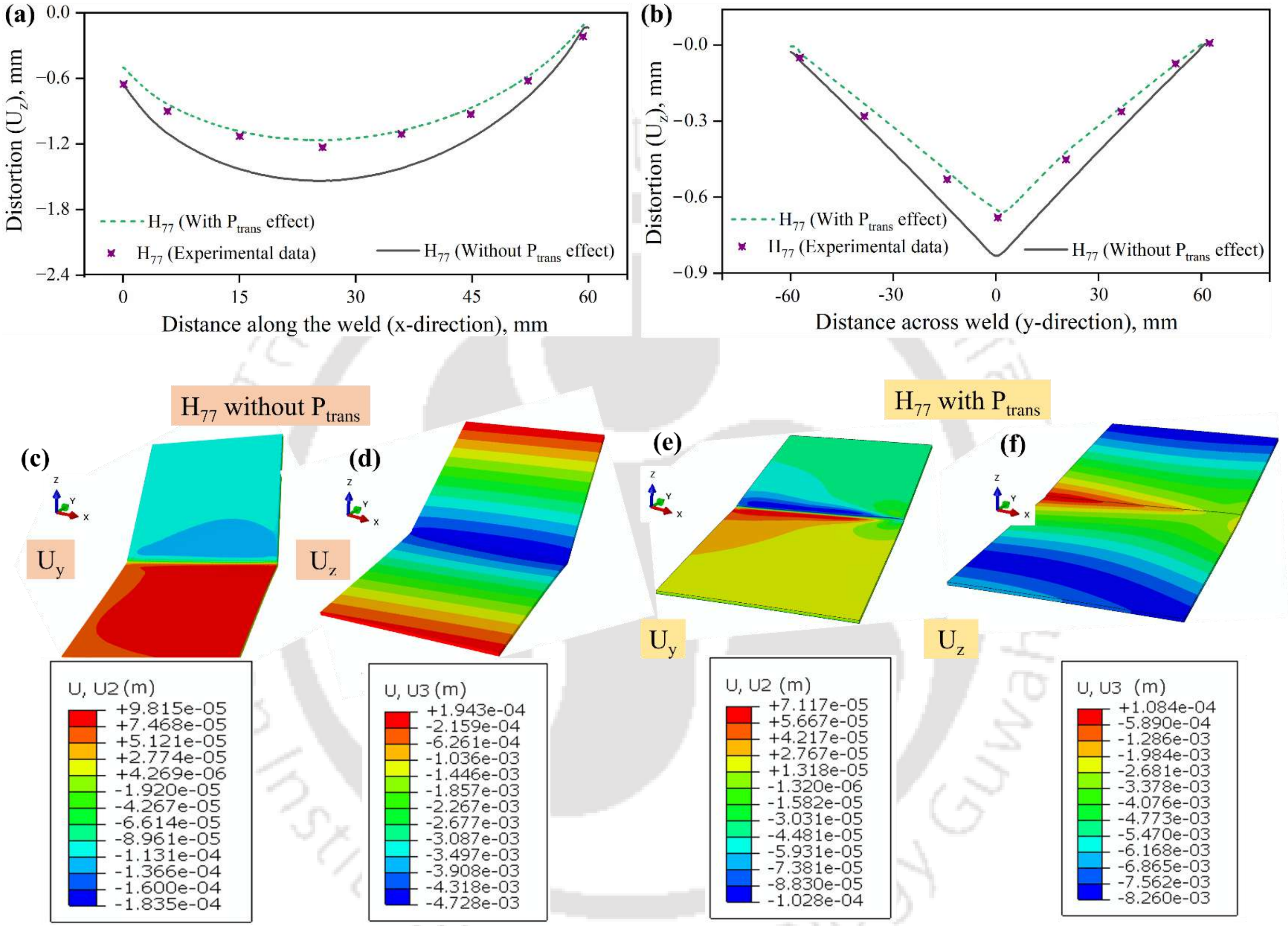

Fig. 5.56 (a) Distortion along the longitudinal direction (U_x), (b) out of the plane distortion (U_z); distortion contour for U_y and U_z (c, d) without phase transformation, and (e, f) with phase transformation for H_{77} process condition.

5.5 Summary

The present chapter presents a detailed experimental and numerical analysis on similar ($Cu_{90}Ni_{10}$) and dissimilar joining (SS316L-SS310 and Cu(T2)-SS304) using micro-plasma and gas tungsten arc welding processes. A comprehensive investigation is carried out to establish the micro-plasma arc welding schedule through microstructural and mechanical characterization of 700-µm thick cupronickel ($Cu_{90}Ni_{10}$) alloy. The work focuses on controlling defect formation via optimum heat supplied in continuous mode, and applying the least heat supplied is recommended in compliance with full penetration depth. The lowest heat input for pulse current yields the best results in terms of fine equiaxed morphology, reduced secondary dendritic arm spacing, and the lowest number of internal pores. The highest joint efficiency (~100%) is achieved using pulse current.

Further, the current chapter presents an in-depth study into dissimilar joining of SS304 and Cu(T2) metals to form a bimetallic joint. The bimetallic joint is fabricated using a gas tungsten arc welding process with different values of arc offset (towards Cu-side), 1.3, 2.0, and 2.7 mm at ~308 J/mm. The critical findings suggest that the joint demonstrates a variation from welding to a weld-brazing mode with an increased arc offset. Accordingly, the failure mode changes from ductile to brittle fracture. With a decreasing percentage of copper in the fusion zone, the resulting microstructure improves the joint properties. Despite the occurrence of porosity and macro-segregation, the outcome of the present experimental investigation displays an exceptional joining capability (~106 % joint efficiency) at ~308 J/mm, 1.3 mm arc offset weld condition.

This chapter also aims to investigate the effect of heat input on the joint properties of dissimilar ASS joints (SS316L-SS310) and mitigation of residual stress by controlling microstructural morphologies that can elude the failures of a welded joint. An increase in heat input is analogous to the reduction in cooling rate that allows the growth of $\delta_{ferrite}$ lath and enhances the inter-dendritic gap. Due to the difference in the magnitude of the thermal expansion coefficient (α_{Ni}~$1.6\ \alpha_{Cr}$), tensile residual stress exists in the γ-region and compressive stress in the dendritic core. A low heat input condition (52 J/mm, highest retained $\delta_{ferrite}$) generates comparatively more compressive stress than high heat input conditions (63 J/mm and 77 J/mm). Hence, the successful joining of dissimilar materials can be achieved by opting for minimum heat input analogous to high $\delta_{ferrite}$ content, relatively finer lath size, and minimum gap between dendritic arms. Combining such characteristics of $\delta_{ferrite}$ aids in reducing the residual stress generated.

Chapter 6

Conclusions and Future Scope

6.1 Introduction

Welding of thin sheets is a complex task since several defects like deflection, porosity, root sagging, under-cut, blowholes, presence of large heat-affected zone and burn-through may occur during the joining process. Therefore, determining optimal process parameters requires careful attention to avoid defects in the resulting structure. The current work aims to join thin sheets in similar ($Cu_{90}Ni_{10}$) and dissimilar (SS316L-SS310 and Cu-SS) combinations by downscaling the traditional arc-based joining (M-PAW and GTAW) process. However, the joining process involves complex interaction of heat and mass transfer influencing the solidification behaviour that directly decides the phase transformation, distortion and induced residual stress. Therefore, precise estimation of temperature distribution and subsequently the residual stress variation in the welded structure is cumbersome due to the welding process's intricacy and the existence of a high temperature gradient. Hence, a FE-based thermo-mechanical and thermal-metallurgical-mechanical (TMM) model is employed to reliably predict time-temperature data, weld dimensions, phase fraction, distortion and residual stress generation. The current work aims to understand the weldability of $Cu_{90}Ni_{10}$ alloy by controlling defect formation via optimum heat supplied in continuous and pulse mode using M-PAW process. In addition, an effort has been made to study the processing-structure-properties relation with reference to arc offset and heat input through microstructural and mechanical characterization of Cu(T2)-SS304 sheets processed by GTAW process. The present experimentation also aims to join a different combination of austenitic stainless steels (SS316L-SS310) using the M-PAW process and to establish a correlation linking the influence of heat input on the joint properties and to investigate the mitigation of residual stress by controlling microstructural morphologies that can elude the failures of a welded joint.

6.2 Conclusions

The current examination deals with studying the joint behaviour of $Cu_{90}Ni_{10}$ weld joints by conducting a range of characterization (destructive and non-destructive) to ensure the quality of the joints produced, followed by applying current pulsation to enhance the weld properties. Further, a numerical method is also explored to predict the magnitude of maximum temperature, distortion, and residual stresses in the weld joints. Further, joining of Cu(T2) and SS304 is accomplished without filler material in butt configuration. The outcome of the current experimental evaluation aids in understanding the significance of arc offset and joining mode. Finally, dissimilar joining of austenitic stainless steels (SS316L-SS310) is carried out to identify the influence of SSPT on residual stress developed. After a wide range of testing methods used to assess the joint's sustainability, the following notable inferences are drawn from the current investigation:

- The importance of heat supplied and pulsed current to minimize defect formation and enhance joint properties of micro-plasma arc welded $Cu_{90}Ni_{10}$ alloy is investigated. With a reduction in heat input, the cooling rate increases, resulting in a finer dendritic structure in the weld joints and enhanced mechanical properties. The variation in the G/R ratio is responsible for the deviation in the solidification from columnar (near the FB) to equiaxed (at the weld center).
- For the $Cu_{90}Ni_{10}$ alloy, an increasing amount of heat supplied (35.80, 66.67, 96.06 J/mm) results in higher agitation due to extended exposure in the fusion zone, which corresponds to increased degradation of the weld surface (R_a: 0.399, 2.76, 5.01 μm), and reduces the corrosion resistance due to the decreasing stability of the passive layer. Additionally, with increased heat supplied, the loss of material also increases.
- The cooling rate governs the resulting microstructural morphology. In $Cu_{90}Ni_{10}$ alloy, finer and coarser microstructural morphology are observed for 35.08 J/mm and 66.67 J/mm weld conditions, respectively. In contrast, along with coarser morphology, solidification cracks are also observed for 96.03 J/mm weld condition. The joint properties degrade with decreasing cooling rate (1434, 1179, 886 K/s).
- The joint properties remain a function of weld defects and microstructural features. For $Cu_{90}Ni_{10}$ alloy, the UTS and %EL values decrease ~95 %, ~52 % ⟶ ~88 %, ~30 %, and ~77 %, ~22 % with an increase in the heat supplied (35.80, 66.67, 96.06 J/mm). The UTS value is primarily a function of porosity, metal loss, and SDAS value. The least magnitude of the above-listed parameters corresponds to the highest joint quality.

- For $Cu_{90}Ni_{10}$ alloy, the pulsed current (35.50 J/mm) allows better control over the heat supplied, which results in refined morphology (39.52 to 35.53 µm) and increased joint efficiency (~95 % to ~100 %) compared to continuous current (35.80 J/mm).
- The FE-based thermo-mechanical model shows reasonable agreement between the computed and experimental measurements, with a maximum error of ~11% in weld size, ~6% in peak temperature, ~5% in residual stress, and ~11% in distortion, which authenticates the reliability of the applied numerical model for the $Cu_{90}Ni_{10}$ alloy.
- Porosity is one of the most prevalent defects associated with the fusion welding of $Cu_{90}Ni_{10}$ alloys. At a higher value of heat input (96.03 J/mm), the chances of pore formation and coalescence increase. Meanwhile, at lower value of heat input, the emergence of pores is restricted, resulting in minimum quantity and size of pores.
- It is well understood that joint properties are influenced by solidification behaviour and SDAS, which are directly linked to the amount of heat supplied for the fabrication of the $Cu_{90}Ni_{10}$ joint. Thus, low heat input should be opted for the joining of $Cu_{90}Ni_{10}$ thin sheets to achieve enhanced weld properties.
- The limited solubility of Cu and SS leads to microstructural inhomogeneities. Metallurgical non-uniformities (macro-segregation) correspond to different microstructural features, including Cu-rich globules in an Fe-rich matrix, Fe-rich globules in a copper matrix, Fe-rich Island, Fe-rich peninsula, Cu-rich dendritic structures, and Fe-rich dendritic structures.
- Microstructural non-uniformities and unique morphology like fish-hook and jagged-teeth structures also significantly contribute to the joint properties of Cu-SS bimetallic joints. As the joining mode changes from welding to weld-brazing, the mode of failure changes from fine and coarse dimples to brittle mode.
- Arc offset (towards the Cu-side) is identified as the most dominant factor governing the joining mode and joint properties in the GTAW of dissimilar ferrous (SS304) and non-ferrous (Cu-T2) metals. The evaluated values of UTS and %EL follow a decreasing trend with increasing arc offset values ~222 MPa, 28 % (1.3 mm); ~211 MPa, 22 % (2.0 mm); and ~183 MPa, 16 % (2.7 mm). The decrease in the tensile properties directly correlates with the percentage of Cu, the occurrence of porosity, and the mode of joining. An optimum arc offset results in minimal melting of Cu and the least number of pores, leading to enhanced joint strength.

- As the arc offset value increases (1.3, 2.0, 2.7 mm), the percentage of Cu also increases, and the mode of joining modifies from welding (1.3, 2.0 mm) to weld-brazing mode (2.7 mm). The increase in Cu content negatively impacts the Cu-SS bimetallic joints.
- Excessive heat input causes the formation of solidification cracks, significantly reducing the joint strength of Cu-SS bimetallic joints (~172 MPa). The severity of defects in the Cu-SS bimetallic joints follows the order: solidification cracking > porosity > macro-segregation.
- Despite the occurrence of porosity and macro-segregation, the results of the present experimental investigation demonstrate an exceptional joining capability (~106 % joint efficiency) at an arc offset value of 1.3 mm for the fabricated Cu-SS bimetallic joint.
- Joining of SS316L and SS310 is carried out to predict the retained δ_{ferrite}, identify the influence of SSPT on the residual stress developed, and study the effect of heat input on the dissimilar joints fabricated by the micro-plasma arc welding process.
- For the dissimilar ASS joints, the evaluated $Cr_{eq.}/Ni_{eq.}$ ratio ranges from 1.54 to 1.77, which suggests FA mode of solidification exists, where the FZ consists of δ_{ferrite} (skeletal and lathy) within the austenitic matrix. The retained δ_{ferrite} decreases (11.2, 9.7, 7.9 %) with an increase in heat input (52, 63, 77 J/mm). An increase in heat input corresponds to a reduction in cooling rate (1063, 832, 583 K/s) that allows the growth of δ_{ferrite} laths (412, 723, 1040 nm) and enhances the inter-dendritic gap (10, 15, 20 μm).
- Lower amount of heat input leads to a higher level of δ_{ferrite}, and reduced inter-dendritic spacing within the fusion zone. These metallurgical changes results in the highest joint efficiency for 52 J/mm (~115 %) as compared to 77 J/mm (~101 %) for the fabricated SS316-SS310 joints.
- X-ray CT reveals that a higher value of heat input results in a greater number of pores and the formation of larger pores. A higher value of heat input results in a low cooling rate, which enhances pore formation in the ASSs weld joints.
- Composition analysis of the dissimilar ASSs weld joint shows a significant difference in the percentage of chromium present in joints prepared with different values of heat input. A lower value of heat input leads to a higher chromium percentage, which is beneficial corrosion resistance. A higher value of heat input leads to a lower cooling rate, allowing more time for chromium to combine with carbon, forming chromium carbide (sensitization effect).

- The phase fraction and residual stresses are computed using a finite element-based thermal-metallurgical-mechanical (TMM) model, which includes the effect of SSPT. The reasonable agreement between the computed and experimental measurements with a maximum error of ~9% in weld size, ~7.5% in peak temperature, ~16% in retained $\delta_{ferrite}$, ~17% in residual stress, and ~5% in distortion demonstrates the reliability of the developed model.
- The difference in the magnitude of the thermal expansion coefficient ($\alpha_{Ni} \sim 1.6\ \alpha_{Cr}$) leads to tensile residual stress in the γ-region (where Ni content is high) and compressive stress in the dendritic core (where Cr content is high). A low heat input condition (52 J/mm-L_{52}, highest retained $\delta_{ferrite}$) generates comparatively more compressive stress than higher heat input conditions (63 J/mm and 77 J/mm).
- Based on the experimental results of dissimilar ASS (SS316L-SS310) joints, it is safe to mention that the weld condition depends critically on the amount of heat supplied. Hot cracking is not detected for any of the weld joints, but sensitization/weld-decay is observed for the weldments fabricated with a high heat input value.
- Overall, it is recommended to join dissimilar ASSs (SS316L-SS310) with a lower value of heat input, resulting in improved metallurgical properties, higher joint efficiency, increased corrosion resistance, and a reduction in the number and size of the pores formed. A lower value of heat input corresponds to high $\delta_{ferrite}$ content, relatively finer lath size, and a minimum gap between dendritic arms. The combination of these $\delta_{ferrite}$ characteristics aids in reducing the residual stress generated.

6.3 Novelty and recommendation to industry

The experimental and numerical work carried out in the present thesis attempts to provide novel contributions to the welding community, along with recommendations to industry. The following notable contributions are identified from the current investigation:

- The current experimental examination reports the importance of heat supplied and the technique employed (pulsed current) to enhance weld properties of the $Cu_{90}Ni_{10}$ alloy. The understanding of process parameters and weld enhancement techniques tremendously aids in obtaining joints of acceptable properties, which can be employed by industries to avoid repetition of work (directly influencing economic aspects) for joining $Cu_{90}Ni_{10}$ thin sheets.

- The current research successfully joined Cu (T2) and SS304 using the GTAW process. An effort was made to study the processing–structure–properties relation with reference to arc offset and heat input through microstructural and mechanical characterization data. Compared to the joint efficiency reported in the past literature on the GTAW process for fabricating Cu-SS bimetallic joints, the present investigation exhibits the highest value. Based on this outcome, the current work can be recommended for industrial applications where Cu-SS bimetallic joints are critically required, such as defence systems, power generation and steam turbine power plants, aerospace and chemical industries, nuclear sectors, and heat exchange components, where high joint efficiency and reliable mechanical performance are essential.
- The current work studied the effect of heat input on the dissimilar steel (SS316L-SS310) joint formation and established a correlation linking the varying microstructural morphology, changes in joint strength, failure modes, and pore formation. Further, the work also aims to investigate the mitigation of residual stress by controlling microstructural morphologies, to understand the solidification behaviour of the weld metal and its correlation with delta ferrite formation and residual stress distribution. Thus, the outcomes of the present work can be recommended for industrial use, as austenitic stainless steels account for nearly 70% of the total stainless-steel consumption.

6.4 Scope of future work

The current research explores the joining of similar and dissimilar materials using the M-PAW and GTAW processes, including both experimental and numerical work, and highlights the significance of process parameters. It also identifies a research gap, specifically in the joining of materials yet to be explored using the M-PAW and GTAW processes. The following proposed work can be incorporated by future researchers using the M-PAW and GTAW processes:

- Similar joining of commonly welded materials (using different fusion joining processes) yet to be addressed by the M-PAW process, include various grades of steel (TRIP steel, Dual-phase steel, HSLA steel, Ferritic SS, and Martensitic SS), Hastelloy X, Hastelloy C-276, AZ31 Mg alloy, and Grade 2 Ti alloy.
- Dissimilar combinations of materials yet to be explored by the M-PAW process include Al-Steel, Al-Mg, Cu-SS, Ti-Al, Ti-Steel, P91-Incoloy 800 HT alloy, P92 Steel-Alloy 617, and IN617-SS304L. Additionally, dissimilar grades of the same material yet to be

joined include Austenitic SS-Ferritic SS, Austenitic SS-Martensitic SS, Martensitic SS-Duplex SS, and SDSS-HSLA (X-70).

- Generally, in the case of dissimilar materials, due to differences in physical and chemical properties, commonly occurring challenges include improper mixing, segregation, and intermetallic evolution. With the application of arc oscillation technique (Dinda et al., 2019; Kar et al., 2019, 2016; Zhou et al., 2022) and ultrasonic vibration (Sonia et al., 2021; Su et al., 2022; Zhao et al., 2022), such complications can be reduced while performing dissimilar joining using GTAW process. Arc oscillation may also be employed for similar material joining to enhance joint properties (Yue et al., 2022).
- Generally, the M-PAW process has explored for the evaluation of thin sheets ≤ 1 mm (except a few). There is a scope to join thicker sheets by employing (i) activated flux (Vidyarthy and Dwivedi, 2019), (ii) varying the composition of shielding gas (Van Nguyen et al., 2020; Vidyarthy and Dwivedi, 2019), and (iii) using hybrid joining techniques (M-PAW + GTAW or M-PAW + LBW or M-PAW + Induction welding-IW) (Biswal and Pal, 2024; Saha and Pal, 2024; Taban, 2008).
- Distortion can be mitigated by using proper fixture and clamping elements (Kumar et al., 2020), while residual stresses can be reduced to a considerable extent by post-weld heat treatment (Dhakal and Swaroop, 2018; Kumar et al., 2022; Wang et al., 2022; Zhang et al., 2024), or by inducing compressive stresses (before/after joining) using shot/laser shock peening techniques (Benchouia et al., 2019). Additionally, distortion and residual stress can be minimized by opting for suitable groove geometry (Kumar and Pandey, 2023). Cracking tendency can also be reduced by employing heat treatment (Pandey et al., 2018).
- The current pulsation technique also enhances microstructural properties by providing better control over the heat input, which leads to improved solidification behaviour and enhanced weld properties (Generoso et al., 2023; Pal and Pal, 2011).
- The occurrence of solidification cracking requires careful selection of process parameters to eradicate the formation of cracks in the fusion zone (Dhilip et al., 2022). Additionally, the addition of TiC nanoparticles helps to mitigate crack formation, particularly in Al alloys (Abdollahi et al., 2022; Fattahi et al., 2015; Sokoluk et al., 2019), Mg alloys (Qin et al., 2018), and Ti-Al alloys (Li et al., 2022), while the addition of TiO_2 nanoparticles in mild steel enhances impact toughness (AlIthari et al., 2023).

References

Abbas, M., Shafiee, M., Simms, N., 2019. Corrosion Behaviour of Cupronickel 90/10 Alloys in Arabian Sea Conditions and its Effect on Maintenance of Marine Structures. Presented at the ASME 2019 38th International Conference on Ocean, Offshore and Arctic Engineering, American Society of Mechanical Engineers Digital Collection.

Abdollahi, A., Nganbe, M., Kabir, A.S., 2022. On the elimination of solidification cracks in fusion welding of Al7075 by TiC-nanoparticle enhanced filler metal. J. Manuf. Process. 81, 828–836.

Abdollahi, A., Shamanian, M., Golozar, M.A., 2018. Comparison of pulsed and continuous current gas tungsten arc welding in dissimilar welding between UNS S32750 and AISI 321 in optimized condition. Int. J. Adv. Manuf. Technol. 97, 687–696.

Agrawal, B.P., Chauhan, A.K., Kumar, R., Anant, R., Kumar, S., 2017. GTA pulsed current welding of thin sheets of SS304 producing superior quality of joint at high welding speed. J. Braz. Soc. Mech. Sci. Eng. 39, 4667–4675.

Ahn, J., He, E., Chen, L., Wimpory, R.C., Dear, J.P., Davies, C.M., 2017. Prediction and measurement of residual stresses and distortions in fibre laser welded Ti-6Al-4V considering phase transformation. Mater. Des. 115, 441–457.

Akbari, D., Sattari-Far, I., 2009. Effect of the welding heat input on residual stresses in butt-welds of dissimilar pipe joints. Int. J. Press. Vessels Pip. 86, 769–776.

Akella, M.S., Harinadh, M.V., Krishna, M.Y., Buddu, M.R.K., 2014. A welding simulation of dissimilar materials SS304 and copper. Procedia Mater. Sci. 5, 2440–2449.

AlIthari, A.S., Thahab, S.M., Al-Obbaidi, A.F., 2023. Effect of adding TiO_2 nanoparticles on the impact toughness for welding joints of mild steel. Aust. J. Mech. Eng. 21, 13–26.

Anawa, E.M., Olabi, A.-G., 2008. Control of welding residual stress for dissimilar laser welded materials. J. Mater. Process. Technol. 204, 22–33.

Arif, N., Chung, H., 2014. Alternating current-gas metal arc welding for application to thin sheets. J. Mater. Process. Technol. 214, 1828–1837.

Astm, 2011. Standard Test Method for Determining Volume Fraction by Systematic Manual Point Count. Practice 1–7.

Aumpiem, A., Prateepasen, A., 2021. An Effective Quality Assessment Method for Plasma Welding Based on the Plasma Gas Flow Rates in Titanium Grade 2. Int. Trans. J. Eng. Manag. Appl. Sci. Technol. 12, 12A1E-1.

Avrami, M., 1940. Transformation-time relations for random distribution of nuclei kinetics of phase change II. J Chem Phys 8, 212.

Babu, N.K., Raman, S.G.S., Mythili, R., Saroja, S., 2007. Correlation of microstructure with mechanical properties of TIG weldments of Ti–6Al–4V made with and without current pulsing. Mater. Charact. 58, 581–587.

Bag, S., Amin, M.R., 2020. Investigation on ultrashort pulse laser welding of dissimilar metallic materials expending phase-lag influence. J. Therm. Sci. Eng. Appl. 12, 051014.

Bag, S., De, A., 2010. Computational modelling of conduction mode laser welding process. Laser Weld. Eng. Electr. Electron. Eng. Sciyo 133–160.

Bag, S., Trivedi, A., De, A., 2009. Development of a finite element based conduction mode heat transfer model for laser welding process using an adaptive volumetric heat source. Int J Therm. Sci 48, 1923–31.

Balasubramanian, M., Jayabalan, V., Balasubramanian, V., 2008a. Process parameter optimization of the pulsed current argon tungsten arc welding of titanium alloy. J. Mater. Sci. Technol. 24, 423–426.

Balasubramanian, M., Jayabalan, V., Balasubramanian, V., 2008b. Effect of microstructure on impact toughness of pulsed current GTA welded α–β titanium alloy. Mater. Lett. 62, 1102–1106.

Balasubramanian, V., Ravisankar, V., Reddy, G.M., 2008. Effect of pulsed current welding on fatigue behaviour of high strength aluminium alloy joints. Mater. Des. 29, 492–500.

Bansal, A., Sharma, A.K., Das, S., Kumar, P., 2016. On microstructure and strength properties of microwave welded Inconel 718/stainless steel (SS-316L). Proc. Inst. Mech. Eng. Part J. Mater. Des. Appl. 230, 939–948.

Baruah, M., 2017. Experimental investigation and numerical modeling of plasma and laser microwelding processes (PhD Thesis).

Baruah, M., Bag, S., 2017a. Characteristic difference of thermo-mechanical behavior in plasma microwelding of steels. Welding in the World 61, 857–871.

Baruah, M., Bag, S., 2017b. Influence of pulsation in thermo-mechanical analysis on laser micro-welding of Ti6Al4V alloy. Opt. Laser Technol. 90, 40–51.

Baruah, M., Bag, S., 2016. Influence of heat input in microwelding of titanium alloy by micro plasma arc. J. Mater. Process. Technol. 231, 100–112.

Benchouia, S., Merakeb, N., Adjel, S., Ehlers, S., Baccouche, M., Kaddour, A., 2019. Fatigue life enhancement of TIG-welded 304L stainless steels by shot peening. Int. J. Adv. Manuf. Technol. 100, 2885–2893.

Bhattacharya, A., Kumar, R., 2016. Dissimilar Joining Between Austenitic and Duplex Stainless Steel in Double-Shielded GMAW: A Comparative Study. Mater. Manuf. Process. 31, 300–310.

Bhogendro Meitei, R.K., Maji, P., Kumar, P., Karmakar, R., Paul, P., Ghosh, S.K., Saha, S.C., 2022. Induction Welding of 304L Stainless Steel and Copper in Vacuum Environment. J. Mater. Eng. Perform. 31, 7220–7227.

Bhogendro Meitei, R.K., Maji, P., Samadhiya, A., Karmakar, R., Ghosh, S.K., Saha, S.C., 2020. An Experimental Investigation on Joining of Copper and Stainless Steel by Induction Welding Technique. Int. J. Precis. Eng. Manuf. 21, 613–621.

Biswal, S.K., Pal, S., 2024. Influence of Induction Heating on Thermal Characteristics and Residual Stress for Plasma Arc Welding of Structural Steel Plate, in: Ray, R.K., Bora, S.N., Maiti, D.K. (Eds.), Advances in Theoretical and Applied Mechanics. Springer Nature, Singapore, pp. 371–379.

Camilleri, D., Comlekci, T., Gray, T.G.F., 2005. Computational prediction of out-of-plane welding distortion and experimental investigation. J. Strain Anal. Eng. Des. 40, 161–176.

Cao, X., Nolting, A., 2019. Autogenous fiber laser welding of 70/30 Cu-Ni alloy plates. Mater. Des. 181, 108075.

Casalino, G., Angelastro, A., Perulli, P., Casavola, C., Moramarco, V., 2018. Study on the fiber laser/TIG weldability of AISI 304 and AISI 410 dissimilar weld. J. Manuf. Process. 35, 216–225.

Cha, J.H., Choi, H.W., 2022. Characterization of dissimilar aluminum-copper material joining by controlled dual laser beam. Int. J. Adv. Manuf. Technol. 1–12.

Chakraborty, N., Chakraborty, S., 2007. Modelling of turbulent molten pool convection in laser welding of a copper–nickel dissimilar couple. Int. J. Heat Mass Transf. 50, 1805–1822.

Chakravarthy, M., Ramanaiah, N., Sundara Siva Rao, B., 2014. Effect of laser welding on mechanical properties of 70/30 Cu-Ni alloy welds. Proc. Inst. Mech. Eng. Part B J. Eng. Manuf. 228, 1153–1161.

Chande, T., Mazumder, J., 1984. Estimating effects of processing conditions and variable properties upon pool shape, cooling rates, and absorption coefficient in laser welding. J. Appl. Phys. 56, 1981–1986.

Chandra, K., Mahanti, A., Singh, A.P., Kain, V., Gujar, H.G., 2019. Microbiologically influenced corrosion of 70/30 cupronickel tubes of a heat-exchanger. Eng. Fail. Anal. 105, 1328–1339.

Chang, W.-S., Na, S.-J., 2002. A study on heat source equations for the prediction of weld shape and thermal deformation in laser microwelding. Metall. Mater. Trans. B 33, 757–764.

Chattopadhyay, A., Muvvala, G., Sarkar, S., Racherla, V., Nath, A.K., 2022. Mitigation of cracks in laser welding of titanium and stainless steel by in-situ nickel interlayer deposition. J. Mater. Process. Technol. 300, 117403.

Chaudhari, R., Ingle, A., 2019. Experimental Investigation of Dissimilar Metal Weld of SA335 P11 and SA312 TP304 Formed by Gas Tungsten Arc Welding (GTAW). Trans. Indian. Inst. Met. 72, 1145–1152.

Chaudhary, J., 2015. Investigations on autogeneous joining of thin stainless steel sheets by pulsed micro plasma trnsferred Arc (MTech Thesis). Discipline of Mechanical Engineering, IIT Indore.

Chaudhary, J., Jain, N.K., Pathak, S., Koria, S.C., 2019. Investigations on thin SS sheets joining by pulsed micro-plasma transferred arc process. Journal of Micromanufacturing 2, 15–24.

Chen, L., Hu, Y.N., He, E.G., Wu, S.C., Fu, Y.N., 2018. Microstructural and failure mechanism of laser welded 2A97 Al–Li alloys via synchrotron 3D tomography. Int. J. Lightweight Mater. Manuf. 1, 169–178.

Chen, L., Lu, L., Zhu, L., Yang, Z., Zhou, W., Ren, X., Zhang, X., 2024. Microstructure Evolution and Mechanical Properties of Multilayer AA6061 Alloy Fabricated by Additive Friction Stir Deposition. Metall. Mater. Trans. A 55, 1049–1064.

Chen, L., Mi, G., Zhang, X., Wang, C., 2019. Numerical and experimental investigation on microstructure and residual stress of multi-pass hybrid laser-arc welded 316L steel. Mater. Des. 168, 107653.

Chen, S., Huang, J., Xia, J., Zhang, H., Zhao, X., 2013. Microstructural characteristics of a stainless steel/copper dissimilar joint made by laser welding. Metall. Mater. Trans. A 44, 3690–3696.

Chen, S., Huang, J., Xia, J., Zhao, X., Lin, S., 2015. Influence of processing parameters on the characteristics of stainless steel/copper laser welding. J. Mater. Process. Technol. 222, 43–51.

Chen, S., Li, L., Chen, Y., Huang, J., 2011. Joining mechanism of Ti/Al dissimilar alloys during laser welding-brazing process. J. Alloys Compd. 509, 891–898.

Cheng, Z., Huang, J., Ye, Z., Chen, Y., Yang, J., Chen, S., 2019. Microstructures and mechanical properties of copper-stainless steel butt-welded joints by MIG-TIG double-sided arc welding. J. Mater. Process. Technol. 265, 87–98.

Cheng, Z., Liu, H., Huang, J., Ye, Z., Yang, J., Chen, S., 2020. MIG-TIG double-sided arc welding of copper-stainless steel using different filler metals. J. Manuf. Process. 55, 208–219.

Cherepanov, A.N., Shapeev, V.P., Fomin, V.M., Semin, L.G., 2006. Numerical simulation of thermophysical processes at laser beam welding. J Appl. Mech. Tech. Phys. 88–96.

Chuaiphan, W., Srijaroenpramong, L., 2019. Optimization of gas tungsten arc welding parameters for the dissimilar welding between AISI 304 and AISI 201 stainless steels. Def. Technol. 15, 170–178.

Collins, M.G., 2002. Quantifying ductility-dip cracking susceptibility in nickel-base weld metals using the strain-to-fracture test, in: 6th International Trends in Welding Research Conference Proceedings, April, 2002. pp. 586–590.

Correa, E.O., Costa, S.C., Santos, J.N., 2008. Weldability of iron-based powder metal materials using pulsed plasma arc welding process. J. Mater. Process. Technol. 198, 323–329.

Das, A., Chaurasia, P.K., Mandal, G.K., Goecke, S.F., De, A., 2023. Analytical estimation of thermomechanical distortion and interface layer thickness for gas metal arc lap joining of dissimilar sheets. Weld. World 67, 33–49.

Das, B., Yadaiah, N., Ozah, R., Chowdhury, S., Mondal, A.K., Muralidhar, M., 2018. A perspective review on estimation of keyhole profile during plasma arc welding process. Mater. Today Proc. 5, 6345–6350.

Das, S., Satpathy, M.P., Pattanaik, A., Routara, B.C., 2019. Experimental investigation on ultrasonic spot welding of aluminum-cupronickel sheets under different parametric conditions. Mater. Manuf. Process. 34, 1689–1700.

De, A., DebRoy, T., 2011. A perspective on residual stresses in welding. Sci. Technol. Weld. Join. 16, 204–208.

De, A., Maiti, S.K., Walsh, C.A., Bhadeshia, H.K.D.H., 2003a. Finite element simulation of laser spot welding. Sci. Technol. Weld. Join. 8, 377–384.

Debin, S., Ting, W., Siyuan, J., Liang, Z., 2020. Microstructure and Mechanical Properties of Copper–steel Laminated and Sandwich Joints Prepared by Electron Beam Welding. J. Mater. Eng. Perform. 29, 4251–4259.

Deng, D., 2009. FEM prediction of welding residual stress and distortion in carbon steel considering phase transformation effects. Mater. Des. 30, 359–366.

Deng, D., Murakawa, H., 2013. Influence of transformation induced plasticity on simulated results of welding residual stress in low temperature transformation steel. Comput. Mater. Sci. 78, 55–62.

Deng, D., Murakawa, H., 2008. FEM prediction of buckling distortion induced by welding in thin plate panel structures. Comput. Mater. Sci. 43, 591–607.

Deng, D., Zhou, Y., Bi, T., Liu, X., 2013. Experimental and numerical investigations of welding distortion induced by CO2 gas arc welding in thin-plate bead-on joints. Mater. Des. 1980-2015 52, 720–729.

Depradeux, L., Jullien, J.-F., 2004. Experimental and numerical simulation of thermomechanical phenomena during a TIG welding process, in: Journal de Physique IV (Proceedings). EDP sciences, pp. 697–704.

Devendranath Ramkumar, K., Maruthi Mohan Reddy, P., Raja Arjun, B., Choudhary, A., Srivastava, A., Arivazhagan, N., 2015. Effect of Filler Metals on the Weldability and Mechanical Properties of Multi-pass PCGTA Weldments of AISI 316L. J. Mater. Eng. Perform. 24, 1602–1613.

Devletian, J.H., Sullivan, M.J., Engineer, C.W., 2006. Flux Cored Arc Welding of CuNi 90/10 Piping with CuNi 70/30 Filler Metal. San Diego Portland State Univ.

Dhakal, B., Swaroop, S., 2018. Laser shock peening as post welding treatment technique. J. Manuf. Process. 32, 721–733.

Dhilip, A., Nampoothiri, J., Senthilkumar, M., Kirubanandan, N., 2022. Machine learning predictive approaches for hot crack mitigation in modified TIG welded AA7075 joints. Mater. Manuf. Process.

Dhinakaran, V., Shanmugam, N.S., Sankaranarayanasamy, K., 2017. Experimental investigation and numerical simulation of weld bead geometry and temperature distribution during plasma arc welding of thin Ti-6Al-4V sheets. J. Strain Anal. Eng. Des. 52, 30–44.

Dhinakaran, V, Siva Shanmugam, N., Sankaranarayanasamy, K., Rahul, R., 2017. Analytical and numerical investigations of weld bead shape in plasma arc welding of thin Ti-6al-4v sheets. SIMULATION 93, 1123–1138.

Diegel, C., Mattulat, T., Schricker, K., Schmidt, L., Seefeld, T., Bergmann, J.P., Woizeschke, P., 2023. Interaction between local shielding gas supply and laser spot size on spatter formation in laser beam welding of AISI 304. Appl. Sci. 13, 10507.

Dinda, S.K., kar, J., Jana, S., Gopal Roy, G., Srirangam, P., 2019. Effect of beam oscillation on porosity and intermetallics of electron beam welded DP600-steel to Al 5754-alloy. J. Mater. Process. Technol. 265, 191–200.

Dixit, U.S., Bag, S., 2017. Special Theme: Modelling of Manufacturing Processes. J. Inst. Eng. India Ser. C 98, 3–4.

Du, H., Hu, L., Liu, J., Hu, X., 2004. A study on the metal flow in full penetration laser beam welding for titanium alloy. Comput. Mater. Sci. 29, 419–427.

Durgaprasad, K., Pal, S., Das, M., 2023. Influence of cusp magnetic field on the evolution of metallurgical and mechanical properties in GTAW of SS 304. Int. J. Adv. Manuf. Technol. 126, 5199-5214.

Dwibedi, S., Bag, S., 2024. Critical assessment on the influence of process parameters in micro-plasma arc welding process: a review. Weld. Int. 38, 583–617.

Dwibedi, S., Bag, S., 2018. Plasma arc welding in small scale welding process. Weldfab Tech Times.

Dwibedi, S., Jain, N.K., 2016. Investigation on autogenous joining of stainless steel sheets of different thickness using micro Plasma Transferred Arc (μ-PTA) process (M.Tech Thesis). Discipline of Mechanical Engineering, IIT Indore.

Eagar, T.W., Tsai, N.S., 1983. Temperature fields produced by traveling distributed heat sources. Weld. J. 62, 346–355.

Elata, D., Abu-Salih, S., 2005. Analysis of a novel method for measuring residual stress in micro-systems. J. Micromechanics Microengineering 15, 921.

ElSheikh, A., Barakat, N., Abu-Nabah, B.A., Hamdan, M.O., 2022. Thermal diffusivity estimation in metallic alloys using a one-dimensional flux-based thermography. Infrared Phys. Technol. 127, 104411.

Ezuber, H.M., Al Shater, A., 2016. Influence of environmental parameters on the corrosion behavior of 90/10 cupronickel tubes in 3.5% NaCl. Desalination Water Treat. 57, 6670–6679.

Farid, M., Molian, P.A., 2000. High-brightness laser welding of thin-sheet 316 stainless steel. J. Mater. Sci. 35, 3817–3826.

Fattahi, M., Mohammady, M., Sajjadi, N., Honarmand, M., Fattahi, Y., Akhavan, S., 2015. Effect of TiC nanoparticles on the microstructure and mechanical properties of gas tungsten arc welded aluminum joints. J. Mater. Process. Technol. 217, 21–29.

Ferro, P., Bonollo, F., Tiziani, A., 2005. Laser welding of copper–nickel alloys: a numerical and experimental analysis. Sci. Technol. Weld. Join. 10, 299–310.

Feujofack Kemda, B.V., Barka, N., Jahazi, M., Osmani, D., 2021. Modeling of phase transformation kinetics in resistance spot welding and investigation of effect of post weld heat treatment on weld microstructure. Met. Mater. Int. 27, 1205–1223.

Frewin, M.R., Scott, D.A., 1999. Finite element model of pulsed laser welding. Weld. J.-N. Y.- 78, 15-s.

Fukumoto, S., Fujiwara, K., Toji, S., Yamamoto, A., 2008. Small-scale resistance spot welding of austenitic stainless steels. Mater. Sci. Eng. A 492, 243–249.

Gage, R.M., 1957. Arc torch and process.

Gavrish, P.A., Perig, A.V., 2020. Improvement of the heat state in welding copper with steel. Adv. Mater. Process. Technol. 6, 703–717.

Generoso, V.M.A., Souza, L.M. de, Pereira, E.C., Monteiro, S.N., de Azevedo, A.R., 2023. Influence of Pulsed Arc Parameters on the Tig Welding Process for the Stainless Steel Duplex UNS S31803. Materials 16, 6870.

Ghafouri, M., Ahn, J., Mourujärvi, J., Björk, T., Larkiola, J., 2020. Finite element simulation of welding distortions in ultra-high strength steel S960 MC including comprehensive thermal and solid-state phase transformation models. Eng. Struct. 219, 110804.

Gil, T.P.S., Mudali, U.K., Seetharaman, V., 1988. Effect of Heat Input and Microstructure on Pitting Corrosion in AISI 316L Submerged Arc Weids. Corros. Sci. 44, 6.

Goldak, J., 1985. A double ellipsoid finite element model for welding heat sources. IIW Doc No 212.

Goldak, J., Chakravarti, A., Bibby, M., 1984. A new finite element model for welding heat sources. Metall. Trans. B 15, 299–305.

Goldak, J.A., Akhlaghi, M., 2006. Computational welding mechanics. Springer Science & Business Media.

Guo, S., Zhou, Q., Kong, J., Peng, Y., Xiang, Y., Luo, T., Wang, K., Zhu, J., 2016. Effect of beam offset on the characteristics of copper/304stainless steel electron beam welding. Vacuum 128, 205–212.

Haglon, N., Bolot, R., Tomashchuk, I., Mathieu, A., Lafaye, S., 2024. Dissimilar welding between Cu–6Al–2Ni alloy and stainless steel 316L using continuous ytterbium YAG laser. Proc. Inst. Mech. Eng. Part J. Mater. Des. Appl. 14644207241245264.

Haldar, V., Pal, S., 2024a. Influence of Fusion Zone Metallurgy on the Mechanical Behavior of Ni-Based Superalloy and Austenitic Stainless Steel Dissimilar Joint. J. Mater. Eng. Perform. 33, 5735–5753.

Haldar, V., Pal, S., 2024b. Characterization of Mechanical Behavior in Solution-Treated Micro Plasma Arc Welded Blanks of Inconel 625. Met. Mater. Int.

Hamelin, C.J., Muránsky, O., Smith, M.C., Holden, T.M., Luzin, V., Bendeich, P.J., Edwards, L., 2014. Validation of a numerical model used to predict phase distribution and residual stress in ferritic steel weldments. Acta Mater. 75, 1–19.

Harjo, S., Tomota, Y., Ono, M., 1998. Measurements of thermal residual elastic strains in ferrite–austenite Fe–Cr–Ni alloys by neutron and X-ray diffractions. Acta Mater. 47, 353–362.

Hayat, F., 2011. The effects of the welding current on heat input, nugget geometry, and the mechanical and fractural properties of resistance spot welding on Mg/Al dissimilar materials. Mater. Des. 32, 2476–2484.

He, X., DebRoy, T., Fuerschbach, P.W., 2004. Composition change of stainless steel during microjoining with short laser pulse. J. Appl. Phys. 96, 4547–4555.

Homporova, P., Poletti, C., Stockinger, M., Warchomicka, F., 2011. Dynamic phase evolution in titanium alloy Ti-6Al-4V, in: Proc. 12th World Conference on Titanium. pp. 19–42.

Hondeos, E.D., McLean, D., 1974. Cohesion margin of copper. Philos. Mag. 29, 771–796.

Hosseini, H.S., Shamanian, M., Kermanpur, A., 2011. Characterization of microstructures and mechanical properties of Inconel 617/310 stainless steel dissimilar welds. Mater. Charact. 62, 425–431.

Hsieh, C.-C., 2008. Microstructural Evolution and Examination of α’-Martensite during a Multi-Pass Dissimilar Stainless Steel GTAW Process. Met. Mater. Int. 14, 643–648.

Hsieh, C.-C., Wang, P.-S., Wang, J.-S., Wu, W., 2014. Evolution of microstructure and residual stress under various vibration modes in 304 stainless steel welds. Sci. World J. 2014.

Hsieh, C.-C., Wu, W., 2011. Phase transformation of δ→σ in multipass heat-affected and fusion zones of dissimilar stainless steels. Met. Mater. Int. 17, 375–381.

Hsu, Y.F., Rubinsky, B., 1988. Two-dimensional heat transfer study on the keyhole plasma arc welding process. Int. J. Heat Mass Transf. 31, 1409–1421.

Hu, A., Janczak-Rusch, J., Sano, T., 2019. Joining technology innovations at the macro, micro, and nano levels. Appl. Sci. 9, 3568.

Huang, H., Wang, J., Li, L., Ma, N., 2016. Prediction of laser welding induced deformation in thin sheets by efficient numerical modeling. J. Mater. Process. Technol. 227, 117–128.

Huang, H.-Y., 2010. Research on the activating flux gas tungsten arc welding and plasma arc welding for stainless steel. Metals and Materials International 16, 819–825.

Ireland, C.L.M., 1990. Current state of power laser technology and future trends. Manuf. Technol.

Ishigami, A., Roy, M.J., Walsh, J.N., Withers, P.J., 2017. The effect of the weld fusion zone shape on residual stress in submerged arc welding. Int. J. Adv. Manuf. Technol. 90, 3451–3464.

Ismail, M.I.S., Okamoto, Y., Okada, A., Uno, Y., 2011. Experimental investigation on micro-welding of thin stainless steel sheet by fiber laser. Am. J. Eng. Appl. Sci. 4, 314–320.

Jahanzeb, N., Shin, J.-H., Singh, J., Heo, Y.-U., Choi, S.-H., 2017. Effect of microstructure on the hardness heterogeneity of dissimilar metal joints between 316L stainless steel and SS400 steel. Mater. Sci. Eng. A 700, 338–350.

Jain, R., Pal, S.K., Singh, S.B., 2017. Finite element simulation of temperature and strain distribution during friction stir welding of AA2024 aluminum alloy. J. Inst. Eng. India Ser. C 98, 37–43.

Janaki Ram, G.D., Venugopal Reddy, A., Prasad Rao, K., Madhusudhan Reddy, G., 2004. Control of Laves phase in Inconel 718 GTA welds with current pulsing. Sci. Technol. Weld. Join. 9, 390–398.

Jenkins, W.D., Digges, T.G., Johnson, C.R., 1957. Tensile Properties of Copper, Nickel, and 70-Percent-Cop. J. Res. Natl. Bur. Stand. 58, 201.

Jiang, Z., Chen, X., Li, H., Lei, Z., Chen, Y., Wu, S., Wang, Y., 2020. Grain refinement and laser energy distribution during laser oscillating welding of Invar alloy. Mater. Des. 186, 108195.

Jiang, Z., Tao, W., Yu, K., Tan, C., Chen, Y., Li, L., Li, Z., 2016. Comparative study on fiber laser welding of GH3535 superalloy in continuous and pulsed waves. Mater. Des. 110, 728–739.

Jiru, W.G., Sankar, M.R., Dixit, U.S., 2019. Laser surface alloying of aluminum for improving acid corrosion resistance. J. Inst. Eng. India Ser. C 100, 481–492.

Joo, S.-M., Bang, Hee-Sun, Bang, Han-Sur, Park, K.-S., 2016. Numerical investigation on welding residual stress and out-of-plane displacement during the heat sink welding process of thin stainless steel sheets. Int. J. Precis. Eng. Manuf. 17, 65–72.

Joshi, G.R., Badheka, V.J., 2020. Metallographic and microstructure analysis of gas tungsten arc-welded bimetallic copper-to-stainless steel joints. Metallogr. Microstruct. Anal. 9, 180–193.

Joshi, G.R., Badheka, V.J., 2019. Processing of bimetallic steel-copper joint by laser beam welding. Mater. Manuf. Process. 34, 1232–1242.

Jou, M., 2003. Experimental study and modeling of GTA welding process. J Manuf Sci Eng 125, 801–808.

Kalpana, J., Rao, P., 2017. A review on techniques for improving the mechanical properties of fusion welded joints. Eng. Solid Mech. 5, 213–224.

Kangazian, J., Shamanian, M., 2019a. Effect of Pulsed Current on the Microstructure, Mechanical Properties and Corrosion Behavior of Ni-Based Alloy/Super Duplex Stainless Steel Dissimilar Welds. Trans. Indian Inst. Met. 72, 2403–2416.

Kangazian, J., Shamanian, M., 2019b. Electron Back Scattered Diffraction Study of Dissimilar Welding Between the Super Duplex Stainless Steel and the Ni-Based Superalloy. Met. Mater. Int. 25, 1287–1300.

Kangazian, J., Shamanian, M., 2019c. Micro-texture and corrosion behavior of dissimilar joints of UNS S32750 stainless steel/UNS N08825 Ni-based superalloy. Mater. Charact. 155, 109802.

Kangazian, J., Shamanian, M., 2018. Characterization of Structure–Property Relationship of Incoloy 825 and SAF 2507 Dissimilar Welds. Trans. Indian Inst. Met. 71, 1747–1757.

Kar, J., Chakrabarti, D., Roy, S.K., Roy, G.G., 2019a. Beam oscillation, porosity formation and fatigue properties of electron beam welded Ti-6Al-4V alloy. J. Mater. Process. Technol. 266, 165–172.

Kar, J., Dinda, S.K., Roy, G.G., Roy, S.K., Srirangam, P., 2018. X-ray tomography study on porosity in electron beam welded dissimilar copper–304SS joints. Vacuum 149, 200–206.

Kar, J., Roy, S.K., Roy, G.G., 2016. Effect of beam oscillation on electron beam welding of copper with AISI-304 stainless steel. J. Mater. Process. Technol. 233, 174–185.

Karunaratne, M.S.A., Kyaw, S., Jones, A., Morrell, R., Thomson, R.C., 2016. Modelling the coefficient of thermal expansion in Ni-based superalloys and bond coatings. J. Mater. Sci. 51, 4213–4226.

Kastner, J., Heinzl, C., 2018. X-Ray Tomography, in: Ida, N., Meyendorf, N. (Eds.), Handbook of Advanced Non-Destructive Evaluation. Springer International Publishing, Cham, pp. 1–72.

Kay, W.D., 1993. ASM Handbook: Welding, Brazing, Soldering. ASM International, Metals Park, OH.

Kesavan Nair, P., Vasudevan, R., 1995. Residual stresses of types II and III and their estimation. Sadhana 20, 39–52.

Kianersi, D., Mostafaei, A., Amadeh, A.A., 2014. Resistance spot welding joints of AISI 316L austenitic stainless steel sheets: Phase transformations, mechanical properties and microstructure characterizations. Mater. Des. 61, 251–263.

Kim, B.-C., Kim, T.-H., Kim, K.-B., Kim, J.-S., Lee, H.-Y., 2002. Investigation on the effect of laser pulse shape during Nd:YAG laser microwelding of thin Al sheet by numerical simulation. Metall. Mater. Trans. A 33, 1449–1459.

Kohli, D., Rakesh, R., Sinha, V.P., Prasad, G.J., Samajdar, I., 2014. Fabrication of simulated plate fuel elements: Defining role of stress relief annealing. J. Nucl. Mater. 447, 150–159.

Kondapalli, S.P., Chalamalasetti, S.R., Damera, N.R., 2012. Optimization of Fusion Zone Grain Size, Hardness and Ultimate Tensile Strength of Pulsed Current Micro Plasma Arc Welded Inconel 625 Sheets Using Genetic Algorithm. J. Manuf. Sci. Prod. 12.

Krolczyk, J.B., Gapiński, B., Krolczyk, G.M., Samardžić, I., Maruda, R.W., Soucek, K., Legutko, S., Nieslony, P., Javadi, Y., Stas, L., 2016. Topographic inspection as a method of weld joint diagnostic. Teh. Vjesn. 23, 301–306.

Kubiak, M., Piekarska, W., 2016. Comprehensive model of thermal phenomena and phase transformations in laser welding process. Comput. Struct. 172, 29–39.

Kumar, A., Bhattacharyya, A., Pandey, C., 2023a. Structural Integrity Assessment of Inconel 617/P92 Steel Dissimilar Welds Produced Using the Shielded Metal Arc Welding Process. J. Mater. Eng. Perform.

Kumar, A., Guguloth, K., Pandey, S.M., Fydrych, D., Sirohi, S., Pandey, C., 2023b. Study on Microstructure-Property Relationship of Inconel 617 Alloy/304L SS Steel Dissimilar Welds Joint. Metall. Mater. Trans. A 54, 3844–3870.

Kumar, A., Pandey, C., 2023. Structural integrity assessment of Inconel 617/P92 steel dissimilar welds for different groove geometry. Sci. Rep. 13, 8061.

Kumar, B., Bag, S., 2019a. Phase transformation effect in distortion and residual stress of thin-sheet laser welded Ti-alloy. Opt. Lasers Eng. 122, 209–224.

Kumar, B., Bag, S., Mahadevan, S., Paul, C.P., Das, C.R., Bindra, K.S., 2021a. On the interaction of microstructural morphology with residual stress in fiber laser welding of austenitic stainless steel. CIRP J. Manuf. Sci. Technol. 33, 158–175.

Kumar, B., Bag, S., Paul, C.P., 2020a. Influence of heat input on welding induced distortion for Yb-fibre laser welded thin sheets. Mater. Today Proc. 26, 2040–2046.

Kumar, B., Bag, S., Paul, C.P., Das, C.R., Ravikumar, R., Bindra, K.S., 2020c. Influence of the mode of laser welding parameters on microstructural morphology in thin sheet Ti6Al4V alloy. Opt. Laser Technol. 131, 106456.

Kumar, B., Dwibedi, S., Bag, S., 2022a. On the interaction of cooling rate with thermal-microstructural-mechanical characteristics of laser-welded α + β titanium alloy. Adv. Mater. Process. Technol. 8, 774–789.

Kumar, B., Dwibedi, S., Bag, S., Mahapatra, M., Gupta, R., 2022b. A comparative study on microstructural and mechanical behaviour of spot welded Ti-6Al-4V alloy in as-welded and solution treated condition. Adv. Mater. Process. Technol. 8, 2637–2651.

Kumar, B., Kebede, D., Bag, S., 2018. Microstructure evolution in thin sheet laser welding of titanium alloy. Int. J. Mechatron. Manuf. Syst. 11, 203–229.

Kumar, B., Maharana, B.R., Sahu, A.K., Dwibedi, S., Jena, A., Das, S., Prasad, S., 2022c. Influence of Squeeze Time on Fracture Mode of SS304 Spot Weldments, in: Recent Advances in Manufacturing, Automation, Design and Energy Technologies. Springer, pp. 305–313.

Kumar, B., Nagamani Jaya, B., 2023. Thermal Stability and Residual Stresses in Additively Manufactured Single and Multi-material Systems. Metall. Mater. Trans. A 54, 1808–1824.

Kumar, C., Das, M., 2021. Exploration of Parametric Effect on Fiber Laser Weldments of SS-316L by Response Surface Method. J. Mater. Eng. Perform. 30, 4583–4603.

Kumar, K.S., Gejendhiran, S., Prasath, M., 2014. Comparative investigation of mechanical properties in GMAW/GTAW for various shielding gas compositions. Mater. Manuf. Process. 29, 996–1003.

Kumar, N., Pandey, C., Kumar, P., 2023. Dissimilar welding of Inconel alloys with austenitic stainless-steel: A review. J. Press. Vessel Technol. 145, 011506.

Kumar, R., Dilthey, U., Dwivedi, D.K., Ghosh, P.K., 2009a. Thin sheet welding of Al 6082 alloy by AC pulse-GMA and AC wave pulse-GMA welding. Mater. Des. 30, 306–313.

Kumar, R., Dilthey, U., Dwivedi, D.K., Sharma, S.P., Ghosh, P.K., 2009b. Welding of thin sheet of Al alloy (6082) by using Vario wire DC P-GMAW. Int. J. Adv. Manuf. Technol. 42, 102.

Kumar, R., Mahapatra, M.M., Pradhan, A.K., Giri, A., Pandey, C., 2023. Experimental and numerical study on the distribution of temperature field and residual stress in a multi-pass welded tube joint of Inconel 617 alloy. Int. J. Press. Vessels Pip. 206, 105034.

Kumar, S., Shahi, A.S., 2011. Effect of heat input on the microstructure and mechanical properties of gas tungsten arc welded AISI 304 stainless steel joints. Mater. Des. 32, 3617–3623.

Kumar, S.R., Singh, A.K., Sandeep, S., Aravind, P., 2018. Investigation on Microstructural behavior and Mechanical Properties of plasma arc welded dissimilar butt joint of austenitic- ferritic stainless steels. Mater. Today Proc. 5, 8008–8015.

Kumar, T.S., Balasubramanian, V., Sanavullah, M.Y., 2007. Influences of pulsed current tungsten inert gas welding parameters on the tensile properties of AA 6061 aluminium alloy. Mater. Des. 28, 2080–2092.

Kuryntsev, S.V., Morushkin, A.E., Gilmutdinov, A.K., 2017. Fiber laser welding of austenitic steel and commercially pure copper butt joint. Opt. Lasers Eng. 90, 101–109.

Kuryntsev, S.V., Shiganov, I.N., 2018. Welding austenitic steel to copper with the defocused radiation of a fibre laser. Weld. Int. 32, 50–53.

Ledbetter, H.M., 1982. Temperature behaviour of Young’s moduli of forty engineering alloys. Cryogenics 22, 653–656.

Lee, Y., Nordin, M., Babu, S.S., Farson, D.F., 2014. Effect of fluid convection on dendrite arm spacing in laser deposition. Metall. Mater. Trans. B 45, 1520–1529.

Li, J., Cai, Y., Yan, F., Wang, C., Zhu, Z., Hu, C., 2020. Porosity and liquation cracking of dissimilar Nd: YAG laser welding of SUS304 stainless steel to T2 copper. Opt. Laser Technol. 122, 105881.

Li, S., Hu, L., Dai, P., Bi, T., Deng, D., 2021. Influence of the groove shape on welding residual stresses in P92/SUS304 dissimilar metal butt-welded joints. J. Manuf. Process. 66, 376–386.

Li, Y., Tang, X., Lu, F., Xu, L., Cui, H., Shao, C., 2022. Dual beam laser fusion-brazed Ti6Al4V/AA7075 dissimilar lap joint: Crack inhibition via inoculation with TiC nanoparticles. Mater. Charact. 191, 112127.

Li, Z., Feng, G., Deng, D., Luo, Y., 2021. Investigating welding distortion of thin-plate stiffened panel steel structures by means of thermal elastic plastic finite element method. J. Mater. Eng. Perform. 30, 3677–3690.

Liang, W., Mao, Z., Hu, L., Deng, D., 2024. Estimating welding deformation of ultra-thin mild steel bead-on-plate joints by means of inherent strain method. Thin-Walled Struct. 111825.

Lin, Y.-C., Chou, C.P., 1995. A new technique for reducing the residual stress induced by welding in type 304 stainless steel. J. Mater. Process. Technol. 48, 693–698.

Lindgren, L.-E., 2006. Numerical modelling of welding. Comput. Methods Appl. Mech. Eng., Computational Metal Forming 195, 6710–6736.

Liu, P., Bao, J., Bao, Y., 2019. Mechanical Properties and Fracture Behavior of an EBW T2 Copper–45 Steel Joint. Materials 12, 1714.

Liu, X., Lan, S., Ni, J., 2014. Analysis of process parameters effects on friction stir welding of dissimilar aluminum alloy to advanced high strength steel. Mater. Des. 59, 50–62.

Liu, X., Lang, Q., Wang, J., Song, G., Liu, L., 2024. Effect of Alloying Elements in Steels on the Interfacial Structure and Mechanical Properties of Mg to Steel by Laser-GTAW Hybrid Direct Lap Welding. Materials 17, 1624.

Liu, Z., Zhang, D., Jin, X., Yu, C., 2023. Suppression of deformation and enhancement of weld properties in thin stainless steel using synchronous heat sink+ ultrasonic hybrid laser welding. J. Mater. Process. Technol. 322, 118215.

Lusch, C., Borsch, M., Heidt, C., Magginetti, N., Sas, J., Weiss, K.P., Grohmann, S., 2015. Qualification of electron-beam welded joints between copper and stainless steel for cryogenic application, in: IOP Conference Series: Materials Science and Engineering. IOP Publishing, p. 012017.

Ma, C., Peng, Q., Mei, J., Han, E.-H., Ke, W., 2018. Microstructure and corrosion behavior of the heat affected zone of a stainless steel 308L-316L weld joint. J. Mater. Sci. Technol. 34, 1823–1834.

Madhusudhan Reddy, G., Mohandas, T., Sambasiva Rao, A., Satyanarayana, V.V., 2005. Influence of welding processes on microstructure and mechanical properties of dissimilar austenitic-ferritic stainless steel welds. Mater. Manuf. Process. 20, 147–173.

Magnabosco, I., Ferro, P., Bonollo, F., Arnberg, L., 2006. An investigation of fusion zone microstructures in electron beam welding of copper–stainless steel. Mater. Sci. Eng. A 424, 163–173.

Mai, T.A., Spowage, A.C., 2004. Characterisation of dissimilar joints in laser welding of steel–kovar, copper–steel and copper–aluminium. Mater. Sci. Eng. A 374, 224–233.

Mannucci, A., Tomashchuk, I., Vignal, V., Sallamand, P., Duband, M., 2018. Parametric study of laser welding of copper to austenitic stainless steel. Procedia CIRP 74, 450–455.

Martikainen, J., 1995. Conditions for achieving high-quality welds in the plasma-arc keyhole welding of structural steels. J. Mater. Process. Technol. 52, 68–75.

Martikainen, J.K., Moisio, T.J.I., 1993. Investigation of the effect of welding parameters on weld quality of plasma arc keyhole welding of structural steels. Weld. J.-N. Y.- 72, 329-s.

Maurya, A.K., Chhibber, R., Pandey, C., 2023. Studies on residual stresses and structural integrity of the dissimilar gas tungsten arc welded joint of sDSS 2507/Inconel 625 for marine application. J. Mater. Sci. 58, 8597–8634.

Mazumder, J., Steen, W.M., 1980. Heat transfer model for CW laser material processing. J. Appl. Phys. 51, 941–947.

McAuley, I., 1991. Copper-nickel brake tubing in the automotive industry. Mater. Des. 12, 228–230.

Meng, Y., Li, X., Gao, M., Zeng, X., 2019. Microstructures and mechanical properties of laser-arc hybrid welded dissimilar pure copper to stainless steel. Opt. Laser Technol. 111, 140–145.

Mi, G., Xiong, L., Wang, C., Hu, X., Wei, Y., 2016. A thermal-metallurgical-mechanical model for laser welding Q235 steel. J. Mater. Process. Technol. 238, 39–48.

Moharana, B.R., Sahu, S.K., Maiti, A., Sahoo, S.K., Moharana, T.K., 2020. An experimental study on joining of AISI 304 SS to Cu by Nd-YAG laser welding process. Mater. Today Proc.

Moharana, B.R., Sahu, S.K., Sahoo, S.K., Bathe, R., 2016. Experimental investigation on mechanical and microstructural properties of AISI 304 to Cu joints by CO2 laser. Eng. Sci. Technol. Int. J. 19, 684–690.

Mousavi, S.A., Miresmaeili, R., 2008. Experimental and numerical analyses of residual stress distributions in TIG welding process for 304L stainless steel. J. Mater. Process. Technol. 208, 383–394.

Munro, C., 2013. The Effects of Repeated Weld Repairs on the Mechanical Properties of Copper-Nickel Pipe Joints.

Nayak, L.J., Roy, G.G., 2021. Effect of heat input on microstructure, mechanical and corrosion properties of electron beam welded zircaloy-4 sheets. Weld. World 65, 987–1005.

Neissi, R., Shamanian, M., Hajihashemi, M., 2016. The Effect of Constant and Pulsed Current Gas Tungsten Arc Welding on Joint Properties of 2205 Duplex Stainless Steel to 316L Austenitic Stainless Steel. J. Mater. Eng. Perform. 25, 2017–2028.

Nélias, D., Jullien, J.-F., Deloison, D., 2010. Experimental investigation and finite element simulation of laser beam welding induced residual stresses and distortions in thin sheets of AA 6056-T4. Mater. Sci. Eng. A 527, 3025–3039.

Nevcanoğlu, A., Bozkurt, Y., Salman, S., 2021. The Effect of TIG Welding Parameters and Automatization for Non-Heat Treated Inconel 718 Sheets. Arab. J. Sci. Eng. 46, 12613–12623.

Nguyen, N.T., Ohta, A., Matsuoka, K., Suzuki, N., Maeda, Y., 1999. Analytical solutions for transient temperature of semi-infinite body subjected to 3-D moving heat sources. Weld. J.-N. Y.- 78, 265-s.

Nguyen, Q., Azadkhou, A., Akbari, M., Panjehpour, A., Karimipour, A., 2020. Experimental investigation of temperature field and fusion zone microstructure in dissimilar pulsed laser welding of austenitic stainless steel and copper. J. Manuf. Process. 56, 206–215.

Niedermayer, J., 2022. Parameter study for 3D printing of Al5356, Al4047 and Al4043 by directed energy deposition with transferred plasma arc (PhD Thesis). Technische Universität Wien.

Nowacki, J., Sajek, A., Matkowski, P., 2016. The influence of welding heat input on the microstructure of joints of S1100QL steel in one-pass welding. Arch. Civ. Mech. Eng. 16, 777–783.

Olabi, A.G., Hashmi, M.S.J., 1993. Review of methods for measuring residual stresses in components, in: Proceedings of 9th Conf. on Manufacturing Research Sep.

Omar, H.D., 2016. The analysis of copper-iron metallic mixture by means of XRD and XRF. Int. Lett. Chem. Phys. Astron. 64, 130–134.

Onink, M., Brakman, C.M., Tichelaar, F.D., Mittemeijer, E.J., Van der Zwaag, S., Root, J.H., Konyer, N.B., 1993. The lattice parameters of austenite and ferrite in Fe-C alloys as functions of carbon concentration and temperature. Scr. Metall. Mater. States 29.

Pal, K., Pal, S.K., 2011. Effect of Pulse Parameters on Weld Quality in Pulsed Gas Metal Arc Welding: A Review. J. Mater. Eng. Perform. 20, 918–931.

Pandey, C., Mahapatra, M.M., Kumar, P., 2018a. A comparative study of transverse shrinkage stresses and residual stresses in P91 welded pipe including plasticity error. Arch. Civ. Mech. Eng. 18, 1000–1011.

Pandey, C., Mahapatra, M.M., Kumar, P., 2018b. Effect of post weld heat treatments on fracture frontier and type IV cracking nature of the crept P91 welded sample. Mater. Sci. Eng. A 731, 249–265.

Pascu, A., Stanciu, E.M., Voiculescu, I., Ţierean, M.H., Roată, I.C., Ocaña, J.L., 2016. Chemical and Mechanical Characterization of AISI 304 and AISI 1010 Laser Welding. Mater. Manuf. Processes. 31, 311–318.

Pasek-Siurek, H., 2014. Plasma welding: processes and equipment. Weld. Int. 28, 672–678.

Pavelic, V., 1969. Experimental and computed temperature histories in gas tungsten arc welding of thin plates. Weld. J. Res. Suppl. 48, 296–305.

Phanikumar, G., Manjini, S., Dutta, P., Chattopadhyay, K., Mazumder, J., 2005. Characterization of a continuous CO 2 laser-welded Fe-Cu dissimilar couple. Metall. Mater. Trans. A 36, 2137–2147.

Piccini, J., Svoboda, H., 2012. Effect of the plasma arc welding procedure on mechanical properties of DP700 steel. Procedia Mater. Sci. 1, 50–57.

Poo-arporn, Y., Duangnil, S., Bamrungkoh, D., Klangkaew, P., Huasranoi, C., Pruekthaisong, P., Boonsuya, S., Chaiprapa, J., Ruangvittayanon, A., Saisombat, C., 2020. Gas tungsten arc welding of copper to stainless steel for ultra-high vacuum applications. J. Mater. Process. Technol. 277, 116490.

Powell, C., Corrosion and Biofouling Resistance Evaluation of 90-10 Copper-Nickel 10.

Powell, C., Webster, P., Copper Alloys for Marine Environments 32.

Prasad, K.S., Rao, C.S., Rao, D.N., 2011. Prediction of weld pool geometry in pulsed current micro plasma arc welding of SS304L stainless steel sheets. Int. Trans. J. Eng. Manag. Appl. Sci. Technol. 2, 325–336.

Prasad, S., 2019. Investigation and analysis of micro plasma arc welding of ss 316l sheet.

Prasad, S., Dwibedi, S., Purohit, A., 2024. An Experimental Study to Probe Defect Formation and Failure Mode in Dissimilar Spot Joints, in: Tambe, P., Huang, P., Jhavar, S. (Eds.), Advances in Mechanical Engineering and Material Science, Lecture Notes in Mechanical Engineering. Springer Nature Singapore, Singapore, pp. 307–315.

Priyadharshini, G.S., Subramanian, R., Murugan, N., Sathiskumar, R., 2017. Influence of friction stir processing parameters on surface modified 90Cu-10Ni composites. Mater. Manuf. Process. 32, 1416–1427.

Qi, Y., Ma, X., Ma, L., Zhou, C., Jiang, Z., Zhao, J., 2024. A Study on the Microstructural Evolution, Interfacial Diffusion and Mechanical Properties of Ultra-thin Stainless Steel–Copper Composites Fabricated by Roll Bonding. Met. Mater. Int. 30, 2925–2941.

Qin, B., Yin, F., Xie, F., Shen, J., Xie, J., Wu, D., 2018. Effects and distribution of TiC on the nanoparticle strengthening A-TIG welded AZ31 magnesium alloy joints. Mater. Res. Express 6, 026543.

Quigley, M.B.C., 1986. High power density welding, in: The Physics of Welding. Elsevier, pp. 306–329.

Rafiei, M., Mostaan, H., 2019. The effect of filler metal and butter layer on microstructural and mechanical properties of pure Cu to AISI304 stainless steel dissimilar joint. Proc. Inst. Mech. Eng. Part J. Mater. Des. Appl. 233, 1894–1905.

Ragavendran, M., Vasudevan, M., 2020. Laser and hybrid laser welding of type 316L (N) austenitic stainless steel plates. Materials and Manufacturing Processes 35, 922–934.

Raghav, A.K., Vignesh, R.V., Kalyan, K.P., Govindaraju, M., 2020. Friction Welding of Cast Iron and Phosphor Bronze. J. Inst. Eng. India Ser. C 1–8.

Rahimi, A., Shamanian, M., Atapour, M., 2021. Effect of Pulse Current Frequency on Microstructure and Hot Corrosion Behavior of Tungsten Inert Gas-Welded Joints of N155 Superalloy. J. Mater. Eng. Perform. 30, 7494–7509.

Rahimi, A., Shamanian, M., Szpunar, J.A., 2020. Effect of Pulsed Current Frequency on Microstructure and Mechanical Properties of Gas-Tungsten-Arc-Welded Joints of UNS R30155. J. Mater. Eng. Perform. 29, 2635–2647.

Rahimi, Amirkeyvan, Shamanian, M., Rahimi, Ahmadreza, Kangazian, J., 2018. A Comparative Study on Direct and Pulsed Current Micro-plasma Arc Welding of Alloy Ti–6Al–4V. Trans. Indian Inst. Met. 71, 3103–3110.

Rajendran, A.R., Fahad, M., Manoharan, D.A., Ajmal, A.H.P., Salam, N.A., Vijayan, J., 2024. Investigation of Intermetallic Compound Formation in Dissimilar Metal Welds between Copper and Stainless Steel using Gas Tungsten Arc Welding. J. Adv. Res. Appl. Mech. 114, 163–172.

Ramachandran, S., Lakshminarayanan, A.K., 2020. An insight into microstructural heterogeneities formation between weld subregions of laser welded copper to stainless steel joints. Trans. Nonferrous Met. Soc. China 30, 727–745.

Ravichandran, M., Sabarirajan, N., Sathish, T., Saravanan, S., 2016. Effect of welding parameters on mechanical properties of plasma transferred arc welded SS 202 plates. Appl. Mech. Mater. 852, 324–330.

Raymond, T., Slatter, E., 1998. The plasma advantage in automated welding. Weld. J. 77, 55–57.

Reutzel, E.W., Kern, L., Sullivan, M.J., Tressler, J.F., Avalos, J., 2007. Laser-GMA Hybrid Pipe Welding System. PENNSYLVANIA STATE UNIV UNIVERSITY PARK APPLIED RESEARCH LAB.

Reyaz, M.S.B., Sinha, A.N., Mehdi, H., Murtaza, Q., 2024. Effect of Pulsed TIG Welding Parameters on the Microstructural Evolution and Mechanical Properties of Dissimilar AA6061-T6 and AA7075-T6 Weldments. Arab. J. Sci. Eng. 49, 10891–10911.

Rezghi Maleki, H., Hamedi, M., Kubouchi, M., Arao, Y., 2019. Experimental investigation on drilling of natural flax fiber-reinforced composites. Mater. Manuf. Process. 34, 283–292.

RK, B.M., Maji, P., Samadhiya, A., Ghosh, S.K., Roy, B.S., Das, A.K., Saha, S.C., 2018. A study on induction welding of mild steel and copper with flux under applied load condition. J. Manuf. Process. 34, 435–441.

Rong, Y., Huang, Y., Xu, J., Zheng, H., Zhang, G., 2017. Numerical simulation and experiment analysis of angular distortion and residual stress in hybrid laser-magnetic welding. J. Mater. Process. Technol. 245, 270–277.

Rosenthal, D., 1941. Mathematical theory of heat distribution during welding and cutting. Weld. J. 20, 220s–234s.

Roy, C., Pavanan, V.V., Vishnu, G., Hari, P.R., Arivarasu, M., Manikandan, M., Ramkumar, D., Arivazhagan, N., 2014. Characterization of metallurgical and mechanical properties of commercially pure copper and AISI 304 dissimilar weldments. Procedia Mater. Sci. 5, 2503–2512.

Roy, R.K., Singh, S., Gunjan, M.K., Panda, A.K., Mitra, A., 2011. Joining of 304SS and pure copper by rapidly solidified Cu-based braze alloy. Fusion Eng. Des. 86, 452–455.

Russell, M., 1942. Welding torch.

Saha, D., Pal, S., 2024. Joining Behaviour of Thick PlaTe using high-frequency inducTion assisTed arc Welding 69, 675–683.

Saha, D., Pal, S., 2019. Microstructure and Work Hardening Behavior of Micro-plasma Arc Welded AISI 316L Sheet Joint. Journal of Materials Engineering and Performance 28, 2588–2599.

Sahu, A.K., 2021. Laser and micro plasma arc welding of thin sheet inconel 718 and aisi 316l stainless steel at similar and dissimilar combinations.

Sahu, A.K., Bag, S., 2021. Influence of current pulsation on solidification parameters during micro-plasma arc welding of thin sheet Alloy 718. Weld. World 65, 2403–2419.

Sahu, A.K., Bag, S., 2020. Probe Pulse Conditions and Solidification Parameters for the Dissimilar Welding of Inconel 718 and AISI 316L Stainless Steel. Metall. Mater. Trans. A 51, 2192.

Sahu, A.K., Bag, S., Huang, K., 2020. Mitigation of micro-cracks in dissimilar welding of Inconel 718 and austenitic stainless steel. Philos. Mag. Lett. 100, 365–374.

Sahu, N., Naik, R.K., Panda, D., Sahoo, S.K., Kar, P.K., Badjena, S.K., 2024. Weld Morphology and Corrosion Characteristics of Flux-Assisted Gas Tungsten Arc-Welded Super Duplex Stainless Steel. J. Mater. Eng. Perform.

Sahul, Miroslav, Tomčíková, E., Sahul, Martin, Pašák, M., Ludrovcová, B., Hodúlová, E., 2020. Effect of disk laser beam offset on the microstructure and mechanical properties of copper—AISI 304 stainless steel dissimilar metals joints. Metals 10, 1294.

Saida, K., Nishijima, Y., Ogiwara, H., Nishimoto, K., 2015. Prediction of solidification cracking in laser welds of type 310 stainless steels. Weld. Int. 29, 577–586.

Saikia, T., Baruah, M., Bag, S., 2019a. On the effect of heat input in plasma microwelding of maraging steel. Proc. Inst. Mech. Eng. Part B J. Eng. Manuf. 233, 807–822.

Saikia, T., Baruah, M., Bag, S., 2019b. On the effect of heat input in plasma microwelding of maraging steel. Proc IMechE, Part B: J Engineering Manufacture 233, 807–822.

Samanta, S.K., Mitra, S.K., Pal, T.K., 2008. Microstructure and Oxidation Characteristics of Laser and GTAW Weldments in Austenitic Stainless Steels. J. Mater. Eng. Perform. 17, 908–914.

Saranarayanan, R., Lakshminarayanan, A.K., Venkatraman, B., 2019. A combined full-field imaging and metallography approach to assess the local properties of gas tungsten arc welded copper—stainless steel joints. Arch. Civ. Mech. Eng. 19, 251–267.

S.C., V., Yadavalli, P., George, R.P., C., M., U., K.M., 2018. Development of hydrophobic cupronickel surface with biofouling resistance by sandblasting. Surf. Coat. Technol. 345, 89–95.

Shamanian, M., Kangazian, J., Derakhshi, M.A., Szpunar, J.A., 2019. Microstructure and Mechanical Properties of Inconel 617/AISI 310 Electron Beam Welds. Metall. Mater. Trans. A 50, 3164–3173.

Shamanian, M., Valehi, M., Kangazian, J., Szpunar, J.A., 2020. EBSD characterization of the L-605 Co-based alloy welds processed by pulsed Nd: YAG laser welding. Opt. Laser Technol. 128, 106256.

Shen, L., He, Y., Liu, D., Gong, Q., Zhang, B., Lei, J., 2015. A novel method for determining surface residual stress components and their directions in spherical indentation. J. Mater. Res. 30, 1078–1089.

Shinde, N.V., Telsang, M.T., 2016. Effect of Alternate Supply of Shielding Gases of Tungsten Inert Gas Welding on Mechanical Properties of Austenitic Stainless Steel. J. Inst. Eng. India Ser. C 97, 299–307.

Shiri, S.G., Nazarzadeh, M., Sharifitabar, M., Afarani, M.S., 2012. Gas tungsten arc welding of CP-copper to 304 stainless steel using different filler materials. Trans. Nonferrous Met. Soc. China 22, 2937–2942.

Shit, G., Kuppusamy, M.V., Ningshen, S., 2019. Corrosion Resistance Behavior of GTAW Welded AISI type 304L Stainless Steel. Transactions of the Indian Institute of Metals 72, 2981.

Sichani, H.R., Atapour, M., Ashrafizadeh, F., Galati, M., Saboori, A., 2024. Mechanical, electrochemical and permeability behaviour of Ti6Al–4V scaffolds fabricated by electron beam powder bed fusion for orthopedic implant applications: The role of cell type and cell size. J. Mater. Res. Technol. 28, 3240–3257.

Siddiquee, A.N., Khan, N.Z., Gangil, N., Bajaj, D., Mohammed, S., Chen, D.L., 2024. Autogenous dissimilar welding of copper-to-stainless steel via electron beam welding: a novel strategy for achieving defect-free joints. Metall. Mater. Trans. A 55, 635–651.

Siddiquee, A.N., Khan, N.Z., Gangil, N., Bajaj, D., Mohammed, S.M.A.K., Chen, D.L., 2023. Autogenous Dissimilar Welding of Copper-to-Stainless Steel via Electron Beam Welding: A Novel Strategy for Achieving Defect-Free Joints. Metall. Mater. Trans. A.

Singh, G., Saxena, R.K., Pandey, S., 2021. Investigating the effect of arc offsetting in AISI 304 stainless steel and copper welding using gas tungsten arc welding. J. Braz. Soc. Mech. Sci. Eng. 43, 174.

Singh, G., Saxena, R.K., Pandey, S., 2020. An examination of mechanical properties of dissimilar AISI 304 stainless steel and copper weldment obtained using GTAW. Mater. Today Proc. 26, 2783–2789.

Singh, R., Slathia, R.S., 2016. Effect of cryogenic treatment on sensitization of 304 stainless steel in TIG welding. J. Inst. Eng. India Ser. C 97, 127–130.

Sokoluk, M., Cao, C., Pan, S., Li, X., 2019. Nanoparticle-enabled phase control for arc welding of unweldable aluminum alloy 7075. Nat. Commun. 10, 98.

Soltani, H.M., Tayebi, M., 2018. Comparative study of AISI 304L to AISI 316L stainless steels joints by TIG and Nd:YAG laser welding. J. Alloys. Compd. 767, 112–121.

Sonia, P., Jain, J.K., Saxena, K.K., 2021. Influence of ultrasonic vibration assistance in manufacturing processes: A Review. Mater. Manuf. Process. 36, 1451–1475.

Soysal, T., Kou, S., Tat, D., Pasang, T., 2016. Macrosegregation in dissimilar-metal fusion welding. Acta Mater. 110, 149–160.

Straight, M.R., Sudarshan, T.S., Wilson, J.H., 1988. Significance of defects in fatigue of Cu-Ni/steel welds. Eng. Fract. Mech. 31, 673–681.

Su, H., Zhao, Q., Chen, J., Wu, C., 2022. Homogenizing the intermetallic compounds distribution in Al/Cu dissimilar friction stir welding joint with the assistance of ultrasonic vibration. Mater. Today Commun. 31, 103643.

Suhuddin, U., Mironov, S., Sato, Y.S., Kokawa, H., 2010. Grain structure and texture evolution during friction stir welding of thin 6016 aluminum alloy sheets. Mater. Sci. Eng. A 527, 1962–1969.

Sun, J., Liu, X., Tong, Y., Deng, D., 2014a. A comparative study on welding temperature fields, residual stress distributions and deformations induced by laser beam welding and CO2 gas arc welding. Mater. Des. 63, 519–530.

Sun, J., Liu, X., Tong, Y., Deng, D., 2014b. A comparative study on welding temperature fields, residual stress distributions and deformations induced by laser beam welding and CO2 gas arc welding. Mater. Des. 63, 519–530.

Sundaresan, S., Ram, G.J., Reddy, G.M., 1999. Microstructural refinement of weld fusion zones in α–β titanium alloys using pulsed current welding. Mater. Sci. Eng. A 262, 88–100.

Taban, E., 2008. Joining of Duplex Stainless Steel by Plasma Arc, TIG, and Plasma Arc+TIG Welding Processes. Mater. Manuf. Process. 23, 871–878.

Tanmay, Panda, S.S., 2023. Microstructure and Mechanical Characterization of Stainless Steel and Copper Joint by Metallurgical Modification in GTAW Process. Metall. Mater. Trans. A 54, 1010–1023.

Taraphdar, P.K., Kumar, R., Giri, A., Pandey, C., Mahapatra, M.M., Sridhar, K., 2021a. Residual stress distribution in thick double-V butt welds with varying groove configuration, restraints and mechanical tensioning. J. Manuf. Process. 68, 1405–1417.

Taraphdar, P.K., Kumar, R., Pandey, C., Mahapatra, M.M., 2021b. Significance of Finite Element Models and Solid-State Phase Transformation on the Evaluation of Weld Induced Residual Stresses. Met. Mater. Int. 27, 3478–3492.

Taraphdar, P.K., Mahapatra, M.M., Pradhan, A.K., Singh, P.K., Sharma, K., Kumar, S., 2021c. Effects of groove configuration and buttering layer on the through-thickness residual stress distribution in dissimilar welds. Int. J. Press. Vessels Pip. 192, 104392.

Taraphdar, P.K., Thakare, J.G., Pandey, C., Mahapatra, M.M., 2020. Novel residual stress measurement technique to evaluate through thickness residual stress fields. Mater. Lett. 277, 128347.

Taylor, G.A., Hughes, M., Strusevich, N., Pericleous, K., 2002. Finite volume methods applied to the computational modelling of welding phenomena. Appl. Math. Model. 26, 311–322.

Thakur, L., Aravindan, S., 2024. Dissimilar joining of AZ31B and Ti–6Al–4V sheets in lap joint using cold metal transfer welding. J. Adhes. Sci. Technol. 1–17.

Thibault, D., Bocher, P., Thomas, M., Gharghouri, M., Côté, M., 2010. Residual stress characterization in low transformation temperature 13% Cr–4% Ni stainless steel weld by neutron diffraction and the contour method. Mater. Sci. Eng. A 527, 6205–6210.

Toloei, A., Stoilov, V., Northwood, D., 2015. Simultaneous effect of surface roughness and passivity on corrosion resistance of metals. WIT Trans Eng Sci 90, 355–367.

Toloei, A., Stoilov, V., Northwood, D., 2013. The relationship between surface roughness and corrosion, in: ASME International Mechanical Engineering Congress and Exposition. American Society of Mechanical Engineers, p. V02BT02A054.

Tong, H., Ueyama, T., Harada, S., Ushio, M., 2001. Quality and productivity improvement in aluminium alloy thin sheet welding using alternating current pulsed metal inert gas welding system. Sci. Technol. Weld. Join. 6, 203–208.

Tosto, S., Nenci, F., Jiandong, H., Corniani, G., Pierdominici, F., 2003. Microstructure of copper–AISI type 304L electron beam welded alloy. Mater. Sci. Technol. 19, 519–522.

Trivedi, A., Bag, S., De, A., 2007. Three-dimensional transient heat conduction and thermomechanical analysis for laser spot welding using adaptive heat source. Sci. Technol. Weld. Join. 12.

Trivedi, A., Suman, A., De, A., 2006. Integrating Finite Element Based Heat Transfer Analysis with Multivariate Optimization for Efficient Weld Pool Modeling. ISIJ Int. 46, 267–275.

Tsirkas, S.A., Papanikos, P., Kermanidis, T., 2003. Numerical simulation of the laser welding process in butt-joint specimens. J. Mater. Process. Technol. 134, 59–69.

Tümer, M., Yılmaz, R., 2016. Characterization of microstructure, chemical composition, and toughness of a multipass welded joint of austenitic stainless steel AISI316L. Int. J. Adv. Manuf. Technol. 87, 2567–2579.

Türker, M., Ertürk, A.T., Karakulak, E., Güven, E.A., 2018. Effects of Different Heat Treatments on Microstructure, Toughness and Wear Behavior of GX 10CrNiMoNb 18-10 Cast Austenitic Stainless Steel. Trans. Indian. Inst. Met. 71, 1033–1040.

Urena, A., Otero, E., Utrilla, M.V., Munez, C.J., 2007. Weldability of a 2205 duplex stainless steel using plasma arc welding. J. Mater. Process. Technol. 182, 624–631.

Valiente Bermejo, M.A., 2012. A Mathematical Model To Predict δ- Ferrite Content In Austenitic Stainless Steel Weld Metals. Weld. World. 56, 48–68.

Van Nguyen, A., Tashiro, S., Ngo, M.H., Le, A.H., Van Bui, H., Tanaka, M., 2020. Influence of shielding gas composition on molten metal flow behavior during plasma keyhole arc welding process. J. Manuf. Process. 53, 431–437.

Vasantharaja, P., Vasudevan, M., Maduraimuthu, V., 2018. Effect of arc welding processes on the weld attributes of type 316LN stainless steel weld joint. Trans. Indian. Inst. Met. 71, 127–137.

Vashishtha, H., Taiwade, R.V., Sharma, S., Patil, A.P., 2017. Effect of welding processes on microstructural and mechanical properties of dissimilar weldments between conventional austenitic and high nitrogen austenitic stainless steels. Journal of Manufacturing Processes 25, 49–59.

Velu, M., Bhat, S., 2013. Metallurgical and mechanical examinations of steel–copper joints arc welded using bronze and nickel-base superalloy filler materials. Mater. Des. 47, 793–809.

Vidyarthy, R.S., Dwivedi, D.K., 2019. Effect of shielding gas composition and activating flux on the weld bead morphology of the P91 ferritic/martensitic steel. Mater. Res. Express 6, 0865f7.

Wang, J., Chen, X., Yang, L., Zhang, G., 2022. Effect of preheat & post-weld heat treatment on the microstructure and mechanical properties of 6061-T6 aluminum alloy welded sheets. Mater. Sci. Eng. A 841, 143081.

Wang, Y., Chen, Q., 2002. On-line quality monitoring in plasma-arc welding. J. Mater. Process. Technol. 120, 270–274.

Wei, S., Xu, L., He, K., Li, J., Feng, W., Du, R., 2015. Experimental study on manufacturing metal bellows forming by water jet incremental forming. Int. J. Adv. Manuf. Technol. 81, 129–133.

Weigl, M., Schmidt, M., 2010. Influence of the feed rate and the lateral beam displacement on the joining quality of laser-welded copper-stainless steel connections. Phys. Procedia 5, 53–59.

Weman, K., 2011. Welding processes handbook. Elsevier.

Wu, C., Wang, H.G., Zhang, Y.M., 2006. A new heat source model for keyhole plasma arc welding in FEM analysis of the temperature profile. Weld. J.-N. Y.- 85, 284.

Wu, C.S., Huo, Y.S., 2013. Numerical analysis of keyhole geometry and temperature profiles in plasma arc welding. J. Manuf. Process. 15, 593–599.

Wu, C.S., Wang, L., Ren, W.J., Zhang, X.Y., 2014. Plasma arc welding: Process, sensing, control and modeling. J. Manuf. Process. 16, 74–85.

Xing, S., Bai, S., Liu, R., Liu, Y., Qi, J., Hou, J., Zhang, D., 2023. Characterization of Corrosion Behavior and Corrosion Production Property of 90-10 Cupronickel Welding Joints in Flowing Seawater. Metals 13, 294.

Xu, Y., Hou, X., Shi, Y., Zhang, W., Gu, Y., Feng, C., Volodymyr, K., 2021. Correlation between the microstructure and corrosion behaviour of copper/316 L stainless-steel dissimilar-metal welded joints. Corros. Sci. 191, 109729.

Yadaiah, N., Bag, S., 2014. Development of egg-configuration heat source model in numerical simulation of autogenous fusion welding process. Int. J. Therm. Sci. 86, 125–138.

Yadaiah, N., Bag, S., 2012. Effect of heat source parameters in thermal and mechanical analysis of linear GTA welding process. ISIJ Int. 52, 2069–2075.

Yaghi, A.H., Hyde, T.H., Becker, A.A., Sun, W., 2008. Finite element simulation of welding and residual stresses in a P91 steel pipe incorporating solid-state phase transformation and post-weld heat treatment. J. Strain Anal. Eng. Des. 43, 275–293.

Yan, S., Shi, Y., Liu, J., Ni, C., 2019. Effect of laser mode on microstructure and corrosion resistance of 316L stainless steel weld joint. Opt. Laser Technol. 113, 428–436.

Yao, C., Xu, B., Zhang, X., Huang, J., Fu, J., Wu, Y., 2009. Interface microstructure and mechanical properties of laser welding copper–steel dissimilar joint. Opt. Lasers Eng. 47, 807–814.

Yousefi, M., Farghadin, M.H., Farzadi, A., 2015. Investigate the causes of cracks in welded 310 stainless steel used in the Flare tip. Eng. Fail. Anal. 53, 138–147.

Yue, C., Geng, S., Guo, L., Han, C., Jiang, P., 2022. Dendrite remelting during arc oscillation welding of magnesium alloys: A phase-field study. Appl. Phys. A 128, 437.

Zacharia, T., David, S.A., Vitek, J.M., Debroy, T., 1989. Heat transfer during Nd: Yag pulsed laser welding and its effect on solidification structure of austenitic stainless steels. Metall. Trans. A 20, 957–967.

Zhang, B., Jian, Z., Li, X., Feng, J., 2014. Electron beam welding of 304 stainless steel to QCr0. 8 copper alloy with copper filler wire. Trans. Nonferrous Met. Soc. China 24, 4059–4066.

Zhang, H., Xu, M., Kumar, P., Li, C., Dai, W., Liu, Z., Li, Z., Zhang, Y., 2021a. Enhancement of fatigue resistance of additively manufactured 304L SS by unique heterogeneous microstructure. Virtual Phys. Prototyp. 16, 125–145.

Zhang, H., Xu, M., Liu, Zhendong, Li, C., Kumar, P., Liu, Zhenhua, Zhang, Y., 2021b. Microstructure, surface quality, residual stress, fatigue behavior and damage mechanisms of selective laser melted 304L stainless steel considering building direction. Addit. Manuf. 46, 102147.

Zhang, K., Li, C., Qian, X., Chen, J., Lu, H., 2024. Non-synchronous deformation under shot peening post-treatment of SUS304 bar-plate rotary friction weld generates non-monotonic evolution on material and fatigue property. J. Mater. Res. Technol.

Zhang, X., Wang, L., Du, S., Li, Q., Zhang, L., Li, H., Chen, Z., Yang, D., Zhang, Xiaoyong, Wang, K., 2024. Microstructure evolution and mechanical properties of new Co-free maraging steel produced by wire arc additive manufacturing. Mater. Sci. Eng. A 898, 146399.

Zhang, Y., Chen, Y., Zhou, J., Sun, D., Li, H., 2020. Experimental and numerical study on microstructure and mechanical properties for laser welding-brazing of TC4 Titanium alloy and 304 stainless steel with Cu-base filler metal. J. Mater. Res. Technol. 9, 465–477.

Zhang, Y., Huang, J., Chi, H., Cheng, N., Cheng, Z., Chen, S., 2015. Study on welding–brazing of copper and stainless steel using tungsten/metal gas suspended arc welding. Mater. Lett. 156, 7–9.

Zhang, Y.M., Liu, Y.C., 2007. Control of dynamic keyhole welding process. Automatica 43, 876–884.

Zhao, J., Wu, C., Shi, L., 2022. Effect of ultrasonic field on microstructure evolution in friction stir welding of dissimilar Al/Mg alloys. J. Mater. Res. Technol. 17, 1–21.

Zhao, Y., Long, Y., Li, Z., 2022. Research progress of transition layer and filler wire for laser welding of steel and aluminum dissimilar metals. Int. J. Adv. Manuf. Technol. 1–10.

Zhao, Y., Zhang, Y., Hu, W., Lai, X., 2012. Optimization of laser welding thin-gage galvanized steel via response surface methodology. Opt. Lasers Eng. 50, 1267–1273.

Zhou, J., Zhou, D., Liu, J., 2022. Effect of oscillating laser beam on the interface and mechanical properties of Ti/Al fusion welding joint. J. Mater. Res. Technol. 19, 1993–2007.

Zhou, W., Jia, C., Zhou, F., Wu, C., 2023. Dynamic evolution of keyhole and weld pool throughout the thickness during keyhole plasma arc welding. J. Mater. Process. Technol. 322, 118206.

Zhou, Y., Cheng, L., Li, Y., Wang, J., Zhan, X., 2024. Interfacial microstructure evolution and mechanical properties in laser welded Invar alloy/TC4 dissimilar joints. Intermetallics 166, 108171.

Zhou, Y., Hu, A., Khan, M.I., Wu, W., Tam, B., Yavuz, M., 2009. Recent progress in micro and nano-joining, in: Journal of Physics: Conference Series. IOP Publishing, p. 012012.

Zhu, L., Zhou, Q., Song, C., Liu, L., Zhang, L., Fan, K., Zhang, Y., Lu, H., Hu, Q., Sheng, Z., 2024. Microstructure and mechanical properties of T2 copper/316L stainless steel explosive welding composite with small size wavy interface. J. Mater. Res. Technol. 28, 668–682.

Zolfaghari, Abolfazl, Zolfaghari, Amin, Kolahan, F., 2018. Reliability and sensitivity of magnetic particle nondestructive testing in detecting the surface cracks of welded components. Nondestruct. Test. Eval. 33, 290–300.

Zubairuddin, M., Albert, S.K., Chaudhari, V., Suri, V.K., 2014. Influence of phase transformation on thermo-mechanical analysis of modified 9Cr-1Mo steel. Procedia Mater. Sci. 5, 832–840.

Bibliography

Dawes, C.T., 1992. Laser welding: a practical guide. Woodhead Publishing.

Feng, Z., 2005. Processes and mechanisms of welding residual stress and distortion. Elsevier.

Friedman, E., 1975. Thermomechanical analysis of the welding process using the finite element method.

Granjon, H., 1991. Fundamentals of welding metallurgy. Elsevier.

JF lancaster Metallurgy of welding 5th edition, chapman and hall, 1993, pp. 158-159.

Khan, M.I., 2007. Welding science and technology. New Age International.

Kou, S., 2003. Welding metallurgy. N. J. USA 431–446.

Lippold, J.C., Kotecki, D.J., 2005. Welding metallurgy and weldability of stainless steels.

Timings, R., 2008. Fabrication and welding engineering. Routledge.

Zhou, Y.N., 2008. Microjoining and nanojoining. Elsevier.

Indian Institute of Technology Guwahati

भारतीय प्रौद्योगिकी संस्थान गुवाहाटी • Indian Institute of Technology Guwahati •

List of Publications

Referred Journals

1. **S. Dwibedi** and S. Bag: Tailoring microstructural properties of dissimilar fusion welding to weld-brazing by arc offset, ***Metallography, Microstructure, and Analysis***, 14(6), 1149-1170, 2025.

2. **S. Dwibedi** and S. Bag: Optimizing heat input in continuous and pulse current mode to control defect formation and weld properties in cupronickel alloy, ***Journal of Materials Engineering and Performance***, 34(17), 19572–19590, 2025.

3. **S. Dwibedi**, B. Kumar and S. Bag: Phase transformation effect on residual stress development in fusion welding of dissimilar stainless steels with different thickness, ***Archives of Civil and Mechanical Engineering*****,** 24, 148, 2024.

✦4. **S. Dwibedi** and S. Bag: Critical assessment on the influence of process parameters in micro-plasma arc welding process: A Review, ***Welding International***, 38(9), 583-617, 2024.

5. **S. Dwibedi** and S. Bag: Joint Characteristics of Cu-Ni Alloy Fabricated by GTAW and MPAW Processes: A Comparative Study, ***Indian Welding Journal***, 57(1), 40-50, 2024.

✦✦6. **S. Dwibedi** and S. Bag: Development of micro-plasma arc welding system for different thickness dissimilar austenitic stainless steels, ***Journal of The Institution of Engineers (India): Series C***, 102(3), 657-671, 2021.

✦✦✦7. **S. Dwibedi** and S. Bag: Influence of process parameters on microstructural evolution, solidification mode and impact strength in joining of stainless steel thin sheets, ***Advances in Materials and Processing Technologies***, 8(Sup3), 1089-1104, 2021.

Book Chapter and Conference Proceedings

8. **S. Dwibedi** and S. Bag, D. K. Lodhi and A. Kalita: Joining of different thickness dissimilar materials SS 316l/SS 310 by µ-PAW process, In: Shunmugam, M., Kanthababu, M. (eds), ***Advances in Additive Manufacturing and Joining*****:** Lecture Notes on Multidisciplinary Industrial Engineering. Springer, Singapore, pp. 569-578, 2020.

TH-3924_166103014

9. **S. Dwibedi** and S. Bag: Assessment by destructive and non-destructive approach to characterize 90/10 cupronickel weldments, ***Materials Today: Proceedings**,* 33 (8), 5014-5018, 2020.

✦**Best Paper Award,** selected by The Editors of Welding International Journal (Talyor & Francis Group), as one of the three distinguished papers for the year 2024.

✦✦**Awarded Corps of Electrical and Mechanical Engineers' Prize** for the Paper Titled Development of Micro-plasma Arc Welding System for Different Thickness Dissimilar Austenitic Stainless Steels under Production Engineering Division Board (PRDB), The Institution of Engineers (IEI) (India), 16th December 2022.

✦✦✦**Best Paper Award** during the 12th International Conference on Materials Processing and Characterization (12th ICMPC) conference held at National Institute of Technical Teachers' Training and Research (NITTTR), Chandigarh, India from 6th-9th October 2021.

Indian Institute of Technology Guwahati

भारतीय प्रौद्योगिकी संस्थान गुवाहाटी
Indian Institute of Technology Guwahati